Study of the Strangeness Photoproduction Process in the $\gamma d \rightarrow \Lambda X$ Reaction at Photon Energies up to 1.08 GeV

東北大学

Brian O'Neil Beckford

Graduate School of Science, Department of Physics

Tohoku University

A thesis submitted to the Graduate School of Science and Department of Physics
in partial fulfillment of the requirements of

Doctor of Philosophy in Physics (Ph.D.)

2012

Inspiration

> Without education he lives within the narrow, dark and grimy walls of ignorance. Education, on the other hand, means emancipation. It means light and liberty. It means the uplifting of the soul of man into the glorious light of truth, the light by which men can only be made free. To deny education to any people is one of the greatest crimes against human nature.

Frederick Douglass

> Fall in love with some activity, and do it! Nobody ever figures out what life is all about, and it doesn't matter. Explore the world. Nearly everything is really interesting if you go into it deeply enough. Work as hard and as much as you want to on the things you like to do the best. Don't think about what you want to be, but what you want to do. Keep up some kind of a minimum with other things so that society doesn't stop you from doing anything at all.

Richard P. Feynman

> A true leader is not a seeker of consensus, but instead, is a molder of consensus.

Dr. Martin Luther King Jr.

> A man is as old as his arteries and as young as his ideas.

Bruce Lee

> It's not that I'm so smart, it's just that I stay with problems longer.

Albert Einstein

Who in the world am I? Ah, that's the great puzzle.

Lewis Carroll

Emancipate yourself from mental slavery, none but ourselves can free our minds

Robert Marley

You see things; and say, Why?
But I dream things that never were; and I say, Why not?

George Bernard Shaw

This thesis is dedicated to the memories of Miguel Angel Escobar and Professor Osamu Hashimoto.

Acknowledgements

Where does one start on the task of pointing out the significant people that have helped one along the way, the easiest way is to simply praise them in name: Claudia Dardon (CD), Esther Oziel (Blondie), Malika O. Beirstein (Malik) and the entire Bierstein entourage, Joseph Rojas (J-Rhyme), Emmanuel Calixte (Stephan), Dr. Luis Lebolo (Morde), Priscilla Pamela (Pris-cilla), Cristobal Ceron (Padawan), Dr. Vannessa Gautney-Werner, Robert Alvarez (Rob), Dennis John Moore (DJ), Pablo de Souza, Chester N. McDonald (Nick), Michael McKinney (Mr. Pink), Mary Lou PFieffer, and Elizabeth Perez (Liz).

To some of my past instructors and mentors: Prof. Brian Raue, who can teach any course, Prof. Pete Markowitz, Prof. Oren Maxwell, Prof. Minna Shore, Dr. Harold Shore, Prof. Paul Draper, Dr. J. Scott Hamilton, James Gilham, Yaiqumi Pla, and Frank Nieves,

I am sincerely thankful to the assistance of Abe A. Bailey in a most troublesome period of my young adult life.

I must specifically thank Prof. Joerg Reinhold that has been a mentor, teacher, and most importantly a friend. Through various obstacles that would have deterred most professors from continuing to assist a student, you have continued to be in my corner.

My sincerest thanks are expressed to the late Professor Osamu Hashimoto for providing me with the chance to study at Tohoku University. It has been a unique learning experience filled with more than a handful unforeseen challenges, broken wires, shattered timelines, and tremors of the earth. However, it has been a rewarding and life changing experience. I thank you for guiding my growth and for not quitting on me, even when I felt like quitting on myself. I was honored to have met you. There was always a sense of comfort in your presence, and a genuine tone to your words. I think that you truly cared about my well being not only as a student, but as a person. It was unfortunate that you passed prior to the completion of the thesis, but I have endeavored to produce something that you would be proud to have been associated with. Be at peace.

To all the members of the ELPH research facility, the professors, staff, and to the past and present students of the experimental nuclear and middle energy physics group at Tohoku University. In particular, I am thankful to Dr. K. Futatsukawa, Dr. Y. Ma, Dr. Y. C. Han, Dr. K. Shirotori, and soon to be, Dr. T. Gogami, Dr. K. Hosomi, Dr. C. Kimura, Dr. T. Fujii and Dr. F. Yamamoto. I am forever indebted for your endless patience and unwavering commitment to helping me further my education. I am thankful to Mr. N. Chiga and Mrs. M. Shimaya for granting me so much of their time and patience.

I would like to specially thank Prof. Masashi Kaneta, for his help with the drift chamber tracking analysis and for tolerating my endless questions. To Takeshi Koike, by your actions, your gentle nature, and deep and penetrating words I have learned so much, and still have much to learn. I hope one day to become the type of genuine and compassionate being that you are.

I am grateful to Prof. Satoshi N. Nakamura, Prof. Hirokazu Tamura, Prof. Hiroki Kanda and specifically Prof. Kazushige Maeda whom became my advisor late in the game. He was always willing and able to provide me with his patience and guidance, and was able to deal with my unique nature.

This research was possible due to the funding provided though IGPAS-SDC program and fellowship. Special thanks is extended to Ms. Yamada and Mrs. Hori of the DIRECT department.

In the pursuit of a life of higher education that is balanced with a fulfilling personal life, I have had the honor of meeting and learning everyday what is means to be a friend from Dr. Alejandro De la Puente. We started the journey towards the completion of a PhD in physics together and though we went onto different paths, I could have never accomplished half of what I did, without you being there. You are probably the smartest, kindest and most humble person I have ever met. There have been many times during the course of our friendship when one of us has carried the other. These times have made our friendship stronger and it is one that I trust will continue.

To the woman to whom I owe so much, Thelma Swabby, I will never forget the happiest times of life with you nor shall I ever neglect to remember the numerous life lessons that you shared with me.

To my family, near and far, I am who I am, and what I will become only because you have always believed in me. To the one of the strongest women I have ever met, my grandmother Mavis Coke, it is only by the strength that

you have passed on to me that I can do anything.

To my brother, Dean Beckford, who has been so much more. Anything I have ever accomplished would not have been possible without your endless encouragement and enduring belief in me.

For my mother, Millicent Beckford, absolutely the strongest, most independent, determined and supporting person that I have had the chance to know. I'm always proud of her. Even though we were not wealthy, I never felt not provided for nor not loved. She taught me and gave me the most important things a mother can give and none of which were material, nor can be purchased with money. I am most fortunate to have someone in my corner that has always supported me from the rural concrete jungle of Jamaica to the urban street corners of Miami, and to the paved sidewalks of Japan. You have always said how you don't understand how I do the many things I do, how I maintain my drive, and don't give up. You have wondered how my interests span mythology, design, drawing, chess, budo, physical fitness, photography, science, philosophy, and others. Simply, I believe in the wonder of our existence. I believe in myself, but mostly I believe in you. I treasure you.

Nothing is possible without help and support. To all those that have made the contributions to help me along my path, though I did not mention you by name, you have my thanks.

Declaration

The data presented in this thesis was gathered in experiments performed by the NKS2 collaboration at the ELPH research facility, Tohoku University, Sendai, Japan. I hereby declare that I have written without the prohibited assistance of third parties and without making use of aids other than those specified. Contributions taken over directly or indirectly from other sources have been identified and cited as such. This dissertation has not previously been presented in identical or similar form to any other examination board. The thesis work was conducted from October 2008 to 2012 under the supervision of Professors Osamu Hashimoto and Kazushige Maeda at Tohoku University.

Brian O. Beckford

Abstract

Exploration of the photoinduced production of strangeness has been meticulously investigated on the proton and as of late the prominence is being veered to the neutron to ascertain a comprehensive description of the process for all isospin channels. Since a free neutron target is inaccessible, and in virtue of the low binding energy of deuteron, it serves as an effective target to provide a loosely bound neutron. Reactions on the deuteron can also be compared to results on a free proton to gain insight into the nuclear medium effect.

Substantial effort was placed on advancing the investigation on the neutron and due to the favorable outcome of previous experiments with the Neutral Kaon Spectrometer (NKS) and NKS2 experiments [1, 2, 3] at the Research Center for Electron Photon Science (ELPH), Tohoku University in Sendai Japan, the spectrometer was upgraded by the replacement of the inner detectors in order to improve upon the acceptance.

This thesis reports on the inclusive measurements of Λ in the $\gamma d \rightarrow \Lambda X$ reaction at threshold energies. Exploratory data with the upgraded NKS2+ was taken at ELPH in 2010. The experiment was performed with tagged photon beams in the range of $0.8 \leq E_\gamma \leq 1.08$ GeV that were directed to a liquid deuterium target positioned as the center of the spectrometer. The produced Λ (roughly 400 events) was detected in the $p\pi^-$ decay channel with a corresponding width of 2.87 ± 0.19 MeV/c (σ).

The focus of the work has been the determination of the energy dependence of Λ photoproduction, the momenta and angular distributions and also reports on the recoil polarization. The integrated cross sections of the $\gamma d \rightarrow \Lambda X$ reaction in the angular integration regions of $0.9 \leq \cos\theta_\Lambda^{LAB} \leq 1.0$ and $0.75 \leq \cos\theta_\Lambda^{LAB} \leq 1.0$ were derived and compared with the experimental results of the NKS2 [4, 5]. In addition, the momentum spectra for two separate photon energy ranges, of $0.9 \leq E_\gamma \leq 1.0$ and $1.0 \leq E_\gamma \leq 1.08$ GeV was also procured. The differential cross section as a function of the Λ scattering angle in the laboratory was additionally deduced. The Λ recoil polarization was determined for three energy ranges, $E_\gamma = 0.90-1.0$, $0.95-1.05$ and $1.00-1.08$ GeV. Incor-

porating results of theoretical calculations, the total cross section of $\gamma d \to \Lambda X$ and $\gamma d \to K^0 \Lambda p$ were approximated and the latter compared with published findings.

The results were compared to a handful of contemporary theoretical calculations, in particular, the Kaon-MAID (KM) [6] and Saclay-Lyon A (SLA) [7] isobar models, and the more recently introduced Regge-Plus-Resonance (RPR-2007) model [8, 9]. Regarding the measured cross sections of the angle integrated Λ momentum dependent differential cross sections, the KM calculations replicate the general shape of the distributions in both energy bins and scattering angles. Nonetheless, it was deficient in converging with the magnitude at the most forward angles, in which it underscored the cross section by approximately 20-40% at Λ momenta between $0.65 \leq P_{\Lambda}^{LAB} \leq 0.90$. GeV/c. On the other hand, the SLA model calculations had an admirable consensus with the shape and magnitude of the data with $r_{K_1 K_\gamma} = -1.4$, where $r_{K_1 K_\gamma}$ is a free fitting parameter for the photo-coupling in the t-channel that arises from the ratio of the charged and neutral channels ($r_{K_1 K\gamma} = g_{K_1^0 K^0 \gamma}/g_{K_1^+ K^+ \gamma}$).

The RPR model produces an impressive description for the results of the integrated and total cross sections in both angular hemispheres, and exceptionally reproduces the shape of the angular distributions in all measured energy bins. The SLA model with a fitted coupling constant of $r_{K_1 K_\gamma} = -1.4$, exhibit fairly good agreement with the data, describing well, the shape of the momentum and angular distributions, and most significantly the energy dependent integrated cross section. The KM calculations under predict the integrated and total cross sections by roughly 20%.

The results reported in this dissertation are consistent across the board with the previous $\gamma d \to \Lambda X$ measurement and the estimated $\gamma d \to K^0 \Lambda p$ cross section of the NKS2 collaboration [4], as well as with SLA predictions. The most significant conclusion that can be drawn is the relatively equivalent magnitude of the $\gamma d \to K^0 \Lambda p$ and $\gamma p \to K^+ \Lambda$ processes, which are predicted to have strikingly dissimilar cross sections, here I conclude that they are in fact on par.

LIST OF FIGURES

LIST OF TABLES

LIST OF TABLES

CONTENTS

CHAPTER

ONE

INTRODUCTION

> Each of us, in our own way walks a path. Some of us are further along than others, some of us have stumbled and lost out way in the forest. Some have taken a simple and straight forward path, others have to take a long, grueling and little-traveled road.

Wayne Muromoto.

1.1 Overview and Structure of the Thesis

The reaction of interest discussed in this thesis is the photoproduction of neutrally charged strange particles, Λ and K^0, from a deuteron target, particular focus has been placed on the production of the former. The first chapter will briefly review the current description of nuclear structure. It will then discusses existing experimental data, present the motivation for studying this reaction, the relevance of its study and clearly identifies the aim of this particular study. The second chapter explains the kinematics involved in the $\gamma n \rightarrow \Lambda K^0$ reaction, and proceeds to review existing theoretical models. The third chapter is concerned with the experimental hall, beam line and apparatus. The fourth chapter shall expound upon the calibration of data, the data analysis technique, and the assessment of the various analysis efficiencies. The fifth chapter presents the experimental findings, including the results of the inclusive measurements of the incident photon energy dependence of the integrated cross section, the momentum and angular distributions, as a function of the Λ scattering angle and the results of the Λ recoil polarization. That chapter closes with a comparison of the results to previous NKS2 experimental results. The thesis moves to a discussion of the findings, where they are extensively compared to the

predictions of the few current theoretical calculations. It concludes with brief summary and treatise on findings.

1.2 Nuclear and Hadron Physics

A concise description of the structure of matter and the interactions betweens its constituents at the nuclear scale are the focus of the research conducted by a nuclear physicist. The goal of course is to understand the nature of matter, the means is studying the nucleus [39]. The motivation to conduct nuclear experiments lie profoundly in the rich and complex structure of nuclei, of which, the fundamental forces that serve to hold the very fabric of nature together are still not fully understood. Moreover nucleons are the stuff all things are originated from [40], which are a vast, intricate world, similar to wonderland if one was actually able to stroll around. By studying nuclei and the forces that play the dominant role at that scale, we can determine the cardinal originator and strength of the interactions. The nuclear force is a residual leakage of the force of quark interactions and the most intriguing aspect of the study of nuclear physics. The nucleon is not a point particle but a composite structure of more intricately complex objects and our understanding of one the basic forces of nature is still far from thoroughly unraveled.

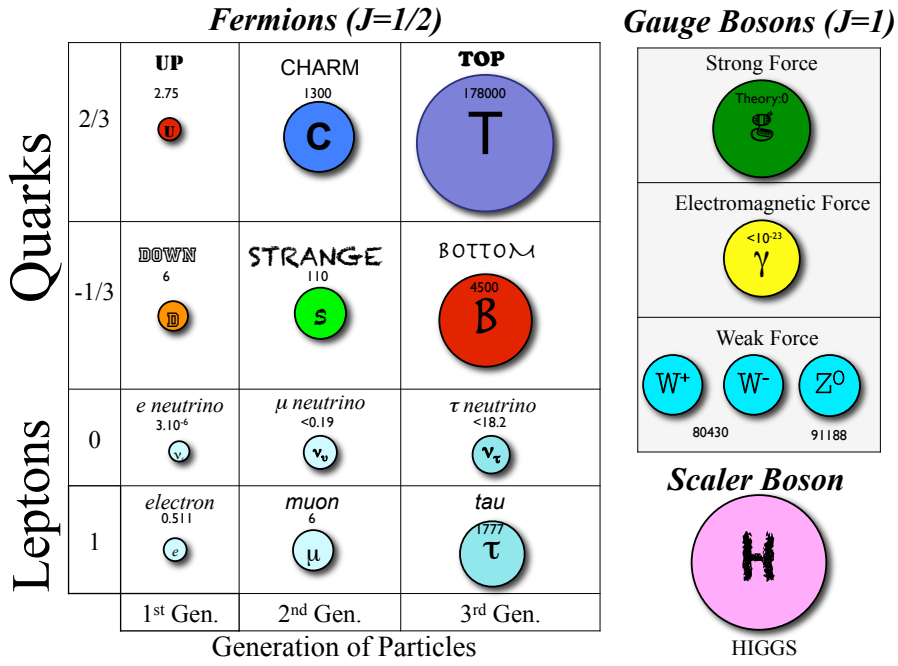

Figure 1.1: The contemporary description of subatomic particles and forces is called the standard model.

Matter as we know it presently, is formed from particles that all carry an intrinsic spin of $\frac{1}{2}$ and are named fermions, which include two types of particles that are believed to have no further internal structure and thus considered point like in their nature. Quarks and leptons are the name of these so-called structureless point like particles. Classically and by Quantum Field Theory (QFT) forces are propagated through a field and before that, the mysterious ether. All interactions are thought of being mediated by a particle in the present standard model shown in Figure 1.1. The figure is an none realistic image of the particle sizes, and the difference in spheres is to simulate the differences in mass. The standard model states that interactions are achieved via the exchange of particles defined as gauge bosons. There are four fundamental forces, but not simply four analogous force-carrying particles. There are eight generators of the strong nuclear force that correspond to eight gluons. The weak interaction is mediated by three distinct particles, and at present time there is no concise quantization of the gravitational force. The distinguishing properties of the gauge bosons are all have an integer spin of 1. The quarks are denoted as q were experimentally observed to also have an antiparticle with an opposite sign in their quantum numbers denoted as $\bar{q}$. All matter assembled from combinations of quarks are defined as hadrons and are held together by the strong force. Hadrons are composed of quarks that interact between each other by the means of a mediator termed gluons, can be subdivided into either baryons or mesons. Those that are by the combination of three quarks, resulting in a "white" or color neutral particle, due to the additional color property of quarks are called Baryons. At the moment, success in the resolving a cartogram of the baryon spectrum is still nestled in the forefront of hardon physics. Nucleons are the lowest mass baryons, where the proton is a combination of (uud) and the neutron (udd). Quark and anti-quark pairs form mesons, which at the nuclear level is the mediator of the strong nuclear force predicted by Yukawa. The lightest meson observed is the pion (π), existing in three possible charged states (π^+, π^-, π^0). The ground state spin $\frac{1}{2}$ baryons and pseudoscaler mesons can be grouped in such a way that they form an octet and nonet of which the typical arrangement structure is shown in Figure 1.2. The red and light blue axes are associated to the charge and strange number of the mesons or baryons respectively.

1.3 History of Strangeness Photoproduction

The analysis of cosmic ray experiments revealed the discovery of a neutral particle that subsequently decayed at rest into two charged particles. These charged particles were actually a proton and a negatively charged pion. This neutral particle, thereafter named Λ, was a baryon whose mass was a bit heavier than that of the nucleons. Most intriguing

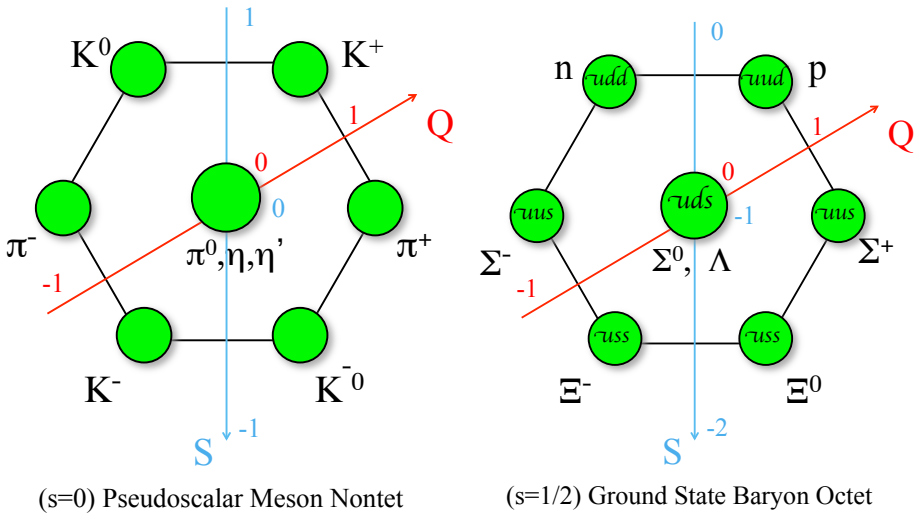

Figure 1.2: Baryon ground state octet (left) and psuedoscaler meson nonet (right)

in its discovery was in its production by the strong interaction but decaying weakly, a characteristic of strange particles [41].

Investigation of the physical process of strangeness production has been carried out since the middle of the last century, but more recently, production by the electromagnetic interaction is gaining stronger interest and has moved to the forefront of contemporary hadron physics, thanks to new accelerator facilities and advanced detector systems. A couple of pioneers of strangeness physics were H. Thom and T. Kuo [42, 43] in the 1960's. The earliest analysis of photoproduction experiments were conducted on bubble chamber data from DESY [44] and SLAC [45] and at the 2.5 GeV electron synchrotron in BONN [46] now used in ELSA experiments.

The production process facilitates the creation of strange quark anti-quark pairs from the sea of the nucleon, and thus, introduces an additional degree of freedom, in addition to numerous nucleon and resonance states that are nonexistent in a non strange reaction [39]. Most central to this quark anti-quark production mechanism is the latent prospect to study the nucleon's composition [26]. The creation of kaons is always paired with the production of hyperons in order to satisfy conservation of strangeness. It is now recognized that strangeness production experiments conducted at lower energy are excellent tools to reveal that the elementary production process. Therefore, the investigation into Λ and kaon photoproduction imparts vital information describing the strangeness production mechanism [20].

The exploration into strangeness production in the threshold energy region allows for the frontier of physics to be explored, particularly concerning the experimental measure-

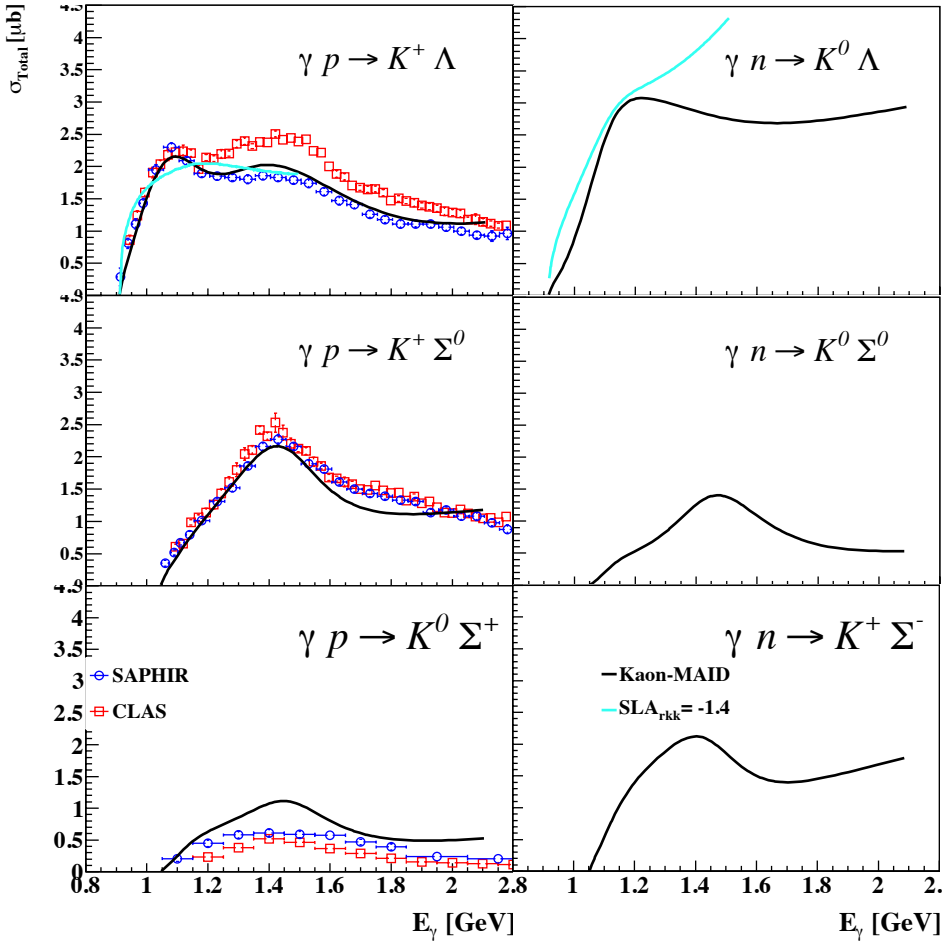

Figure 1.3: Total cross sections of kaon photoproduction on nucleons. The curves are predictions based on Kaon-MAID and Saclay-Lyon A calculations to the most recently reported SAPHIR and CLAS data [10, 11, 12, 13, 14, 15, 16].

ment of the photo-produced Λ particle's momentum and angular distribution. A clearer understanding of elementary strangeness production process provides the necessary framework for hypernuclear study, which views the multi-body system using strangeness as a degree of freedom. The Λ hyperon consists of a bound state of up, down, and strange quarks, and is an outstanding probe to investigate the nuclear structure, where a normal nucleon could not. This is attributed to the fact that it is a mirror reaction to the $p(\gamma, K^+)\Lambda$ reaction, for which there is quite a bit of experimental data. Therefore high quality data on the elementary photoproduction process will in turn reduce uncertainties in calculation of the electroproduction of hypernuclei [47]. More importantly, it offers key data to theoretically analyze hypernuclear reaction spectra, which only recently became possible to be measured at JLab.

There has not been much effort placed on exploring strangeness by the electromagnetic interaction in respect to neutral channels. In particular, the neutral kaon channel on a neutron partly due to the difficulty of detecting neutral kaons and procuring a suitable target. The direct result of insufficient high quality data has severely stymied the progress of theoretical studies. The current theoretical models have been constructed based mainly on the copious available data of $\gamma p \rightarrow K^{+}\mathrm{Y}$ reactions, which naturally describe well the K^{+} data as seen in Figure 1.3. In Figure 1.3, the data of the SAPHIR experiment summarized in reference [10] is shown. As mentioned, for a reaction near the threshold energy region, many resonances can be suppressed or excluded in the modeling approach, therefore making the theoretical interpretation simpler.

1.4 Recent Experimental Exploration

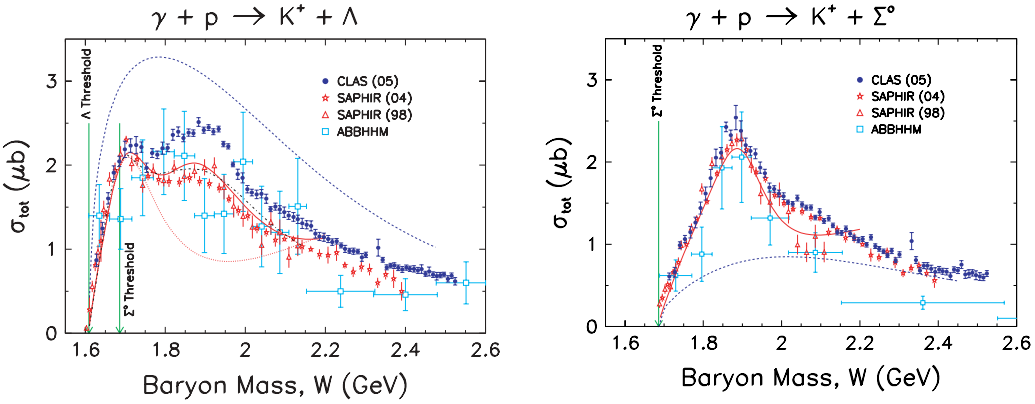

Figure 1.4: Total cross sections of $\gamma p \rightarrow K^{+}\Lambda(\Sigma)$ for the two publications of SAPHIR[11, 12], the ABBHHM collaboration, and the CLAS results. The figure was taken from reference [13].

At present there has been extensive experimental investigation of the elementary kaon photoproduction process on a proton target via the $p(\gamma, K^{+})\Lambda(\Sigma)$ reaction by measuring cross sections and some polarization observables at facilities including JLab(CLAS)[13, 14, 15, 16], Spring-8(LEPS)[48, 49], ELSA (SAPHIR)[11, 12], GRAAL [50, 51] and the MAMI [52]. JLab has a continuous electron beam accelerator that delivers a 6 GeV electron beam into the experimental halls A, B, and C for congruent experiments. Hall A has two high resolution spectometers, Hall B is home to the Large Acceptance Spectrometer (CLAS) and Hall C has two spectrometers, one for short lived particles and the other for high momentum particles. Spring-8's (Laser electron photons at SPring-8) (LEPS) is a detector that has a tagged photon beam with energies up to 2.4 GeV produced from a 8 GeV stored electron beam. The Electron Stretcher Ring (ELSA) began its operation in the late 1980's has dual capabilities to act as a storage ring for synchrotron radiation or as

a pulse stretcher providing a continuous electron beam up to 3.5 GeV. The were a handful of detectors stationed there including Phoenics [53], ELAN [54], GDH [55], SAPHIR, and CBELSA based on the Crystal Barrel detector [56]. The GRAAL experiment is situation at the European Synchrotron Radiation Facility (ESRF) using tagged and polarized photon beams. The electron accelerator MAMI is made up of three racetrack microtrons and a harmonic double-sided microtron [52].

Very recently, few collaborations have used a liquid deuterium target in experiments and have measured neutral kaons in the $\gamma p \rightarrow K^0 Y(\Lambda\Sigma)$ reactions at ELSA and MAINZ [33, 57]. Prior to the decommissioning in 1999, the SAPHIR group reported on the total, differential cross sections and hyperon polarizations in the afore mentioned reactions. The results confirmed that the cross section quickly climbs at 1.1 GeV, plateaus and the declines at photon energies close to 1.45 GeV. The published results in 2004 by SAPHIR were significantly consistent with the previous SAPHIR data. It was their conclusion that there are indeed strong contributions of resonances to the production of Λ at threshold energies and for (Λ, Σ) at approximately 1.45 GeV. It was also found that the hyperons (Λ, Σ^0) are intensively polarized and are produced with opposite polarization signs [11]. At the time of publication, the CLAS collaboration reported the largest set of data for these reactions at photon energies of 1.6$-$2.53 GeV and angles of $-0.85 \leq \cos\theta^{CM}_{K^+}$ 0.95. The total cross section of the $\gamma p \rightarrow K^+\Lambda$ reaction for the CLAS (blues circles), SAPHIR (98) (red stars), SAPHIR (04) (red triangles) and the ABBHHM collaboration [58] (blue squares) are seen in Figure 1.4. The curves are shown for the Regge model, the Kaon-MAID model with the $D_{13}(1895)$ resonance turned off, and Saghai as the dashed blue, solid red and dashed dotted curves respectively. Precise measurements of hyperon recoil polarization and beam asymmetries has also been an experimental focal point of the ESRF (GRAAL) and CLAS collaborations. The CLAS results were fitted to phenomenological descriptions and were well described after the inclusion of the two star resonance $P_{13}(1900)$, where its mass and width are estimated to 1915 $\pm$ 50 MeV and 180 $\pm$50 MeV [14, 59]. Photon asymmetry, double polarization observables O_x and O_z, hyperon recoil polarization and target asymmetry were reported for both $d(\gamma, K^0)\Lambda(\Sigma)$ processes over a large energy range and were compared with the theoretical predictions of Kaon-MAID and Regge-Plus-Resonance models. They found that the photon asymmetry for $K^0\Lambda$ were positive in the forward hemisphere and hinted to a negative value in the backward regions. The hyperon recoil polarization were comparable for forward angles with an increase in photon energies for both the bound neutron and free proton targets [60].

1.5 Strangeness Experiments at LNS/ELPH

Strangeness production explored through the neutral channel, in which there are no charged particles in the $\gamma n \rightarrow K^0\Lambda$ reaction, will bestow the chance for revealing fundamental details governing the processes by emphasizing on the unique processes diagrammatically. Contemporary predictions of recent phenomenological models for $K^+\Lambda$ on a proton are inconsistent for the case of $K^0\Lambda$ production on a neutron, which readily demonstrates the lack of the current understanding of models of strangeness photo production. The first observation of neutral kaon events by a magnetic spectrometer was successfully carried out using the TAGX spectrometer at the 1.3 GeV electron synchrotron of INS, University of Tokyo [61]. However, the statistics of the exploratory report were significantly poor. This lack of reliable experimental data for neutral kaon photoproduction encouraged the start of an experimental program to study photoproduction of neutral kaons off deuterons, by installing the Neutral Kaon Spectrometer (NKS) at the Laboratory of Nuclear Science (LNS) of Tohoku University. At this time, a study into the fundamental physics that determines the strangeness process in threshold region, that of 0.8-1.1 GeV, cannot be accomplished at any other facility, to the high precision available at the Research Center of Electron Photon Science (ELPH), Tohoku University.

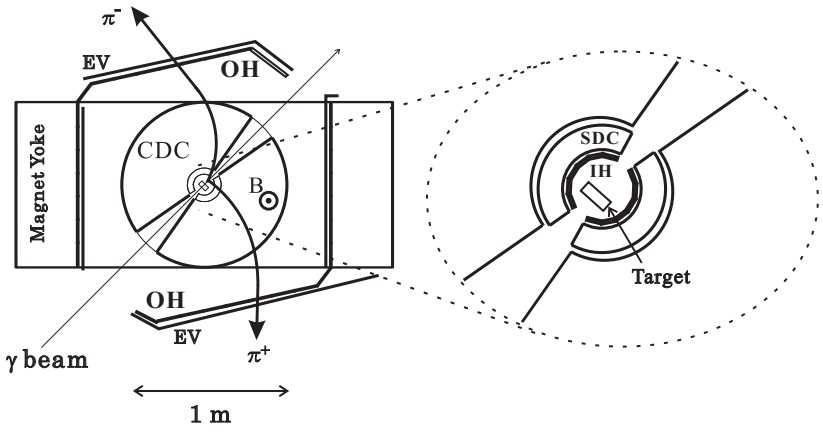

Figure 1.5: A schematic view of NKS. The figure illustrates a slice of the spectrometer along the beam plane. The inner detectors are shown in the right zoomed image. Details of the NKS spectrometer can be referenced in [17].

The NKS and NKS2 collaboration have pioneered the experimental research of strangeness photo-production via the reaction of $\gamma n \rightarrow K^0\Lambda$ near the threshold ($E_\gamma = 0.914$ GeV). The experiments were performed using two generations of magnetic spectrometers, Neutral Kaon Spectrometer and Neutral Kaon Spectrometer 2. The experimental research program was first conducted with the NKS which was based on the quarter-size cyclotron

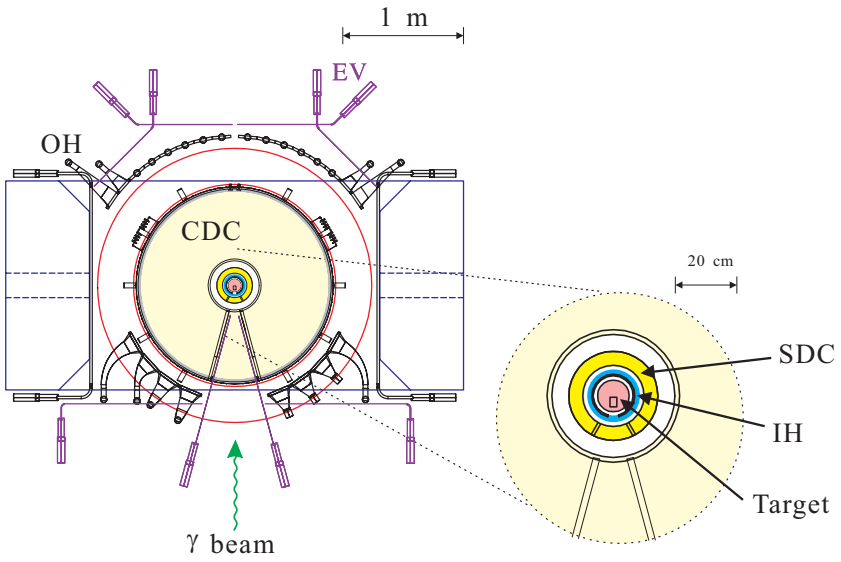

Figure 1.6: A schematic view of NKS2. The figure illustrates a slice of the spectrometer on the beam plane. The inner detector package is shown in the right zoomed image, where it clear the NKS2 covered the forward region that the NKS lacked in its design. Details of the NKS2 spectrometer can be referenced in [5]

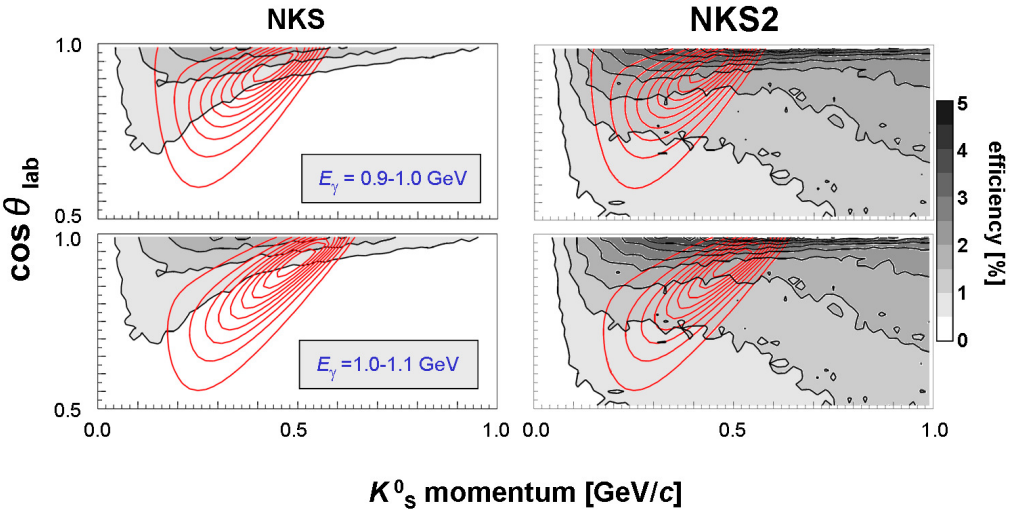

Figure 1.7: Comparison of the acceptance for K^0 for the NKS (left) and NKS2 (right) spectrometers. The red online curves are the theoretical distributions of K^0 estimated by Kaon-MAID and the black lines are the efficiency simulated by GEANT4.

model magnet, TAGX magnet, and yielded ground breaking and quite encouraging results of neutral kaon photo-production measurement.

Following this, a newly constructed second-generation neutral kaon spectrometer (NKS2) utilizing the Tohoku university K=50 MeV cyclotron magnet was commissioned. The NKS2 incorporated a completely renewed central drift chamber (CDC). Figures 1.5 and 1.6 shows the schematic views of the detectors for the previous incarnations. In the first inception of the NKS, the forward and backward regions of the spectrometer were void of detectors for the purpose of quelling the background. The ramifications of such a design was a limited geometrical acceptance, singularly with respect to the forward region. The analysis of the data focused on the $K^0_S \rightarrow \pi^+\pi^-$ decay mode to obtain and identify K^0 events. Finalized results from the NKS experiment that were performed on a carbon target lead to the conclusion that the angular distribution in $n(\gamma, K^0)\Lambda$ reaction was modestly partial to the backward direction in the center-of-mass reference frame [62]. The findings of the integrated cross section for kaon photoproduction off a carbon target are visible in Figure 1.8. These results were for the laboratory frame of reference. The angular integration region for K^+ and K^0 were $10^0 \leq \cos\theta^{Lab}_K \leq 40^0$ and $0.8 \leq \cos\theta^{Lab}_K \leq 1.0$ [1, 18] are shown as the black solid circles and open red triangles respectively in Figure 1.8. Though the angular integration regions slightly differed it can be inferred that the photon energy dependence of K^+ and K^0 photoproduction are roughly on the same order in magnitude.

The reported data provided the first measured information in the neutral channel and demonstrated the importance of the $n(\gamma, K^0)\Lambda$ reaction for the investigation of the strangeness photo-production [1]. These earliest data of the neutral kaon photo-production on a neutron was measured by NKS collaboration and the obtained results has since been published [2, 3]. The K^0 momentum dependent spectra of the measured by the NKS collaboration is displayed in Figure 1.9 along with comparisons to theoretical predictions, where a plane wave impulse approximation (PWIA) was used for spectator kinematics. In the figure the differential cross section for forward angles of $0.9 \leq \cos\theta^{Lab}_K \leq 1.0$, and two photon energy bins of $0.9 \leq E_\gamma \leq 1.0$ and $1.0 \leq E_\gamma \leq 1.1$ are given as (a) and (b) respectively.

As an outcome of the series of the NKS experiments, the re-envisioned Neutral Kaon Spectrometer, NKS2, was newly designed and constructed at LNS in 2004, replacing the original version. Its main purpose was to investigate the photo-production process, particularly the production of neutral strange particles via single K^0 and Λ measurement with an acceptance less biased in the forward region compared with the NKS spectrometer. The NKS2 covered the forward region where NKS crucially lacked acceptance for K^0 as shown in Figure. 1.7, where a comparison of the acceptance for the NKS and NKS2 are given left to right respectively. The systematic error of $\sim$15% was estimated by the data and Monte-Carlo simulation.

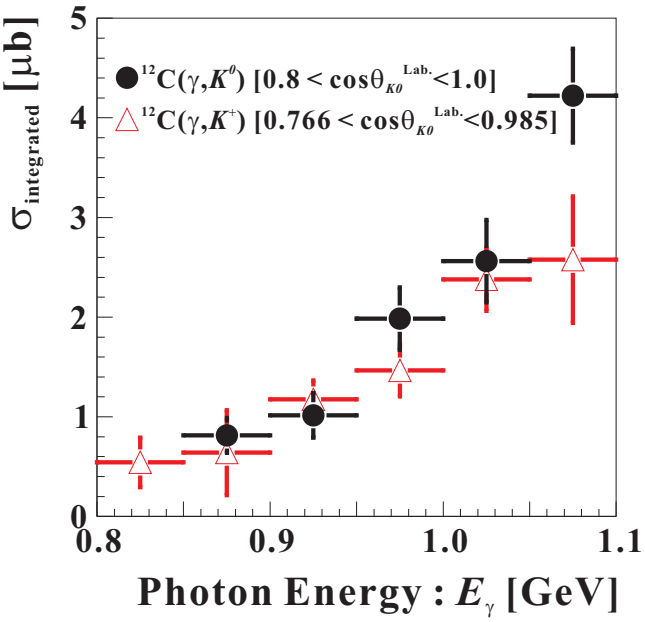

Figure 1.8: The integrated cross section for kaon photoproduction off a carbon target. The results are provided for the laboratory frame of reference, for K^+ integrated over $10^0 \leq \cos\theta_K^{Lab} \leq 40^0$ [18] and K^0 $0.8 \leq \cos\theta_K^{Lab} \leq 1.0$ [1] as the black solid circles and open red triangles respectively.

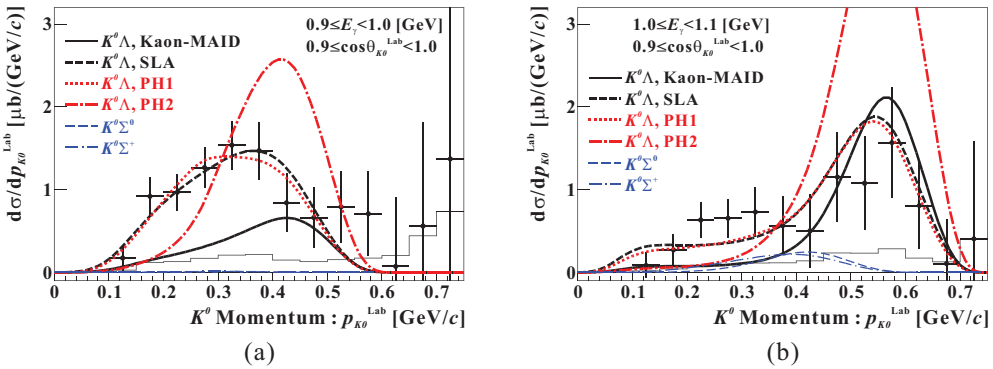

Figure 1.9: K^0 momentum spectra on the deuteron in the photon energy ranges of $0.9-1.0$ (left) and $1.0-1.1$ GeV (right)[2, 3, 17].

The results of the NKS and NKS2 encouraged the expansion of the measurement to encompass the Λ recoil polarization, in the proposed experiment, which also offers another physical observable to further examine the validity of theoretical models. Recent results of the NKS2 experiment for the inclusive measurement of K^0 and Λ are seen in Figure 1.10.

In the figure, the comparison of the measured differential cross sections as a function of K^0 momentum for the NKS and NKS2 in the energy range of $0.9 \leq E_\gamma \leq 1.0$ and angular region of $0.9 \leq \cos\theta_K^{Lab} \leq 1.0$ are shown as black squares and red circles respectively. The cross sections are adequately similar for momentum below 0.3 GeV. Obviously the lack of acceptance in the forward hemisphere had an adverse affect on the results of the NKS measurements, clearly evident by the large statistical errors not present in the NKS2 results.

The integrated energy dependent cross section of Λ photoproduction in the forward angular region of $0.9 \leq \cos\theta_\Lambda^{Lab} \leq 1.0$ was derived and compared with isobar models predictions discussed in section 2.5. The predictions of the SLA model provided the best description of data accounting for the sharp rise after photon energies $E_\gamma \geq 0.9$ GeV.

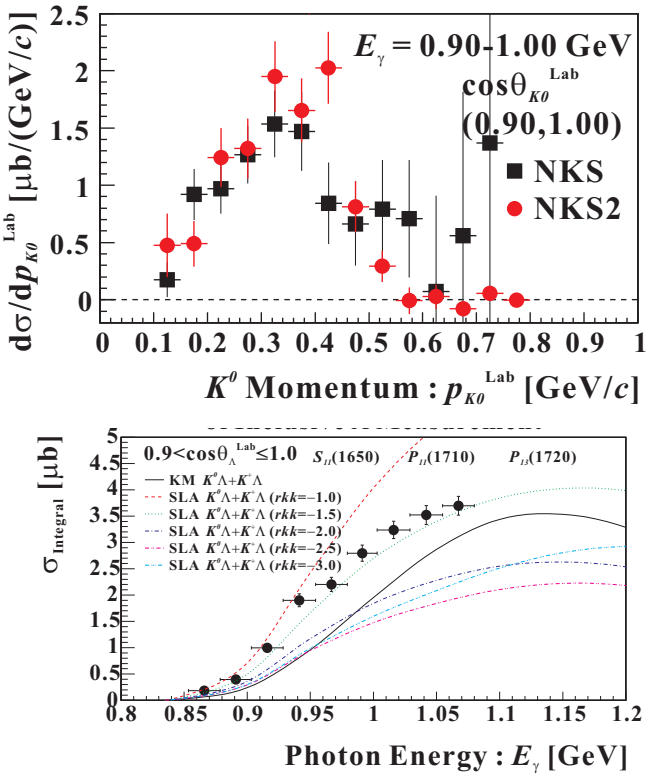

Figure 1.10: Comparison of angle integrated K^0 momentum cross section over forward angles for the NKS [2, 3, 17] and NKS2 [4, 5] as black squares and red circles is shown in the upper figure. The integrated energy dependent cross section for Λ photoproduction on a deuteron target, $d(\gamma, \Lambda)X$, compared with isobar theoretical calculations is given in the lower figure [4, 5].

1.6 Aspiration of Present Study

The strangeness production processes by the electromagnetic interaction can be used as a probe to bestow indispensable information on the strength of meson-baryon coupling and on the internal structure of hadrons with strangeness as a degree of freedom. Moreover, it can help to resolve issues regarding missing resonances that are predicted by quantum chromodynamics (QCD), that are yet to be experimentally observed [63]. Kaon production at lower energies, $1.8 - 2.3$ GeV, may provide insight into new states and confirm resonance parameters of known but weakly established states [21]. The NKS2 has undergone an additional upgrade in order to improve the spectrometers acceptance. The most recent has been the redesign of the inner detector package. The inner detector system has been completely replaced by a newly designed Inner Hodoscope (IH) and a Vertex Drift Chamber (VDC).

These upgrades to the NKS2 spectrometer were completed with the intention of increasing the spectrometers acceptance for four track events and also to improve the vertex resolution in the target region, since two out of four tracks can be identified and momentum-analyzed, thus requiring detection of the two particles only by the inner detector system. A coincidence measurement of $K^0 + \Lambda$ requires four track re-construction of the decay particles. The method we utilized was the decay modes of $K^0_S \rightarrow \pi^+\pi^-$ and $\Lambda \rightarrow p\pi^-$ for a triggered event. The VDC should enable the reconstruction of three dimensional trajectories in the target region. The geometrical acceptance for $K^0\Lambda$ coincidence measurements is expected to increase by a factor of about 7 compared to the NKS2 prior to the upgrade. The detailed description of these detectors can found in sub sections 3.3.4 and 3.3.8. The advantages of measuring Λ and K^0 concurrently in the γn$\rightarrow\Lambda K^0$ reaction are numerous and are as follows: Firstly, it will allow the derivation of the invariant masses of the kaon and Λ hyperon simultaneously and uniquely identify the reaction. Additionally it will permit the elimination of Fermi motion correction of the neutron in deuteron. Lastly, Λ events from γp and γn and reactions can be separated; This should reduce possible background contamination from incorrectly combined pions

The distinct feature of measuring the γn$\rightarrow\Lambda K^0$ reaction lies in the inability of the full determination of a theoretical interpretation based solely on the extensive database gathered from the γp$\rightarrow\Lambda K^+$ reaction. Its uniqueness amongst the six isospin production channels, outlined in Table 2.1, emerges from the ensuing considerations.

- Contrasting the $K^0\Lambda$ and $K^0\Sigma$ production channels one observes that the former only entails the N, N* exchanges states while the latter necessitates the N, N*and Δ, Δ^* states. Where the isospin is 1/2 for the N, N* and 3/2 for the Δ^* terms. The

absence of the Δ^* exchange resonance terms profoundly simplifies the description of the $K^0\Lambda$ channel.

- Moreover, the paucity of charge in the initial and final states of all particles dictates that the t channel Born term does not contribute in the amplitude calculation, ergo, the resonances, K_1 and K^* exclusively contribute. For details refer to Figures 2.3 and 2.7.

- Furthermore, the hadronic coupling constants that are associated with the differing production channels can be correlated if isospin symmetry is adopted such that the constants for the Born terms are related as,

$$gK^+\Lambda p = gK^0\Lambda n, \tag{1.1}$$

$$gK^+\Sigma^0 p = -gK^0\Sigma^0 n = gK^0\Sigma^0 p/\sqrt{2} = -gK^+\Sigma^- n/\sqrt{2}, \tag{1.2}$$

$$gK^+\Sigma^0\Delta^+ = -gK^0\Sigma^0\Delta^0 = -\sqrt{2}gK^0\Sigma^=\Delta^+ = \sqrt{2}gK^+\Sigma^-\Delta^0 \tag{1.3}$$

The goal of this work the investigate strangeness photo-production in the threshold region by focusing on Λ production. In the experiment, that is the focal point of this thesis, I aim to measure and present results on the following topics:

1. Λ momentum dependent differential cross section
2. Λ angle dependent differential cross section
3. Λ photon energy dependent integrated cross section
4. Λ recoil polarization

It is my intention to determine the Λ momentum distribution in two energy ranges integrated over two hyperon angular bins. The NKS2 collaboration measured the energy dependence of the integrated cross section at forward Λ scattering angles [24]. This measurement is a crucial additional ambition of this dissertation, as these anticipated results could possibly cast doubt or substantiate the previous findings and emphasize the importance of a study in threshold energy range with a deuteron. A deduction of the momentum integrated Λ angular distribution in laboratory frame is intended be measured, furnishing an original measurement not previously reported by the NKS/NKS2 collaborations. Along with the above, it is my objective to report on findings of the recoil asymmetry

of the photonuclear produced Λ, particularly concerning any energy dependence on the absolute strength and sign of the polarization. The prominence of spin-flip amplitudes near the threshold energy region for (γ, K) permits the exploration of the spin dependent behavior of Λ in the nuclear potential [64]. The internal spin structure of Λ is of profound interest as it is unknown if the spin structure of Λ is similar to a nucleon. It has been disputed for some time if the origin of hyperon polarizations are indeed attributed to the dynamics of forming a hyperon from the quarks states and a model to describe such a relationship was proposed by Miettienen and DeGrand [65, 66]. Therefore, a determination of the responsible quark(s) that contribute(s) to the measured Λ spin is interesting, or it may be concluded that the spin originates from the gluons [67]. The inclusion of different resonances is expected with an increase in the photon energy but an additional resonance will most likely interfere giving rise to the polarization of the produced Λ.

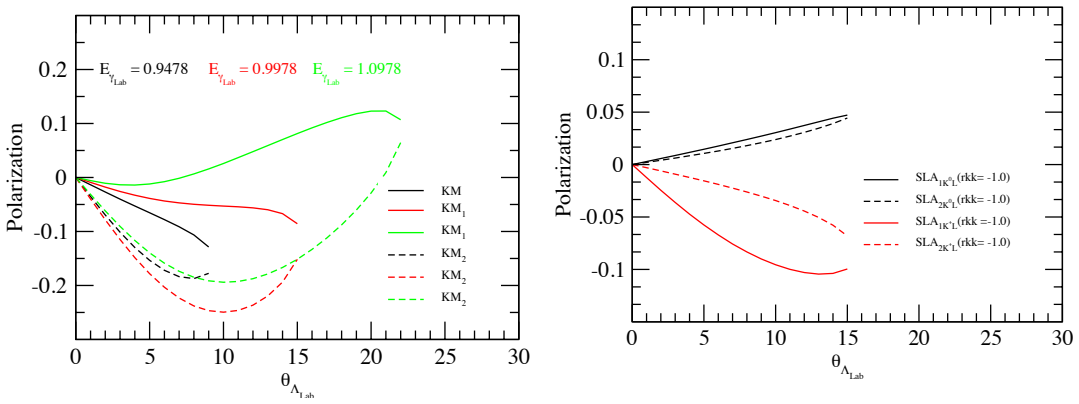

Figure 1.11: Angular dependence of Λ polarization in the laboratory frame. The left figure presents calculations based on the Kaon-MAID model of both results of theΛ polarization, denoted as KM_1 and KM_2 for specific incident photon beam energies of E_γ = 0.9478, 0.9978, and 1.0978 as black, red and green respectively. The right figure presents calculations based on the Saclay-Lyon A model of both results of Λ polarization for $rK_\gamma K_{K^{0/+}} = -1.0$, for $K^0\Lambda$ and $K^+\Lambda$ reactions

The polarization measurement of single Λ hyperons, particularly its sign determination, would give us enough information as suggested by recent calculations shown in Figure. 1.11. The determination of the polarization, including single and double polarizations observables is needed to achieve a complete set of observables and are necessary for constraining the major reaction mechanisms. These observables provide a distinguishing factor amongst models of which cross sections measurements alone are not adequate [41].

Differential cross sections are homologous to transverse scattering amplitudes

$$\sigma = |f^{+}|^2 + |f^{-}|^2 \tag{1.4}$$

which can be further fragmented into spin-flip and non-flip amplitudes g and h respectively and related as,

$$|f^{+}| = g + ih \tag{1.5}$$

$$|f^{-}| = g - ih. \tag{1.6}$$

Theses amplitudes can be expanded into partial waves $g(k,\theta)$ and $h(k,\theta)$, the momentum and scattering angle in the CM system, alluding to the inability to surmise them simply from cross section values [40]. Hence, measurements of polarization observables are paramount.

In Figure 1.11, the angular dependence of Λ polarization in the laboratory frame of reference is exhibited. The curves are based on calculations performed by P. Bydžovský for spectator kinematics. The left figure presents calculations based on the Kaon-MAID isobar model, elaborated upon in detail in section 2.5.1, of both results of the Λ polarization, denoted as KM_1 and KM_2 for specific incident photon beam energies of E_γ = 0.9478, 0.9978, and 1.0978 as black, red and green curves respectively. The right figure presents calculations based on the Saclay-Lyon A Isobar model, section 2.5.2, of the both results of the Λ polarization for $\mathrm{r}K_\Lambda K_{K^{0/+}}$ = -1.0, for the $K^0\Lambda$ and $K^+\Lambda$ reactions.

CHAPTER

TWO

THEORETICAL BACKGROUND

> You have no choice between having a philosophy and not having one. Only between having a good one or a bad one.

Cicero

2.1 Overview

This chapter will treat the kinematics, details of the production mechanism, theoretical models that predict the reaction and explore the experimental observables. In section 2.3 the kinematics for the reactions in the center of mass and the laboratory frames of reference are reviewed. Strangeness photoproduction mechanism via a real photon may proceed by three possible channels coinciding to the exchange of the resonance state of a particular particle. Next, current theoretical descriptions that may implemented for various energy ranges is reviewed. Lastly, the resonances that play a role in the modeling of meson photo production are discussed.

2.2 Photoproduction Process

Strangeness photoproduction in the threshold region may proceed by any of the six isospin channels as dictated in Table 2.1. An advantage of strangeness photoproduction over electroproduction is that in the former only four complex amplitudes are considered rather than six for the latter case.

There has been a substantial amount of experimental focus placed on the $\gamma p \to K^+\Lambda$ and $\gamma p \to K^+\Sigma^0$ reactions as was reviewed in section 1.3. The primary focus of our

Table 2.1: Kaon-hyperon photoproduction isospin channels on a nucleon and threshold energies

Reaction Channel	Threshold Energy E_γ [MeV]
$\gamma + p \rightarrow K^+ + \Lambda$	911.1
$\gamma + p \rightarrow K^+ + \Sigma^0$	1046.1
$\gamma + n \rightarrow K^+ + \Sigma^-$	1052.1
$\gamma + n \rightarrow K^0 + \Lambda$	915.3
$\gamma + n \rightarrow K^0 + \Sigma^0$	1050.6
$\gamma + p \rightarrow K^0 + \Sigma^+$	1047.5

endeavor has been placed on the all neutral production channel, $\gamma n \rightarrow K^0\Lambda$. We proposed to measure the production of strangeness by detecting the K^0_S and Λ strange particles via the following decay channels,

$$K^0_S \rightarrow \pi^+\pi^- \tag{2.1}$$

$$\Lambda \rightarrow p\pi^- \tag{2.2}$$

Table 2.2: Kaon-hyperon photoproduction isospin channels on a deuteron, threshold energies and invariant mass of the total system [25].

Reaction Channel	Threshold Energy E_γ [MeV]	W_{tot} [MeV]
$\gamma + d \rightarrow K^+ + \Lambda + n$	792.12	2548.9
$\gamma + d \rightarrow K^+ + \Sigma^0 + n$	898.20	2625.9
$\gamma + d \rightarrow K^+ + \Sigma^- + p$	903.12	2629.4
$\gamma + d \rightarrow K^0 + \Lambda + p$	795.79	2551.6
$\gamma + d \rightarrow K^0 + \Sigma^0 + p$	901.99	2628.6
$\gamma + d \rightarrow K^0 + \Sigma^+ + p$	899.22	2626.6

In this work, the employed target was a deuteron thus the reactions may occur by any of the following channels outlined in Table 2.2, in which the threshold energies and invariant mass of the total system are listed. These values were taken from reference [25]. The reaction on the deuteron is similar but slightly more intricate than that of the single nucleon as a result of the Fermi momentum within the nucleus. The momentum distri-

bution of the neutron in the deuteron and model descriptions of deuteron wave functions can be referenced in Appendix C.

The neutral kaon is an equal mixture of two states, K_S^0 and K_L^0, and thus not a unique eigenstate. The subscript L denotes the long, because of its longer lifetime, that of $c\tau$ = 15.33 m, and S for the short with a lifetime of $c\tau$ = 2.68 cm. The longer flight length of the K_L^0 prevents its detection in the NKS2 large momentum spectrometer. The future envisioned aim is measure the coincidence given in equation 2.3 of four decay daughter particles in the decay channel, but this was not performed in the this work.

$$\gamma n \rightarrow K^0 \Lambda \rightarrow \pi^+ \pi^- \pi^- p \tag{2.3}$$

The undetected K_L^0 will be accounted in terms of the 50:50 branching ratio in the cross section determination. The Λ hyperon by its intrinsic nature is unstable and therefore must decay. It however decays weakly and fails to conserve parity. A few of the physical properties of K_S^0 and Λ are listed in Table 2.3.

Table 2.3: K_S^0 and Λ physical properties

	K_s^0	Λ
Mass [MeV/c^2]	497.614 $\pm$.024	1115.683 $\pm$.0006
cτ[cm]	2.676	7.89
Decay modes	$\pi^+\pi^-$ (68.8%)	$p\pi^-$ (64%)
	$\pi^0\pi^0$ (31.2%)	$n\pi^0$ (36%)

2.3 Kinematics

Experiments performed in the threshold energy region on a stationary target may generate strange particles of interest. As discussed earlier the particles produced in the reaction cannot be measured directly in the NKS2+. As with most experiments, the decay products are the particles actually measured. From a precise measurement of the daughter particles, the spin, momentum, charge, and mass of the originally created particles can be reconstructed and indirectly measured. A reaction that involves two incoming particles interacting and then producing two outgoing particles can be adequately described by the use of four momentum vectors defined by equation 2.4. An illustration of the scattering between two particles in the lab and center of mass frame is conveyed in Figure 2.1.

$$P = (E, \vec{p}) \tag{2.4}$$

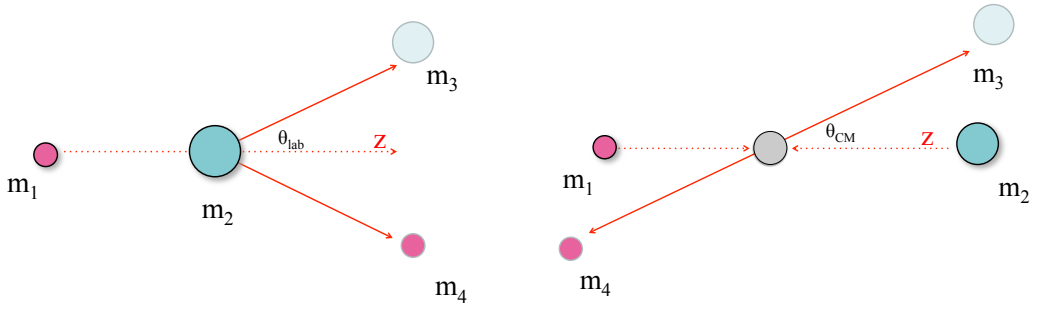

Figure 2.1: A diagrammatic representation of the scattering of two particles in the laboratory (left) and center of momentum (right) frames of reference.

The process may occur via the s, t, or u channels, where s, t, and u are Mandelstam variables; Mandelstam variables are highly useful for many body final states formed from the scattering of two incoming and two outgoing particles, A+B→ C+D, particularly due to being Lorentz invariant quantities [15]. At the tree-level, the diagrams represent the interchange of a hadron that coincides to a specific set of quantum numbers. In terms of four momentum vectors, where A(γ) and B(N) are known, the Mandelstam variables which are equal to the square of the intermediate exchange term are calculated as:

$$s = (\gamma - N)^2 = (K + Y)^2 = W^2 \tag{2.5}$$

$$t = (\gamma - K)^2 = (N - Y)^2 \tag{2.6}$$

$$u = (\gamma - Y)^2 = (N - K))^2 \tag{2.7}$$

$$M^2 = Y^2 = (\gamma + N - K)^2 = \text{Constant} \tag{2.8}$$

In the above equations, s is the energy of the center of mass, and the propagator is a nucleonic resonance (N^*). It follows that t is the four momentum transfer via a kaon resonance and u is the four-momentum transfer via hyperon resonance. Lastly, M^2 is the squared missing mass of the photo-produced hyperon.

The physically accessible section of the Mandelstam variables s and (-t) is illustrated in Figure 2.2, where as q_K ascends from 0 to p for static W, the corresponding point in (t, s) space shifts horizontally from the left blue edge of the physical region to the right blue edge. The figure was taken from reference [19]. As previously stated the particles of interest are short lived requiring a reconstruction of their respective masses, such that the

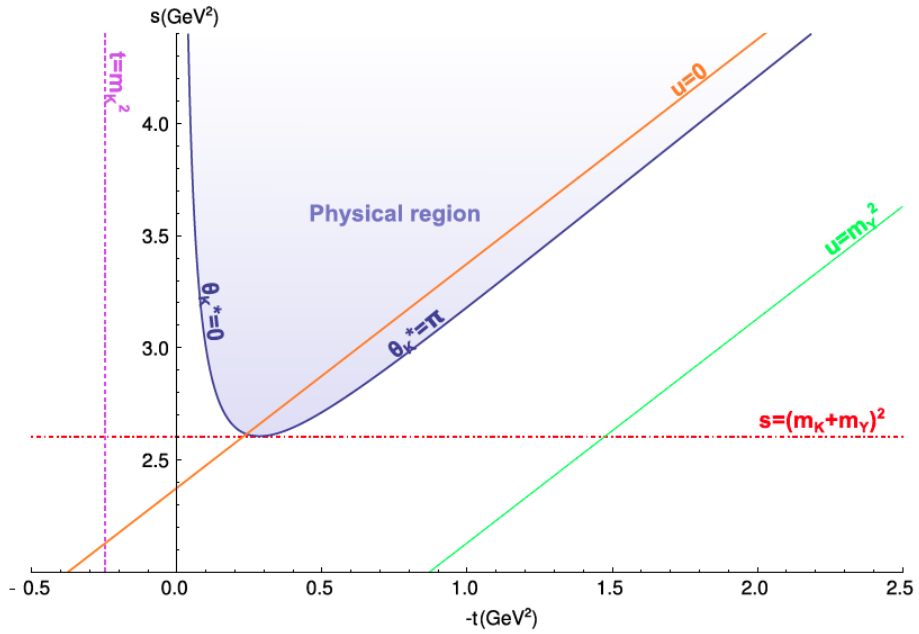

Figure 2.2: The physical region (light blue) as a function of the Mandelstam variables s and (-t). As q_K goes from 0 to p for fixed W, the corresponding point in (t, s) space moves horizontally from the left blue edge of the physical region to the right blue edge. The KY production threshold (s = $(m_K + m_Y)^2$) is indicated with a dash-dotted red line. The purple dashed line corresponds to t = m_K^2 , the full orange line to u = 0, and the thin green line to u = m_Y^2 [19].

squared invariant mass of particle A, in the decay reaction, A→ a+b, will be determined by,

$$M_A^2 = (E_a + E_b)^2 - (\vec{p}_a + \vec{p}_b)^2 \tag{2.9}$$

In the laboratory frame of reference, with respect to the $\gamma n \rightarrow K^0\Lambda$ reaction, the invariant masses can be calculated by the following equations. Starting from equations 2.1 the squared invariant mass of the K^0 and Λ particles are,

$$M_{K_s^0}^2 = (E_{\pi^-} + E_{\pi^+})^2 - (\vec{p}_{\pi^+} + \vec{p}_{\pi^-})^2 \tag{2.10}$$

$$M_\Lambda^2 = (E_p + E_{\pi^-})^2 - (\vec{p}_p + \vec{p}_{\pi^-})^2 \tag{2.11}$$

In addition to the invariant mass technique of reconstructing a particles mass from its decay products is the method is missing mass. In reaction $A + B \rightarrow C + D + X$, the relevant kinematical variables of the incoming particles, A and B, are known. The

generated particles C and D are experimentally detected leaving X as an undetected but expected particle. Its mass may then readily be calculated by the use of the following,

$$M_X^2 = (E_A + E_B - E_C + E_D)^2 - (\vec{p}_A + \vec{p}_B - \vec{p}_C + \vec{p}_D)^2 \tag{2.12}$$

In regards to 2.3 the calculated missing mass may either be the kaon or Λ particle. This is dependent upon the directly detected decay particles, that being either a combination of $\pi^+\pi^-$ or $p\pi^-$. If $\pi^+\pi^-$ are detected, then the squared missing mass, assumed to be around the mass of a lambda is determined by,

$$M_\Lambda^2 = (E_\gamma + E_n - E_{\pi^-} + E_{\pi^+})^2 - (\vec{p}_\gamma + \vec{p}_n - \vec{p}_{\pi^+} + \vec{p}_{\pi^-})^2 \tag{2.13}$$

If the p $+\pi^-$ are detected, then the squared missing mass should be centered around a kaon computed as ,

$$M_K^2 = (E_\gamma + E_n - E_{\pi^-} + E_p)^2 - (\vec{p}_\gamma + \vec{p}_n - \vec{p}_p + \vec{p}_{\pi^-})^2 \tag{2.14}$$

We aimed to measured the four particle decay that came from the Λ and kaon produced on the neutron inside the deuteron target as such, the expected missing mass of this reaction should therefore have the mass around that of a proton and is found by the following equation,

$$M_\Lambda^2 = (E_\gamma + E_d - E_{\pi^-} + E_{\pi^+} - E_{\pi^-} + E_p)^2 - (\vec{p}_\gamma + \vec{p}_n - \vec{p}_{\pi^+} + \vec{p}_{\pi^-} - \vec{p}_p + \vec{p}_{\pi^-})^2 \tag{2.15}$$

Experimentally, there are often times when the use of Feynman diagrams provides a means to express the reaction in terms of the invariant Mandelstam variables. The hadronic vertices represent the strong coupling constants and form factors. Feynman diagrams are implemented to convey the possible reaction mechanisms, and also for the calculation of the reaction amplitudes. A theoretical cross section can be found through the sum of the intermediate states depicted in the Feynman diagrams 2.3. The diagrams provide unique information regarding the dynamics of the process.

2.4 Theory Concerning the Photoproduction of Strangeness

In explaining the strangeness photo-production processes, current theoretical approaches at modeling nature include the Regge [68], Chiral Perturbation [69, 70], multipole [71] and Isobar models. Among them, the Regge model is implemented for high-energy incident photons ($E_\gamma \geq$4GeV), while Chiral Perturbation theory is used up to the threshold region.

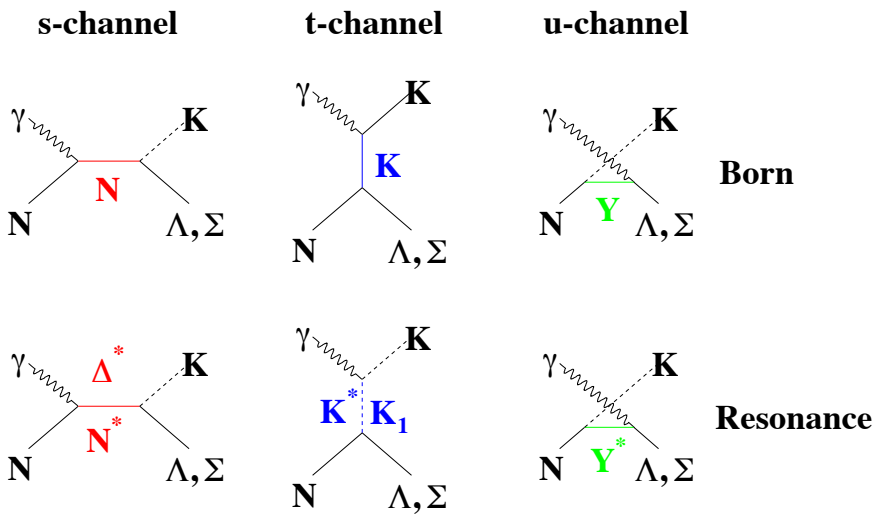

Figure 2.3: Feynmann diagram representations of Kaon photoproduction channels. The square of the intermediate exchange term in each channel is equal to the Mandelstam variables *s, t,* and *u*. The Born terms and resonance terms in each channel are denoted as N, K, Y and N*, K*, Y* respectively. The Δ* term is forbidden as an exchange term in Λ photoproduction

For energies in the resonance region, the isobar model is predominantly used and find their respective differences in the varied inclusion of coupling constants, renounces and the importance placed on the applied coupling constants. In hyper nuclear calculations quarks models [72] are vastly too complex to be practical in their applications [47]. Over the years there has been a myriad of contributors that have explored modeling nature in an attempt to describe strangeness production by the electromagnetic interaction [42, 73, 74, 75, 76].

2.5 Theoretical Models

The goal of any theory that attempts to model nature is to describe the energy and angular dependence of a process [77]. Kaon photoproduction can essentially be represented by four elementary amplitudes that are in essence hadronic degrees of freedom. Such degrees of freedom describe the interaction between particles by the means of an effective Lagrangian approach or regularly referred to as isobaric models. The use of these phenomenological isobaric models avoids the complex difficulties that are apparent in the non-pertubative Quantum ChoromoDynamics (QCD), by considering the involved hadrons as point-like particles. It is common place to use a deuteron as an effective neutron target as the N-N interaction is believed to be know and the largest contribution for kaon photon production is assumed to be from the quasi free process [25]. The reaction may be sufficiently described by the single channel approximation, having said that, they do ignore some of the finer

details of the process by absorbing final state interactions (FSI) and re-scattering effects into coupling constants. These FSI contributions to the cross section can not be fully ignored and is reported as having as large as a 20% effect on the computed results [78]. The production process mechanism as represented by tree-level Feynmann diagrams, illustrated in Figure 2.3, includes Born terms or the hadrons in their ground state and considers resonances, as exchange terms. In such a description, the coupling constants for a unique resonance, or excited state are included as an attempt to reduce the intricacy of the problem. Consequently, it is regarded as a free parameter to be determined by fits to data. However, isobar models based of Feynmann diagrammatical models used to describe the reactions in the region of low energy have been found to diverge with increasing energies. The inner structure of the hadron is accounted for by the usage of form factors at the vertices [79], but viewing nucleons, which are composite structures, not as such, neglects some of the inner details of the strong force interaction [80]. Nevertheless, they are applicable for lower threshold energies where interaction amplitudes may be computed. The isobar impulse approximation on a deuteron explains the reaction such that the photon interacts with only one nucleon, producing the strange baryon and meson, leaving the other nucleon undisturbed. The unstuck nucleon in a reaction on the deuteron acts as a spectator of the process to the first order.

The amplitudes in isobar models emerge from resonance exchanges and Born terms and are determined as,

$$M_{fi} = M_{BORN} + \sum_{N^*} M_s + \sum_{K_1,K^*} M_t + \sum_{Y^*} M_u \tag{2.16}$$

A consequence of the interpreting the $N(\gamma, K)\Lambda, \Sigma$ reaction in terms of only hadronic degrees of freedom is the unphysically large cross section predictions. In response to such sizable cross sections there are usually three approaches to suppress the Born term contribution and return the cross sections to practical descriptions. The methods are the introduction of form factors, hyperon resonances, or to simply ignore the predicted range of the $g_{K\Lambda p}$ and $g_{K\Sigma^0 p}$ coupling constants that materialize from broken SU(3) symmetry [78]. A commonly used phenomenological dipole hadron form factor introduced at each strong vertex is [79],

$$F_x(\Lambda) = \frac{\Lambda^4}{\Lambda^4 + (x - M^2)^2} x = s, t, u \tag{2.17}$$

where x is the respective Mandelstam variable and Λ is the cut off parameter indicating the limit where the model is expected to fail.

A weak coupling constant permits the use of a single channel analysis to sufficiently

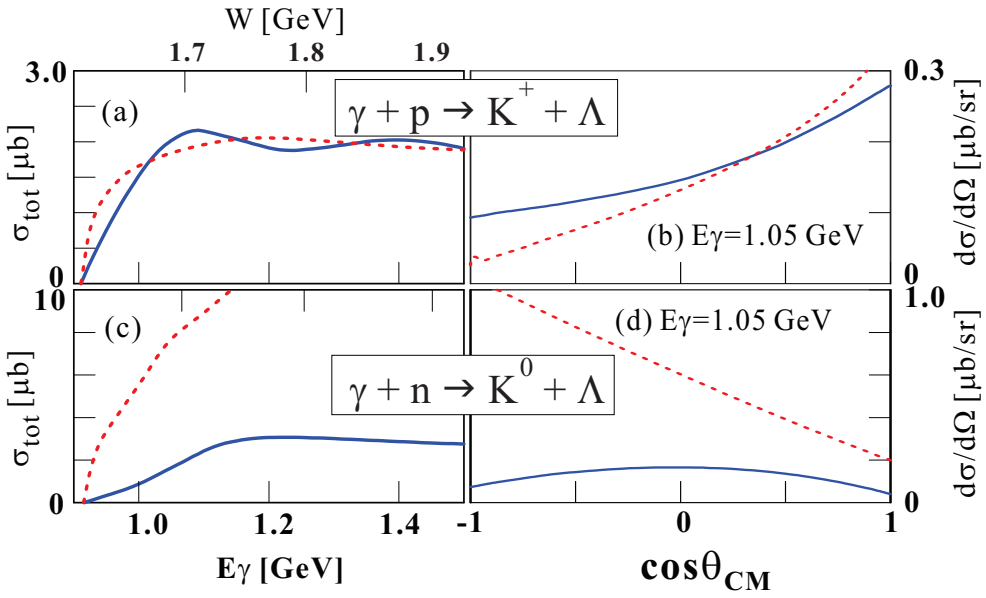

Figure 2.4: Total cross section predictions for $K^+\Lambda$ and $K^0\Lambda$. The predictions shown by the solid blue and dashed red curves are for the Kaon-MAID [6, 20, 21] and Saclay-Lyon (SLA) [7] models respectively. The upper figures are for $K^+\Lambda$ and the lower for $K^0\Lambda$. The cross section as a function of the photon energy are displayed on the left and the angular distribution in the center of momentum frame is on the right.

describe the process [81]. In regards to the reaction that this thesis is focused upon the coupling constant, $g_{KN\Lambda}$, contains information regarding the interaction strength between the neutron, kaon, and Λ particles.

In addition, the use of the experimentally gathered data from a neutron will permit for improvements to be placed on the free parameters in the numerous possible reaction channels. All current models agree well for $K^+\Lambda$ reaction on the proton in the threshold region, but differ model by model for the $K^0\Lambda$ production on the neutron. The comparison of predictions between the Kaon-MAID [6, 20, 21] and Saclay-Lyon A [7]models which deviate in s-channel and u-channel resonances, the approach to the hadron structure and the data set to which the extraction of free parameters were fitted to [82] are given in Figure 2.4. The predictions shown by the solid blue and dashed red curves are for the Kaon-MAID and Saclay-Lyon A models respectively. The left figures are the total cross sections as a function of incident photon energy and the right are differential cross sections as a function of angle, where θ is the angle of the kaon in relation to the photon beam. It is obviously apparent that they have similar prediction in the $K^+\Lambda$ case, which is to be expected since the majority of the development has been centered on this channel. In

contrast, the $K^0\Lambda$ curves manifest striking differences, due to the lack of abundance of data in this reaction channel. Experimental data that have been obtained for the production of $K^+\Lambda$ are not sufficient to predict the cross section of the neutral channel. This justifies the importance of $K^0\Lambda$ on the deuteron. Thus, the investigation of K^0 and Λ production near the threshold is the key to the study of strangeness photoproduction process, as it may facilitate significantly important data about the dynamics of the elementary process [83].

2.5.1 Kaon-MAID (KM)

The Kaon-MAID program is a used to generate theoretical predictions based on the theoretical isobar model created by the collaboration of Bennhold and T. Mart [6, 20, 21]. The model is one of the most recent isobar model that is able to describe the production of kaons in all six channels, while being able to exclude the final state interaction (FSI) by the assumption that are included in the strong coupling constants that are fitted to data [83]. This however leads to an oversimplification of the meson baryon re-scattering process.

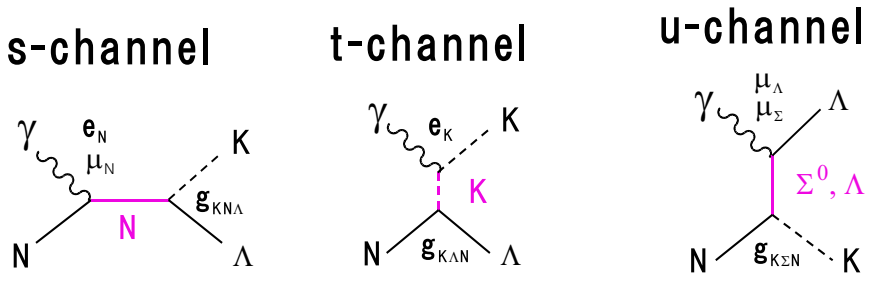

Figure 2.5: Feynmann diagrams of kaon photoproduction where the hadronic coupling constant are g_{KYN}

It primarily focuses on the s-channel in which nucleon resonances N^* are the exchange term, the Kaon-MAID strategy includes four of these resonances. Generally in effective field theory the coupling constants are determined not by the theory, but are extracted as fitting parameters from global fits to the full experimental data set [78]. In the framework of the Kaon-Maid model, the hadronic coupling constants that are associated with differing production channels can be transformed, if isospin symmetry is adopted, such that the constants for the Born terms are related as,

$$g_{K^+\Lambda p} = g_{K^0\Lambda n}, \tag{2.18}$$

$$g_{K^+\Sigma^0 p} = -g_{K^0\Sigma^0 n} = g_{K^0\Sigma^0 p/\sqrt{2}} = -g_{K^+\Sigma^- n/\sqrt{2}}, \tag{2.19}$$

$$g_{K^+\Sigma^0\Delta^+} = -g_{K^0\Sigma^0\Delta^0} = -\sqrt{2}g_{K^0\Sigma=\Delta^+} = \sqrt{2}g_{K^+\Sigma^-\Delta^0} \tag{2.20}$$

In respect to the hadronic vertices the coupling constants of the resonances terms can be found if we adopt the following method.

$$g_{K^+\Lambda N^{*+}} = g_{K^0\Lambda N^{*0}}, \tag{2.21}$$

The relationships between electromagnetic coupling were wrested from experimental specifics in contrast to the hadronic coupling constants. Regarding the electromagnetic interaction vertices, the partial decay width for the radioactive decay of a resonance to a ground state can be provided in terms of the photo coupling helicity amplitudes [26]. With these defined relations and assuming the disparity of nucleon masses to be negligible we find that the coupling constants of the resonance exchanges associated to the helicity amplitudes of spin 1/2 resonance terms are [21],

$$\frac{gN^{*0}n\gamma}{gN^{*+}p\gamma} = \frac{A^n_{1/2}}{A^p_{1/2}} \tag{2.22}$$

in the case of spin 3/2 resonance terms, the two couplings constants are found as,

$$\frac{g^{(1)}N^{*0}n\gamma}{g^{(1)}N^{*+}p\gamma} = \frac{\sqrt{3}A^n_{1/2} \pm A^n_{3/2}}{\sqrt{3}A^p_{1/2} \pm A^p_{3/2}} \tag{2.23}$$

$$\frac{g^{(2)}N^{*0}n\gamma}{g^{(2)}N^{*+}p\gamma} = \frac{\sqrt{3}A^n_{1/2} - (m_n/m^*_n)A^n_{3/2}}{\sqrt{3}A^p_{1/2} - (m_n/m^*_n)A^p_{3/2}} \tag{2.24}$$

The ratios of coupling constants of the neutral and charged channel for the nucleon and its resonance is related to the known helicity amplitudes. The transition moment for the neutral transition is exploited in place of the $g_{K^{*+}K^+\gamma}$ for K^+ photoproduction [21]. The moments directly correspond to the known decay width of the established $K^*(829)$ meson. The ratio of the decay width for the $K^*(829)$ meson, having been restricted by quark model calculation is,

$$r_{K^*K^\gamma} = -\sqrt{\frac{\Gamma_{K^{*0}\to K^0\gamma}}{\Gamma_{K^{*+}\to K^+\gamma}}} = -1.53. \tag{2.25}$$

Where,

$$\Gamma_{K^{*0}\to K^0\gamma} = 117 \pm 10\text{keV} \tag{2.26}$$

$$\Gamma_{K^{*+}\to K^+\gamma} = 50 \pm 5\text{keV} \tag{2.27}$$

Currently, the decay width of the K_1 meson, that plays an important role in the description of kaon photoproduction, is unknown, hence it is extracted from fits performed to the experimental data [84]. This is one of the sources of differences between the two isobar models discussed in this thesis. It is fitted to data in the KM framework at a value of $r_{K_\gamma K_*} = -0.45$, but is left as a free parameter in the Saclay-Lyon A model.

2.5.2 Saclay-Lyon A (SLA)

Another frequently implemented isobar model is the Saclay-Lyon model [85], however, the slightly less complex generation, that does not take into consideration the $\frac{5}{2}$ and $\frac{1}{2}$ spin resonances of the nucleon is known as the Saclay-Lyon A (SLA) model [7]. In the SLA approach, the photo-coupling in the t-channel emerges from the ratio of the charged and neutral $r_{K_1K\gamma} = g_{K_1^0K^0\gamma}/g_{K_1^+K^+\gamma}$. This constant cannot be directly determined and therefore it is treated as a free fitting parameter. The reduction in intricacy of the Saclay-Lyon A model arrives from the exclusion of the $P_{11}(1440)$ and $D_{15}(1675)$ resonance terms. It does consider some well known resonances, having its uniqueness structured around the use of four hyperon resonances. Only one nucleon resonance and two kaonic resonance terms are inserted, these are the $P_{11}(1710)$, $K^*(829)$ and $K_1(1270)$ respectively. The four resonances implemented in the calculation of the u-channel are $S_{01}(1450)$, $S_{01}(1670)$, $P_{01}(1810)$, and $P_{11}(1660)$.

2.5.3 Regge-Plus-Resonance (RPR) Point of View

At higher energies the implementation of isobar models are still viable but not the most advantageous option. At energies extending beyond 2 GeV hadronic models tend to fail in their respective production predictions by overestimating the cross section and breaching the Froissant limit [19, 86]. They also suffer from the need to include numerous free parameters. The Regge model idea is founded on the premise of treating groups of particles with the same quantum numbers the same and placing them in a so-called family. These families are furthered named Regge trajectories, which are treated as an exchange group in the production amplitude rather than simple a lone particle. The exchange of the lightest exchange terms in the t-channel, K(494) and K*(892) trajectories, are implemented in the higher energy regime as depicted in Figure 2.6, a typical Chew-Frautschi plot. These are functions $\alpha(t)$, that relate the spins to the squared masses of the affiliated family were found to be linear in estimation.

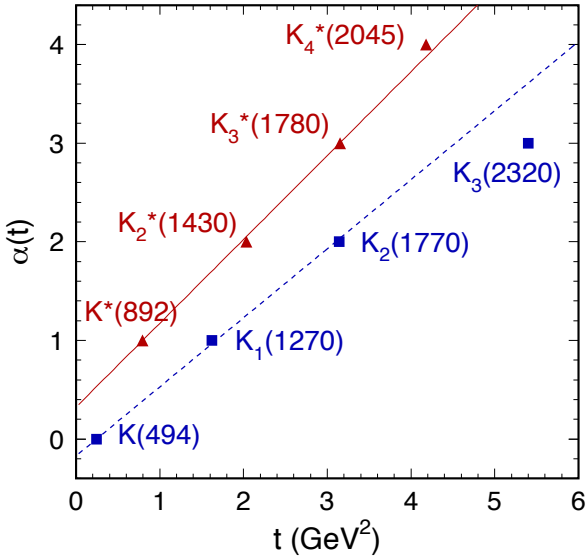

Figure 2.6: K and K^* Regge trajectories taken from [22]

The Regge-Plus-Resonance model (RPR) is an amalgamated model of Regge and a typical Isobar, that extends into the resonance region by the inclusion of resonances associated with the s-channel into the Regge model, and has progressed through a string of iterations RPR, RPR-2007, and most recently RPR-2011 [9, 26, 28, 29, 82, 87, 88]. One of the goals is to uncouple the resonance and Born term contributions to the coupling constants [9, 26]. The model is targeted at forward angle production in which the resonance shape is governed by the s-channel similar to the isobar approach. It incorporates some isobar characteristics in the lower energy region but is still able to maintain its usefulness at higher photon energies. Therefore, the RPR model is applicable in a wider energy range than a conventional hadronic model and is able to supply predictions from the threshold to photon energies up to 16 GeV [26]. Isobar models described earlier in section 2.5 necessitate the inclusion of numerous Born terms, t-channel mesons, and hyperon resonances in stark contrast to RPR model that incorporates two t-channel exchanges and three coupling constants [25]. Moreover hadronic models have significantly limited predictive capabilities. The strategy of the RPR approach is to utilize the afore mentioned trajectories to model the copious amounts of $K^+\Lambda$ production data.

The amplitudes in the RPR framework emerge from pseudo scalar and vector meson exchanges as well as a resonance in the s-channel and is determined as,

$$M_{fi} = M_{Regge}^{K^+494} + M_{Regge}^{K^{*+}892} + M_{Feynmann}^{K^+494} \times P_{Regge}^{K^+494} \times (t - m_{K^+}^2) + \sum_{N^*} M_s \qquad (2.28)$$

where the propagators are assumed with a constant (1) or rotating ($e^{-i\pi\alpha(t)}, \alpha(t)$) is

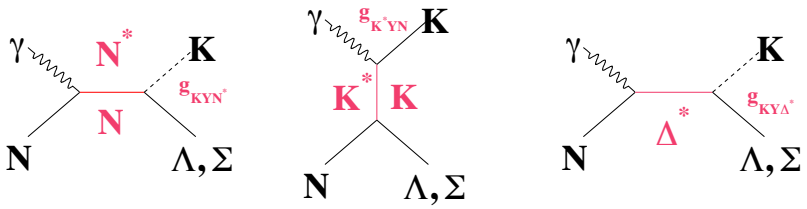

Figure 2.7: Particular prominence is attributed to the strong interaction vertices as shown in the tree-level diagrams examined in the RPR theoretical framework.

the Regge trajectory phase [19, 28, 29, 82]. The gauge invariance in the amplitude is restored by the addition of the electric part of s-channel term which is needed for the $K^+(\Lambda\Sigma)$ channels, but unnecessary for $K^0(\Lambda^0\Sigma^0)$, where the t-channel kaon exchange term does not participate. It should be noted that for the case involving the production of $K^+\Sigma^-$ from a neutron, the electric contribution of the u-channel Born term is included to maintain gauge invariance as a consequence of the neutral s-channel Born term. In Figure 2.7 it is evident that the strong interaction vertices are the prime concern in the tree level diagrams. In the RPR strategy a gaussian shaped form factor is used at the hadronic vertices, defined as [25],

$$F_G(s) = exp(\frac{-(s - m^2_{N*})^2}{\Lambda^4_{\text{resonance}}}) \tag{2.29}$$

where, s is the Mandelstam variable and $\Lambda_{\text{resonance}}$ is the cut off parameter or the *failpoint* of the model, which for the RPR case is roughly 1.6 GeV. A comparison of the conventional dipole form factor used in most isobar models to the gaussian form factor used in the RPR approach is given in Figure 2.8.

Strangeness production from a nucleon in the RPR framework is showcased in Figure 2.9, where at energies greater than 3 GeV the Regge trajectories describe the cross section. Once a extension into the resonance region sufficiently describes the overall tendency of the data, the model is then optimized by the inclusion of the resonance-exchange diagram while maintaing the Regge parameters extracted at the higher energy regime constant [25]. The resonances that are incorporated include well known, predicted and two star resonances. The well known resonances are $S_{11}(1650)$, $P_{11}(1710)$, and $P_{11}(1720)$. The predicted and as yet unobserved resonance, $D_{13}(1900)$, is taken into account after attempts at fitting $K^+\Lambda$ data [89]. $P_{13}(1900)$, a two star resonance, is an additional term used in RPR calculations. The highlighting advantage of the RPR model from the RPR-2007 version to its latest incarnation is the established predictive applicability for all $N(\gamma, K)Y$ channels.

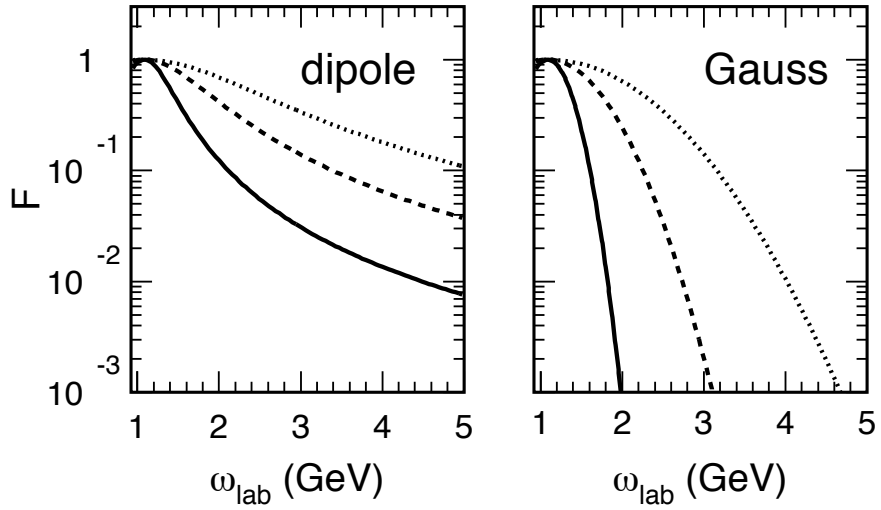

Figure 2.8: Photon energy dependence (W_{lab}) of a dipole and gaussian form factor for a resonance with a mass of 1710 MeV. The solid, dashed, and dotted curves are for the cutoff value, $\Lambda_{\text{resonance}}$, at 800, 1200, and 1600 MeV respectively [23].

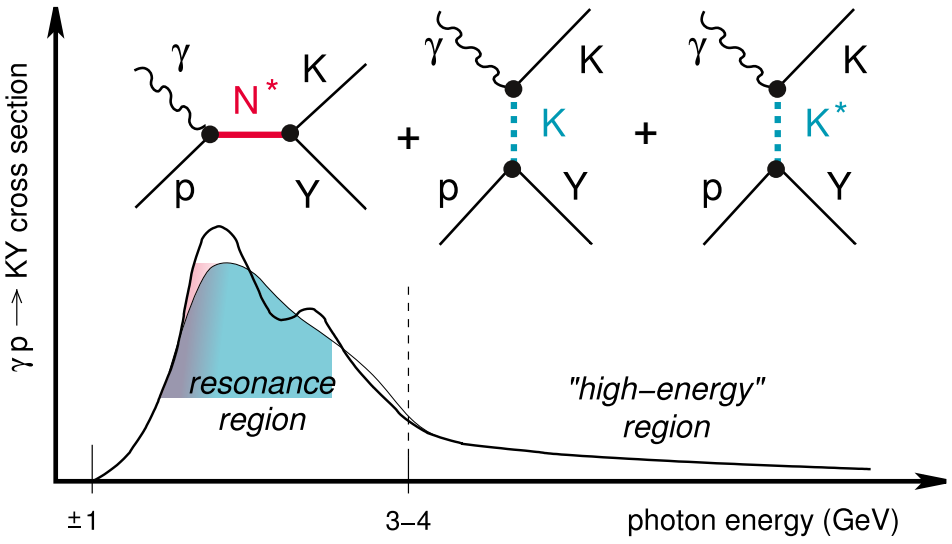

Figure 2.9: The RPR view of the strangeness production by the electromagnetic interaction on a nucleon [22].

2.6 Resonances (N*,K*,Y*)

One of the pivotal topics in nuclear physics conducted at lower energies is understanding the excited states of the nucleon (N*) [78]. Currently the Particle Data Group (PDG) has listed four resonances as important in $K^+\Lambda$, however only the $S_{11}(1650)$ resonance has a current three star ranking [37]. In the previous sections, 2.5– 2.5.3, the framework of two popular isobar models KM and SLA, and the composite RPR model were reviewed. However, they are not the only attempts at modeling the meson photo production process. In Table 2.4 are the nucleon resonance terms that are included in assorted pseudo scalar models. Table 2.5 lists the Born and resonance terms (N, N*), (K, K*) and (Y, Y*) that are included in the KM, SLA, and RPR-2007 models to which the experimental findings will be compared at length in section 6.3. The process is not fully dominated by any single resonance so the distinction between isobar models is found in the varying resonances inclusions [90]. In Figure 2.10 the contributions to the cross section of $\gamma n \rightarrow K^0\Lambda$ at E_γ =1 GeV for SLA and KM are seen, in which the coupling constants for the Born terms $g_{K\Lambda N}$ and $g_{K\Sigma N}$ are $-3.2, 0.8$ and $-3.8, 1.2$ for SLA and KM respectively. The Born terms, hadronic form factors, hyperon exchanges, and K_1 contributions to the cross section are denoted at B, B+hff, B+h, and KM/SLA-K1 respectively. The $r_{K_1K\gamma}$ parameter is -1.405 for SLA and -0.45 for KM [82].

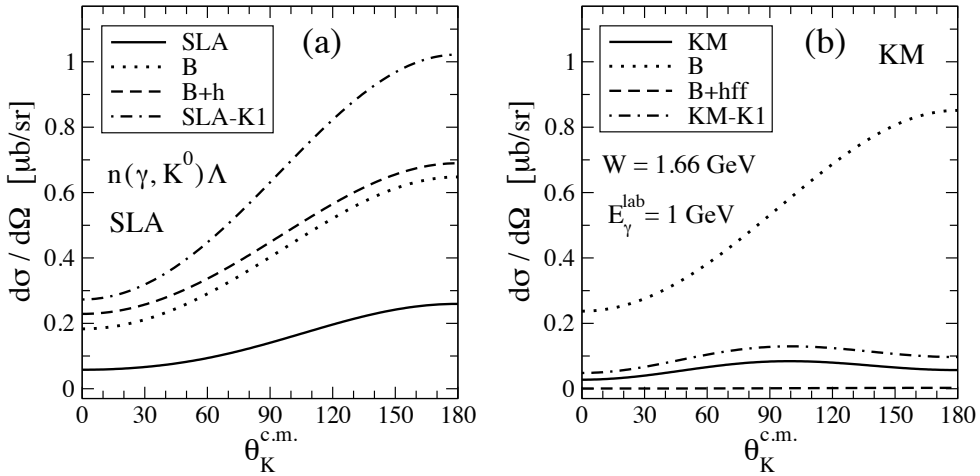

Figure 2.10: Contributions to the $\gamma n \rightarrow K^0\Lambda$ cross section at E_γ =1 GeV for SLA and KM. The curves for the entire model and excluding the K_1 contributions are solid and dashed [82].

Table 2.4: Nucleon resonances (N*) that are considered in a numerous meson photo production analyses. They are presented as $L_{2I2J}(M_*)$, where L is the orbital angular momentum of the πN partial wave, I is the isospin, J is the spin, and M_* is the mass of the resonance term. Table taken from reference [37]

Analysis	P_{11} (1440) ****	D_{13} (1520) ****	S_{11} (1535) ****	S_{11} (1650) ****	D_{15} (1675) ****	F_{15} (1680) ****	D_{13} (1700) ***
RPR-2011 [19, 37]			√	√		√	
B-G [91]	√	√	√	√	√	√	
EBAC-DCC [92]		√	√	√			
Gent-Isobar [93]				√			
Giessen [94]				√			
Kaon-MAID [6, 20, 21]				√			
RPR-2007 [25, 28]				√			
Saclay-Lyon [85]	√			√	√		
SAID [95]	√	√	√	√	√	√	
US/SSL [96, 97]	√	√	√	√			√
	P_{11} (1710) ***	P_{13} (1720) ****	D_{13} (1900) m	P_{13} (1900) **	P_{11} (1900) m	F_{15} (2000) ***	J≥7/2
RPR-2011 [19, 37]		√	√	√	√	√	
B-G [91]	√	√					√
EBAC-DCC [92]			√	√	√		
Gent-Isobar [93]	√	√					
Giessen [94]	√	√			√		
Kaon-MAID [6, 20, 21]	√	√	√	√			
RPR-2007 [25, 28]	√	√	√	√	√		
Saclay-Lyon [85]		√					
SAID [95]		√				√	√
US/SSL [96, 97]	√	√					

Table 2.5: Elements (N, N*), (K, K*) and (Y, Y*) used in calculations of N(γ,K)Λ photoproduction process in the KM, SLA, and RPR-2007 theoretical models

			I(J^P)	KM	SLA	RPR
BORN terms	s-channel					
		N (p or n)	$\frac{1}{2}(\frac{1}{2}^-)$	$\surd$	$\surd$	$\surd$
	t-channel					
		K	$\frac{1}{2}(0^-)$	$\surd$	$\surd$	$\surd$
	u-channel					
		Λ	$0(\frac{1}{2}^+)$	$\surd$	$\surd$	$\surd$
		Σ	$1(\frac{1}{2}^-)$	$\surd$	$\surd$	$\surd$
Resonance terms	s-channel					
		$S_{11}(1650)$	$\frac{1}{2}(\frac{1}{2}^-)$	$\surd$		$\surd$
		$P_{11}(1710)$	$\frac{1}{2}(\frac{1}{2}^+)$	$\surd$		$\surd$
		$P_{13}(1720)$	$\frac{1}{2}(\frac{3}{2}^+)$	$\surd$	$\surd$	$\surd$
		$P_{13}(1900)$	$\frac{1}{2}(\frac{3}{2}^-)$			$\surd$
		$D_{13}(1900)$	$\frac{1}{2}(\frac{3}{2}^-)$	$\surd$		$\surd$
	t-channel					
		$K_1(1270)$	$\frac{1}{2}(1^+)$	$\surd$	$\surd$	$\surd$
		K*(892)	$\frac{1}{2}(1^-)$	$\surd$	$\surd$	$\surd$
	u-channel					
		$S_{01}(1405)$	$0(\frac{1}{2}^-)$		$\surd$	
		$S_{01}(1670)$	$0(\frac{1}{2}^-)$		$\surd$	
		$P_{01}(1810)$	$0(\frac{1}{2}^+)$		$\surd$	
		$P_{01}(1660)$	$1(\frac{1}{2}^+)$		$\surd$	
Form factor				$\surd$		$\surd$
Contact				$\surd$		

CHAPTER

THREE

EXPERIMENTAL INSTRUMENTATION

> I think what we are seeking is an experience of being alive, so that our life experiences on the purely physical plane will have resonances within our own innermost being and reality, so that we actually feel the rapture of being alive.

Joseph Campbell

3.1 Overview

This chapter pertains to the detailed review of the experimental facility and apparatus. It will first give a brief overview of the experimental technique. This will be followed by a description of the generated photon beam and sutagging system, the radiator and its control system, and the photon beam duty cycle. This shall lead into a discussion of the NKS2+ spectrometer and into components. The chapter shall conclude with a brief discussion of the target system utilized for the experiment and the associated electronics.

3.2 STB Tagging System and Photon Beam Line

The Tohoku University Laboratory of Nuclear Science (LNS) has been recently renamed the Research Center for Electron Photon Science (ELPH) and utilizes a 300 MeV electron linear accelerator (LINAC) as a injector for experiments performed in the second experimental hall. Although the LINAC has the capacity to insert electrons at a maximum energy of 300 MeV, it is typically used in the range of $150 - 200$ MeV. The electrons are injected from the LINAC and accelerated up to the maximum energy of 1.2 GeV by the STretcher-Booster (STB) ring, 49 meters in diameter, in roughly 1.2 seconds. For the

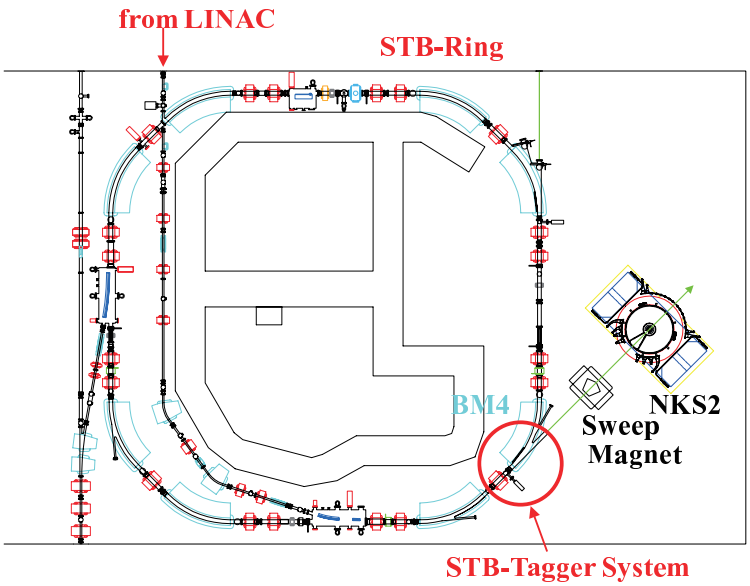

Figure 3.1: Schematic of the Neutral Kaon Spectrometer (NKS2+), sweep magnet, tagger system, and STB-ring in the 2^{nd} experimental hall at the Research Center for Electron Photon Science (ELPH).

generation of the photon beam, a movable a carbon wire radiator ($\phi 11\mu$m), capable of being remotely controlled, is inserted into the path of the electron beam as a radiator target to dispense the photon beam by the bremsstrahlung process. High-energy electrons predominately lose energy in matter by bremsstrahlung, the electromagnetic radiation produced from an accelerating charged particle, at a rate nearly proportional to its energy. This occurs due to scattering of electrons from the electric fields of the nuclei and dominates above a critical energy of $E_{critical}$ =10 MeV. The emitted photon enters into the NKS2+ spectrometer and the simultaneously the recoiled electron is then tagged by the STB-Tagger system.

3.2.1 Radiator Control

The insertion of the 11μm carbon wire is controlled remotely by a computer in the counting room. During the electron injection and acceleration time the radiator is kept outside the electron beam path. A five phase stepping motor to which an aluminum frame is attached serves as transport for the carbon wire. The radiator movement has a maximum displacement of 100 mm and can be shifted in position at the highest velocity of 80 mm/s. The lower limit of the displacement in position that may be achieved is 2μm [98]. For production experimentation periods, the usage of a continuous quasi-monochromatic photon is achieved by tuning the insertion speed and position.

3.2.2 STB Tagger System

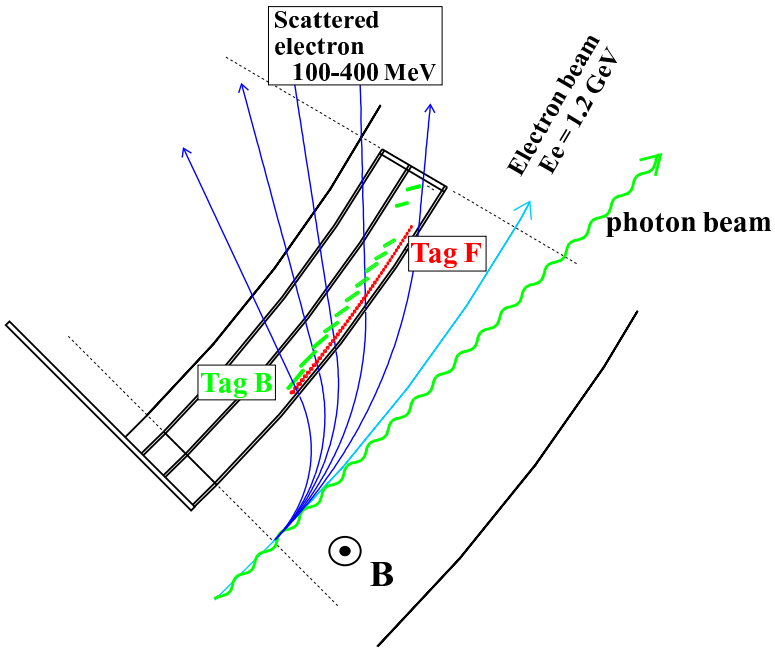

Figure 3.2: Schematic of the photon tagger package. A scattered electron will strike the scintillation counters, TagF and TagB, where its energy is determined by which segments it strikes, directly related to its deflection angle.

The STB tagger system is located along the Bending Magnet 4 (BM4) on the STB ring. The components include the aforementioned carbon radiator, the BM4, and two arrays of individual tagging counters defined as TagF and TagB. TagF is assembled from 48 finger segments of plastic scintillators, and TagB consists of twelve segments of plastic scintillation counters. Each scintillator counter is connected and read out to a scaler. The use of TagB in coincidence with TagF is primarily to reduce the recording of accidental coincidence hits on TagF. Figure 3.2 shows a schematic view of the tagger. At the target position, the photon beam diameter in on the order of $3-5$ mm. The system additionally incorporates a dipole magnet that may be used for analyzing the momentum of recoil electrons. A coincidence hit signal, TagF$\otimes$TagB, verifies that there was indeed a scattered electron. The tagger system is capable of tagged photon energies over a range of $0.8-1.1$ GeV with an accuracy of $\pm$ 10 MeV on the produced photon beam [98]. A precise calibration of the tagging detectors results in a correlation between the tagger segment number and the energy of the photon incident on the target, thus, it provides information of the photon energy and the number of the photons. The photon energy calibration can be accomplished by directing the photon beam incident on a copper wire of approximately

0.9 mm, generating an electron-positron pair, via the reaction $\gamma \rightarrow e^{-}e^{+}$. The pair is detected by a drift chamber allowing for a momentum reconstruction and determination. Finally, the energy of each is calculated as they egress downstream. The photon energy is known by conservation of energy, and therefore determined by,

$$E_{\gamma} = E_{e} - E_{e'} \tag{3.1}$$

Where E_{γ} is the energy of the photon, E_{e} is the energy of the electron in the STB ring and $E_{e'}$ is the energy of the electron as measured in the tagging system. The energy of the scattered electron can determined with an accuracy of $\pm$ 10 MeV by the amount of deflection. In addition to this method the kinematical complete measurement of $\gamma d \rightarrow pp\pi^{-}$ has been successfully established as a method of calibrating the photon tagging system [99]. Using timing coincidence requirements as discussed in section 4.12.2 and shown in Figures 4.33 can ensure the reaction products correspond with the electron detected at the tagger.

3.2.3 Beam Position Monitor (BPM)

The Beam position monitor is composed of 16 finger counters that provides a two dimensional image of the photon impact position upon the target. It also incorporates a pair of trigger counters and a veto counter. In the experimental period, the BPM is monitored continuous to ensure the beam impact on the target is optimal.

3.2.4 Duty Factor

A typical beam cycle is presented in Figure 3.3 where the x and y-directions are the time axis and to the beam current [I] respectively. The flat top and waiting time can be changed upon user request and is specified by a contracted power limit previously established with the electric power company of Tohoku area, Tohoku denryoku. The time for ramping both up and down are established at 1.4 seconds. The duty factor of the beam operational conditions is calculated by the following,

$$\frac{WR}{RU + FT + RD + WT} \tag{3.2}$$

where the variables in the formula are: WR, RU, RD, FT, WT are the Working time of the radiator, the Ramping-up time (1.4 sec), the Ramping-down (1.4 sec) time, the Flat top time, and the Waiting time for the next injection respectively.

The WR is found as flat top (FT) – 2secs. Both FT and W time periods can be adjusted upon demand. In the production runs that took place in the 2006-2007 experimental periods [5], the flat top was 40 seconds and the waiting time was 8 sec and the duty

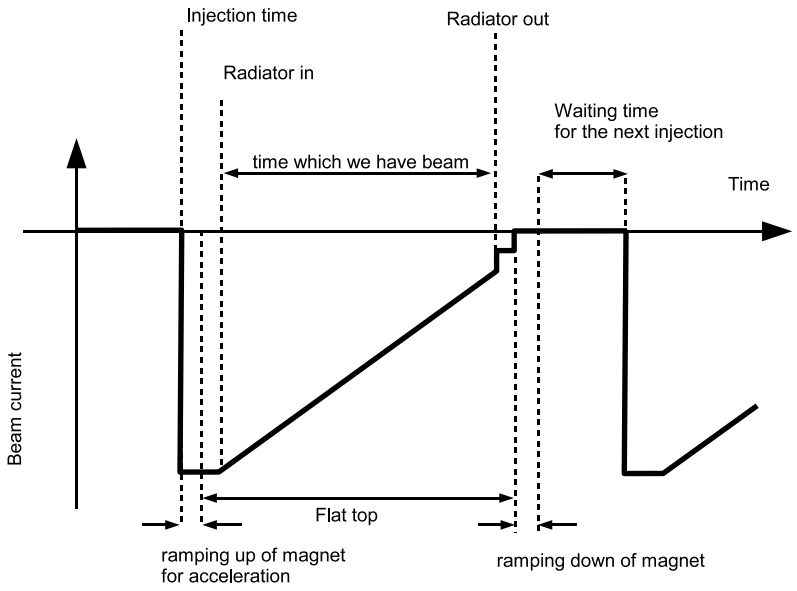

Figure 3.3: A time chart of the usual beam cycle. The x and y-directions are the time axis and to the beam current [I] respectively. The time periods required for ramping up and down are approximately 1.4 secs. The flat top is typically 20 secs and waiting time is $8-20$ secs (these values are dependent upon the power supplied to the ELPH facility). The specific time that the radiator is placed in the path of the electron beam in calculated as the flat top -2 secs.

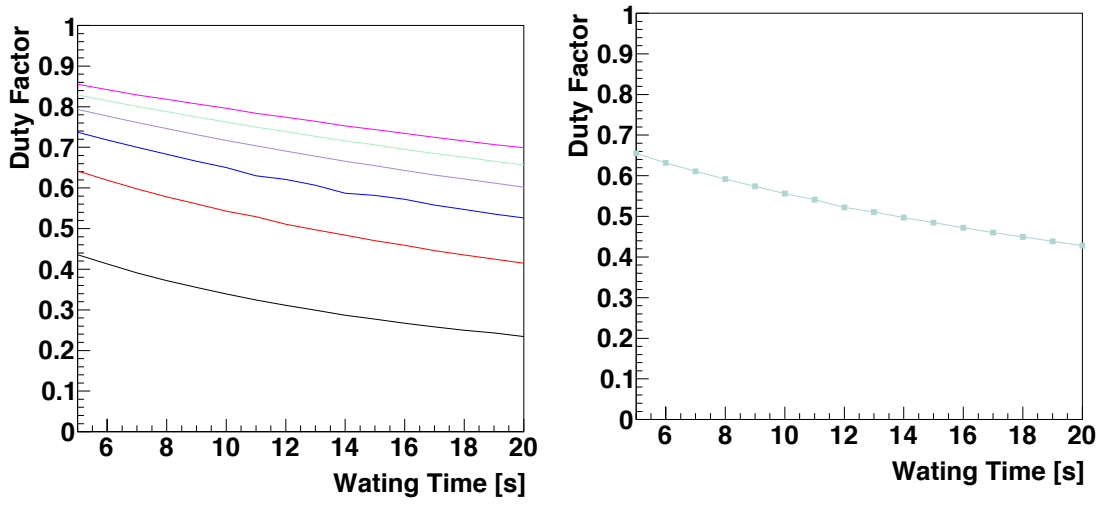

Figure 3.4: The duty factor of STB ring as a function of waiting time is shown in the left figure for various flat top time settings. The flat top was set to 21 seconds for the data analyzed in this thesis and the corresponding beam duty factor is displayed in the right figure.

factor is about 75%. Recently, new buildings were constructed at ELPH for new physics research. Accordingly, the power consumption of the NKS2+ has significantly been reduced. An example of such was detector efficiency test runs conducted at the conclusion of June in 2010. The flat top was set at 20 sec and waiting time was varied between 8 seconds during the overnight period and 20 seconds during the day time operational period. It was decided that a 21 second time interval for the flat top setting would mostly likely increase the stability of the beam intensity during each spill duration. As the beam waiting time interval fluctuated between $8-20$ seconds, the average beam time was estimated at 51%. A plot of the possible duty factor curves as a function of waiting time is shown in the left of Figure 3.4 for various flat top time settings. The flat top was set to 21 seconds for the data analyzed in this thesis and the corresponding beam duty factor is displayed on the right Figure 3.4.

3.2.5 Sweep Magnet

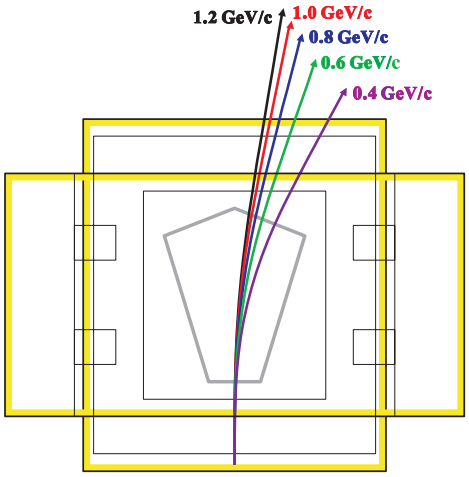

Figure 3.5: The sweep magnet and examples of deflection paths for various electron momenta.

The large number of e^+e^- pairs that are created upstream from the photon beam is substantially reduced by placing the sweep magnet between the radiator and the spectrometer. It consists of a pentagonal shaped dipole magnet that generates a 1.1 Tesla field at 300 A in design. A schematic view and examples of deflection paths for several electron momenta are shown in Figure. 3.5. In front of the sweep magnet is a lead collimator comprised of five blocks, that reduce the beam halo. The collimator aperture is 1.0 cm in diameter. The sweep magnet being located before the main spectrometer efficiently suppresses the background contribution in the data and improves the data acquisition rate.

3.3 The NKS2+ Spectrometer

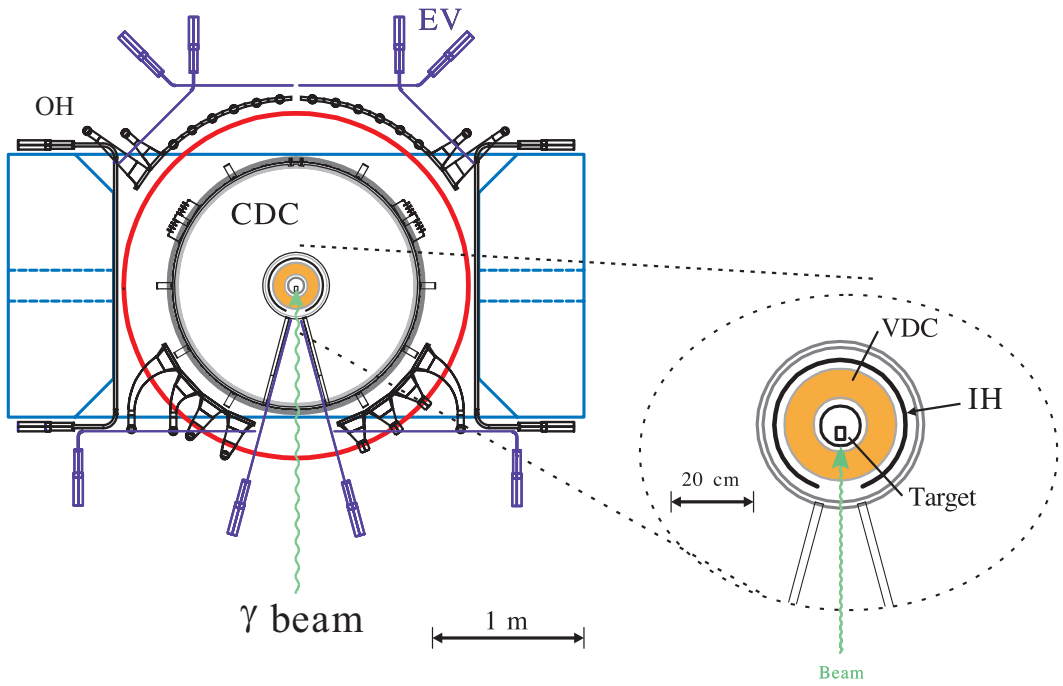

Figure 3.6: The schematic view of NKS2+ after upgrade where a slice of the spectrometer along the beam plane is shown. Inner detectors are shown in the zoomed image.

The NKS2 was installed at the Laboratory of Nuclear Science of Tohoku University (LNS) in 2004, completely replacing the original Neutral Kaon Spectrometer (NKS). Most recently, since 2007-2010, it was further renovated with the addition of new inner detectors in order to increase the acceptance for four track events and also to improve the vertex resolution in the target region, and hence forth was referred to as the NKS2+ or NKS2 upgrade. A schematic view of detectors for NKS, NKS2 and NKS2+ are illustrated in Figures. 1.5, 1.6 and 3.6 respectively. It is positioned along the fourth bending magnet (BM4) in the second experimental hall at the ELPH facility. The NKS2 consists of an assortment of detectors centered on a target that is contained within a vacuum chamber. Moving from the inner most position outwards, is the target, which is surrounded by a Vertex Drift Chamber (VDC), section 3.3.4, and an Inner Hodoscope (IH), section 3.3.8, comprised of twenty plastic scintillator segments, which acts as the initiation time trigger for time of flight measurements. This pair of detectors are then surrounded and fully enclosed in a Cylindrical Drift Chamber (CDC). All detectors are located in between the poles of a dipole magnet, section 3.3.1, with 680 mm apeture. An outer plastic scintillator

hodoscope (OH), section 3.3.9, the stop trigger for time of flight measurement, is located outside the drift chambers. Lastly, in order to improve trigger efficiency, and reduce the level of background as a result of pair production from the photon beam, Electron Veto (EV), section 3.3.10, detectors are installed on a zero degree plane perpendicular to the beam line. Only generated in the forward direction. However, only the EV counters setup at the backward angles are used in the trigger to minimize the bias to the acceptance of the NKS2+ spectrometer at the forward angles.

3.3.1 680 Dipole Magnet

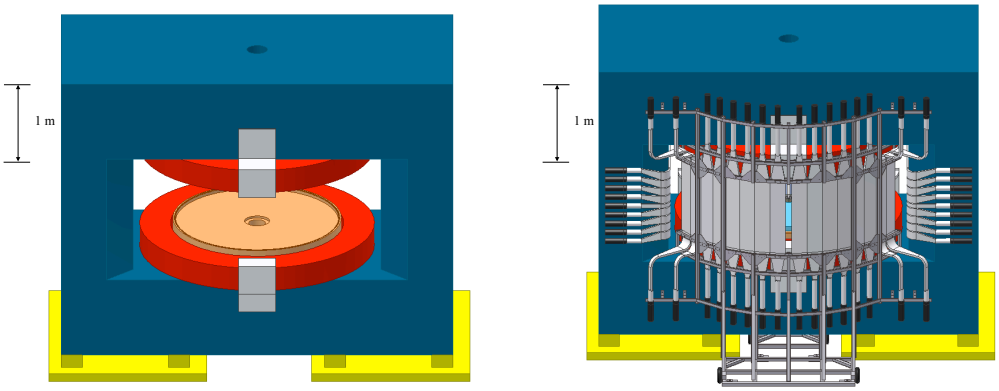

Figure 3.7: Dipole magnet is shown in the left figure prior to the installation of the inner detectors. The figure on the right illustrates the detectors installed with the OHV counters placed in their downstream location.

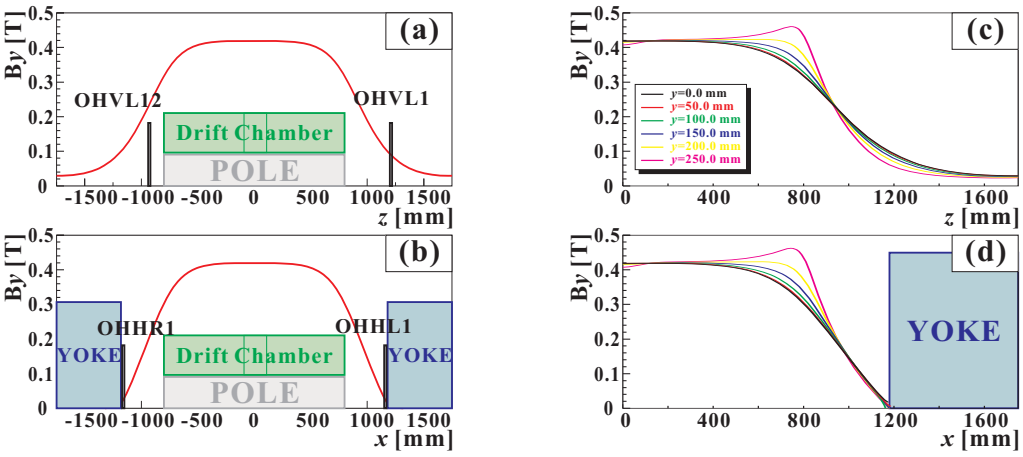

Figure 3.8: 680 dipole magnet field distributions generated by the TOSCA program [5].

The NKS2+ is designed around a dipole magnetic magnet. It was previously extensively used in experiments performed at Cyclotron Radioisotope Center (CYRIC), Tohoku University. A downstream view of the 680 magnet is shown in Figure 3.7, where the magnet prior to the installation of the detectors is shown on the left and following the full installation of the detector package on the right. It generates a magnetic field of approximately 0.42 Telsa with a operational current of 1000 (A). The magnetic field has been calculated by the TOSCA program and the field distributions are seen in Figure 3.8. The distribution of the magnetic field at the mid-plane level along the beam line are shown parallel and perpendicular with respect to the beam line in figures (a) and (b) respectively. The y-axis dependence of the magnetic field is given along the z and x axes in figures (c)and (d). The dipole magnet has a vertical hole of 120 mm in diameter, located at its center, for the purpose of target insertion and removal.

3.3.2 Drift Chambers

The detection of particle tracks and their momenta are determined by the combination of a pair of drift chambers, the Cylindrical Drift Chamber (CDC) and the Vertex Drift Chamber (VDC). The fundamental principle lies in the ability of a drift chamber to detect a charged particle as it transits the detector by the ionization of the drift gas that produces a seed electron. This ionized electron is then multiplied resulting in an avalanche of electrons that are accelerated along the electromagnetic field lines and finally arrive at the anode wire of the chamber.

3.3.3 Drift Gas

The choice of drift gas was Ar+Ethane (50:50) which is also the same gas choice used in CDC. Full details of the drift gas properties can be found in reference [100] A cosmic-ray test of the VDC performance yielded a layer efficiency $\geq 99\%$ for all layers. We explored the option of changing the gas combimation by introducing ethanol into the mixture. Further details concerning the VDC commissioning and the results of the gas study are given in Appendix B.1.

3.3.4 Vertex Drift Chamber (VDC)

The spectrometer received an overhaul in the inner detector sections the most important of which was installation of a drift chamber for vertex reconstruction and three dimensional tracking of the decay particles. The earlier drift chamber was a Straw Type Drift Chamber (SDC), that was capable of only accomplishing two-dimensional tracking. It is positioned

inside Cylindrical Drift Chamber (CDC) and due to its unique design, will be capable of performing three-dimensional tracking of the decay particles.

3.3.5 Wire Geometry

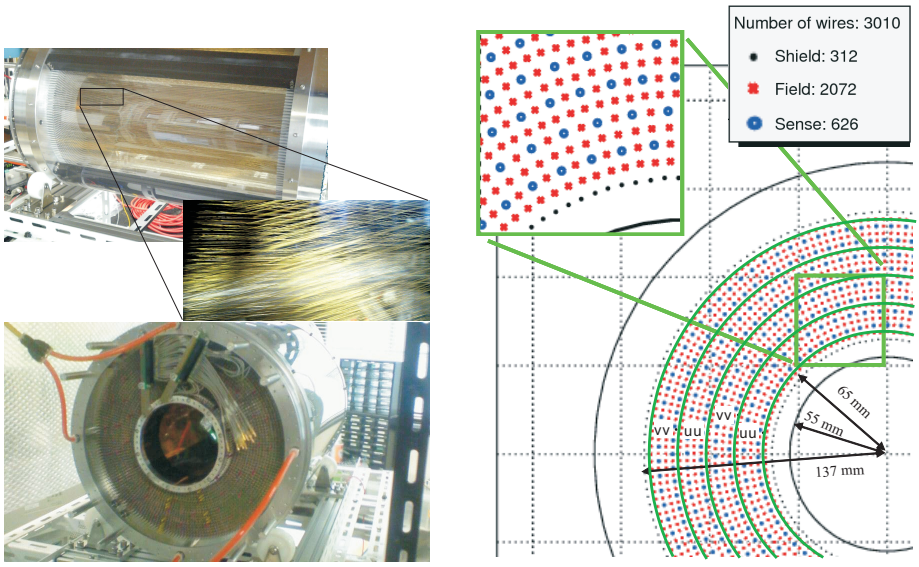

Figure 3.9: VDC detector and cell geometry shown left to right respectively.

The diameter of the VDC is 330 mm with a height of 506 mm and a solid angle about three times that of CDC. The detector is composed 626 sense wires placed at stereo angles such that they created eight layers in a $U, U', V, V', U, U', V, V'$ structure. The cells are trapezoidal in shape with a half-cell size of approximately 4 mm. Each sense wire was made from gold plated tungsten with a diameter of 20 microns. The VDC was designed to have symmetric wire alignment, hence there were significant wire material on the beam line upstream of the target capable of contributing to photon conversion. In order to increase the data acquisition capabilities the wires in the upstream direction along the beam line have been removed. As the result, the order of material in upstream region is equivalent to previous experiments. Table 3.1 shows the cell size and stereo angle for all of layers.

3.3.6 Read Out Card

A GNA-220 signal read-out card was designed to fit into the limited a space in the inner detector region. The GNA-220 has 32 channel inputs/digital outputs and used an Amplifier-Shaper-Discriminator (ASD) chip (SONY CXA3183Q) [101]. The threshold

Table 3.1: VDC cell size and wire specifications.

group number	layer number	half-cell size radial [mm]	half-cell size azimuthal [mm]	stereo angle [deg]	number of sense wires
1	1 (U)	4	3.89	6.35	59
2	2 (U')	4	4.31	7.03	59
3	4 (V)	4	3.88	7.72	72
4	3 (V')	4	4.23	8.41	72
5	5 (U)	4	3.88	9.09	85
6	6 (U')	4	4.18	9.77	85
7	7 (V)	4	3.92	10.44	97
8	8 (V')	4	4.18	11.12	97
				TOTAL	626

Table 3.2: Amplifier-Shaper-Discriminator (ASD) specifications

Pre-Amplifier gain	0.8V/pC
Main- Amplifier gain	7
Feedback resistor	16kΩ
Integration time	16 [ns]
input impedance	80 Ω
Output impedance	open
Comparator	LVDS output

voltage $V_{th} = -1$ V corresponds to 8.93×10^{-3} pC in GNA-220. The charge of the VDC signal is estimated about $0.14-0.16$ pC. Hence, the VDC signal will not be impeded even at the maximum threshold value of -7 V.

The SONY ASD chip only provides a logical output signal (LVDS), which is a differential logic signal whose upper and lower limits are determined by the current value. The TDC board, AMT, can receive either a ECL and LVDS signal. The GNA-220 has a 32 channel output that was attached to a 68 pin connector. Also, we utilized a multi-hit TDC of AMSC AMT-VME module for the accumulation of signals from the drift chambers. The AMT used a 34 pin MIL connector. The output from the chip however is voltage not the required current. Thus a resistance board was mounted onto a rack to convert the voltage signal to a current prior be fed into the AMT module.

3.3.7 Cylindrical Drift Chamber (CDC)

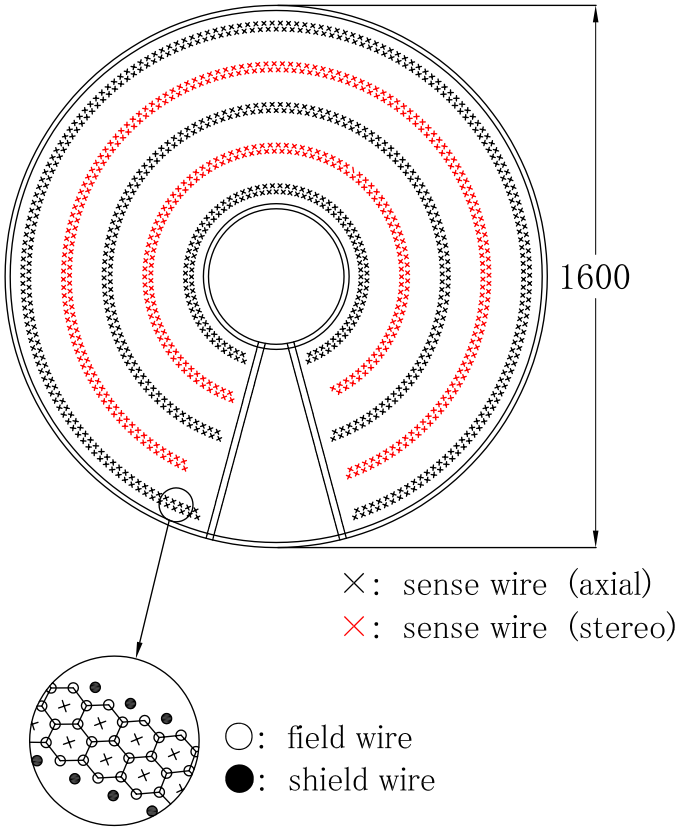

Figure 3.10: Schematic display of Cylindrical Drift Chamber (CDC), where the cell structure is shown on the lower left of the figure.

The cylindrical honeycomb drift chamber (CDC), seen in Figure 3.10, is designed with a total diameter of 160 cm and consited of ten layers. These ten layers were furthered defined into a groups consisting of two layers within each group. the third of the group was tilted at a stereo angle of 6.5 degrees. The angular of coverage of the chamber ranged from $-165 - 165°$ in the horizontal direction, and radial coverage of $23.8 - 76.0$ cm, from the edge of the field wire. A complete explanation of the CDC characteristics are provided in Table 3.3. The cell shape was hexagonal honeycomb shape structure. Each sense wire was made from gold plated tungsten with a diameter of 20 microns with a set tension of 50 gw. Conversely, each of the shield and field wires were 100 μm in diameter and made from Cu-Be (gold plated copper and beryllium) with a set tension of 50 gw. The gas used was the same as for the VDC, an equally premixed combination of Argon and Ethane. The maximum drift time in a cell was roughly 250 ns. The combination of the CDC and

VDC permits the tracking of charged particles in three dimensions, and are a necessary detector to measure the momentum and determine the decay tracks of the protons and charged pions.

Table 3.3: CDC cell size and wire specifications

group number	layer number	cell size [mm]	stereo angle [deg]	radius [mm]	number of sense wires
1	9 (X)	10.36		250	68
	10 (X')	11.10		268	67
2	11 (U)	10.36	6.2164	370	89
	12 (U')	11.10	6.5188	388	90
3	13 (X)	10.36		490	119
	14 (X')	11.10		508	120
4	15 (V)	10.36	−6.4420	610	143
	16 (V')	12.05	−6.6321	628	144
5	17 (X)	11.78		730	175
	18 (X')	12.07		748	176
				TOTAL	1191

3.3.8 Inner Hodoscope (IH)

In most spectrometers the position of particles are measured by hodoscopes, which are simply an arrangement of detectors to measure the position of a particle that is moving perpendicular its configuration [102] The IH, a Time Of Flight (TOF) counter, is added into the logic as a start trigger. Each segment is attached to a light guide and a fine mesh dynode type photomultiplier, HAMAMATSU H6152-01B, that operates on a negative high voltage setting and allows for operation within the 0.42 T magnetic field supplied by the 680A magnet. The IH counter segments are arranged to enclose the VDC. The size of each segment was specifically designed considering the probability of multiple hits on one segment and the PMT peak operational singles rate. The desired requirement was that of a less than 2% probability of multi-hits and a singles rate $\leq$ 200 kHz. The reduction of multiple hits on one counter is necessary to avoid discarding $\pi^+\pi^- p\pi^-$ events, where two or more decay particles transverse the same IH segment. IH $(5-8)$ have scintillators 38.0^Hx 7.53^Wx 0.5^T cm in size. IH2 is 38.0^Hx 1.83^Wx 0.5^T cm, and was designed with a thinner width, 1.83 cm, than the remaining segments to reduce the counting rate. The results of a GEANT4 simulation revealed that the incoming bremsstrahlung photons of

energy of 5MeV to 1.2GeV resulted in a singles rate of 160 kHz at a tagged photon rate of roughly 2 MHz. The details of the angular coverage and dimensions of each segment are listed in Table 3.5. Figure. 3.11 presents the all IH counters mounted upon VDC body.

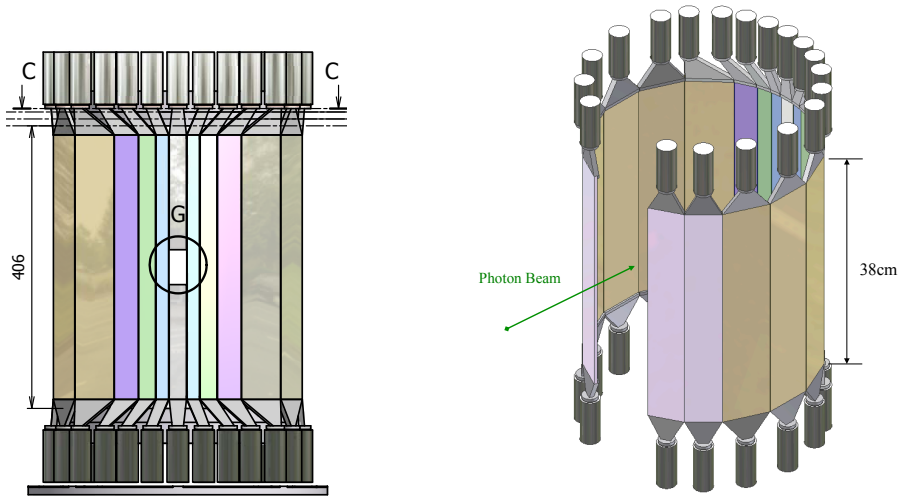

Figure 3.11: Full Inner Hodoscope (IH) assembled on the VDC

3.3.9 Outer Hodoscope (OH)

As the IH is used as a start counter, the outer hodoscope (OH) is used as stop counter and is a necessary part of the trigger system in that it it was able to detect two particle existing the inner detector package sufficiently providing coverage of $\pi^+\pi^-$, $p\pi^-$ or four particle decay event. The OH is constructed from two sections one of which is arranged in a vertical position (OHV) and the other arranged horizontally (OHH) and further divided into right and left components. The vertical component consisted of a total of twenty four segments, having twelve arranged on either side of the beam line, defined as outer hodoscope vertical left (OHVL) and right (OHVR). OHV $1-8$, use scintillator counters of 74.8^Hx 7.53^Wx 2.0^T cm in size, and are placed downstream in relation to the target position. OHV $9-12$ are placed upstream and have scintillators 50.0^Hx 5.64^Wx 2.0^T cm in size. The orientation of OH counters is shown in Figure 3.20. A concise detail of all the OH counters is listed in Table 3.5.

The horizontal component of the OH had nine segments for the left and right side, and since they were arranged parallel to the beam direction, they would detect particles with a high curvature. The OHH counters that were arranged on the plane of the beam line were thinner in design for the purpose of lowering the count rate. OHV $7-12$ and all OHH plastic segments were affixed to folded light guides in order to transport the

signals outside of the magnetic dipole region because of a photomultipliers performance sensitivity to strong magnetic fields. The vertical segments were 60 cm in height and 2 cm in thickness.

3.3.10 Electron Veto (EV)

The photon beam will contribute a lot of background signals via the pair production process and was be the main contamination at the trigger level. In an attempt to reduce this, an electron veto counter was constructed. The light mass of the electrons will result in a small opening angle for the created pairs. The EV was placed on a zero degree plane perpendicular to the beam line. There are 8 detectors arranged in four pairs that comprise the entire EV package, referred to as EV1 - EV4, where the numbering of the counters grows in relation from the downstream to upstream potion. A detailed description of the EV counters is given in Table 3.4 and is illustrated in Figure 3.12. The aim is to reject electron and positron pairs because the conversion probability is much larger than the $\gamma + n \rightarrow K^0 + \Lambda$ reaction. However, there is the chance of discarding pions and proton from K^0 and Λ. The Λ hyperon is produced primarily in the forward direction. It follows then that the proton from the Λ particle will move forward especially in comparison to the charged pion decay from the kaon. Consequently, the use of the EV counters downstream has been eliminated and a study was performed to ascertain the effects of their removal from the trigger in terms of the data acquisition capabilities.

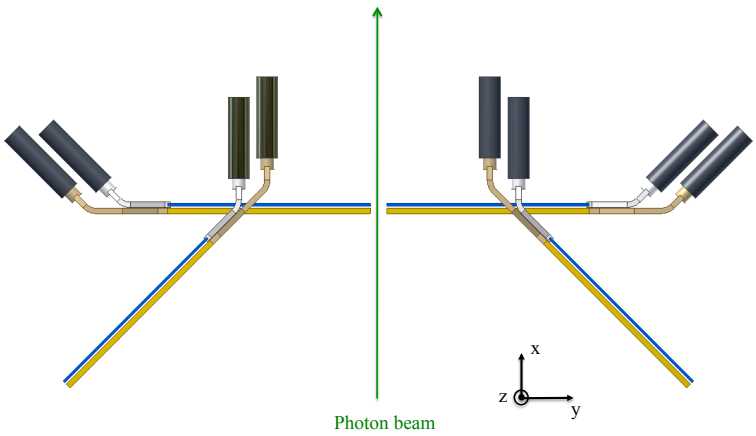

Figure 3.12: Electron veto counters 1 and 2.

Table 3.4: Electron Veto (EV) counters.

Segment ID	Length [cm]	Width [cm]	Thickness [cm]
EV1	75.0	5.0	1.0
EV2	75 .0	5.0	1.0
EV3	125.0	5.0	.5
EV4	60.0	15.0	1.0

3.3.11 Target System

In order to study the photoproduction reaction process on a neutron, it was decided to use the deuteron, the simplest bound system of nucleons. The cross section of $K^0\Lambda$ is roughly on the order of $1\mu b$. Therefore, in order to obtain a significant amount of statistics ,not only is it necessary to have a beam of the highest intensity possible, but a dense target should also be used. The target system was used to condense the deuterium into liquid form. The target is housed in the vacuum chamber placed under the recondenser. The apparatus was designed to be inserted and removed from the spectrometer via an aperture located at the top by a manually operated crane system. The target system and the inner details are shown in Figure 3.13

3.3.12 Target Cell

The target cell is monitored remotely by National Instruments LabVIEW on a Linux machine in the counting room due to the inaccessibility of the experimental hall during the target irradiation period. Constant monitoring ensures that the target is maintained at a safe operational temperature and does not solidify. During the course of the experimental runs the target temperature and absolute pressure were monitored enabling the calculation of the density of the liquid deuterium target and subsequently the number of the target neutrons.

The vacuum chamber, cylindrical in shape, was designed with a thickness of 1.5 mm. It was inserted through a vertical hole in the spectrometer with a diameter of 120 mm, located 15 mm from the center position of the NKS2 into the magnetic yoke, in a configuration such that its axis was parallel to that of the beam line, for the purpose of increasing the photoinduced production of $K\Lambda$. The deuterium in a gaseous state is injected by an inlet port and liquified at the condensor and allowed to drip into the target cell [103]. The target cell is constructed from aluminum with an outer shell thickness of 1 mm and a beam window constructed of Upilex-S film 75μm in thickness clearly visible in Figure 3.14. The

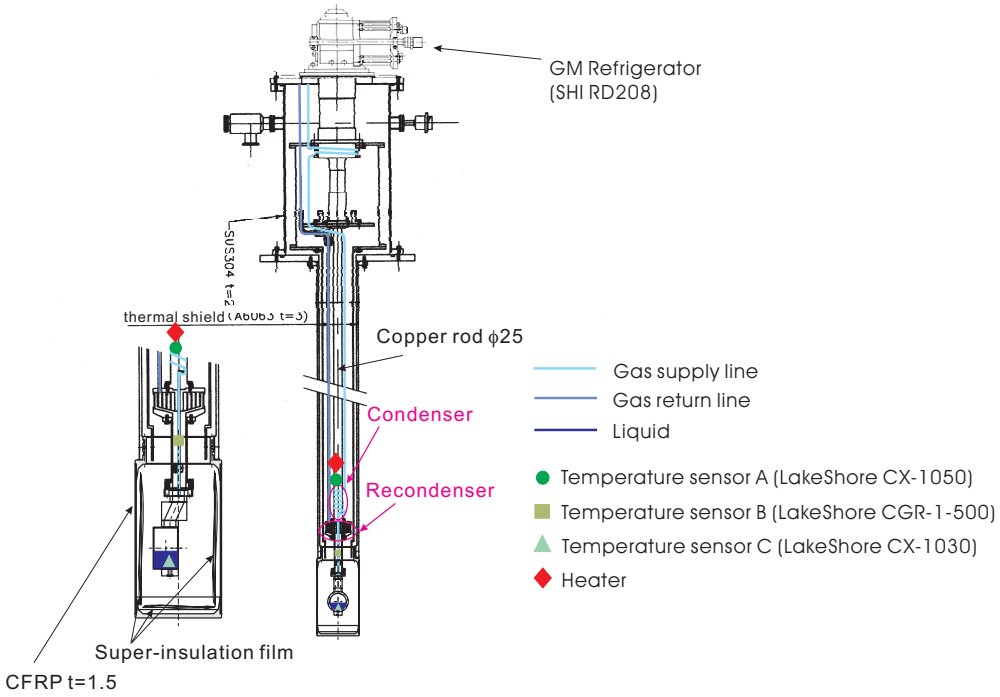

Figure 3.13: The target is stored in the vacuum chamber below the recondenser and was designed to be inserted and removed from the spectrometer via an aperture located at the top by a manually operated crane system.

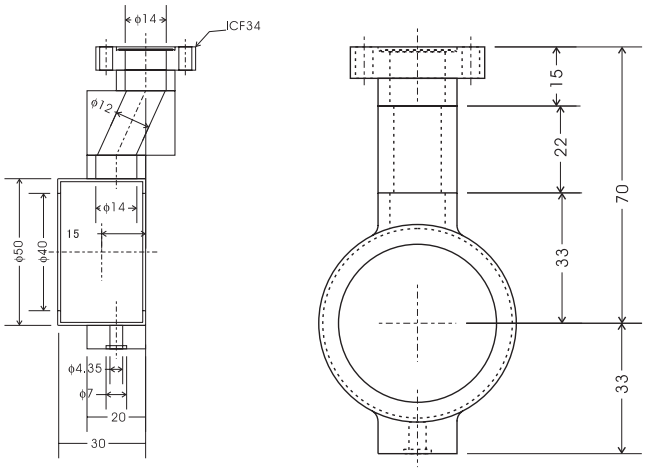

Figure 3.14: Shape of target cell

beam window was designed to 40 mm and the outer diameter of the cell is 50 mm. The target thickness is designed to be 2.97 cm.

3.4 Triggered Event and Associated Electronics

3.4.1 Electronics and Data Acquisition (DAQ)

A trigger is usually a set of detectors that works in combination to indicate when an event of significance has taken place. The trigger determines when the signals of the detector package should be recorded, where the aim to gather the largest yet cleanest data set at the highest beam intensity possible. Therefore, an ideal trigger would eliminate the recording of events not of interest, and increase the retrieval of events that may contain information regarding the physics to be explored. The UNIDAQ on Linux was used as a base system of the NKS2+ data acquisition system. In the experimental counting room the data is collected on three data acquisition machines, which are designated as k0daq0, k0daq1, and k0daq2. Both k0daq0 and k0daq1 are used to record data from the drift chambers and k0daq2 is used for the IH, OH, and EV signals and scaler data. The counter signals are first discriminated by leading edges discriminators and were collected by CAEN VME modules of muti-hit TDC (V775) and QDC (V792).

The signals from the drift chambers were amplified and discriminated by a GNA-220 Amplifier-Shaper-Discrimiator (ASD), the details were given in Table 3.2. We employed a multi-hit TDC of AMSC AMT-VME module for the accumulation of the signals form the drift chambers. The VME information is read via a PCI-VME adapter, SBS Bit3 Model 618 (now it is owned by GE Fanuc). During the commissioning of the NKS2+ and the VDC, we recorded a notable amount of hits in a negative time region under a high tagged photon beam rate. We elected to modify the internal operational program for AMT (Atlas Muon TDC) VME modules, the AMT time resolution (LSB) were roughly 0.78 nsec per channel with a corresponding dymanic range of 1 μs.

3.4.2 Trigger

The trigger logic differed for various data that desired to be taken. As such, full diagrams of the upgraded NKS2+ logic for production data, tagger system calibration as well as for the counters and chambers are given in Figures 3.18, 3.15, and 3.17. The main trigger utilized for physics production experiments required an event trigger from the STB tagging arm and the spectrometer arm. The tagging system portion required an event trigger that was made from a coincidence between the TagF and TagB counters in order to decrease the background and in principle, a tagged electron will have approach on a deflection angle the a photon was produced in the $0.8 - 1.1$ GeV energy range. The trigger requirement on the spectrometer half prescribed that even with to or more charged particles were detected that transferred the spectrometer. Therefore two more particles were required from the

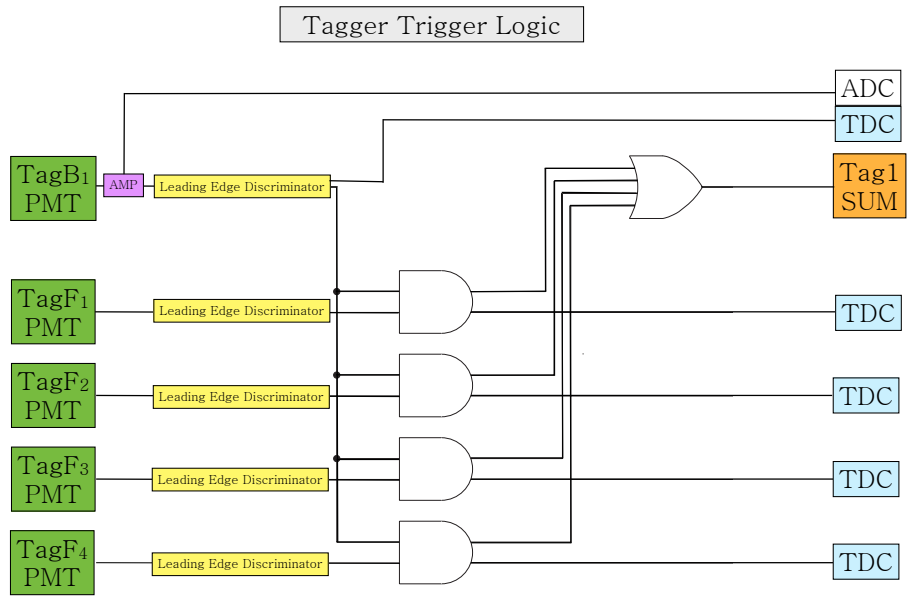

(a) Tagger

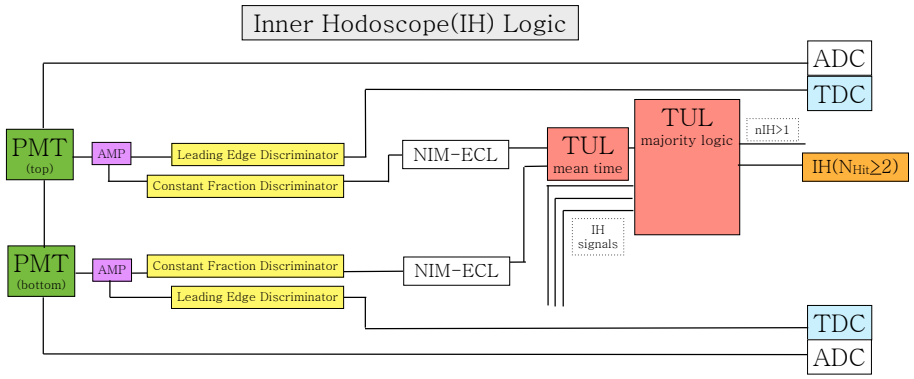

(b) Inner Hodoscope

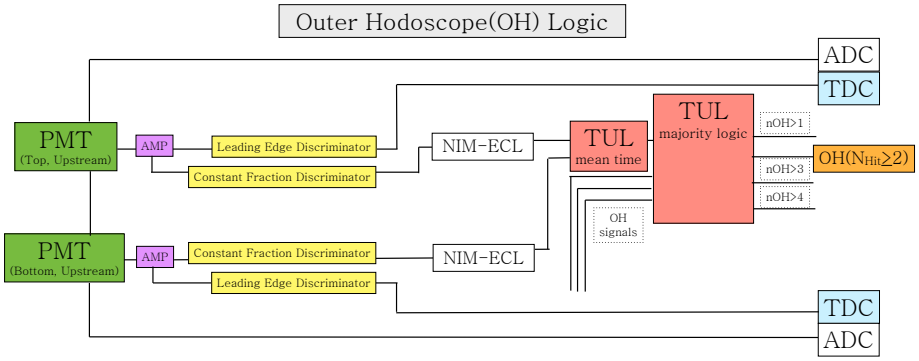

(c) Outer Hodoscope

Figure 3.15: Trigger logic of the Tagger, IH and OH.

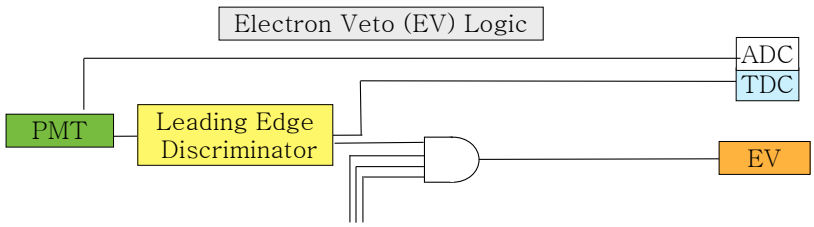

Figure 3.16: Trigger logic of the EV counter.

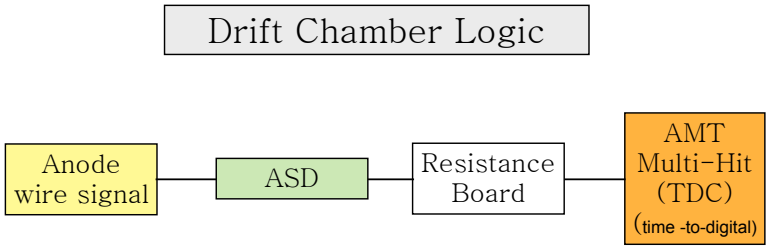

Figure 3.17: Trigger logic of drift chambers. The signals were detected on the anode wire, amplified by the ASD card and read out by the AMT module.

IH and the OH counters. It is possible to also include the signal from the EV counters as a veto of electron coming from photon conversion. We implemented a spill gate, connected with the beginning motion of the radiator to repudiate events that originated from the radiator itself.

The trigger logic for physics runs and for the calibration of the tagger are shown in Figure 3.18 in the upper and lower panels respectively. The logic can be more readily understood be the examination of equation 3.3

$$\text{Trigger} = (\text{nTagSum} \geq 1 \otimes \text{nIH} \geq 2) \otimes \text{nOH} \geq 2 \otimes \overline{\text{EV}} \tag{3.3}$$

where, nTagSum is used to denote a photon being generated and tagged over a range of $0.8 \leq E_\gamma \leq 1.1$ GeV, the energy of the photon is known by tagging the recoiled electron. As defined above the trigger requires that a two particle event is detected by the IH and the OH. For the OH this may occur by combinations between the horizontal and vertical groups. Lastly, the EV is included into the trigger logic as a veto. Thus, if there is a recorded coincidence event by the left and right EV counters the trigger is not provided.

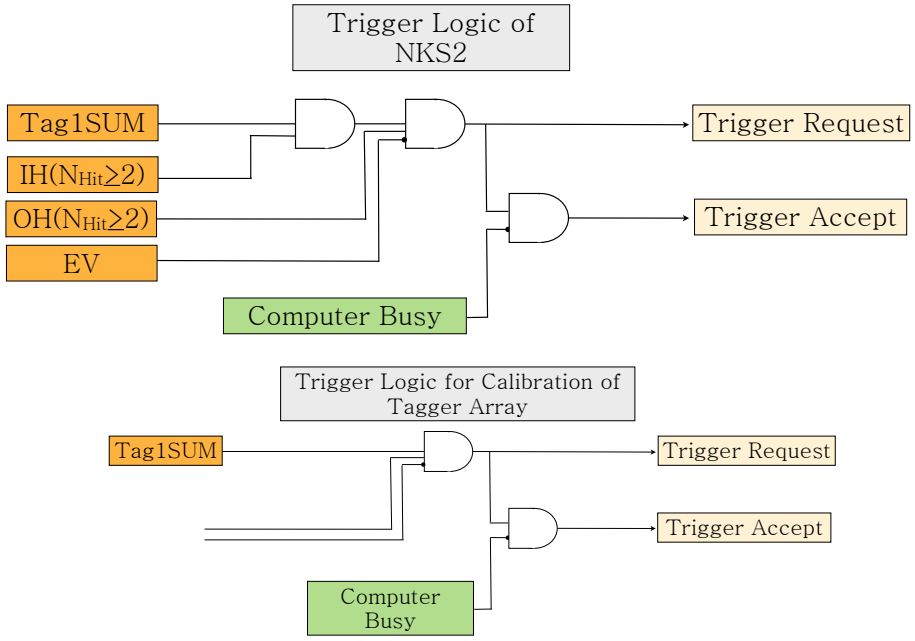

Figure 3.18: Trigger logic of NKS2+ spectrometer for normal data acquisition and tagger calibration.

3.4.3 Tohoku Universal Logic Module (TUL)

A programmable logic unit, referred to as the Tohoku Universal Logic module (TUL-8040) and illustrated in Figure 3.19 was used in the various trigger logics of the NKS2+ spectrometer. The module has the capabilities of several module that are each accessible by switching amongst the installed programs. The propagation time within each module in approximately 50 ns. It was designed with 80 input (ECL/LVDS 64 ch + NIM 16 ch) and 40 (ECL 32 ch + NIM 8 ch) output channels, that are mounted to a FPGA (Field Programmable Gate Array) chip of a ALTERA APEX 20 series [104]. In the NKS2+ package the discriminated outputs of the OH and IH were fed into the TUL-8040 module. We implemented another TUL-8040 module to create the majority logic of the IH and OH capable of recording multiplicity of signals that were greater than 1 ($N_{IH} \geq 1$), & ($N_{OH} \geq 1$) and did not exceeded 4 ($N_{OH} \geq 4$). An additional TUL-8040 module was used in the event matching between the data acquisition computers, and was referred to as the bit-counter. The correct matching of events was ensured by recording the 4 bit signal output supplied front the bit-counter.

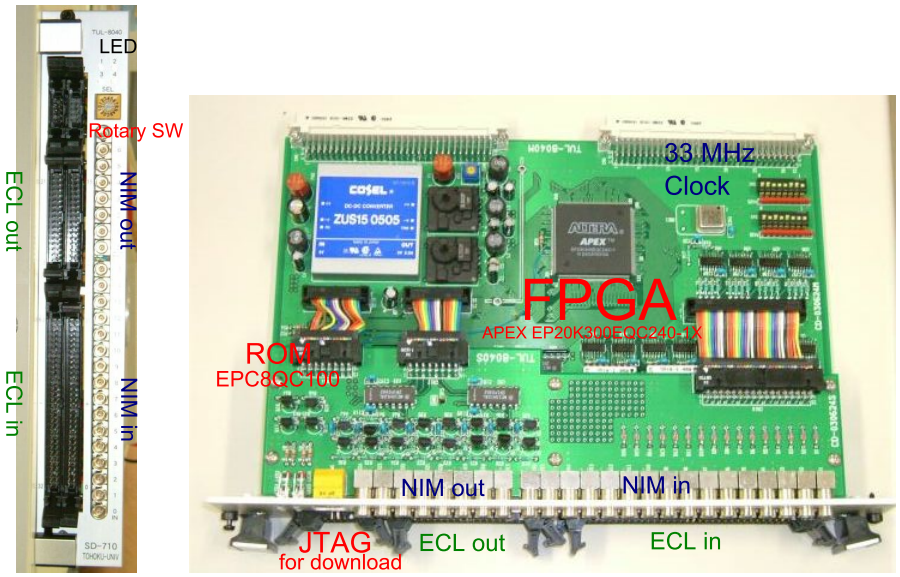

Figure 3.19: The programmable logic unit designated as the Tohoku Universal Logic module (TUL-8040).

3.5 Outer Hodoscope Specifications

The schematic details concerning the orientation and details of the OH counters is given in Figure. 3.20 and Table 3.5.

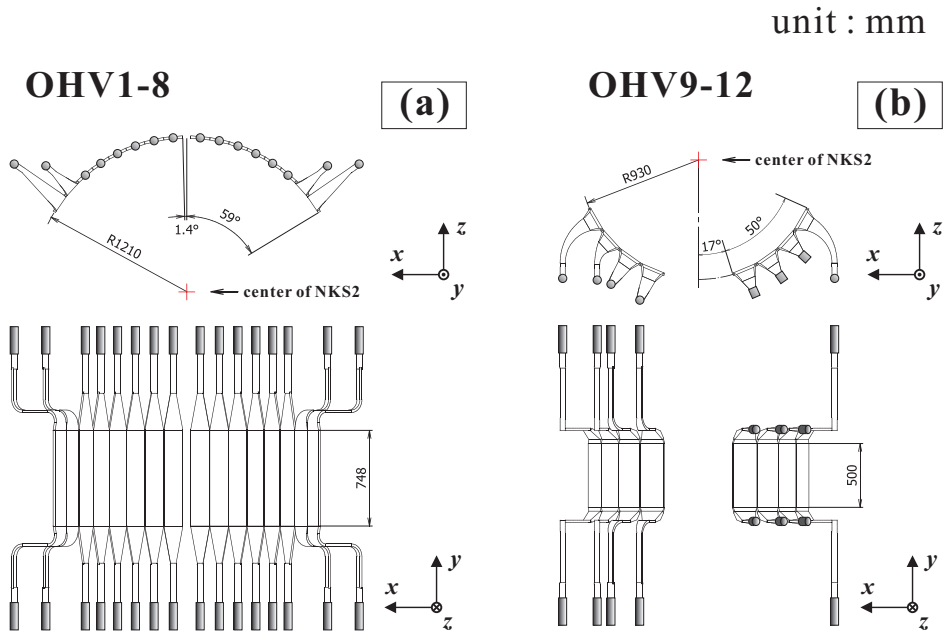

(a) Outer Hodoscope Vertical Components

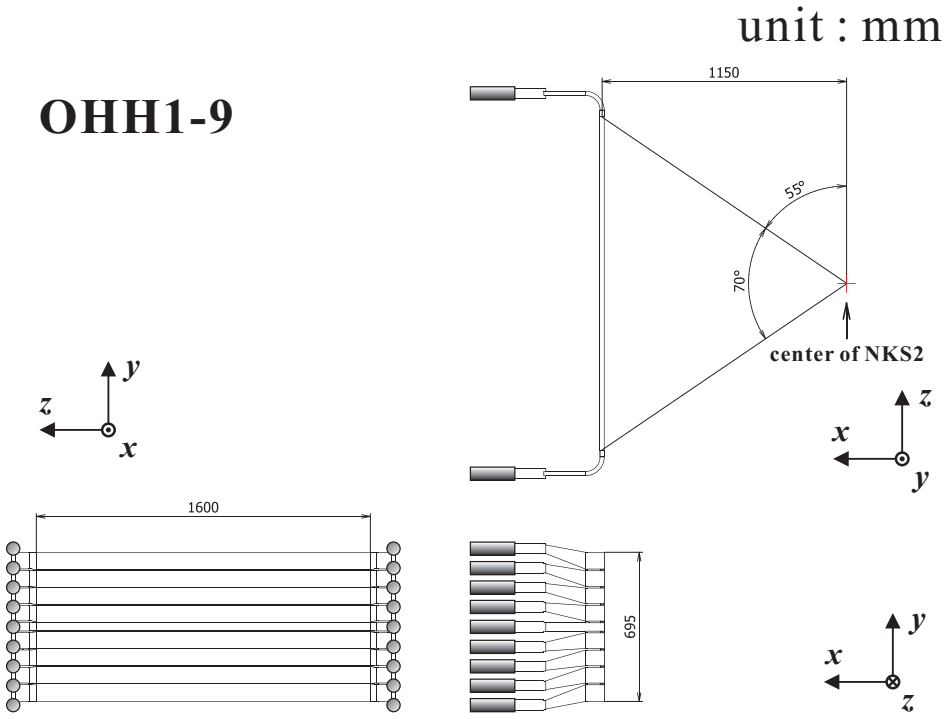

(b) Outer Hodoscope Horzontal Components

Figure 3.20: Outer Hodoscope detector package orientation.

Table 3.5: List of hodoscope TOF counters.

Segment ID	Angle coverage	Dimensions	Radius
IH	[deg]	[cm]	[cm]
IH1	± (-4 −+4)	16.5^{H}x 2.54^{W}x 0.5^{T}	
IH2	± (4 − 10)	38.0^{H}x 1.83^{W}x 0.5^{T}	
IH3	± (10 − 18)	38.0^{H}x 2.47^{W}x 0.5^{T}	
IH4	± (18 − 30)	38.0^{H}x 3.74^{W}x 0.5^{T}	
IH5	± (30 − 54)	38.0^{H}x 7.53^{W}x 0.5^{T}	
IH6	± (54 − 78)	38.0^{H}x 7.53^{W}x 0.5^{T}	
IH7	± (78 − 102	38.0^{H}x 7.53^{W}x 0.5^{T}	
IH8	± (102 − 126)	38.0^{H}x 7.53^{W}x 0.5^{T}	
IH9	± (126 − 144)	38.0^{H}x 5.64^{W}x 0.5^{T}	
IH10	± (144 − 162)	38.0^{H}x 5.64^{W}x 0.5^{T}	
OHV	[deg]	[cm]	[cm]
OHV1	± (-1.4−8.6)	74.8^{H}x 2.54^{W}x 2.0^{T}	121.0
OHV2	± (8.6− 15.8)	74.8^{H}x 1.83^{W}x 2.0^{T}	121.0
OHV3	± (15.8− 23.0)	74.8^{H}x 2.47^{W}x 2.0^{T}	121.0
OHV4	± (23.0− 30.2)	74.8^{H}x 3.74^{W}x 2.0^{T}	121.0
OHV5	± (30.2− 37.4)	74.8^{H}x 7.53^{W}x 2.0^{T}	121.0
OHV6	± (37.4− 44.6)	74.8^{H}x 7.53^{W}x 2.0^{T}	121.0
OHV7	± (44.6− 51.8)	74.8^{H}x 7.53^{W}x 2.0^{T}	121.0
OHV8	± (51.8− 59.0)	74.8^{H}x 7.53^{W}x 2.0^{T}	121.0
OHV9	± (113.8− 126.2)	50.0^{H}x 5.64^{W}x 2.0^{T}	93.0
OHV10	± (126.2− 138.6)	50.0^{H}x 20.0^{W}x 2.0^{T}	93.0
OHV11	± (138.6− 151.0)	50.0^{H}x 20.0^{W}x 2.0^{T}	93.0
OHV12	± (151.0− 163.4)	50.0^{H}x 20.0^{W}x 2.0^{T}	93.0
OHH	x , y, z [cm]	Size [cm]	[cm]
OHH1	± 115.0, 30.25, 0	1600^{L}x 8.25^{W}x 2.0^{T}	121.0
OHH2	± 115.0, 22.25, 0	1600^{L}x 8.0^{W}x 2.0^{T}	121.0
OHH3	± 115.0, 14.25, 0	1600^{L}x 2.47^{W}x 2.0^{T}	121.0
OHH4	± 115.0, 6.25, 0.	1600^{L}x 3.74^{W}x 2.0^{T}	121.0
OHH5	± 115.0, 0.0, 0	1600^{L}x 7.53^{W}x 2.0^{T}	121.0
OHH6	± 115.0, -6.25, 0	1600^{L}x 7.53^{W}x 2.0^{T}	121.0
OHH7	± 115.0,	1600^{L}x 7.53^{W}x 2.0^{T}	121.0
OHH8	± 115.0,	1600^{L}x 7.53^{W}x 2.0^{T}	121.0
OHH9	± 115.0,	1600^{L}x 5.64^{W}x 2.0^{T}	93.0

CHAPTER

FOUR

ANALYSIS METHODOLOGY

> If you always put limits on everything you do physically or anything else, it will spread into your work and into your life. There are no limits. There are only plateaus and you must not stay there, you must go beyond them.

Bruce Lee

4.1 Overview

In this chapter a summary of the gathered data, the details involved in the analysis procedure, including counter calibration procedure, analysis efficiency, and drift chamber tracking efficiency and resolution shall be reported. This will be followed by an explanation of the event selection, particle identification methods, and an evaluation of the time of flight separation power. Next, the calculation of the measured particle invariant mass, and the momentum and angular distributions will be discussed. Next, an estimation of the background will be presented. Lastly a description of the acceptance calculation is reviewed. The analysis method undertaken to obtain the experimental observables from the raw data followed the structure presented in Figure 4.1.

4.2 Data Summary

Photo production data on a deuteron target was taken over the course of several weeks, that included September and October 2010. The data analyzed in this thesis was the portion taken in September 2010. The data gathered in both experimental period was taken with the same trigger logic and a tagged photon beam intensity ranging from $1.0 - 2.0$ MHz.

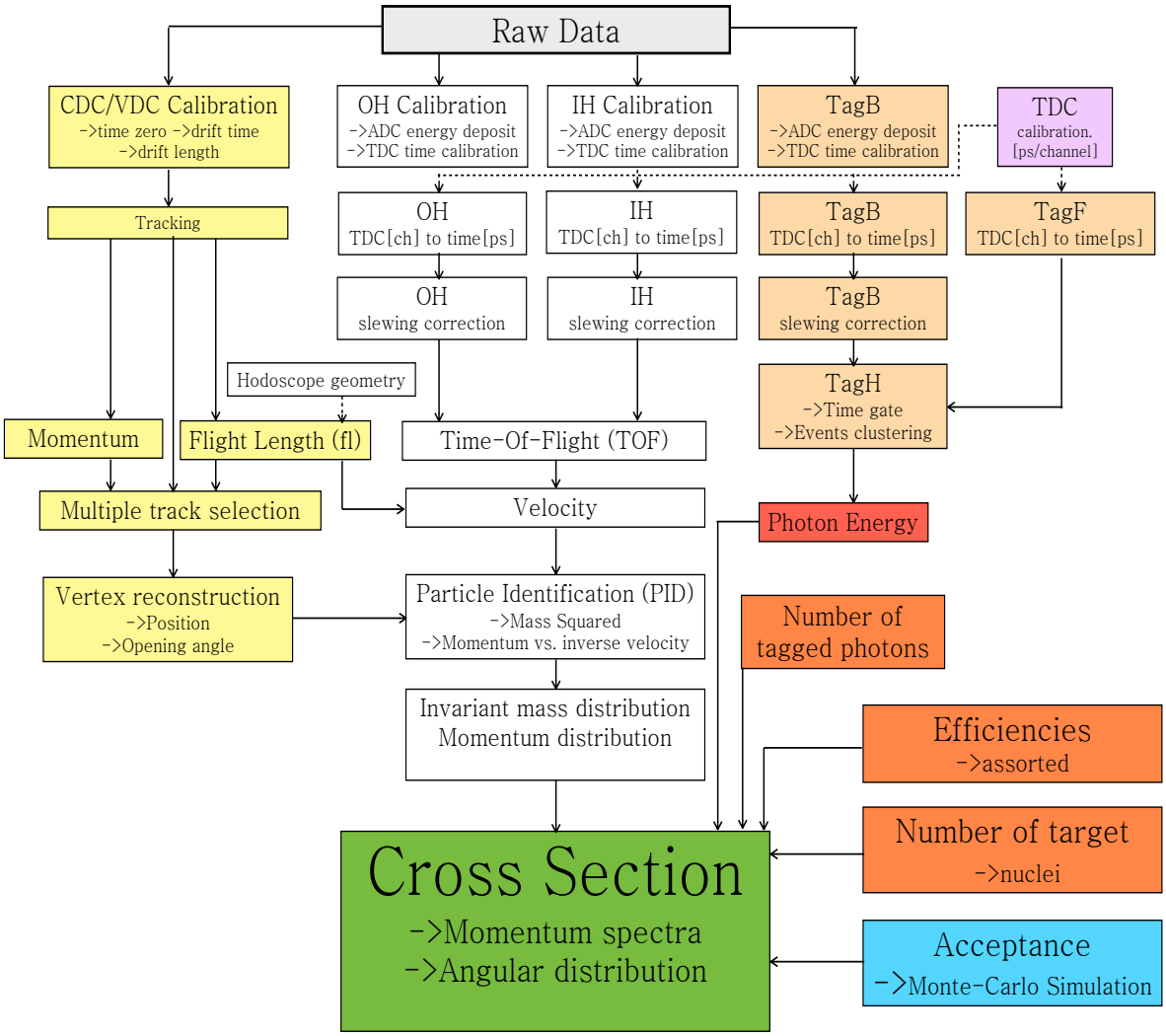

Figure 4.1: Data analysis technique.

Table 4.1: Summary of data for physics production runs.

Experiment Period 2010	Flat Top [s]	Number of Accepted Events	Number of Photons [γ]	Beam Rate [MHz]
September	21	0.64×10^9	0.89×10^{12}	1.5 - 2.5 MHz

4.3 Data Calibration and Processing

The aim of this experiment is to measure physical quantities and correctly interpret these values in order to draw conclusions about a physical process. However, the first task is preparing the raw gathered data for an in depth analysis. An absence of such preparations inevitably hinders the correct and precise extraction of physical quantities and will be plagued with uncertainties. Therefore, each detector assembly in the spectrometer undergoes a calibration procedure to obtain the necessary parameters, to ensure the detectors peak performance is achieved.

4.3.1 TDC and ADC Offset

The hodoscope counters provide essential Time-Of-Flight (TOF) information, energy deposit per unit path length (dE/dx), and vertical hit positions that are used in combination with the signals acquired from the drift chambers to reconstruct the trajectories of the particles. However, it is possible for variations in the pulse height of each photomultiplier to exist due to its respective gain. These variations in the quantum efficiency can be caused due to age and radiation damage. A calibration of both the IH and OH was performed for each hodoscope segment on a run per run basis to optimize the analysis parameters. The time calibration involved the correct assessment of the gain and time offset value of each counter. This offset value is used to adjust the raw TDC spectra peak to the zero position for the pair of PMTs affixed the scintillaiton bars. The self-timing resolution for the outer hodoscopes was calculated by finding the offset values of the TDC distribution, then subtracting the offset time, and fitting the final result to a normal distribution. The standard deviation is the resolution of the detectors in ns. TOF measurements can be enhanced, if various corrections to the raw signals are performed, of which the most notable is a pulse height correction. Following the initial TDC pedestal offset correction, the timing of all hodoscopes counters is supplementally tuned using the IH2 segments as the prime timing counter. A typical TDC spectrum and the fitting procedure by a gaussian distribution for IH and OH counters is displayed in Figure 4.2

4.3.2 ADC Offset and Gain

The technique involved properly identifying the gain and ADC offset value, commonly know as the pedestal, and the first peak. The pedestal is the ADC response in the absence of any signals. This is an offset value that is determined and then subtracted off to obtain the corrected value of the signal corresponding to the energy deposited. The trailing peak is associated with that of a minimum ionizing particle (MIP). The shape of the MIP peak follows a Landau distribution [105]. The gain is defined as the measured number

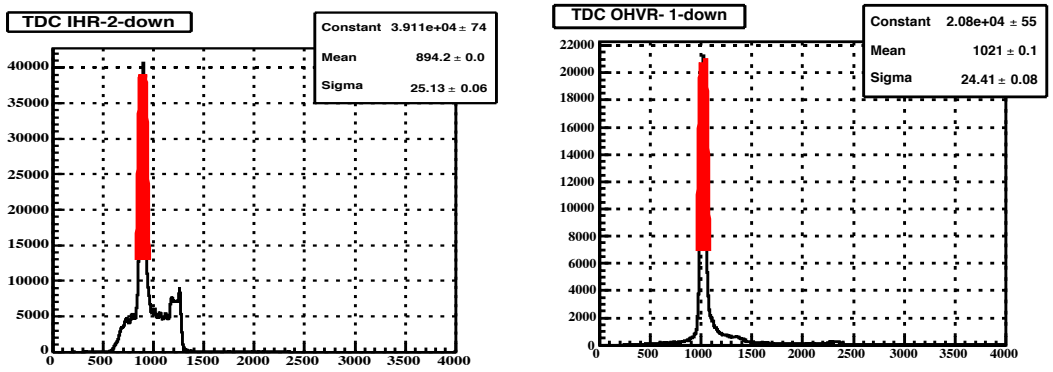

Figure 4.2: Fitting of a typical TDC distribution for timing calibration.

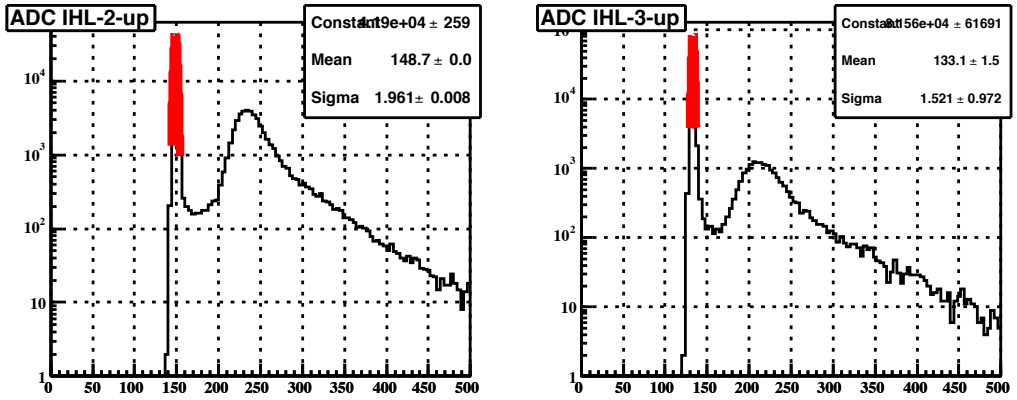

(a) ADC pedestal fitting (IH)

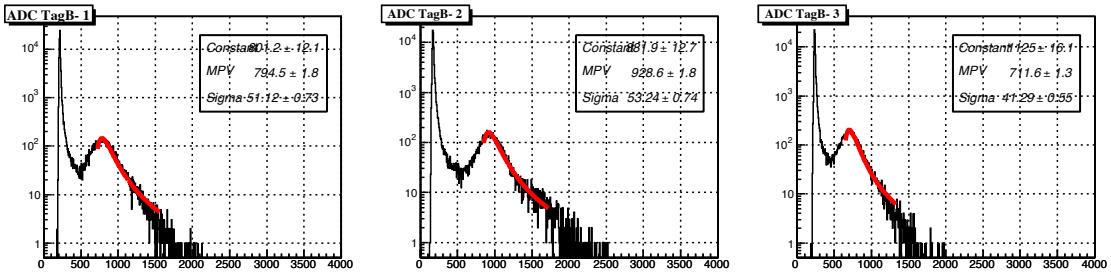

(b) ADC MPV fitting (TagB)

Figure 4.3: Typical ADC spectrum for the IH and TagB counters. Here the fitting of the pedestal (a) and MPV(b) peak is shown.

of ADC channels associated with the difference between the pedestal and the MIP peak. Once the calibration parameters was properly obtained for each PMT in the hodoscope

arrays, the energy deposited can be determined. The accurate energy deposition in the OH is calibrated with knowledge of the plastics mean stopping power of 4 MeV, which is proportional to 2 cm in thickness, for a minimum ionizing pion. This same calibration procedure is applied to the IH, where the plastic bars were 0.5 cm in thickness. The expectation in an energy deposition is in the range of 1 MeV, for a minimum ionizing pion, to approximately 11 MeV, and possibly higher for low momentum protons. The gain of the only TagB segments was calculated due to only the recording of the TDC signals for the TagF finger counters. The fitting procedure for the ADC spectrum was administered using a Landau function [105] as it best describes the distribution; As a result of straggling, the value of interest is the MPV, the most probable value of the energy deposit. In Figure 4.3 a typical ADC spectra and the fitting of the pedestal and MPV is shown.

4.3.3 Pulse Height Correction

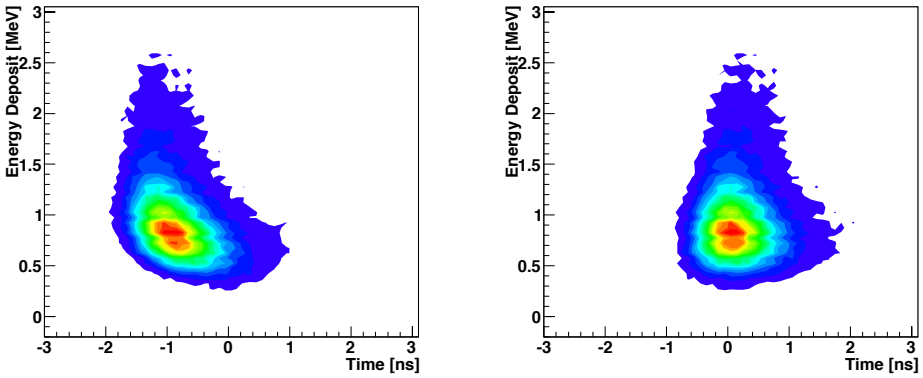

Figure 4.4: The energy deposit vs. time for IHR4D is shown as a color contour plot. The left figure presents the affect of *timewalk* , a result of using a leading edge discriminator. The corrected figure is shown on the right.

The IH signals were fed into a leading edge discriminator, the effect of this being that differences in pulse heights of the signals result in slewing of the TDC recorded time. This slewing is commonly referred to as time-walk. The procedure adopted to correct for this was to first determine the offset channel values and resolve the mean and pedestal value for each counter segment. The procedure was discussed in the previous sections. Following this, a two dimensional histogram of the ADC offset corrected spectrum versus the TDC offset corrected was generated. From projection distributions, points that detailed the described the shape of the energy deposit versus time were again fitted for the purpose of obtaining the fit parameters p1 , p2, and p3, used to the time correction. The time is

corrected by the following equation,

$$t_{corrected} = t_{rawdata} - \frac{p_0}{|dE - p_1|} - p_2 \tag{4.1}$$

In Figure 4.4, the energy deposit (dE/dx) vs. time for the IHR4D counter is presented as a color contour plot. The left figure illustrates vividly the adverse affect of time-walk, a result of using a leading edge discriminator. The corrected energy deposit (dE/dx) vs. time obtained using the above described procedure and equation 4.1 is exhibited on the right of Figure 4.4.

4.4 Hodoscope Performance

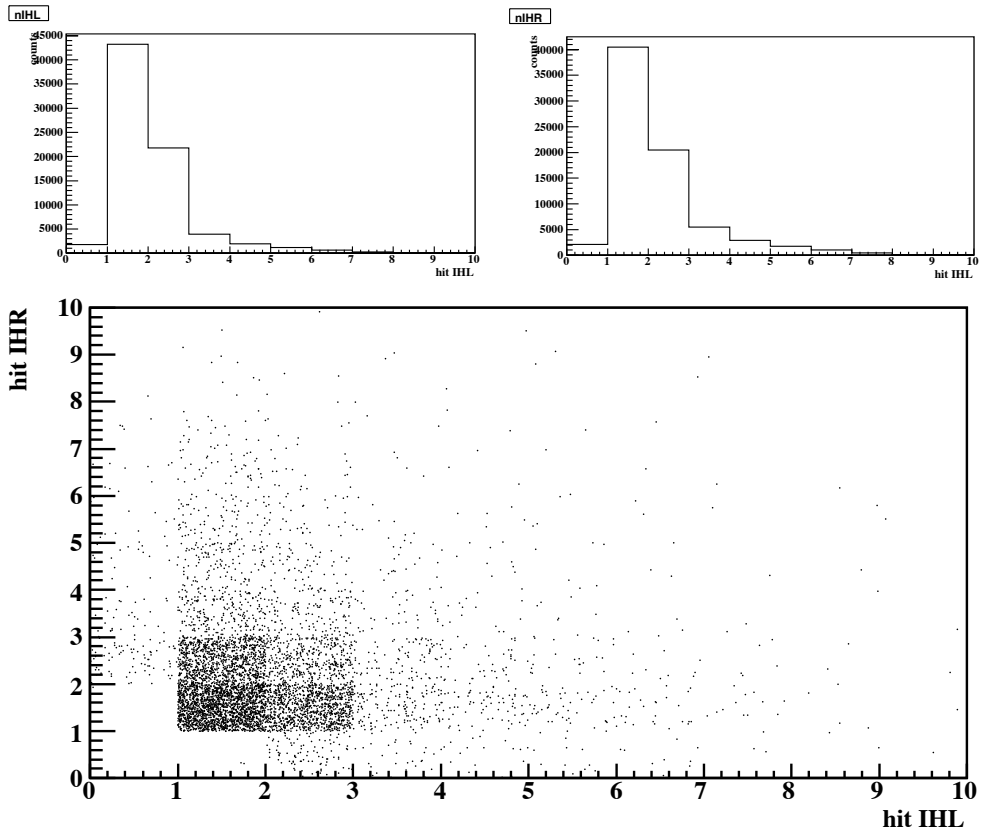

Figure 4.5: Hit patterns of the IH left and right segments are shown.

The second segments of the IH are used in the main trigger based off its high counting rate determined by a GEANT4 simulation. A representative hit pattern of IH counters can be seen in Figure 4.5, irrefutably, the IH2 segments achieve an elevated count rate mainly from electron positron pairs that have a relatively small opening angle. The time

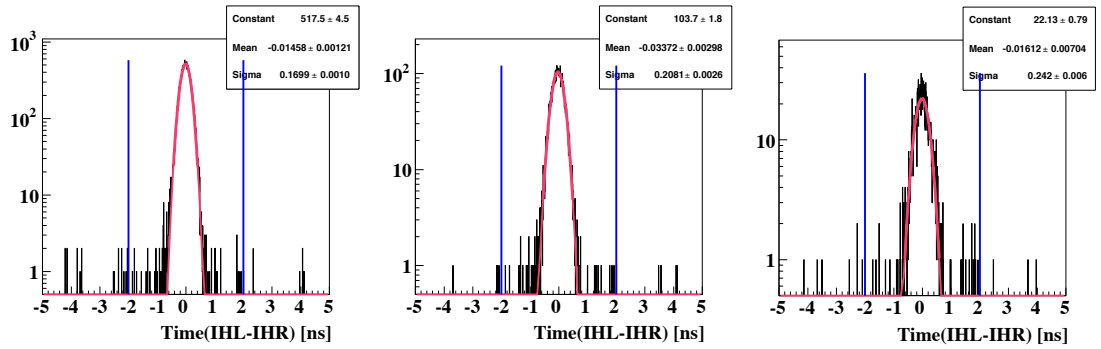

(a) Time difference for IHL2−IIHR2 IHL3−IIHR3, and IHL4−IIHR4 segments

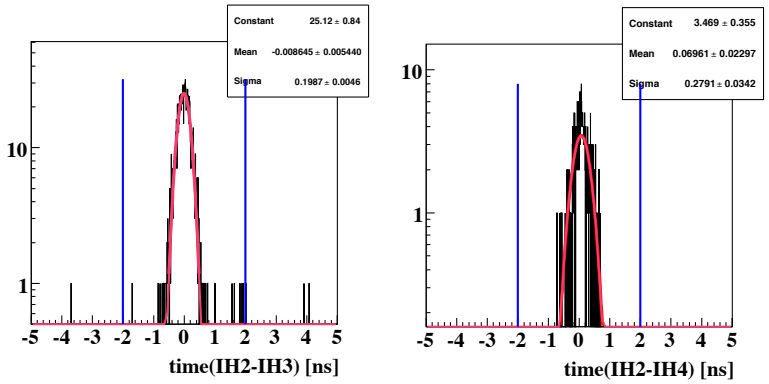

(b) Time difference for IH2−IIH3 and IH2−IIH3 segments. for the selection of charged pions and electron positron events.

Figure 4.6: Time difference for IHL2−IIHR2, IHL3−IIHR3, and IHL4−IHR4 segments (a) for the selection of charged pions and electron positron events. The resolution is determined from fitting as 170, 209, and 246 ps for the IH2, IH3, and IH4 segments respectively. In Figure (b) the time difference for IH2−IH3 and IH2−IH4, segments is shown.

resolution is measurement of the over-all timing uncertainty of a system [106]. The time difference for IHL2−IIHR2, IHL3−IHR3, and IHL4−IHR4 segments for the selection of charged pions and electron positron events are seen in Figure 4.6(a), where the timing resolution is determined from fitting as 170, 209, and 246 ps for the IH2, IH3, and IH4 segments respectively. In Figure 4.6 (b) the time difference for IH2−IH3 and IH2−IIH4, segments, where the selection of charged pions and electron positron events was gated. The relative time resolution of other segments and the trigger selective IH2 segments was found by fitting. The time resolution of the relative timing that can be achieved between the left and right components of the IH hodoscope, determined from fitting, where the black data points are for IHL−IHR for the 2nd, 3rd, and 4th segments are plotted in Figure 4.7. The red data points are the time resolution between IH2 and other IH segments in pico seconds. Lastly, we aimed to ascertain the time resolution between the IH and OH, which

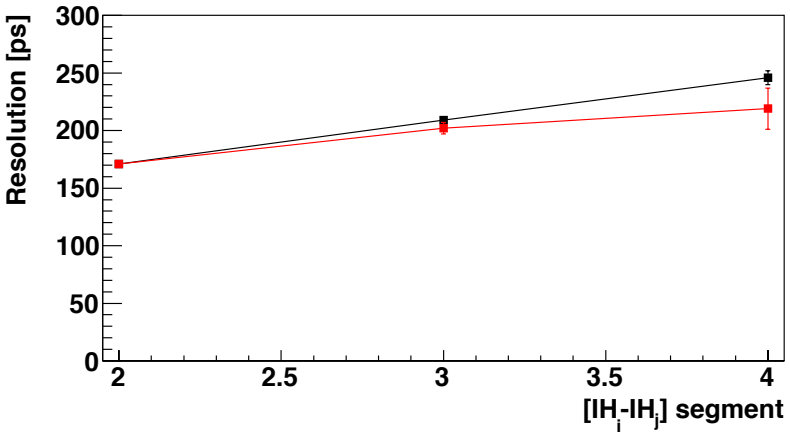

Figure 4.7: Relative timing that can be achieved between the left and right components of the IH hodoscope, determined from fitting, where the black data points are for IHL4−IHR for the 2nd, 3rd, and 4th segments. The red data points are the time resolution between IH2 and other IH segments in ps.

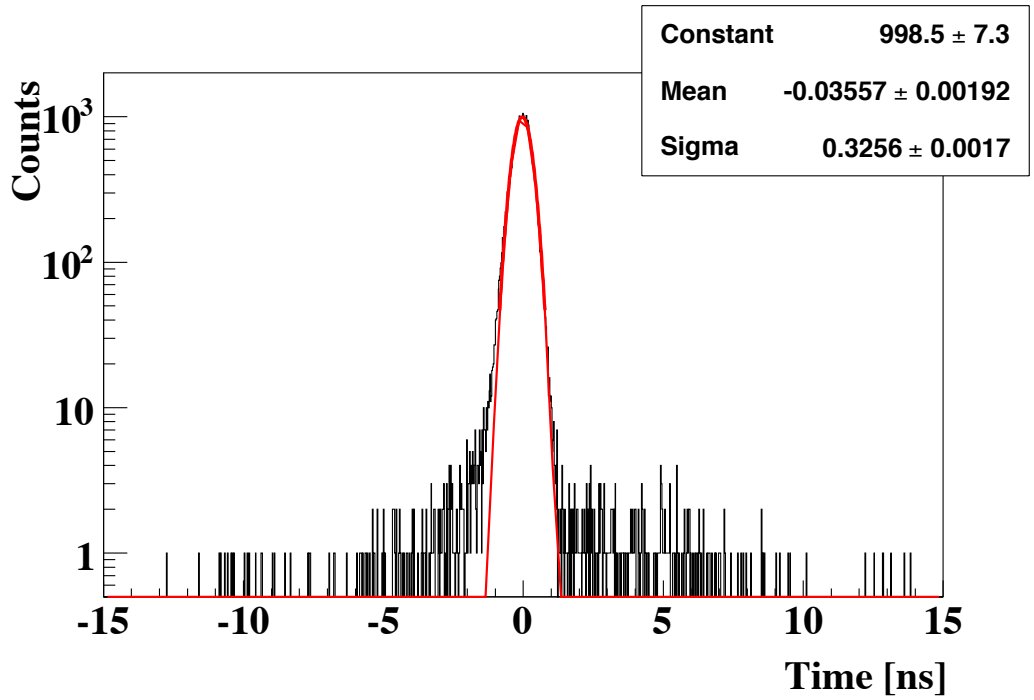

Figure 4.8: Time of flight resolution as determined between the inner hodoscope and the vertical components of the outer hodoscope.

as act as the start and stop triggers respectively. The measured time of flight resolution of 326 ± 2 ps between the OHV and IH is conveyed in Figure 4.8.

4.5 Drift Chambers

A drift chamber is an essential component in a spectrometer for identifying the trajectories of charged particles and for a precise calculation of their momentum. We employed two cylindrical type drift chambers in the NKS2+ spectrometer. The analysis procedure adopted to covert the raw drift chamber signal into vital physics information is detailed in the flow chart shown in Figure 4.9. It outlines the steps taken from the raw data to the finalized track reconstruction. The primary step after the successful recording of the raw chamber data is the generation of TDC distributions. An ordinary TDC histogram for the VDC is seen in Figure 4.10, in which the upper figure shows a two dimensional plot of the TDC signal versus the width of the logic signal formed from the subtraction of the rise and fall times. The lower figures are the corresponding one dimensional TDC histogram. The width information of ASD logic signal is similar to ADC information, simply because the falling and rising timing are related the pulse height.

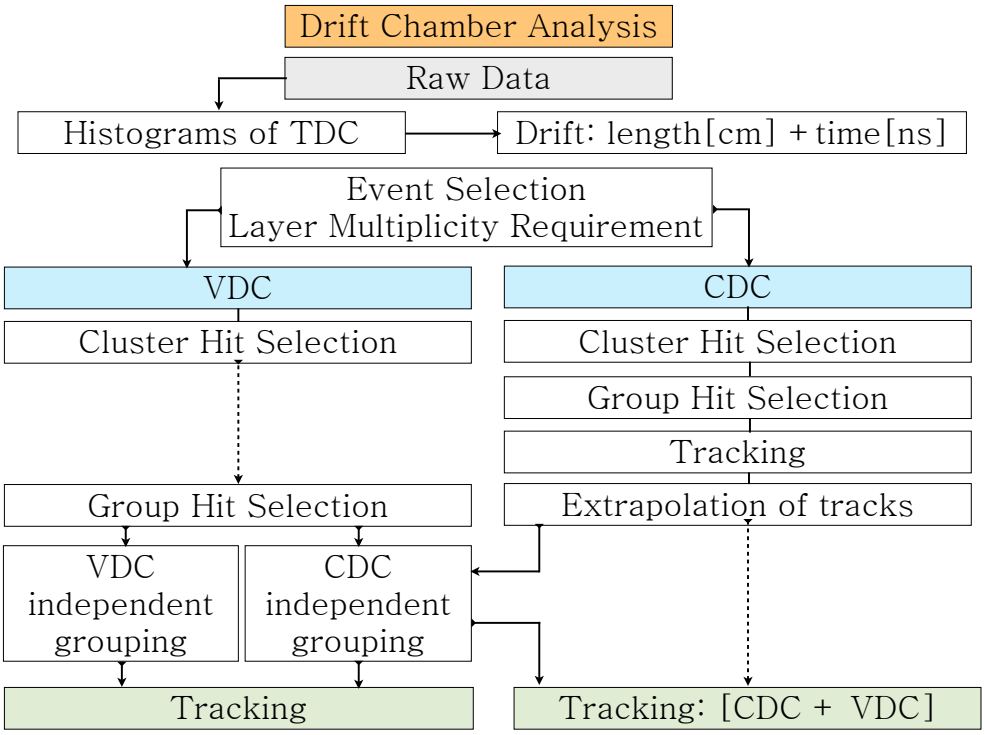

Figure 4.9: Flow chart of drift chamber analysis method

The next step in the proper calibration of the chamber data is obtaining the time zero (t_0) or start time value or each wire. Our procedure involved differentiating the TDC signal and then fitting acquired distribution by a gaussian function and extracting the fit

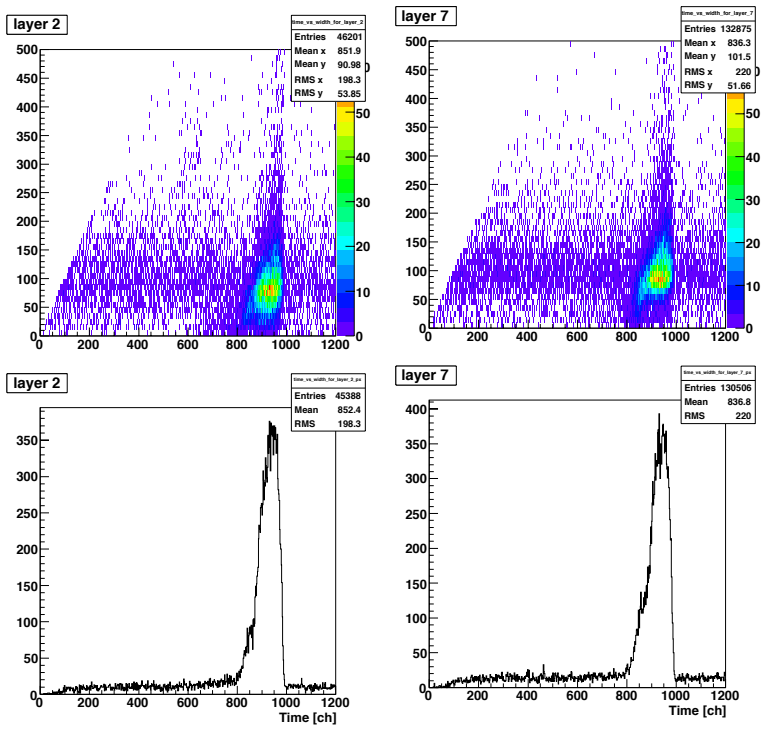

Figure 4.10: Typical VDC layer TDC distribution are shown for an inner and outer layer, 2 and 7 respectively. The upper figure display the TDC distribution versus the width of the rise and fall signal.

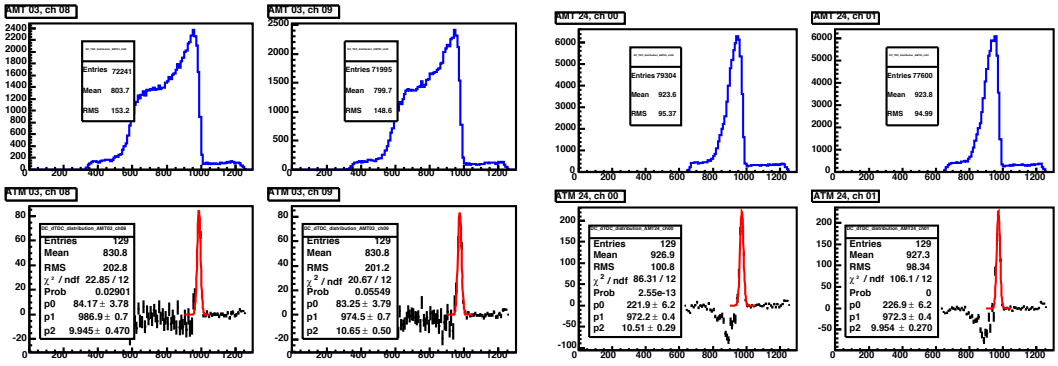

Figure 4.11: Typical drift chamber TDC distribution and the associated differentiated distribution in the lower figure. The gaussian fit is shown in red where the mean time is used for time zero (t_0) parameters acquisition. The TDC distributions for the CDC and VDC are shown as the left two and right two figures respectively.

parameters, of which the mean (μ), should be the needed (t_0). One may assume that this parameter would be constant over the experimental period, however it was found that the values slightly varied from run to run. Thus, the calibration of the (t_0) parameters was undertaken for each wire on the CDC and VDC, on a per run basis. An illustration of

this procedure is provided in Figure 4.11 for the CDC and VDC left to right respectively. In the upper panel are typical TDC distributions of the CDC and VDC drawn as the blue histograms, where the width of the TDC distribution is associated to the variance in cell size. The differentiated distribution is seen in the lower panel corresponding to the TDC histogram located directly above. The gaussian fit is drawn as the red curve.

The time zero parameters can subsequently be used to adjust the raw measured TDC to a start time position of an actual zero value. The adjusted TDC distributions originally given in Figure 4.11 are now seen in Figure 4.12 after the (t_0) parameter shift is applied.

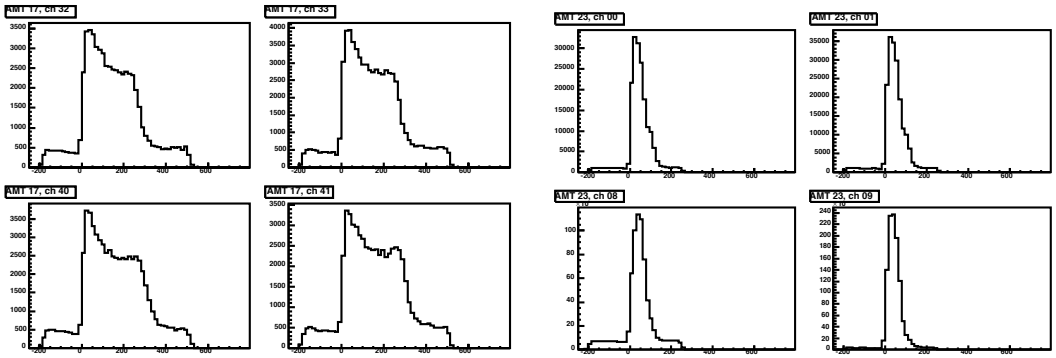

Figure 4.12: drift chamber TDC distribution with time zero parameter

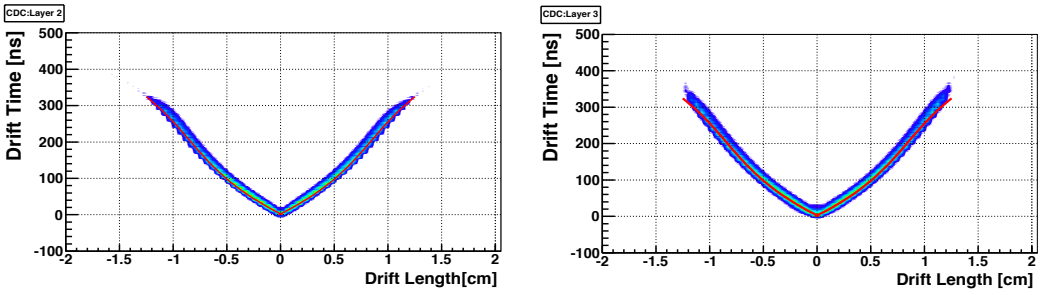

Figure 4.13: Drift chamber drift time [ns] vs drift length[cm]. curves for layers 3(left) and 4(right) of the CDC.

A consequence of a non uniform electric field in the drift space is a non linear relation between the drift time and drift length. The typical drift time versus drift length dependence is drawn as a two dimensional contour color plot in Figure 4.13, in which the $x - t$-curve for layers 2 and 3 of the CDC are left to right in the figure. A fifth order polynomial was assumed to describe the $x - t$ relation. A study of the number of hits $nHit_i$, where i is the layer number, as a function of the tagged photon beam intensity was carried out in preparation for event selection requirements. The $nHit_i$, dependence for tagged photon beam intensities of E_γ= 1.50, 1.75, 2.00 and 2.50 MHz on each VDC layer

is shown as the black circle, red square, green triangle, blue inverted triangle respectively in Figure 4.14. It was found that the average number or recorded hits in each layer was $2-3$, and that the inner layer suffered the largest increase in multi hit counts as the photon beam intensity was extended.

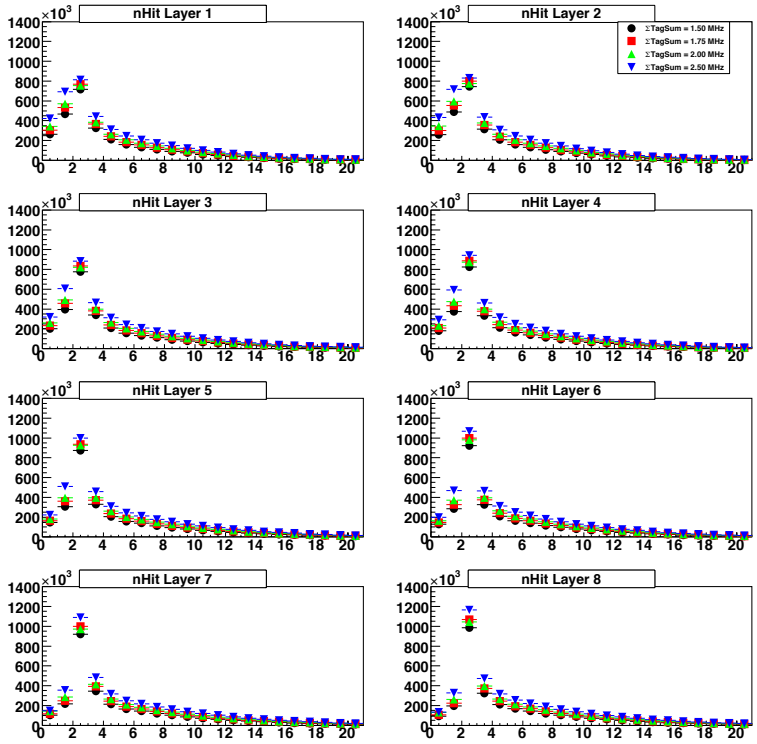

Figure 4.14: Multiplicity hit distribution for various intensity of the incident tagged photon.

4.5.1 Drift Chamber Performance

Tracking Strategy

The current method of analysis used for tracking involves a spline function fit for axial wire hits at first (using B field at Z=0 plane) and then a tilt angle is estimated by the stereo wire hit to obtained the distance of closet approach (DCA) between track and the hits. The NKS2 and NKS2+ used a fitting procedure adopted and detailed in Wind[107].

Postion Resolution

In Figure 4.15, the position resolution of the CDC that was measured during the experimental period is shown. The CDC evidently has a position resolution greater than 350 micrometers for all layers except the very most inner ones, specifically layer 9 and 10.

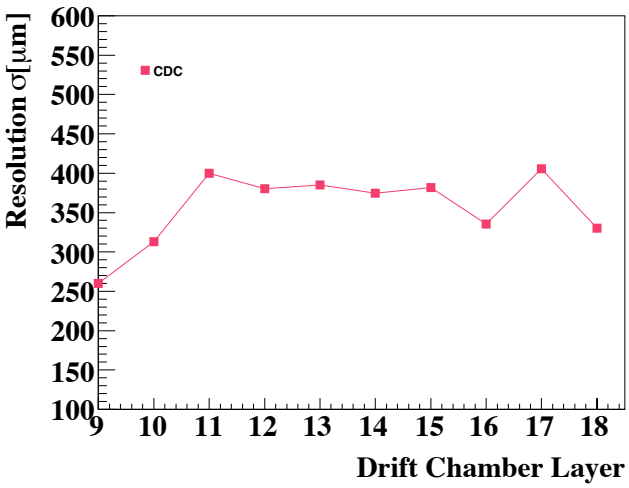

Figure 4.15: CDC layer position resolution.

They were measured to have resolutions of 260 and 310 μm respectively.

4.5.2 Momentum Resolution

In this experiment, the magnetic field strength of 0.43 T was supplied by the 680 magnet, and R was the radius of curvature of the particle trajectory. The radius was found by drift chamber tracking. In a magnetic spectrometer the radius of curvature of a particle was inversely proportional to the magnetic field strength and is directly proportional to the it's momentum. In a general case, the magnetic field B is known in Telsa and radius of curvature resolved by tracking with a drift chamber, the magnitude of the momentum is found as,

$$p = \frac{rqBsin\theta}{0.3} \tag{4.2}$$

The tracking information provided by the drift chamber was in the horizontal direction, the direction normal to the field. The curvature was calculated from the hits detected in the CDC. The vertical component of the momentum is an estimation using the horizontal component along with the particle flight length between the inner and outer hodoscopes, and lastly the vertical hit position on the outer hodoscopes counter, Z_{OH}. A 4th order Runge-Kutta fit method was employed in determination of the flight length. At the trigger level, the electron veto counter is used as a veto for the purpose of reducing the data size. However, in the analysis stage an opening angle cut, that $-0.9 \leq \cos\theta \leq 0.9$, will further reduce the e^+e^- background.

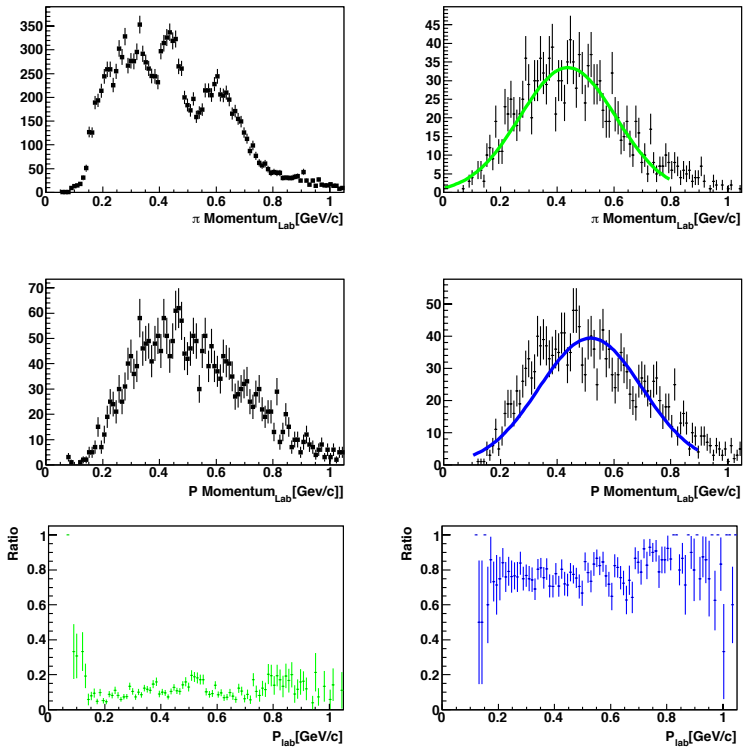

Figure 4.16: The momentum distribution of charged pions from the decay of K_s^0 and Λ are seen here where the proton momentum distribution are on the left and the pion on the right. The top row figures are the momentum of the decay particles with out the opening angle selection are presented in the middle row when applied. The ratio of the distributions in the bottom row.

The measured momentum distribution of charged pions from the decay of K_s^0 and Λ are seen in Figure 4.16, where the proton momentum distribution are on the left and the pion on the right. The top row of figures are the momentum of the decay particles without the opening angle selection and present in the middle row when applied. The proton and π momentum and angular distributions distributions in the laboratory frame of reference reconstructed by the CDC are shown in Figure 4.17 in the right 2 columns and can be readily compared to the simulated proton and π distributions from the $K \to \pi^+\pi^-$ and $\Lambda \to \pi p$ decay channels in the left 2 columns, where the generated events, reconstructed events after the NKS2+ upgrade, and before, are shown as black, blue, and red respectively.

4.6 Tagging Efficiency

At the commencement and ending of each experimental period a measurement of the photon tagging capability of the spectrometer was conducted. This is a measurement of the ratio of the photons that are present on the target to the number of tagged recoil

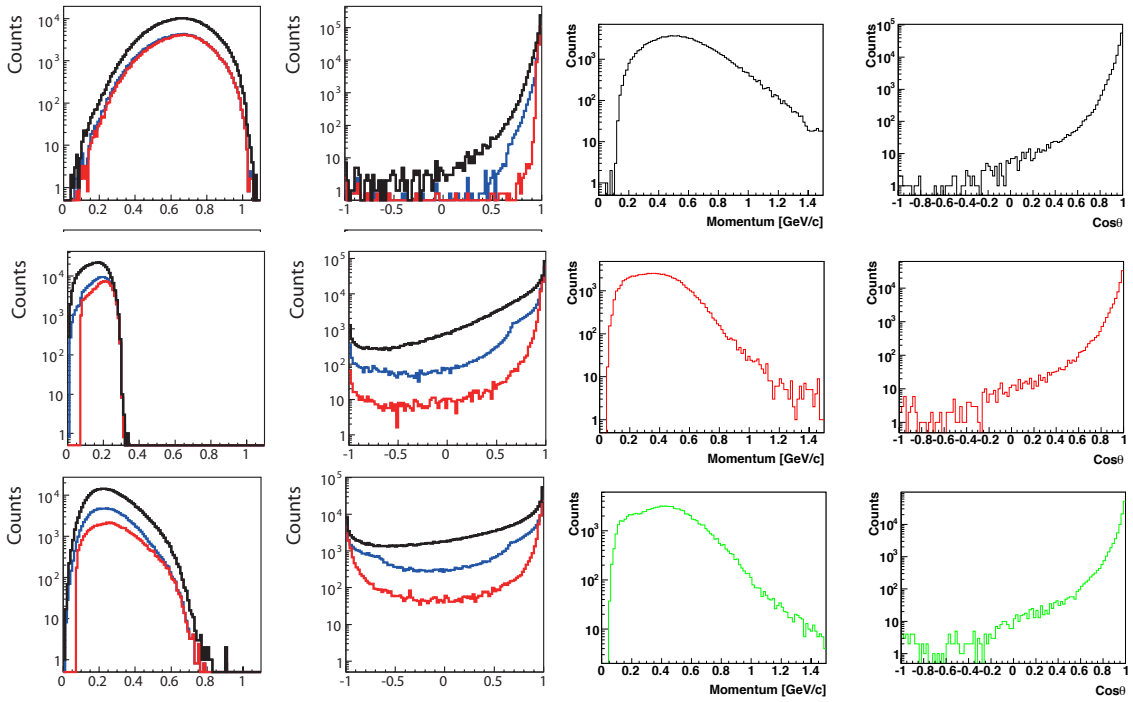

Figure 4.17: The figure presents the simulated momentum distribution of charged pions from the decay of K_s^0 and Λ , the generated events, reconstructed events after the upgrade, and before as shown as black, blue, and red and respectively in the left 2 columns. The measured proton and π momentum and angular distributions distributions in the laboratory frame of reference are seen in the right 2 columns

electrons detected. The number of photons that reached the target was estimated from the scaler counts recorded by the tagger counters. A lead glass Cherenkov counter, 15 x 15 x 30 cm^3 due to is high Z number, is positioned 9.5 m downstream from the target. It is used to measure the number of photons that passed through the spectrometer, that is equivalent to the approximate number that reached the target. A schematic diagram of the detector arrangement is shown in Figure 4.18. The tagging efficiency for the i_{th} TagF counter is calculated as follows:

$$\epsilon_{Tagging} = \frac{1}{\eta_{att}} \frac{N_{\gamma_{LG}}}{N_{\gamma_{TagF}}} \tag{4.3}$$

Where $N_{\gamma_{LG}}$ is the number of photons detector by the lead glass counter and $N_{\gamma_{TagF}}$ is the number of photons detected by the TagF finger counters.

For the determination of the NKS2+ tagging efficiency, the photon beam intensity was kept in the range of a few Hz predominantly due to counting rate capability of the Cherenkov counter, and to reduce the probability of chance coincidences between the lead glass counter and the tagging segments. In principle, this should have no effect on

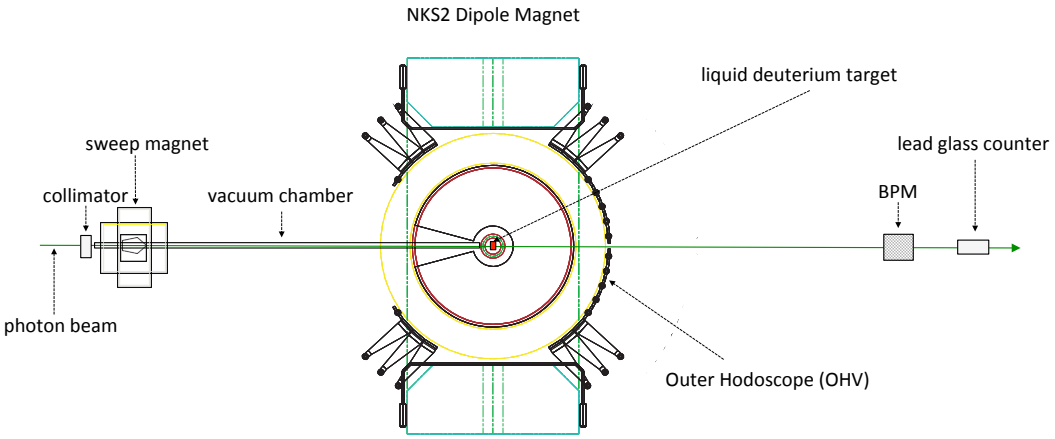

Figure 4.18: Detecter arrangement for tagging efficiency measurement.

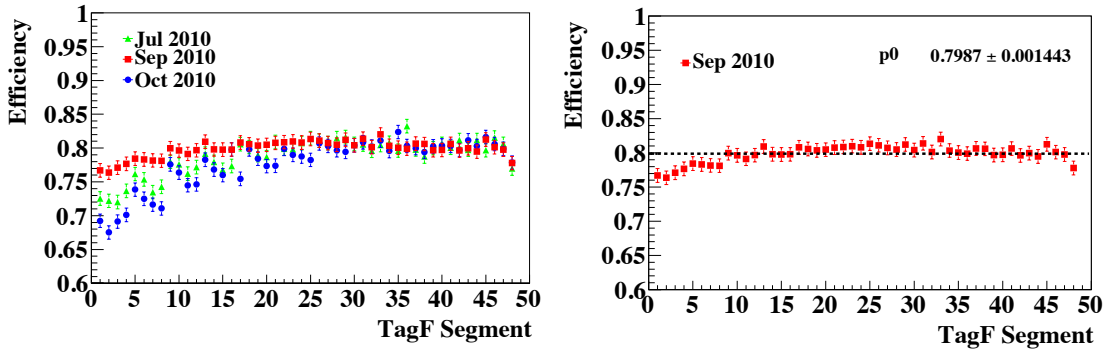

Figure 4.19: Tagging efficiency of the collimated photon beam for the July September, and October 2010.

the measured efficiency. The efficiency calculated is affected due to the reduction of the photons that actually reach the target or from hits on the tagger not correlated to photons detected at the lead glass counter. A percentage of the bremstrahlung generated photons may not reach the target and thus are attributed to the reduction in tagging efficiency due to the following reasons, the first of which is the loss of photons at the collimator. The collimator is comprised of lead blocks 10.0 $\times$ 10.8 $\times$ 5.0 cm^3 in size is located in front of the sweep magnet. An aperture of 1 cm in diameter positioned in the center of the collimator. The motivation of placing the collimator in this location lies in reduction of the beam halo at the cost of the loss of photons emitted at large angles. The reduction in the tagging efficiency is appreciable. Photons may interact with the material that is on the beam line between the radiator and the target. The radiation length was approximated at 3 x $10^{-2}X_0$ [108]. The number of hits on the tagger can be increased as a result of firstly the scattering of an electron on any lingering gas that may be present in the accelerator

Table 4.2: Tagging Efficiency Run

Experiment Period 2010	Flat Top [s]	Number of Spills	Number of Photons [γ]	Beam Rate [kHz]
September	20	200	x 10^6	≤ 10

pipe and the second if a recorded hit on the tagger attributed to Møller electrons that scattered on the radiator. The tagging efficiency for various test and production periods are shown in Figure 4.19 on the left. The apparent structure in the lower TagF segments is believed to originate from the coincidence requirement between the TagB and TagF counters, the sensitivity to the low momentum electrons and the variation of the electron beam orbits for different experimentation periods. The fitted tagging efficiency for the September data set that is analyzed in this thesis yielded a value of 79.9% denoted by the dashed black line on the right of Figure 4.19.

4.7 Vertex Distribution

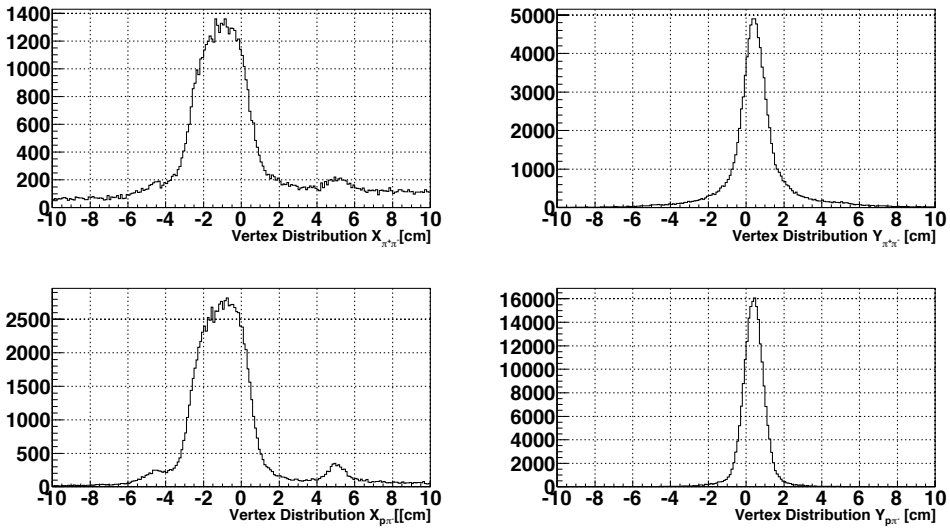

Figure 4.20: Vertex distributions in the $\hat{x}$ and $\hat{y}$ directions are shown left to right respectively. The top row displays distributions associated with the a $\pi^+\pi^-$ events and the right column are for pπ^- identified events

The vertex distributions for two track events are presented in Figure 4.20 where the reconstructed distributions in the $\hat{x}$ and $\hat{y}$ directions are visible left to right. The distributions for two track events corresponding to $\pi^+\pi^-$ identified events or pπ^- events are

shown in the upper and lower figures respectively.

4.7.1 Vertex Resolution

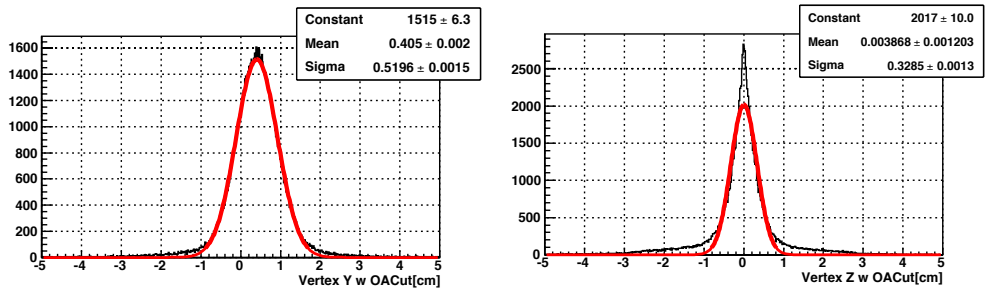

Figure 4.21: The vertex resolution of $p\pi^-$ identified events fitted by a gaussian distribution in the $\hat{x}$ and $\hat{y}$ directions were resolved as 5.20 ± 0.015 mm and 3.29 ± 0.013 mm respectively. The distribution were generated including an opening angle cut of $-0.9 \leq \cos\theta \leq 0.9$

.

The fitted vertex distributions of $p\pi^-$ identified events in the $\hat{x}$ and $\hat{y}$ directions were found to be 5.20 ± 0.015 mm and 3.29 ± 0.013 mm respectively and are provided in Figure 4.21. The distributions were generated with the inclusion of an opening angle selection of $-0.9 \leq \cos\theta \leq 0.9$.

4.8 Liquid Deuterium Target

4.8.1 Target Thickness

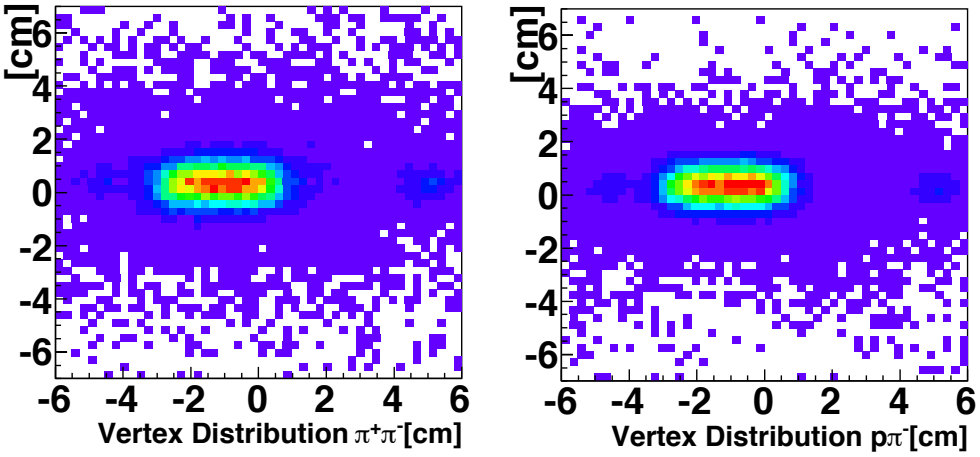

Figure 4.22: Vertex distributions $\hat{x}$ vs. $\hat{y}$ for two track events corresponding to $\pi^+\pi^-$ or $p\pi^-$identified events.

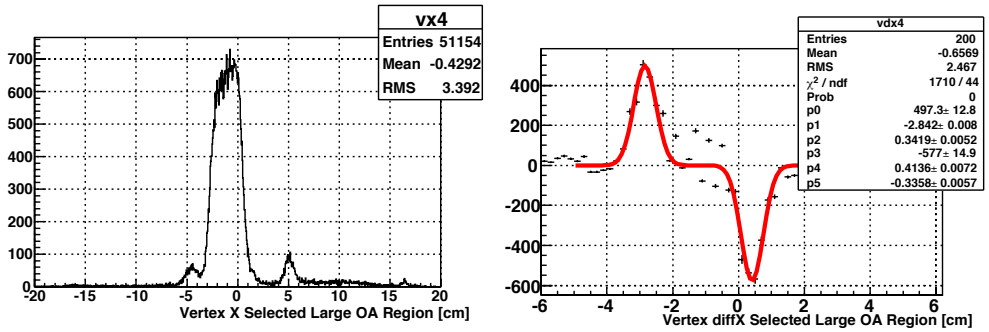

Figure 4.23: Vertex positon $\hat{x}$ direction differential.

The thickness of the target was determined by taking the differential of the vertex position on the $\hat{x}$ direction and is shown in Figure 4.23. For this experiment the target thickness was 3.1839 ± .003 cm, which is slightly larger than the previously detailed size of the target cell. The size of the target cell was designed to be 2.97 cm as discussed in section 3.3.11 on the target cell. However, it is known that the target thickness does fluctuate as a results of thermal expansion such that the film on the target cell will ballon with pressure.

4.8.2 Target Stability

During the experimental period the absolute pressure and temperature of the liquid deuterium were remotely monitored by the LabVIEW on Linux to verify that it remained below its boiling point and to ensure the target stability. Figure 4.24 presents the condition of the target over the course of the data acquisition period. The monitored and corrected values of the target pressure and temperature are shown in each Figure 4.24 as black and blue respectively. The temperature was monitored in Kelvins and the absolute target pressure in kPa. The measured pressure and temperature are presented in the upper figures left to right. The density over the course of the experimentation period is shown in the lower left figure. The fitted density distribution of the liquid deuterium is presented in the lower right figure.

4.8.3 Target Density Calculation

The average density of the target was calculated using the method described by Gunn and Yamada [109] and Chueh and Prausnitz [38]. The usage of the Gunn-Yamada formula is usually applicable only to the cases of a saturated liquid. The average density was calculated by both methods with a difference in α, a scaling factor for the saturated calculated density to a non saturated state, of 0.913925 for the former and 0.99983 for the

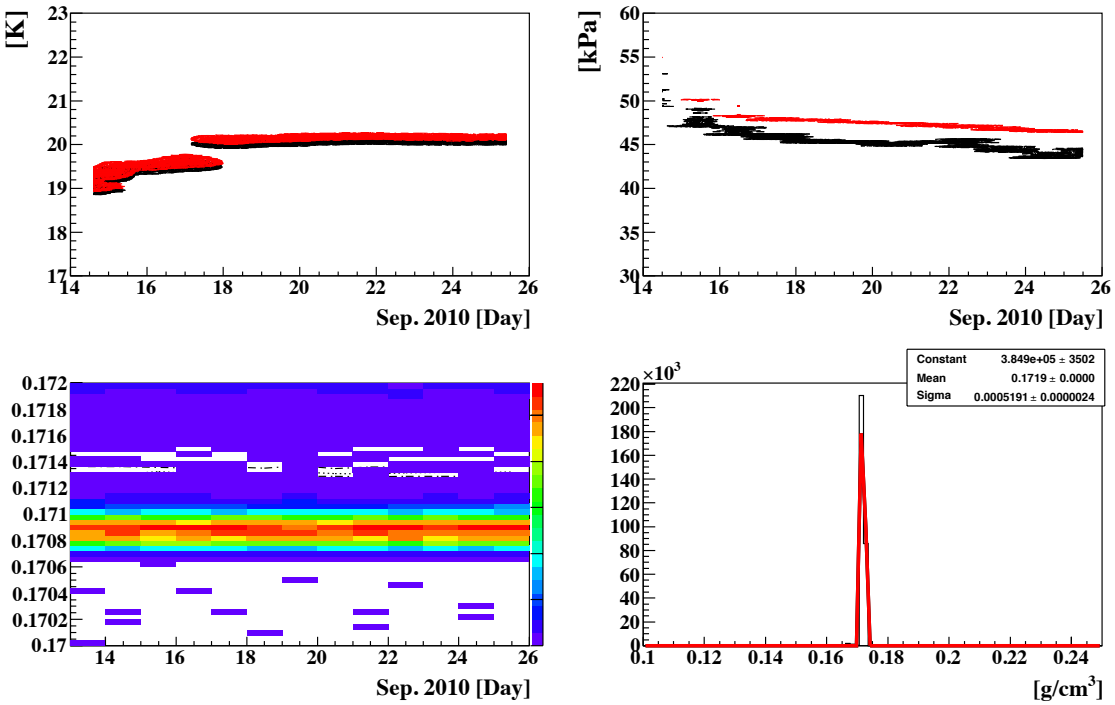

Figure 4.24: The monitored and corrected values of the target pressure and temperature are shown in each figure as black and red respectively. The temperature monitored in Kelvins target absolute pressure in kPa are presented in the upper figures left to right. The density over the course of the experimentation period is shown in the lower left figure. The fitted density of the liquid deuterium target was 0.1719 g/cm^3

later. The calculation was performed using the variables listed in Table 4.3.

In the Gunn-Yamada framework, the saturated molecular volume and reduced temperature as,

$$T_r = \frac{T}{T_c} \tag{4.4}$$

$$V_s = \frac{M}{\rho_s} \tag{4.5}$$

The above definitions allow for the calculation of the saturated volume, V_s, by the following,

$$\frac{V_s}{V_{sc}} = V_r^0(T_r)(1 - \omega\Gamma(T_r)) \tag{4.6}$$

$$\frac{V^R}{V_{sc}} = V_r^0(T^R)(1 - \omega\Gamma(T^R)) \tag{4.7}$$

Table 4.3: Variables and constants in Gunn-Yamada saturated density formula.[38]

Symbol	Meaning	Values
T_b	normal boiling point [K]	23.7
T_c	critical temperature [K]	38.4
T_r	reduced temperature [K]	
T^R	reference temperature [K]	22.7
P_c	critical pressure [atm]	16.4
V_c	critical molecular volume [$cm^3/g \cdot mol$]	60.3
V_s	saturated molecular volume [$cm^3/g \cdot mol$]	
Z_c	critical compressibilty factor	0.314
ω	acentric factor	-0.13
ρ^R	density at reference temperature T^R	0.165
M_D	molecular weight [g/mol]	2.014 U

where V_{sc} is a scaling factor at the reduced temperature assigned as T_r =0.6K, V^R is the volume at the reference temperature. In this framework V_s is expressed as [109] s:

$$V_s = \frac{V_r^0(T_r)(1-\omega\Gamma(T_r))}{V_r^0(T^R)(1-\omega\Gamma(T^R))} \times V^R \tag{4.8}$$

here $\Gamma(T_r)$ and V_r^0 are

- $\Gamma(T_r)$= 0.29607 - 00.09045T_r - 0.04842T_r^2
- V_r^0= 0.33593 - 0.33593T_r + 1.51941T_r^2 - 2.02512T_r^3 + 1.11422T_r^4

thus, the density of the target is found as,

$$\rho_s = \frac{M}{V_s} \tag{4.9}$$

Implementing the above technique in the calculation of the liquid deuterium target was successfully performed. The results of the calculated density are shown in the lower right in Figure 4.24. The average density of the experimentation period determined by fitting was 0.172 g/cm^3. The calculated value of the target density prior to the correction of the measured temperature and absolute pressure was 0.1736 g/cm^3 thus the difference between the non-corrected and corrected values was roughly 0.2%.

4.8.4 Calculation of the Number of Deuteron Target

The measured thickness of the target cell resolved from the vertex distributions shown in Figures 4.23, 4.20, and 4.22 was 3.25 $\pm$ 0.3 cm, which is more than the described designed value of 2.97 cm discussed in section 3.3.11. The disparity between the two quantities can

Table 4.4: Average target parameters in September 2010 experimental period

Period 2010	Temperature [K]	Pressure [kPa]	Thickness [cm]	Density [g/cm^3]	Deuteron target [μb^{-1}]
September	20.1± 0.1	47.1± 0.5	3.25 ± 0.3	0.172	0.168 ± .006

be attributed to the distension in the target cell that was not suppressed by the Upilex-S film. The pressure dependence on the overall resultant shape has been evaluated and is known to be spherical [103]. The estimated upper limit of the target cell's bloating is 0.2 cm. The number of target deuterons was calculated by the following:

$$N_{\text{Target}} = \frac{\rho_D \cdot N_A \cdot W_{\text{target}}^{\text{effective}}}{M_D} \tag{4.10}$$

In the above calculation, the density of the liquid deuterium (ρ_D) was 0.172 g/cm^3, the effective thickness of the target ($\text{W}_{\text{target}}^{\text{effective}}$) was 3.25 ± 0.3 cm, the mass of a deuteron (M_D) is 2.0141077803 g/mol^{-1} atom and Avagadro's number (N_A) was 6.01221479 x 10^{23}. Both M_D and N_A values were obtained from the latest listings in the Particle Data Book. Using these values the effective number of target is readily calculated as,

$$N_{\text{Target}} = \frac{0.172 \cdot 6.01221479x10^{23} \cdot 3.25}{2.0141077803} \tag{4.11}$$

In the calculation of the differential cross section by equation 5.2 the number of deuteron target was approximated as 0.168 μb^{-1}. The average target parameters of the experimental period is provided in Table 4.4.

4.9 Data Acquisition Efficiency

The data acquisition efficiency is designated as the total number of triggers accepted divided by the total number of triggers requested. The requested and accepted values were recorded by CAEN VME scaler during the experimental period for every run. It follows that value of the corresponding DAQ. efficiency can be computed as:

$$\epsilon_{daq} = \frac{\Sigma Trigger_{\text{acc}}}{\Sigma Trigger_{\text{req}}} \tag{4.12}$$

where the $\Sigma Trigger_{\text{acc}}$ and $\Sigma Trigger_{\text{req}}$ are the sum of the recorded accepted and requested triggers respectively. In the September experimental run period the average tagged photon beam intensity was 1.7−2.3 MHz. The DAQ efficiency for this period was determined to be roughy 60% ± 0.1%, where the error is systematic in origin.

4.10 Particle Identification Technique (PID)

In modern particle and nuclear experiments PID is of the upmost importance. Particle identification is the correct determination of a particles mass and charge from the physical measurements that can be accomplished experimentally. By utilizing and properly exploiting the physical processes that take place between matter we are able to expand our knowledge of the structure of the at its most basic level. The difficulty in efficiently identifying hadrons lies in the fact that a determination of the momentum alone is not sufficient. A momentum measurement must occur in addition to another independent measurement that has a correspondence to the particles momentum such as ionization energy loss (dE/dx), time-of-flight (TOF) and knowledge of the strength of the magnetic rigidity,(B), is necessary. The most common techniques for the identification of hadrons, are through the use of energy loss (dE/dx) or ionization loss, time of flight (TOF), Cherenkov radiation imaging, and lastly by transition radiation measurements.

4.10.1 Scintillators

The most widely used detectors are scintillation counters, solid-state detectors, proportional tubes, and drift chambers. In modern nuclear and particle experiments the use of a scintillator is common place in the construction of particle identification system. The signals produced, which are electrical in nature, can be digitized and processed in real time or recorded for further analysis using high-speed digital computers. A scintillator is substance that upon exposure to high energy photons or charged particles, absorbs some energy, conventionally called excitation, and the releases this energy as photons, at a wavelength longer than that of the absorbed wavelength. The light produced is usually detected by photomultipliers tubes (PMT) and more recently solid-state detectors.

Scintillators are grouped into two groups, organic and inorganic. Organic liquid crystals such as anthracene are highly effective for measuring beta particles. Inorganic scintillators works via the excitation of valence electrons and can be made from materials with low Z numbers. Typically they are relatively inexpensive to manufacture and have fast response times in the range of ns. These are primarily used for TOF counters, triggers, vetos, and calorimeters. The main advantage of uses scintillators is their ability to achieve high counting rates.

4.10.2 Energy Deposition (dE/dx)

All charged particles can be detected by the electromagnetic force as a result of the ionization of atoms as they pass through bulk matter. In fact, electromagnetic interactions are the most dominant and common of interactions that occur while a charged particle passes

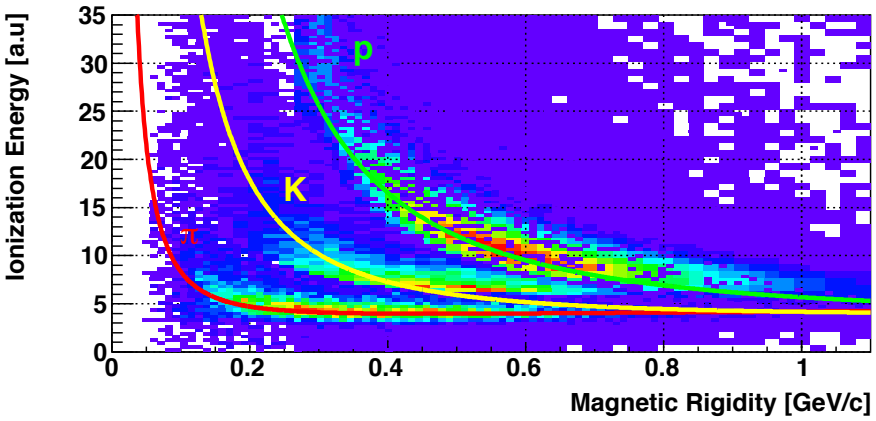

Figure 4.25: Measured energy deposit per unit length (dE/dx) in OH counters. The energy deposit per unit length curves generated by using the Bethe-Bloch formula without the inclusion of the density effect and shell corrections are drawn by the colored lines and compared the measured energy deposit in the OH counters.

through matter. Two distinct events characterize the passage of charged particles, the first being the loss of energy by the particle, and the second being a deflection of the incident particle from its initial trajectory [110]. Of these, the inelastic collision of particles with the atomic electrons has the highest probability of taking place. The collision results in an energy transfer through the excitation and ionization of the atomic electrons. The average energy loss per unit path length is also referred to as the stopping power or dE/dx [111].

The method of particle identification by measuring the specific energy loss (dE/dx), has been successfully used for many years. The energy deposited is dependent upon the charge and velocity of the incoming particle, in conjunction with the absorbing material. Thus, prior knowledge of the mean energy loss for a specified absorber can allow for good particle identification and separations below minimum ionizing [112]. Average energy loss of a particle can be described by the Bethe-Bloch formula.

The Bethe-Bloch formula accurately describes the average energy loss of charged particles as they pass through matter, but this is assuming a uniform loss in energy. The inclusion of the density correction is a result of polarization that may occur in the absorbing material [113]. In the non-relativistic region, dE/dx is proportional to $1/\beta^2$, where at β=0.95 particles reach the minimum ionization point. A minimum ionizing particle has a dE/dx proportional to 2 MeVg-$^{-1}$cm^2. In regards to relativistic particles, the deposited energy increases logarithmically after surpassing the minimum. Ionization energy loss approaches a gaussian distribution for thick absorbers, but with a decrease in absorber thickness the distribution acquires a tail. Ionization of matter is the emphasized principle

in all detector technology. The fluctuation in energy loss for thin absorbers is sometimes called *straggling*, caused by the small number of collisions between atomic electrons and the transiting particle, with a large energy transfer. In essence, thick and thin absorbers have significantly different properties. These fluctuations in energy loss follow the so-called Landau distribution [105]. The Landau distribution is an asymmetric distribution known for its tail. Accordingly, the mean ionization energy loss is not the same as the most probable energy loss value (MPV). Thus, the value of importance when attempting to fit histograms, is the MPV value, not the mean. The expectation in an energy deposition is in the range of 1 MeV, for a minimum ionizing pion, to approximately 11 MeV, and possibly higher for low momentum protons.

The measured energy deposit per unit length in OH counters are shown in Figure 4.25, where the energy deposit per unit length curves generated by using the Bethe-Bloch formula without the inclusion of the density effect and shell corrections are drawn by the colored lines and compared to the measured energy deposit.

4.10.3 Time of Flight (TOF)

The most utilized detector for time of flight (TOF) measurement is the plastic scintillation counter detector system. Details of the scintillation counter are discussed in the data analysis sections. This technique is applicable below 1.0 GeV, in which the velocity of particles, at specific momentum, is mass dependent. Time of flight measurements allow for a particles mass to be determined by knowledge of flight time, the momentum, and the path length L [114]. The time of flight for a particle exiting the IH and passing through the OH is found by the difference of the mean time of the later with that of the former. The TOF particle identification method in combination with a momentum measurement was used for determination of the particle species. The technique was to not select the particles only by their mass but instead by two dimensional histograms of the momentum versus inverse β. From the energy-momentum relation the velocity can be calculated as,

$$\beta = \frac{p}{E} = \frac{p}{m^2 + p^2} \tag{4.13}$$

Therefore the square of the particle's mass is found by,

$$m^2 = (\frac{p}{\gamma\beta})^2 = p^2(\frac{1}{\beta^2 - 1}) \tag{4.14}$$

from equation 4.14 PID of charged pions is specified as,

$$-0.5 \leq m^2 \leq 0.25[\mathrm{GeV}^2/\mathrm{c}^4] \tag{4.15}$$

and for the protons,

$$0.5 \leq m^2 \leq 1.8[\mathrm{GeV}^2/\mathrm{c}^4] \tag{4.16}$$

Figure 4.26 displays the two dimensional plot of the charge of the particle times momentum and inverse beta. This plot was generated with the inclusion of an opening angle requirement for the purpose of rejecting the copious amount of electron positron pairs. The bands around $1/\beta = 1$ are the distributions that correspond to charged pions, indicated in the red regions, and the fainter band is for protons which lie within the blue region. Separation of the particle type is evident when a projection of the $1/\beta$ distribution is produced for a specified momentum region as shown in Figure 4.27.

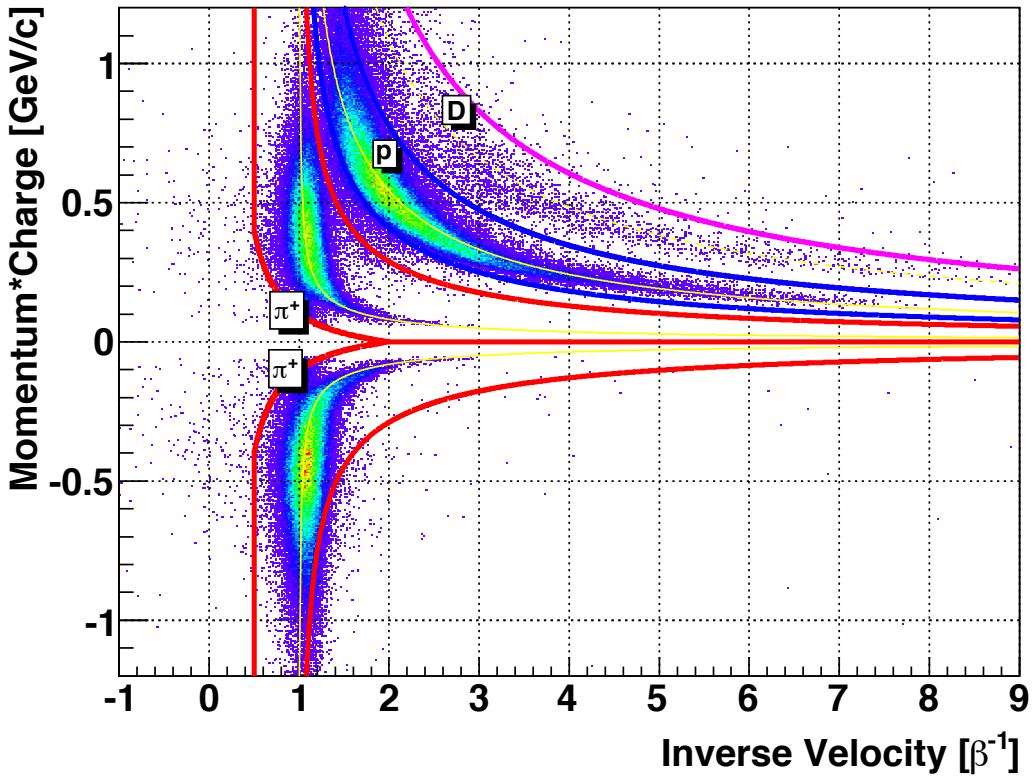

Figure 4.26: The particle momentum multiplied with the particle charge plotted as a function of the inverse velocity is shown in Figure 4.26. The proton and pion selection regions are shown by the blue and red regions respectively. The charged pions are identified by the sign of the momentum.

A study into the separation power of time of flight measurements between protons and pions (π/p) was conducted to quantitatively ascertain the performance of the NKS2+ spectrometer with the inclusion of the new IH [115]. The separation power of the particle species is evident when a projection of the inverse velocity distribution is produced for a

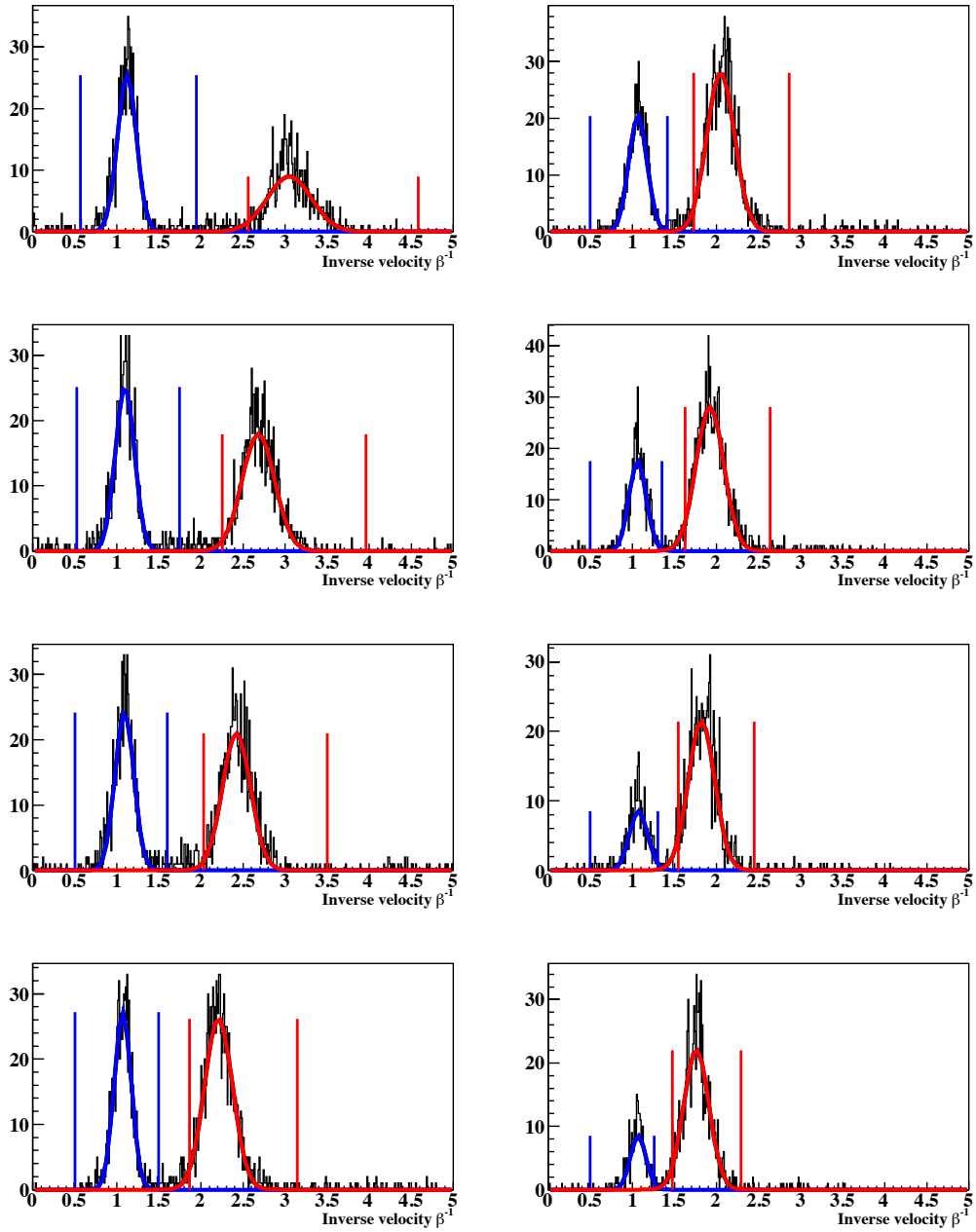

Figure 4.27: $1/\beta$ distributions, where $\beta = (\mathrm{v}/c)$. The figures are for a momentum selection region of $0.20-0.22, 0.30-0.32, 0.40-0.42, 0.50-0.52, 0.60-0.62$, and $0.70-0.72$ GeV/c. The above figure illustrates the particle separation, red for charged pions and blue for protons at different momenta.

specified momentum region as presented in Figure 4.27, where the pion and proton inverse beta distributions are seen left to right respectively. The regions of momenta selection are $0.20-0.25, 0.30-0.35, 0.40-0.4.5, 0.50-0.55, 0.60-0.65$, and $0.70-0.75$ GeV/c. This plot

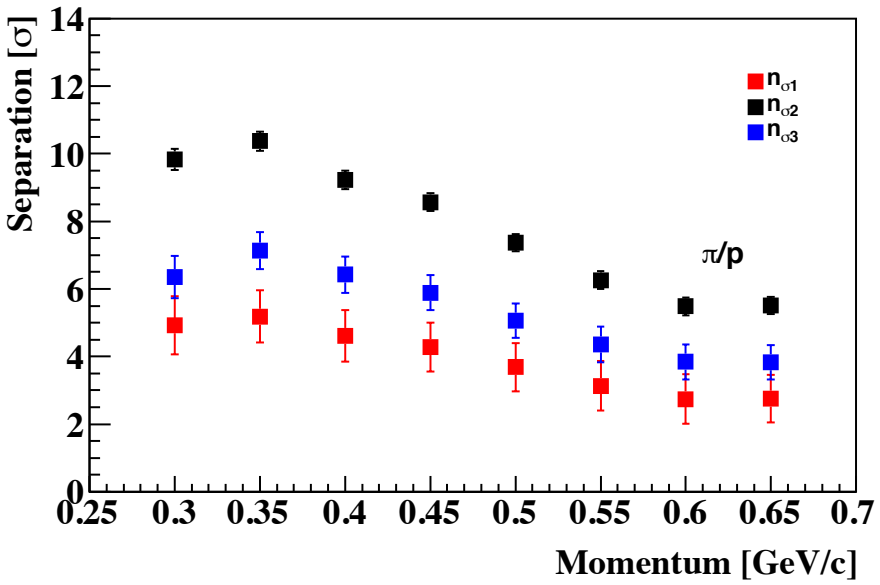

Figure 4.28: Separation power between pions and protons with respect to momentum for momentum selected regions of $0.20-0.25, 0.30-0.35, 0.40-0.4.5, 0.50-0.55, 0.60-0.65$, and $0.70-0.75$ GeV/c

includes an additional requirement for the opening angle such that $-0.9 \leq \cos\theta \leq 0.9$. The opening angle for electron positron pairs is much smaller than that of charged pions from the kaon decay in the energy region of this experiment.

The results of the study of the separation power between pions and protons with respect to momentum was explicitly calculated and we present the computed results in 4.28 where the results calculated by equations 4.17 4.18 4.19 are the solid red, black, and blue squares respectively. The separation power n_{σ_i} was defined by the following equations 4.17 4.18 4.19, where the distribution where first fitted to a Gaussian function. μ_1, μ_2, σ_1 and σ_2 are the mean values and the standard deviations of the gaussian fits of the pion and proton distributions.

The calculation of the TOF separation power n_{σ_i} proceeded as follows,

$$n_{\sigma_1} = \frac{|\mu_1 - \mu_2|}{(\sigma_1 + \sigma_2)/2} \tag{4.17}$$

$$n_{\sigma_2} = \frac{|\mu_1 - \mu_2|}{\sqrt{({\sigma_1}^2 + {\sigma_2}^2)}} \tag{4.18}$$

$$n_{\sigma_3} = \frac{|\mu_1 - \mu_2|}{(\sigma_1 + \sigma_2)} \tag{4.19}$$

As can be understood from the equations the particles species separation power was defined as being proportional to the mean of the sigmas, equation 4.17, the square root of the sum of the squares of the sigmas, equation 4.18, and the sum of the σ, equation 4.19. Therefore, we define the upper bound and lower bound TOF capabilities of the spectrometer as 4.17 and 4.19.

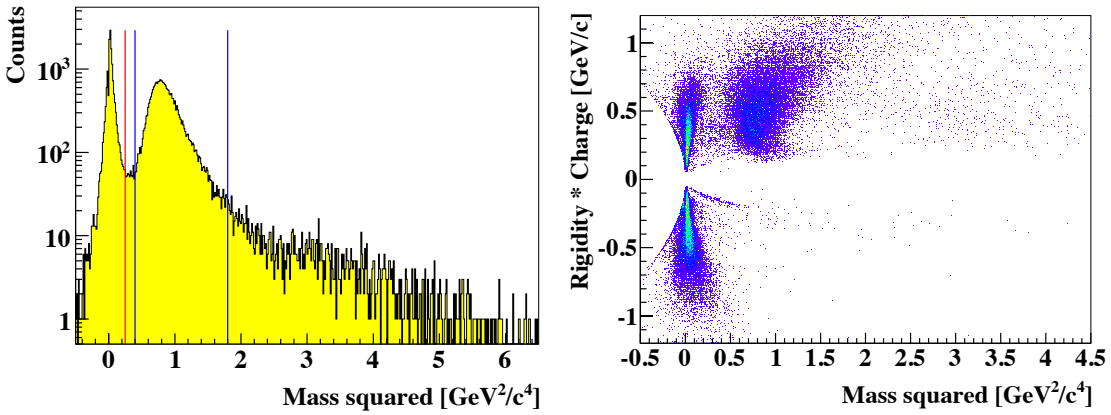

Figure 4.29: Mass squared event distribution (left); Rigidity multiplied by particle charge plotted verses mass squared event distribution (right).

The mass squared distributions of the detected particles versus the momentum that has been multiplied by the charge is shown in Figure 4.29, where again the clear separation of pion and protons is evident and the sign of the charged pion is associated to the sign of the momentum. Event distributions for the squared mass of the charged particles observed by the spectrometer is shown in Figure 4.29, in which the charged pions lies left of the red vertical line, protons within the blue vertical lines, and deuterons to right of the second blue vertical line.

4.11 Momentum Resolution

The study of the momentum resolution was also performed for momentum bins of 0.1 GeV/c spanning the range of $0.1 - 0.7$ GeV/c for pions and $0.3 - 1.0$ GeV/cfor protons. For each bin the square of the masses was generated and fitted by a gaussian function. The mean, squared masses of the particle and relative resolution, obtained from the fitting procedure was plotted a function of the momentum bin. The results of the study are shown in Figure 4.30 where the obtained momentum resolution (FWHM) are plotted versus the particles momentum. The resolution of the measured pions was found to be from $20 - 200$ MeV/c for the momentum range of $150 - 700$ MeV/c, while for protons the determined

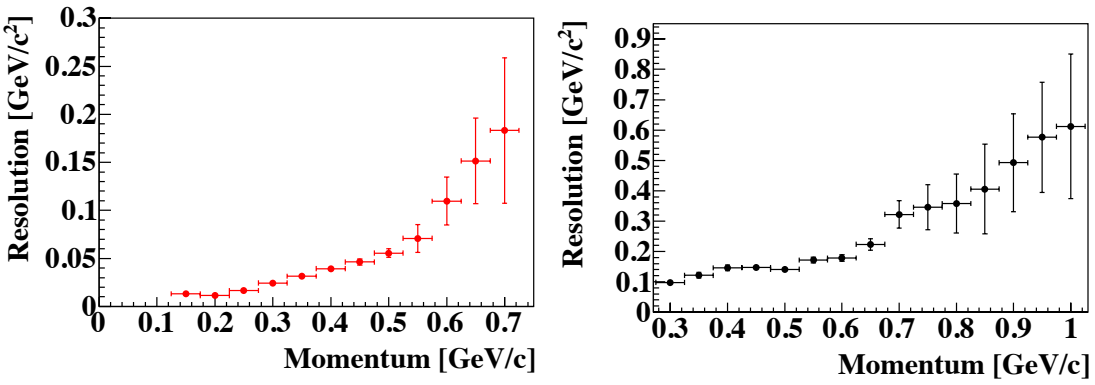

Figure 4.30: The momentum resolution (FWHM) of the detected pions (left) and protons (right) are plotted versus the particles momentum.

resolution was between $100 - 600$ MeV/c for the momentum range of $300 - 1000$ MeV/c.

4.12 Event Selection

This section will describe the selection process and the requirements placed on the gathered raw data in order to obtained the Λ invariant mass with the highest reduction in the background continuum. It will covers the kinematical, timing, tracking, and missing mass requirements in detail.

4.12.1 Kinematical Selection

The details of the photoproduced kaon and Λ particles were listed in Table 2.3 where the life time of the afore mentioned particles in terms of $c\tau$(cm) was given. The focus of the analysis of the thesis was in the inclusive measurement of Λ in which, there lies some uncertainty in the reaction production location. The variables of the center of the target ($t\hat{p}$) production point in the target ($g\hat{p}$), the length of the flight before decay($dlength$), and the site of decay ($d\hat{p}$) are procured as listed below,

$$dlength = \frac{|\vec{p} \cdot (\vec{dp} - \vec{tp})|}{|\vec{p}|} = |\vec{dp} - \vec{gp}| \tag{4.20}$$

$$\vec{gp} - \vec{tp} = \vec{dp} - \vec{tp} - dlength \cdot \frac{\vec{p}}{|\vec{p}|} \qquad \vec{p} \cdot (\vec{dp} - \vec{gp}) \geq 0 \tag{4.21}$$

$$\vec{gp} - \vec{tp} = \vec{dp} - \vec{tp} + dlength \cdot \frac{\vec{p}}{|\vec{p}|} \qquad \vec{p} \cdot (\vec{dp} - \vec{gp}) \leq 0 \tag{4.22}$$

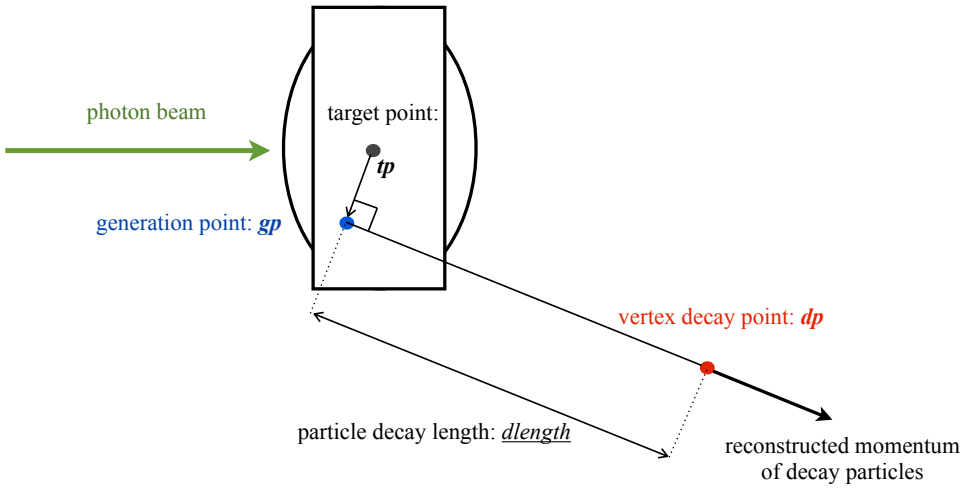

Figure 4.31: Schematic view of production point, flight length (dlength) and explanation of kinematical variables.

An illustration of the kinematical variables, denoting the generation point, the decay site, and the length of the of the flight prior to the decay into the detected charged particles is shown in Figure 4.31

The accepted zone for a valid generation point was set as,

$$\vec{gp} \cdot \hat{x} - \vec{tp} \cdot \hat{x} \leq 2.0[cm] \tag{4.23}$$

$$\vec{gp} \cdot \hat{y} - \vec{tp} \cdot \hat{y} \leq 1.5[cm] \tag{4.24}$$

4.12.2 Timing Requirements

One of the primarily items that was corrected was the time between the TagF and TagB counters. Each segment of the TagB counters is used in coincidence with four corresponding TagF counter to eliminate accidental coincidences, and since the number of photons that reach the target is determined from the recorded scaler counts of the tagger segments an additional study of the possibility misidentified hits or hits of more than one segments from one electron was undertaken. The TagF segments, only provide TDC information while both ADC and TDC information in taken for the TagB counters. The decision was made to only record the time information for the TagF counters was based on a desire to reduce the data size. The time was corrected for all segments as discussed in section 4.3 as well necessary time walk corrections for the eight TagB segments. The time difference between TagF and TagB is shown in Figure 4.32. A time resolution of the 295 nanoseconds

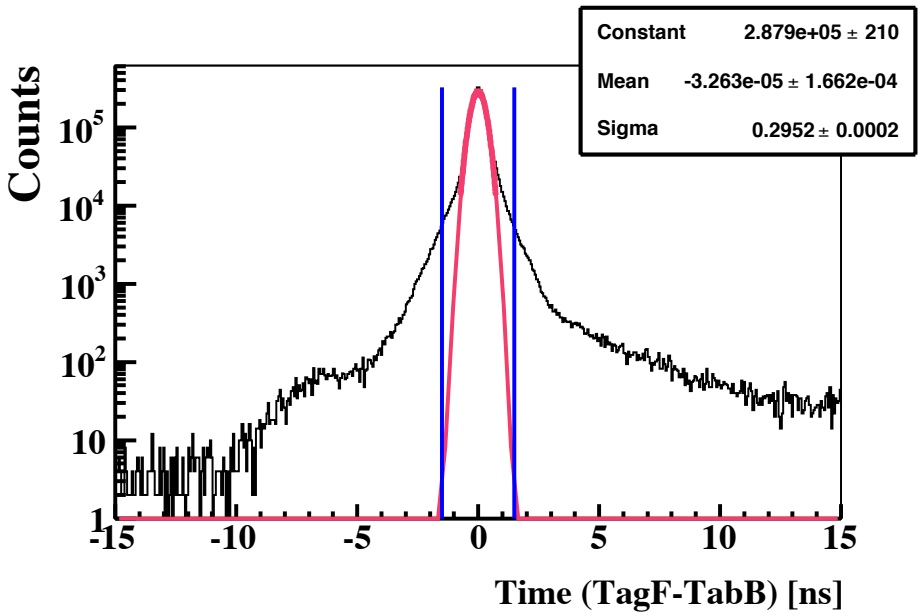

Figure 4.32: Gated time for tagger events. Time selection of real photons gated by the time difference between TagF and TagB counters was specified to be within 2 ns indicated by the solid blue lines in the figure.

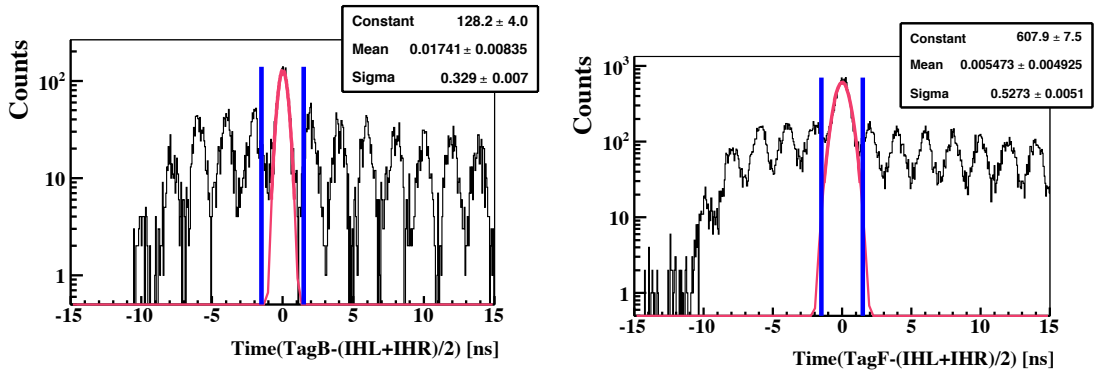

Figure 4.33: Time difference between the TagB (left) and TagF (left) counters, and the mean time of the IHL2 and IHR2 are shown. The resolution was determined from fitting as 374 ps and and 528 ps for the TagB−IH and TagF−IH counters respectively.

as achieved. The distribution however does have an assymetrical shape, a consequence of having performed a time walk corrected only to the TagF segments. The time gate was set to be within $2ns$ indicated by the solid blue lines.

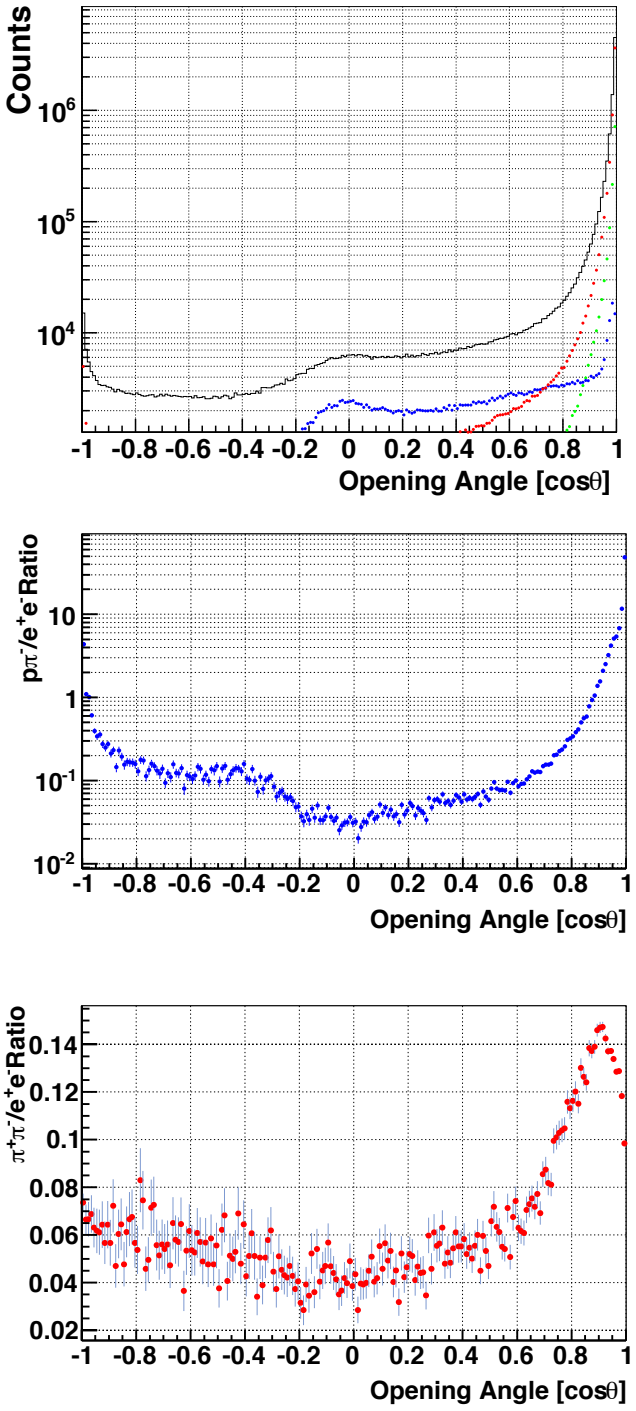

Figure 4.34: The opening angle between two identified charged particles are shown all in black. An overlay with two electrons events as green, a $\pi\pi$ events as red, and a $p\pi^-$ as blue. The ratio of $p\pi^-$ and $\pi^+\pi^-$ events to that of e^+e^- events are shown in the middle and lower figure.

4.12.3 Opening Angle Cut

To reduce the copious amount of positron electron pairs generated in the forward direction primarily of the reaction plane, $\hat{z} = 0$, that were introduced into the recorded data that would be used for further analysis, a selection requirement was placed on the acceptable opening angle between particles in the laboratory frame of reference. The opening angle of detected particles is shown in Figure 4.34. The distributions of detected charged particles, including, e^+e^- pairs, $\pi^+\pi^-$ pairs, and pπ^- shown as black, green, red, and blue respectively. The lower figures are the ratio of of pπ^- and $\pi^+\pi^-$ events to that of e^+e^- events, where the pπ^- ratio is in the middle figure and $\pi^+\pi^-$ events in the lower. It is quite apparent that for $\pi^+\pi^-$ the contamination of e^+e^- pairs, is significant, showing that ratio of less than 10% for angles less than 0.9 degrees. We then implemented a selection requirement of an opening angle cut of $-09 \leq \cos\theta \leq 0.9$.

4.12.4 Drift Chamber Layer Multiplicity Selection

The layer multiplicity was substantially reduced by pattern recognition selections that including clustering and grouping requirements. However, even with the implementation of these types of stipulations there still is a high rate of multiplicity on the drift chamber layers. As such, a selection requiring the maximum number of hits per layer to 20 or less was used in further analysis. The layer multiplicity of the VDC and CDC are shown for all layers (color online) and the accepted region of 20 or less hits is indicated by the blue vertical line. The multiplicity distribution is consistent over all layer of the VDC in contrast to the CDC whose outer layers have roughly an order more hits for a multiplicity greater that 50.

4.12.5 χ^2 Selection

The selection of good events was carried out for the purpose of optimizing the quality of the data analyzed. As such, additional cuts were placed the data set. This included placing a selection on the acceptable value of the χ^2 value associated with the track fitting. The tracking was accomplished, at present, using only the CDC to construct the particle trajectories. A prerequisite such that the χ^2 value be below 10 indicated by the solid blue line and is visible is in Figure. 4.36; The left figure is the χ^2 distribution of pions and the right is for protons.

4.12.6 Hodoscope Hit Residual Selection

The measured distance of a hit position from ahodoscope segment central position was defined as the hit residual distance. The hit position was determined by the particle

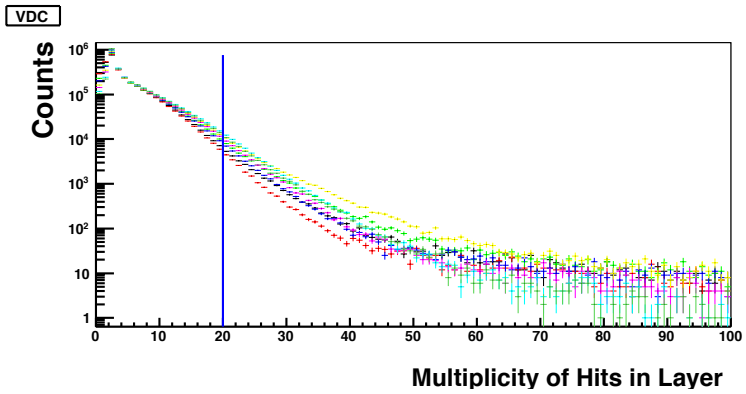

(a) Multiplicity of hits on VDC

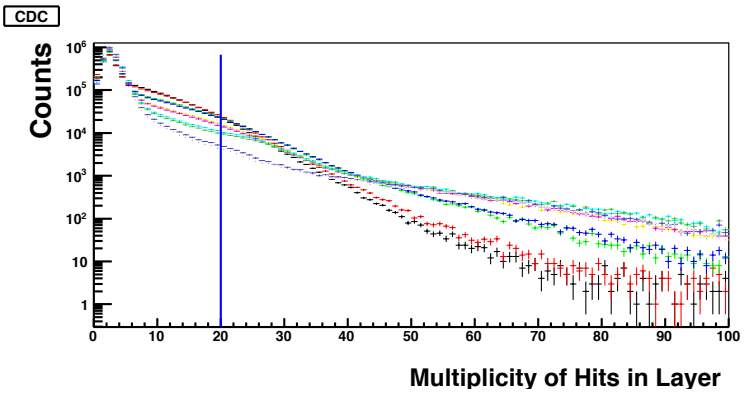

(b) Multiplicity of hits on CDC

Figure 4.35: Multiplicity of hits on layers for the drift chamber, the VDC (a) and CDC (b) distributions over all layer are shown superimposed in the figure.

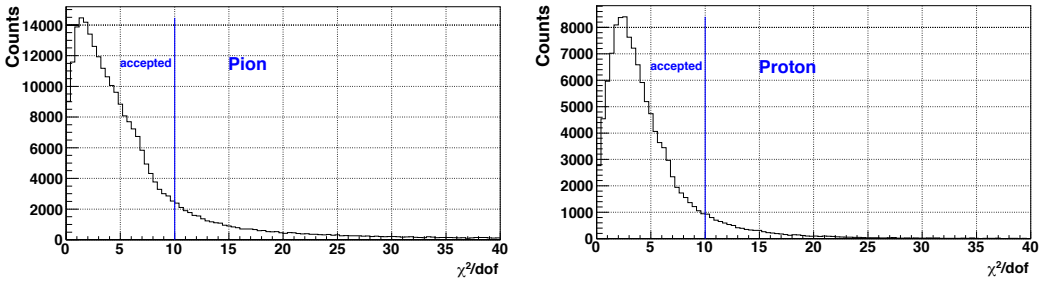

Figure 4.36: The generated χ^2 squared distribution of tracking results as performed by CDC. The selection region is indicated by the solid blue line, where the accepted region was $\chi^2 \leq 10$ .The left figure is the χ^2 distribution of pions and the right is for protons.

path trajectory reconstructed by the CDC. The distributions for the IH and the OHV_{9-12} segments are shown in Figure 4.37. We placed a cut on the accepted region for the IH, of IH distance $\leq$2.5 [cm] and OHV_{1-8} <12.5 ,OHV_{9-12} <10 cm.

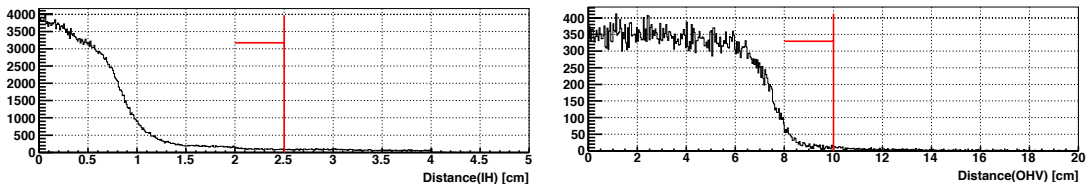

Figure 4.37: Distribution of the distance from the center position of the hodoscope segment and the hit position obtained from the interpolated track path for the IH and the OHV_{9-12} segments.

4.12.7 Distance Between Reconstructed Tracks Selection

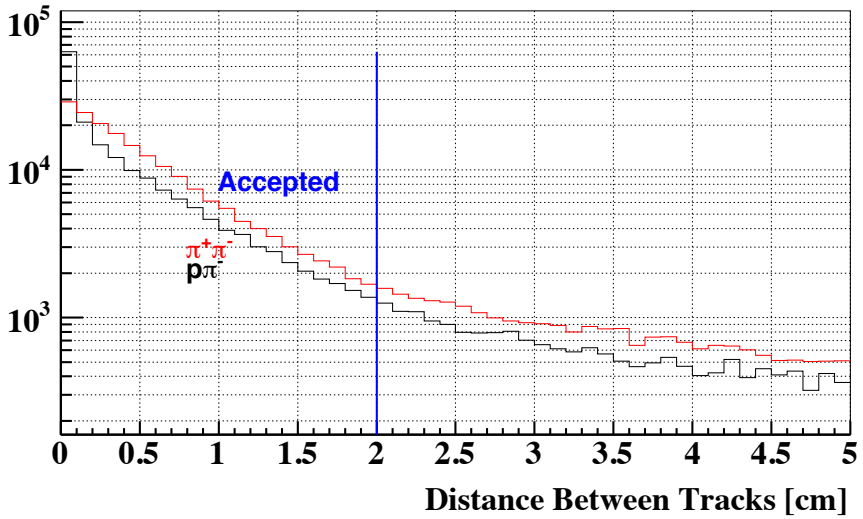

Figure 4.38: The calculated distance between two reconstructed tracks selection. The color online are for $\pi^+\pi^-$ and pπ^- events.

There was a selection requirement placed upon a reasonable acceptable distance between the reconstructed tracks. The decay vertex determination and reconstruction resolution are a direct consequence of the distance between tracks. Only tracks with of 2 cm or less were decided to be used. The distribution of the distance between tracks is shown in Figure 4.38 in which the distribution for $\pi^+\pi^-$ and $p\pi^-$ events are displayed as red and black online respectively.

4.13 Missing Mass

In section 2.3 the missing mass technique was elaborated upon at some length; We now turn to the calculation of the koan missing mass and discuss it's usage as an additional event selection prerequisite. The squared missing mass are calculated as follows,

$$M_{k^0}^2 = (E_\gamma + E_n - E_{\pi^-} + E_{\pi^+})^2 - (\vec{p}_\gamma + \vec{p}_n - \vec{p}_{\pi^+} + \vec{p}_{\pi^-})^2 \tag{4.25}$$

$$M_\Lambda^2 = (E_\gamma + E_n - E_{\pi^-} + E_p)^2 - (\vec{p}_\gamma + \vec{p}_n - \vec{p}_p + \vec{p}_{\pi^-})^2 \tag{4.26}$$

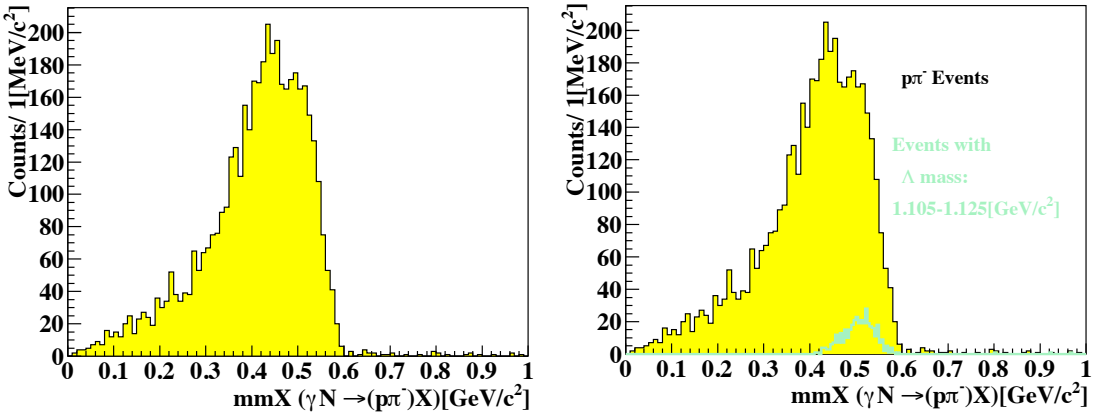

Figure 4.39: Missing mass distribution in the inclusive measurement of γN $\rightarrow$pπ^-X reaction. Events where there was a selection placed on the invariant mass pπ^- of between $1.105 - 1.125$ GeV/c^2 is showed as the green online color.

The missing mass distribution in the inclusive measurement of γN $\rightarrow$pπ^-X reaction are given on the left in Figure 4.39. The accepted region of the kaon missing mass is shown in Figure 4.40, based on the distribution of the events in which a requirement was placed on the invariant mass pπ^- of between $11.105 - 1.125$ GeV/c^2, as seen as the solid green histogram, only events greater than 0.4 GeVc^2 was accepted. This corresponds to the solid red portion in the afore mentioned histogram. Thus, the missing mass requirement is,

$$\gamma N \rightarrow p\pi^- X > 0.4[\mathrm{GeV/c^2}] \tag{4.27}$$

Placing a tight requirement of the Λ particle invariant mass, between $1.105 - 1.125$ GeV/c^2, as previous discussed, the kaon missing mass distribution gated for neutron at rest within the deuteron nucleus was generated. The missing mass resolution was found to be 31 ± 2 MeV/c^2 with a fitted mean value of 504 ± 2.0 MeV/c^2. The spread in the distribution is associated with the Fermi motion within the deuteron and compounded

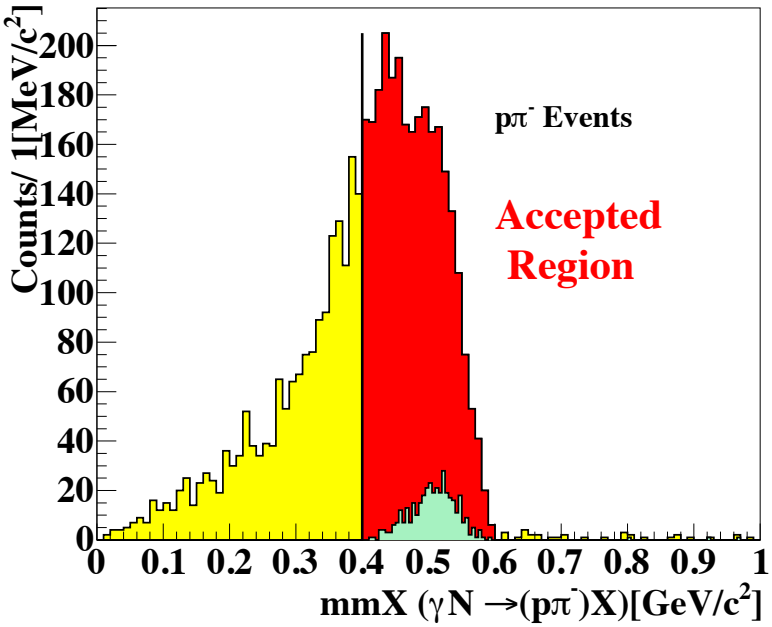

Figure 4.40: Missing mass distribution in the inclusive measurement of $\gamma N \rightarrow p\pi^- X$ reaction. Events where there was a selection placed on the invariant mass $p\pi^-$ of between $1.105 - 1.125$ GeV/c^2 is showed as the green online color. The accepted region is displayed in red.

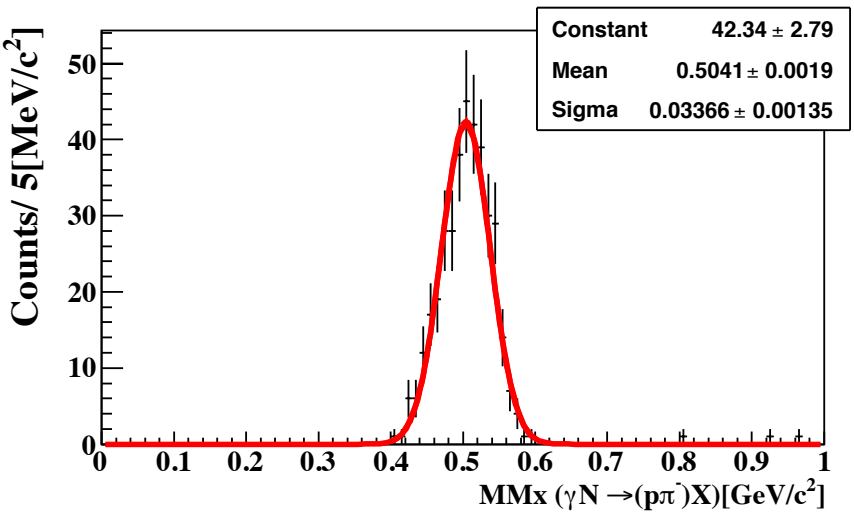

Figure 4.41: Kaon missing mass distribution from the neutron assumed at rest in the deuteron nucleus in the inclusive measurement of $\gamma N \rightarrow p\pi^- X$ reaction, in which there was a selection placed on the invariant mass $p\pi^-$ of between $1.105 - 1.125$ GeV/c^2 .

with the fact that the missing mass spectrum was generated by an inclusive measurement of $p\pi^-$, it is apparent that the missing mass distribution has a contribution from the $K^+\Lambda$

Table 4.5: Listing of data analysis cuts

Cut	Name of Cut	Selection Region
	Timing	
Cut_a	Time_{Gate}	|tagF-tagB| <1.5 [ns] Fig. 4.32
Cut_b	Time_1	$\|\text{IH}_2^{left/right}$ -tagB| < 2 [ns] Fig. 4.33
Cut_c	Time_2	$\|\text{IH}_2^{left}$ -IH_2^{right}| < 2 [ns] Fig. 4.6
	Kinematic	
Cut_d	Opening angle	$-0.9 \leq \cos\theta \leq 0.9$ Fig. 4.34
Cut_e	χ^2	χ^2<10 Fig. 4.36
Cut_f	Number of hits in track	$6 \leq \text{N}_{hits} \leq 8$
Cut_g	IH Distance	IH distance ≤2.5 [cm] Fig. 4.37
Cut_h	OH Distance	OHV_{1-8} <12.5 ,OHV_{9-12} <10 [cm] Fig. 4.37 OHH <10 [cm]
Cut_i	Layer Multiplicity	Hits on layer ≤20 Fig. 4.35
Cut_j	Distance between tracks	Distance ≤2 [cm] Fig. 4.38
Cut_k	Generation point	|(gx-tx)| <2.0 & |(gy-ty)| <2.0 [cm]
Cut_l	Particle ID [p]	$(0.5 \leq m_p^2 \leq 1.8)[\text{GeV}^2/c^4]$Figs. 4.26,4.29
	Particle ID [π^-]	$(-0.5 \leq m_\pi^2 \leq .25)[\text{GeV}^2/c^4]$Figs. 4.26,4.29
Cut_m	Electron Rejection Cut	$0.06 \leq m$ [GeV/c^2]
Cut_n	Out of Target	$2.0< \mid \vec{vp} \cdot x - \vec{tp} \cdot \hat{x} \mid$ [cm] eq. 4.24
Cut_o	Downstream of Target	$1.5< \mid \vec{vp} \cdot y - \vec{tp} \cdot \hat{y}\mid$ [cm] Fig. 4.31
Cut_p	Missing mass	$\gamma\text{N} \rightarrow \text{p}\pi^-\text{X} > 0.4$ [GeV/c^2] Fig. 4.40

and $K^0\Lambda$ processes.

4.14 Invariant Mass

The direct approach to measuring the photo production of strangeness is by reconstructing the invariant mass of the produced particles that contain a strange quark. The squared invariant mass of $\text{p}\pi^-$ was calculated by equation 4.28, numerous cuts were implemented on the raw invariant mass to extract the Λ distribution that was hidden in the continuum.

$$M_{p\pi^-{}^2} = (\sqrt{m_p^2 + |\vec{p}_p|^2} + \sqrt{m_{\pi^-}^2 + |\vec{p}_{\pi^-}|^2})^2 - |\vec{p}_p + \vec{p}_{\pi^-}|^2 \tag{4.28}$$

A complete listing of the all selection requirements previously discussed in section 4.12 is given in Table 4.5. In Figure 4.42 the usefulness of each selection is illustrated starting from the top left to the bottom right, where each figure shows the effect of an additional stipulation on the raw invariant mass spectrum.

The $\text{p}\pi^-$invariant mass distribution in the inclusive $\gamma\text{N} \rightarrow \text{p}\pi^-\text{X}$ measurement is shown

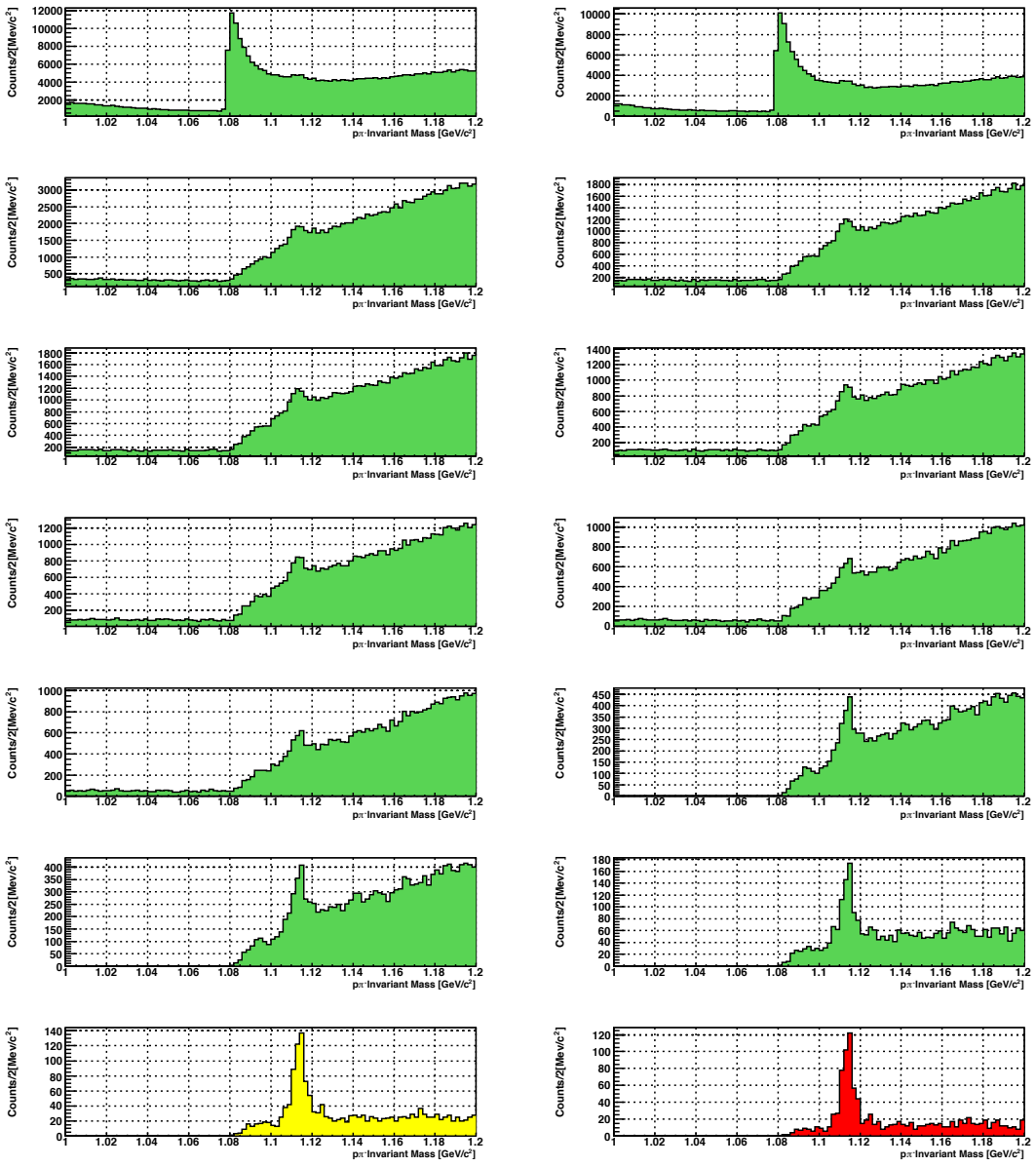

Figure 4.42: The effectiveness of the aggregated application of the data analysis cuts detailed in Table 4.5 on the Λ peak.

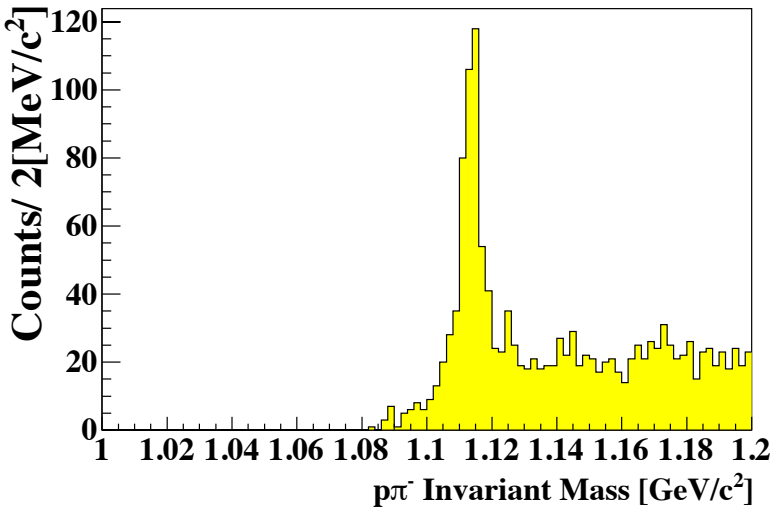

(a) The pπ−invariant mass distribution

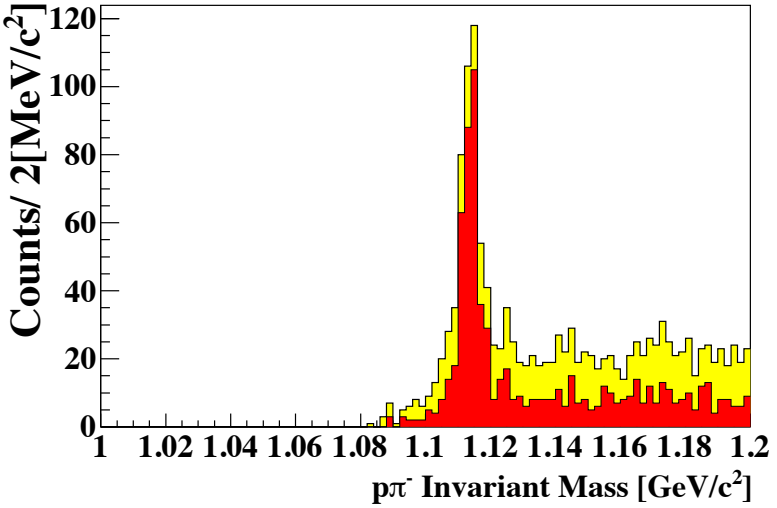

(b) The pπ−invariant mass distribution where the missing mass cut, equation 4.27, is employed

Figure 4.43: The pπ−invariant mass distribution is shown is the upper figure. In the lower figure, invariant mass distribution with and without the inclusion of a missing mass selection is shown as the red and yellow filled histograms respectively.

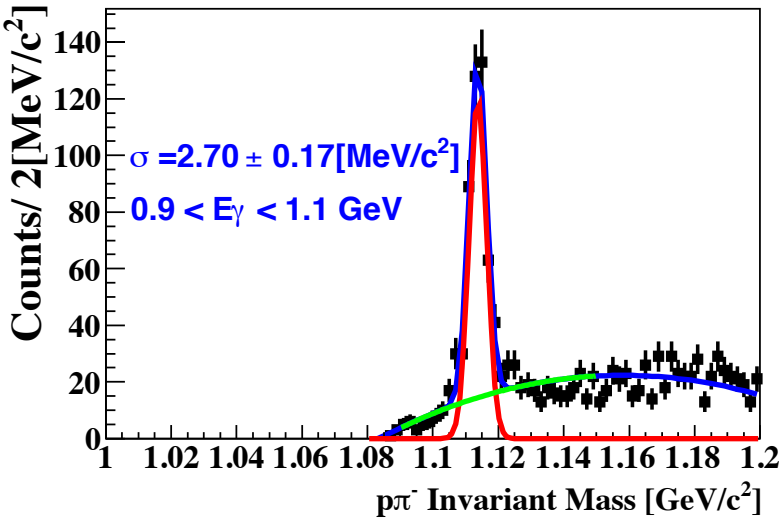

(a) Invariant mass resolution for the energy bin of 0.9 $\leq E_\gamma \leq$1.1 GeV

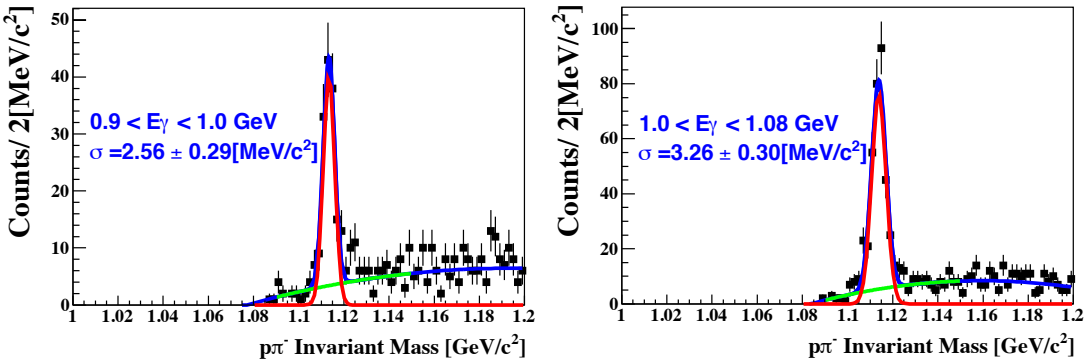

(b) Invariant mass resolution for the energy bins of 0.9$\leq E_\gamma \leq$1.0 and 1.0 $\leq E_\gamma \leq$1.1 GeV

Figure 4.44: Invariant mass resolution for the energy bin of 0.9 $\leq E_\gamma \leq$1.1 GeV (a) was found by fitting as 2.87 $\pm$ 0.19 MeV/c in rms. Invariant mass resolution for the energy bins of 0.9$\leq E_\gamma \leq$1.0 and 1.0 $\leq E_\gamma \leq$1.1 GeV are seen in the Figures(b) left to right respectively. Where the fitted resolution were found to be 2.56 $\pm$ 0.29 MeV/c and 3.26 $\pm$ 0.30 MeV/c in rms.

is the upper panel (a) of Figure 4.43, this distribution is obtained after the inclusion of all cuts outlined in Table 4.5. In the lower figure (b), the p$\pi-$invariant mass distribution prior the inclusion of a missing mass selection, equation 4.27, is shown as the yellow filled histogram, and with the missing mass selection as the red filled histograms respectively in the figure.

The pπ^-invariant mass distribution in the inclusive γN $\rightarrow$pπ^-X measurement is shown (a) in Figure 4.44 for the energy bin of $0.9 \leq E_\gamma \leq$1.08 GeV. The distributions associated with the energy bins of $0.9 \leq E_\gamma \leq$1.0 and $1.0 \leq E_\gamma \leq$ 1.08 GeV can be seen in lower histograms in Figure (b)4.44. The distributions were fitted by the combination of a gaussian and a third degree polynomial function. The resolution of the distribution generated for the energy bin of $0.9 \leq E_\gamma \leq$1.08 GeV was determined to be 2.87 $\pm$ 0.19 MeV/c^2 in RMS. In the two smaller energy bins, $0.9 \leq E_\gamma \leq$1.0 and $1.0 \leq E_\gamma \leq$1.1 GeV, the resolutions were 2.56 $\pm$ 0.2 and 3.26 $\pm$ 0.30 GeV respectively. Full details are listed in Table 4.6.

Table 4.6: pπ^- invariant mass resolution

Inclusive Λ measurement					
Selection	Region E_γ [GeV]	Res.(σ) [MeV/c^2]	Yield (S)	Noise (N)	S/N
E_γ^{all}	0.90 - 1.1	2.87 $\pm$ 0.19	349 $\pm$ 25.49	166$\pm$12.88	2.1
E_γ^1	0.90 - 1.0	2.56 $\pm$ 0.20	102 $\pm$ 14.42	49$\pm$7.00	2.1
E_γ^2	1.0 - 1.1	3.26 $\pm$ 0.30	247 $\pm$ 20.59	72$\pm$10.24	3.4

4.15 Inclusive Λ Measurement: Estimating the Background

For the identification of the Λ particle it was necessary to reconstruct its invariant mass from two particle combination of a negatively charged pion and a proton. However there lies the chance of a fallaciously identified decay vertex point such that the combination of a pion from the kaon decay and a proton from a Λ decay could be made. An example of such is illustrated in Figure 4.45. The background continuum present in the invariant mass spectrum after the application of kinematical and various cuts is attributed mainly to this mis-combination that could be from pions from the koan decay and protons from the Λ decay or with the spectator proton. The overall contribution of mis-combinations was estimated at 60%. The photon induced production of a Δ^0 particle and it's subsequent decay can also contribute to the background and was estimated to be roughly 10%. In order to determine the correct background continuum a study was performed.

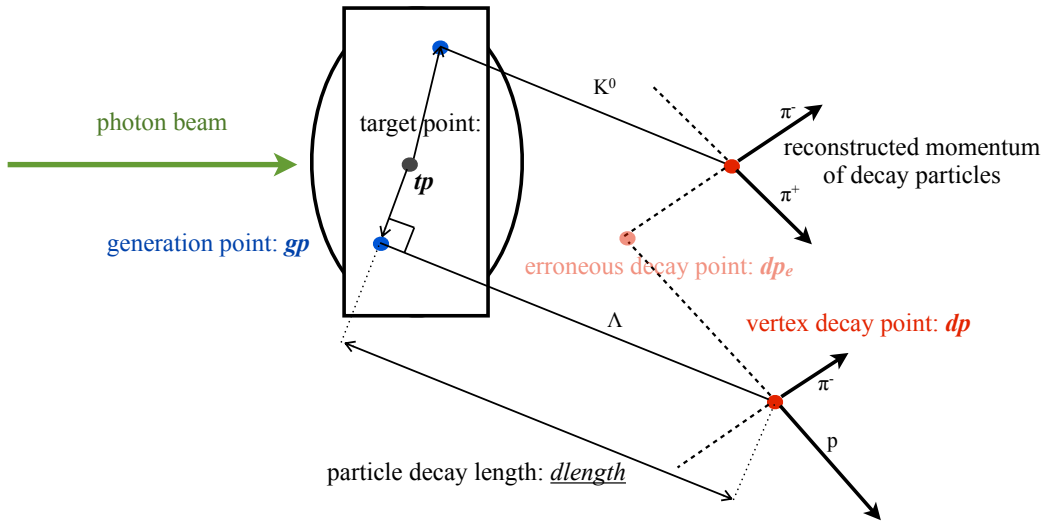

Figure 4.45: Illustration of background candidate in $p\pi^{-}$]invariant mass

The correct assignment of the background was attempted by five procedures here forth designated as BG_{SB}, BGM_{SA}, BGM_{LF}, BGM_{QF} and BGM_{MM}. The technique utilized in BGM_{SB} is the so-called side band method, in this approach the background contribution in the invariant spectrum was estimated as the sum of the side regions denoted as BG_{high} and BG_{low} which are shown in Figure 4.46. In this approach the background regions of the side bands of the Λ peak are defined as,

$$\text{Background}_{\text{low}} = BG_{low} = 1.105 - 1.11[\text{GeV/c}^2] \tag{4.29}$$

$$\text{Background}_{\text{high}} = BG_{high} = 1.12 - 1.125[\text{GeV/c}^2] \tag{4.30}$$

$$BG_{\text{SB}} = BG_{high} + BG_{low} \tag{4.31}$$

The invariant mass gate region of the acquired $p\pi^{-}$ invariant mass spectrum associated with the quasi-free photo production of the Λ particle is selected between $1.11 - 1.120$ GeV/c^2 shown as the filled yellow area of the histogram Figure 4.46, the areas used for the calculation of the background in BGM_{SB} are the filled red and blue regions where their sum corresponds to equation 4.31. The remaining four procedures used to determine the background continuum in $p\pi^{-}$ invariant mass spectrum, BGM_{SA}, BGM_{LF}, BGM_{QF} and BGM_{MM} are shown in Figure 4.47. They are the so-called side area method, a linear fit to the background, a quadratic fit, and the invariant mass distribution generated by

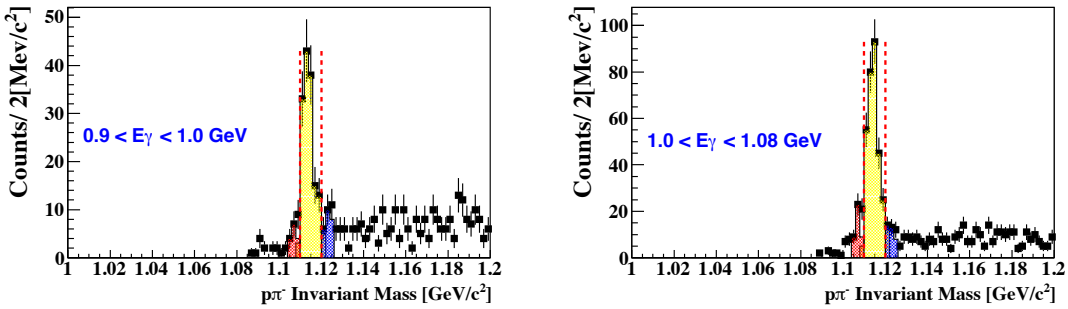

Figure 4.46: Background events in the $p\pi^-$ invariant mass spectrum determined by the side bands, BGM_{SB} are further defined as BG $_1$ and BG $_2$ which are the red and blue colored regions. The accepted invariant mass gate region is shown as the filled yellow area

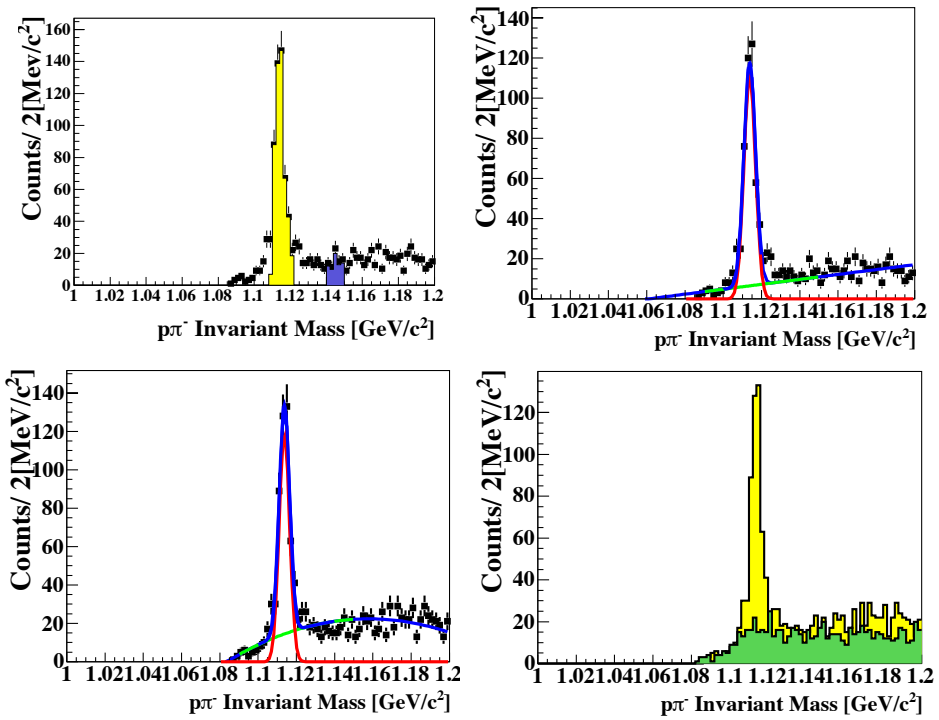

Figure 4.47: The four procedures, BGM_{SA}, BGM_{LF}, BGM_{QF} and BGM_{MM} used to determine the background continuum in $p\pi^-$ invariant mass spectrum. They are the so-called side area method, a linear fit to the background, a quadratic fit, and the invariant mass distribution generated by accepting the missing mass$\leq$ 0.4 GeV/c^2

accepting the missing mass$\leq$ 0.4 GeV/c^2. The side area approach BGM_{SA}, Figure 4.47 (top left), involved using a section of the background area far away from the prompt invariant mass peak as an area for subtraction, illustrated as the purple solid area. This chosen area is $6\sigma_{rms}$ away from the solid yellow region, the accepted part for Λ yield

extraction.

$$\text{Background}_{\text{side}} = \text{BG}_{SA} = 1.140 - 1.15[\text{GeV/c}^2] \tag{4.32}$$

The linear fit approach BGM_{LF}, Figure 4.47 (top right), involved using a linear fit of the background in combination with a gaussian fit of the invariant mass peak. The linear fitting and gaussian fitting range were designated as $1.09 - 1.14$ and $1.11 - 1.12$ GeV/c^2 respectively. The linear fit is shown as the green line and has been extended to the full range of the histogram. The blue fit shows the combination of the gaussian and linear function and the red fit is after the subtraction of the background determined by the parameters obtained using the combination function. Both the blue and red fits have been extended to the full range of the histogram.

The quadratic technique BGM_{QF}, Figure 4.47 (bottom right), involved using a quadratic fit of the background in combination with a gaussian fit of the invariant mass peak. The quadratic fitting and gaussian fitting range were designated as $1.06 - 1.16$ and $1.11 - 1.12$ GeV/c^2 respectively.

In order to distinguish the source of the continuum a simulation was performed by GEANT4. The invariant mass distribution generated from incorrectly combined pion and protons can by seen in as the green filled histogram Figure 4.48 on the top left. Moreover, this obtained distribution was then overlaid with the invariant mass generated from correct combination in the right on the top right of Figure 4.48. The original hypothesis was confirmed as the simulated distribution appropriately describes the shape of the background. Hence, it was concluded that anything outside of the prompt mass peak is not a true Λ event.

A comparison of the simulated Λ invariant mass capable of being resolved by the spectrometer was made to the experimentally obtained spectrum. The experimentally measured invariant mass is shown as the black dots. The simulated distributions and background selection areas, BGM_{SB} and BGM_{SA}, the filled yellow, blue, red and violet regions respectively, are seen in (a) in Figure 4.49. In the right figure are the background regions overlaid with the simulated invariant mass as the red online histogram. The side bands method lead to the incontestable conclusion that they fall well within the Λ peak as evident in the (b) of Figure 4.49 and the side area, the solid violet, is a viable region for selection as it at most contains roughly one count.

Using the results of the simulated Λ invariant mass that can be resolved with the spectrometer we decided to adopt the side area approach for the background subtraction. However, the accepted invariant mass and background region were extended to completely cover the simulated full Λ peak shown as the red line drawn on the experimental data points

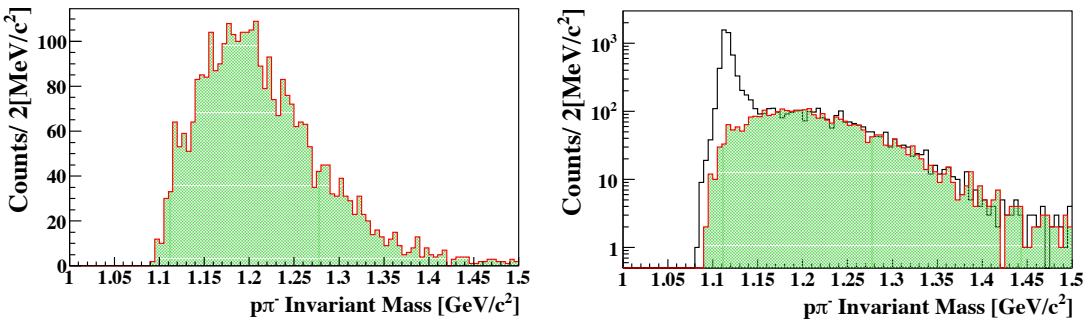

(a)

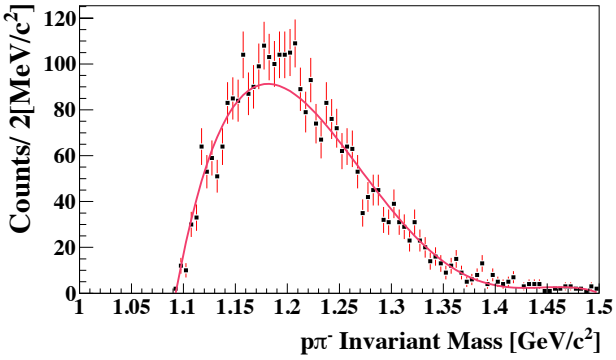

(b)

Figure 4.48: Simulated background spectrum generated from wrong combination of proton and pion and the fitted distribution.

in black as shown on the left in (b) of Figure 4.49. The final accepted regions are drawn as the solid yellow and violet regions overlaid on the experimental data points on the right. The accepted region for the Λ invariant mass was,

$$\text{InvariantMass}^{\Lambda}_{\text{accepted}} = \text{IM}^{\Lambda}_{acc} = 1.105 - 1.125[\text{GeV/c}^2] \tag{4.33}$$

Hence, the following cut condition is applied for Λ yield extraction

$$\text{IM}^{\Lambda}_{acc} = |\text{IM}_{\Lambda} - m_{p\pi^-}| < 10\text{MeV/c}^2 \tag{4.34}$$

Where the mass of Λ has been taken from the PDG determined value of 1.115683 (GeV/c^2). The accepted region for the background subtracted was therefore,

$$\text{Background}_{\text{side}} = \text{BG}^{\text{f}}{}_{SA} = 1.140 - 1.16[\text{GeV/c}^2] \tag{4.35}$$

The side area background region corresponds to a range of

$$5\sigma_{\text{rms}} \leq \text{BG}^{\text{f}}{}_{SA} = |\text{IM}_{p\pi^-} - \text{BG}^{\text{f}}{}_{SA}| \leq 7\sigma_{\text{rms}} \tag{4.36}$$

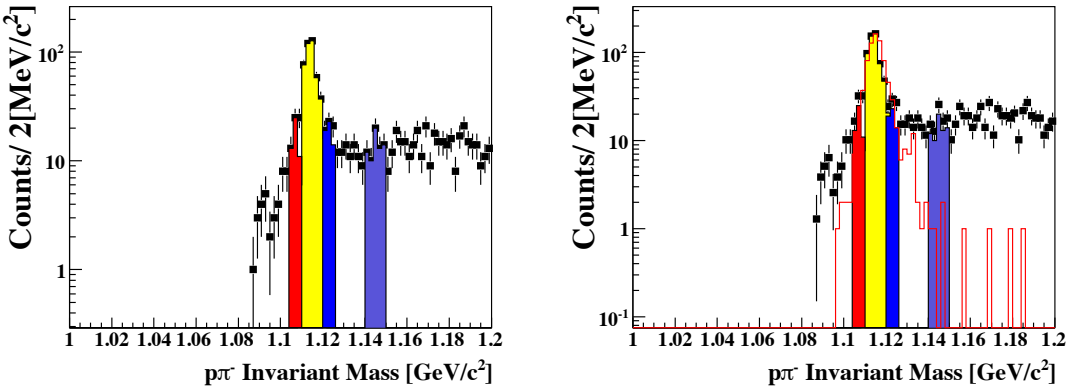

(a) Invariant mass distribution with a comparison to the simulated distributions and background selection areas BGM_{SB} and BGM_{SA} as the filled yellow, blue, red and violet regions respectively.

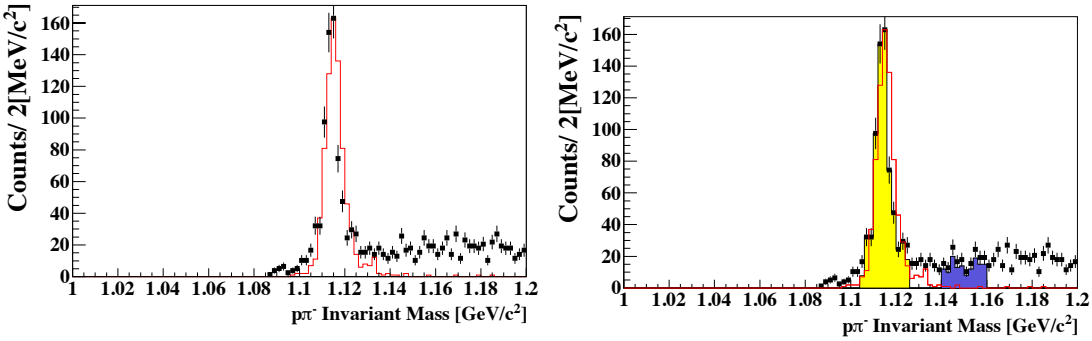

(b) Invariant mass distribution with a comparison to the simulated distributions and background selection regions for background subtractions and yield extraction as the solid violet and yellow sections

Figure 4.49: Invariant mass distribution with a comparison to the simulated distributions and background selection areas.

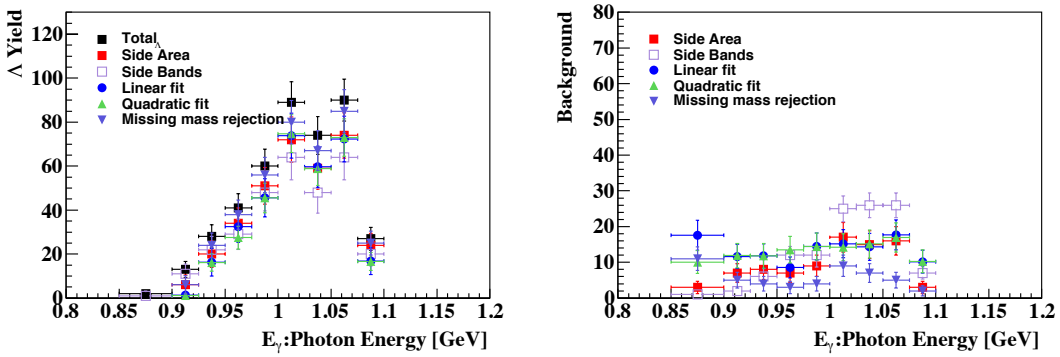

Figure 4.50: Λ yield and background events in the $\mathrm{p}\pi^-$ invariant mass spectrum determined by the five techniques, BGM_{SB}, BGM_{SA}, BGM_{LF}, BGM_{QF} and BGM_{MM}.

The extracted photon energy dependent Λ and background yield for the various background methods are shown in Figure 4.50. The results of BGM_{SB}, BGM_{SA}, BGM_{LF},

BGM_{QF} and BGM_{MM} approaches are the solid red squares, open violet square, solid blue circle, solid green triangle, and the solid inverted violet triangle respectively. Here is it undeniable that the approach decided upon is the background definition and subtraction criteria notably biases the Λ yield. Its influence will be accounted for a source of systematic uncertainty in the cross section calculations.

4.16 Simulated Distributions

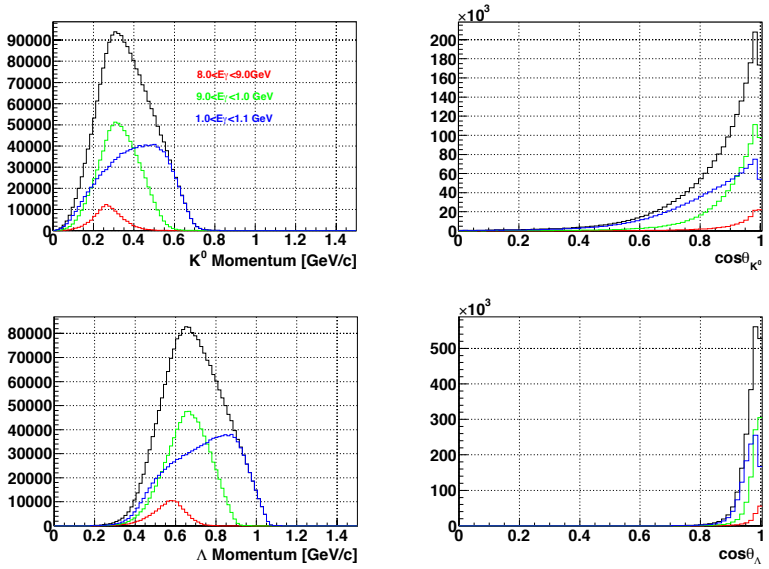

Figure 4.51: Simulated momentum (left) and $\cos\theta^{LAB}$ (right) distributions of K^0_s and Λ in the laboratory frame of reference. The K^0_s distribution and Λ distributions are presented top to bottom respectively.

A monte-carlo simulation was performed with GEANT4 to generate the momentum and angular distributions of K^0 and Λ produced in the $\gamma n \rightarrow K^0\Lambda$ reaction for the laboratory frame. The momentum distributions of K^0 are shown in upper panel and the Λ in lower panel of Figure 4.51. These distributions were procured for photon energies of $0.8 \leq E_\gamma \leq 0.9$, $0.9 \leq E_\gamma \leq 1.0$, and $1.0 \leq E_\gamma \leq 1.1$ GeV/c shown as the red, green and blue histograms respectively and were drawn along with the black online histogram, the distribution for $0.8 \leq E_\gamma \leq 1.1$ GeV, to illustrated the photon energy dependent contribution.

The simulation study was extended to also considered the distributions of based the two most favored isobar models, the Kaon-MAID (KM) and Saclay-Lyon A (SLA) models;. Triggered momentum distributions for the photon energies of $0.8 \leq E_\gamma \leq 0.9$, $0.9 \leq E_\gamma \leq 1.0$, and $1.0 \leq E_\gamma \leq 1.1$ GeV and are illustrated in Figure 4.52 as the black, red and green lines in the figure. The KM and SLA results are given top to bottom respectively. Here

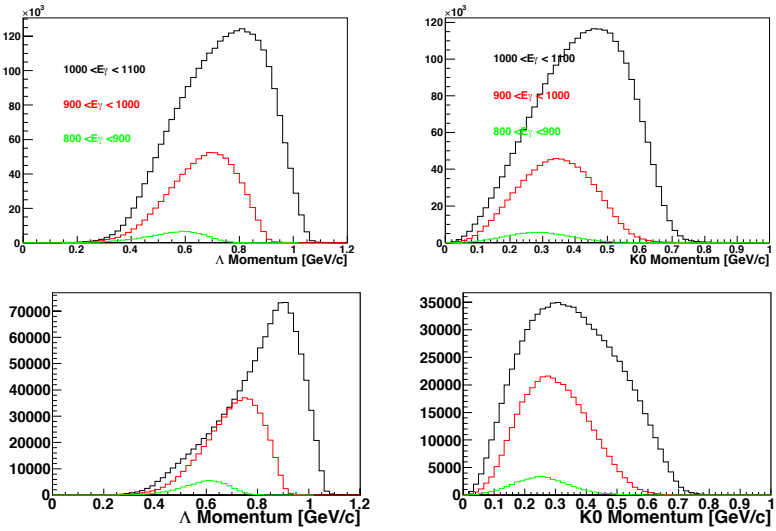

Figure 4.52: Simulated momentum distributions of K^0 and Λ based on KM (top) and the SLA (bottom) models. Triggered events for the energy range of the photon is $0.8 \leq E_\gamma \leq 0.9$, $0.9 \leq E_\gamma \leq 1.0$, and $1.0 \leq E_\gamma \leq 1.1$ GeV/c and are illustrated as the black, red and green lines in the figure.

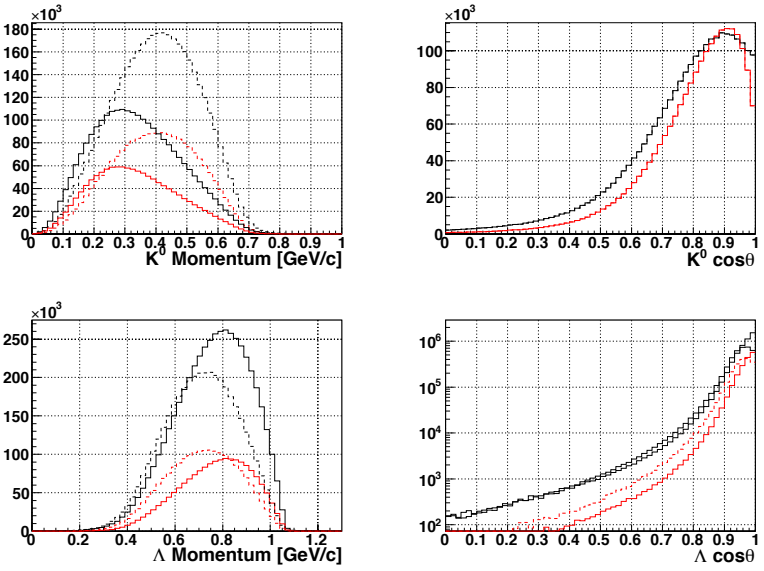

Figure 4.53: Simulated momentum and $\cos\theta^{LAB}$ distributions of K^0_s and Λ in the laboratory frame of reference, based of the Kaon Maid and SLA models. The upper figure displays the K^0_s distribution and the Λ momentum distribution is shown in lower. Generated events and triggered events are shown as the black and red line respectively with the solid lines for the SLA prediction and the dashed for KM

the energy dependence on the shape and size of momentum and angular distributions are quite obvious.

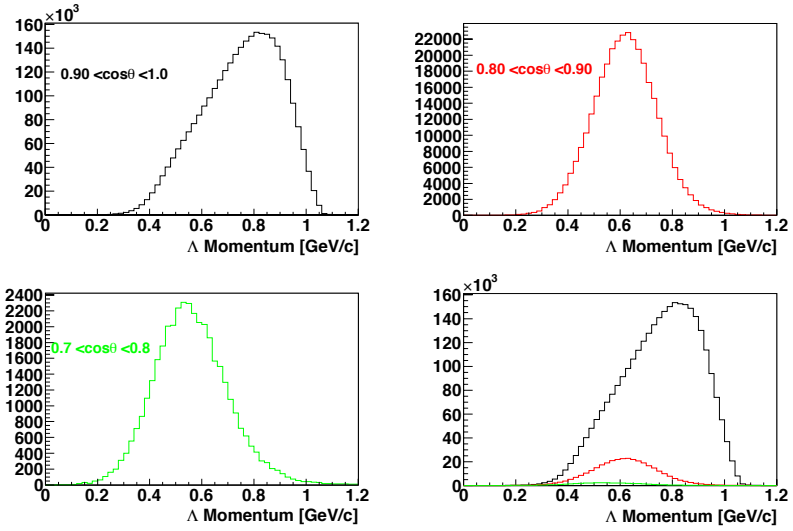

Figure 4.54: Triggered Λ momentum distributions of based of the KM in the laboratory frame of reference for the angular bins of ($\cos\theta_{\Lambda}^{LAB}$) 0.90-1.0, 0.90-0.80, 0.70-0.80

The simulated distributions in the laboratory frame of reference for these models are given in Figure 4.53. The upper figure displays the K_s^0 distribution and the Λ momentum distribution is shown in lower. Generated events and triggered events are shown as the black and red line respectively with the solid lines for the SLA prediction and the dashed for KM.

The angular region dependence for the Λ momentum distributions based of the KM are seen in Figure 4.54 for the bins of ($\cos\theta_{\Lambda}^{LAB}$) $0.90-1.0, 0.90-0.80, 0.70-0.80$. The dominant contribution to the shape of the momentum is from the forward hemisphere, $\cos\theta_{\Lambda}^{LAB}$ = 0.90-1.0, seen as the black histogram.

4.17 Measured Λ Event Distributions

The Λ momentum and angular distributions were measured with the background contributions for the entire spectrum of the bombarding photon beam as well as for specific energy and angular bins. In Figure 4.55 the momentum of Λ is showcased with and without the background in the upper figures. The it was estimated that 60% of background is attributed to the mis-combination of negatively charged pions from the the koan decay and the proton from the Λ decay. The background is associated with the side area background procedure discussed in section 4.15 and defined by equation 4.35 and visible as the red data points in Figure 4.49. The angular event distribution is seen in the lower panel (b). The momentum as well as the angular event distributions are are presented for the energy

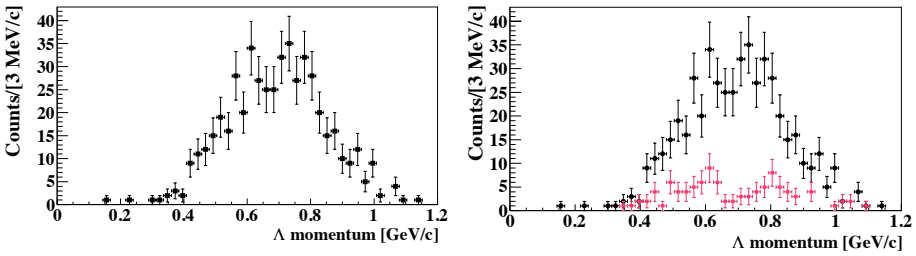

(a) Λ Momentum distributions

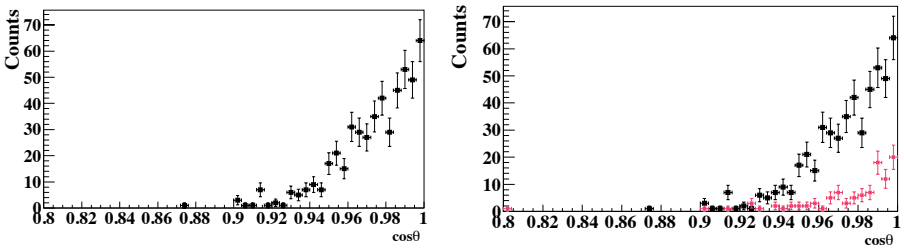

(b) Λ Angular distributions

Figure 4.55: Momentum and angular event distributions of the inclusive Λ measurement with background contribution indicated by red data points.

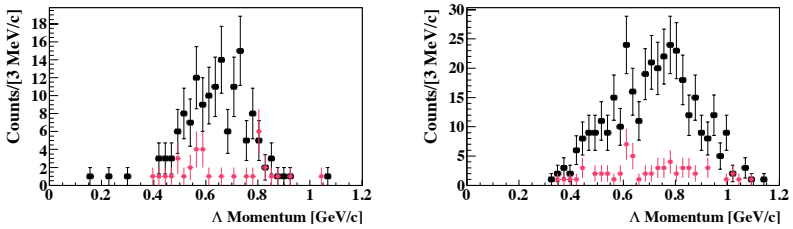

(a) Λ Momentum distributions

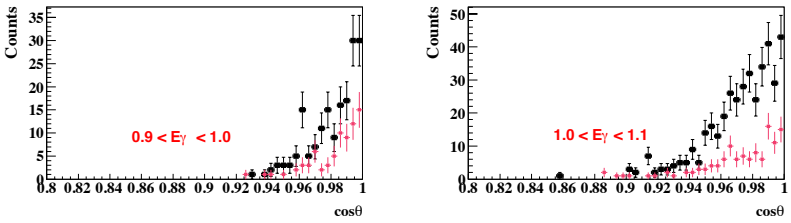

(b) Λ Angular distributions

Figure 4.56: Momentum distributions (a) and angular distributions (b) of the inclusive Λ measurement with background contribution indicated by red points for the energy bins of 0.9 $\leq$ E_γ $\leq$1.0 and 1.0 $\leq$ E_γ $\leq$1.1 GeV

bins of 0.9 $\leq$ E_γ $\leq$ 1.0 and 1.0 $\leq$ E_γ $\leq$ 1.1 GeV in Figure 4.56 left to right respectively. Next, we present the momentum distributions associated with the forward angular zones

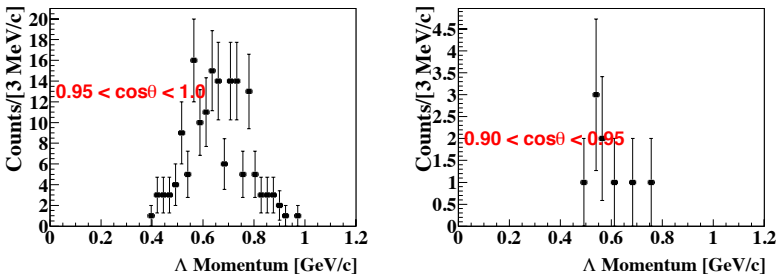

(a) $0.9 \leq E_\gamma \leq 1.0$ GeV

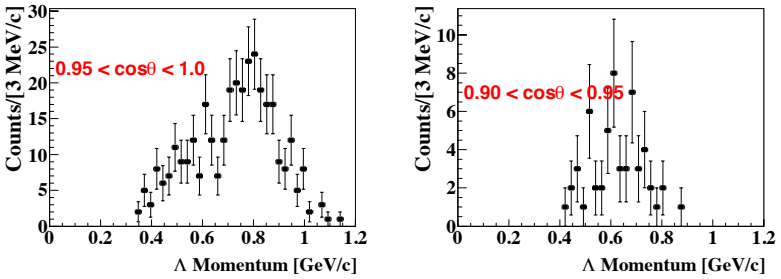

(b) $1.0 \leq E_\gamma \leq 1.1$ GeV

Figure 4.57: Momentum event distributions of Λ for the energy bins of (a) $0.9 \leq E_\gamma \leq 1.0$ GeV and (b)$1.0 \leq E_\gamma \leq 1.1$ GeV are shown. The results of the angular bins of $0.95 \leq \cos\theta_\Lambda^{LAB} \leq 1.0$ and $0.90 \leq \theta^{LAB} \leq .95$ and presented left to right.

of cos $0.95 \leq \cos\theta_\Lambda^{Lab} \leq 1.0$ and $0.90 \leq \cos\theta_\Lambda^{Lab} \leq .95$ are given in Figure 4.57, where the distribution for the angular regions are shown right to left and the increase in the energy bins progresses top to bottom. The measured momentum vs $\cos\theta_\Lambda^{Lab}$ event distributions of Λ in the laboratory frame are compared to the simulated distributions generated based on the KM hadronic model for the energy bins $0.8 \leq E_\gamma \leq 1.1$, $0.8 \leq E_\gamma \leq 0.9$, $0.9 \leq E_\gamma \leq 1.0$ and $1.0 \leq E_\gamma \leq 1.1$ GeV. Apparent in Figure 4.58 is the prediction of the correlation between the P_Λ^{LAB} and of the scattering angle, $\cos\theta_\Lambda^{LAB}$, shown as the black contour plots and measured distribution as the the colored contour plots respectively. This indicates an agreement in the expected distributions yielded from simulations and the experimentally measured data. The two dimensional plot displays the sufficient acceptance coverage of the NKS2+.

4.18 Summarization of Assorted Efficiencies

The assorted cuts that were applied to the data to achieve a clean invariant mass distribution invariably discards true Λ events, thus the efficiency of these requirements was ascertained and used as corrections in cross section calculations. The efficiency of the requirement was calculated as the number of identifiable Λ events with the cut and the

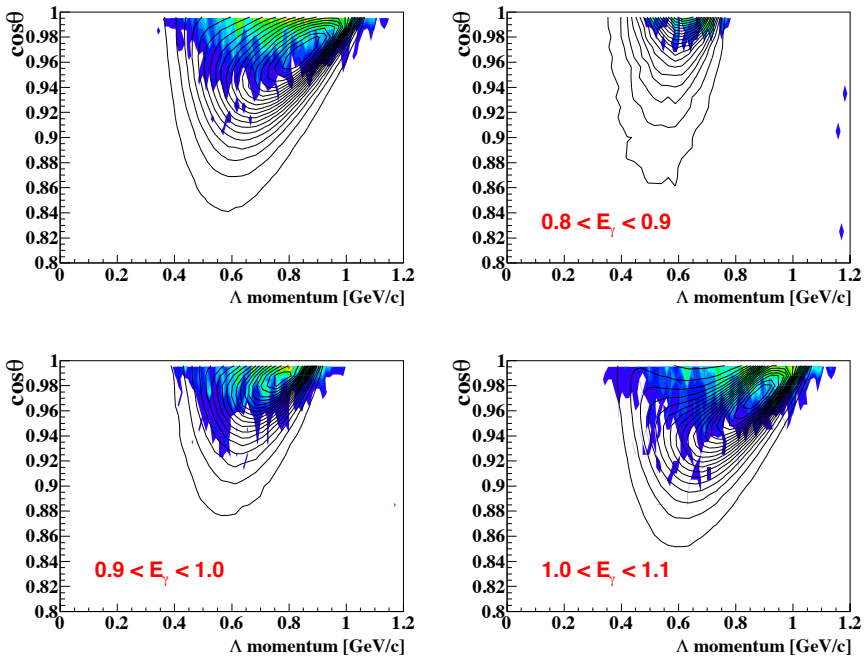

Figure 4.58: The measured Λ momentum distributions compared to simulated distributions generated based on KM for the energy bins $0.9-1.0, 0.8-0.9, 0.9-1.0$ and $1.0-1.1$ GeV. The simulated and measured distributions are shown as the black contour plots and the colored contour plots respectively.

number of Λ events prior to the application of the cut. This is essential in the accurate calculation of the cross section. The efficiency of a cut, in essence, is a measure of the survival ratio of Λ events with a cut applied is calculated by,

$$\varepsilon_i = \frac{N_\Lambda < cut_i}{(N_\Lambda < cut_i) + (N_\Lambda > cut_i)} \tag{4.37}$$

Where, $N_\Lambda > cut_i$ is the number of Λ events discarded by the cut, $N_\Lambda < cut_i$ is the number of events after the cut and i is the efficiency in question. A concise listing of the varied efficiencies which include the number of photons measured, the calculated number of taget deuterons, the data acquisition and the efficiencies of cuts are given in Table 4.7.

4.18.1 Efficiency of Distance Between Tracks Selection

The Λ yield as a function of the cut condition was evaluated firstly for the distance between reconstructed tracks from 0.5−5.0 cm, in increments of 0.5 cm. The distance between tracks stipulation, (DTB), used in the analysis and illustrated in Figure 4.38 was DTB ≤2.0 cm. In Figure 4.59 the yield is shown on the left, where the obvious rapid climb in yield for the cut conditions, DTB ≤3.0 cm, is apparent. Although for DTB ≥2.0 cm this tendency seems to quickly slow and appears to plateau. The Λ yield was normalized

to one at the value of DTB = 3.0 cm, and this provided the means to evaluate the relative yield given on the right in Figure 4.59. The efficiency as the function of distance between tracks was studied with the use of equation 4.37 for $0.5 \leq \text{DBT} \leq 5.0$ cm in 0.5 cm steps and the results are shown in Figure 4.60. The efficiency (ε_{DTB}) of the DTB $\leq$ 3.0 cm requirement of was 91.5 $\pm$ 1.0%.

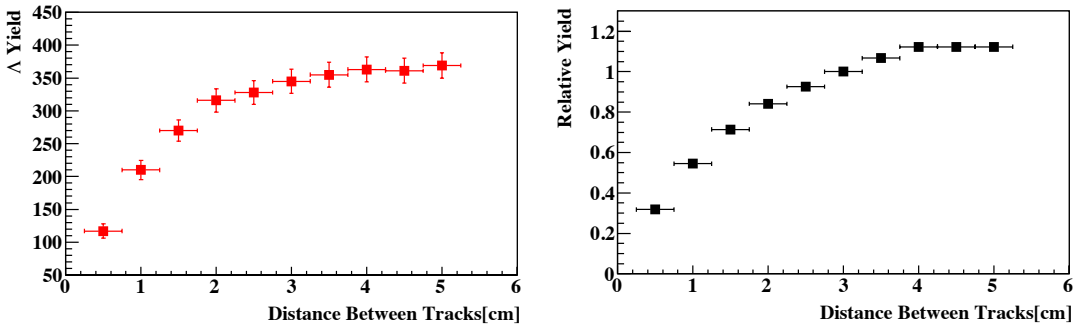

Figure 4.59: Λ total and relative yield as a function of the DTB cut.

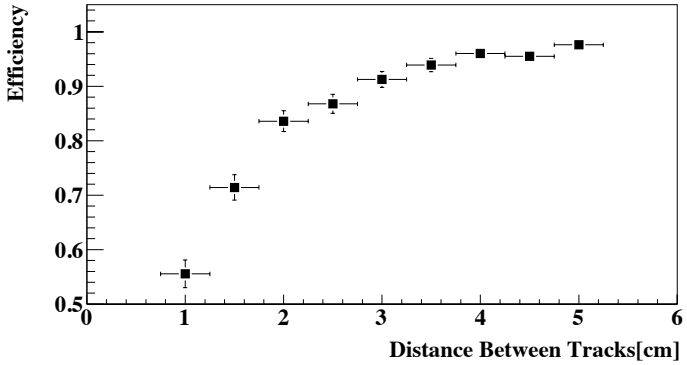

Figure 4.60: Efficiency (ε_{DTB}) of the distance between tracks cut.

4.18.2 Efficiency of Opening Angle Selection

The opening angle requirement associated with the detected charged particles was defined $-0.9 \leq \cos\theta_{OA} \leq 0.9$. The Λ yield as a function of the opening was studied is given on the left in Figure 4.61 for steps of $\cos\theta$ bins = 0.02. The relative yield normalized to 1 at $-0.9 \leq \cos\theta_{OA} \leq 0.9$ is illustrated on the right. Appropriating the method used in the discussion of the DTB cut, and equation 4.37, the results regarding the efficiency dependence as a function of the opening angle cut is present in Figure 4.62. The computed efficiency (ε_{OA}) of the designated opening angle cut was found to be 97.5% $\pm$ 1%.

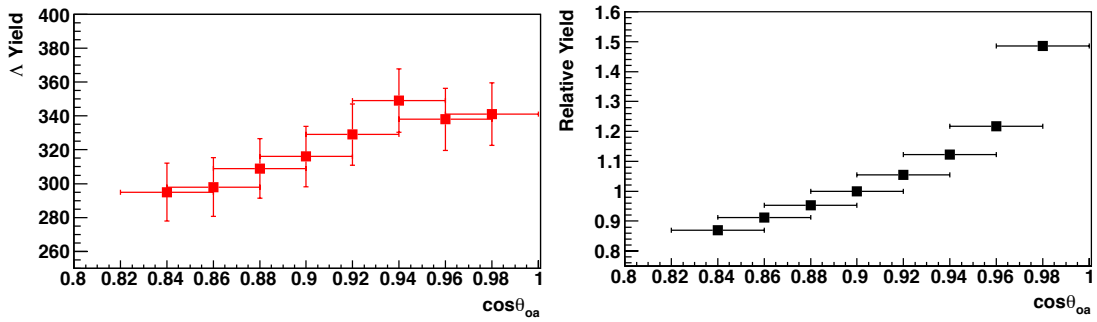

Figure 4.61: Λ total and relative yield as a function of the opening angle selection

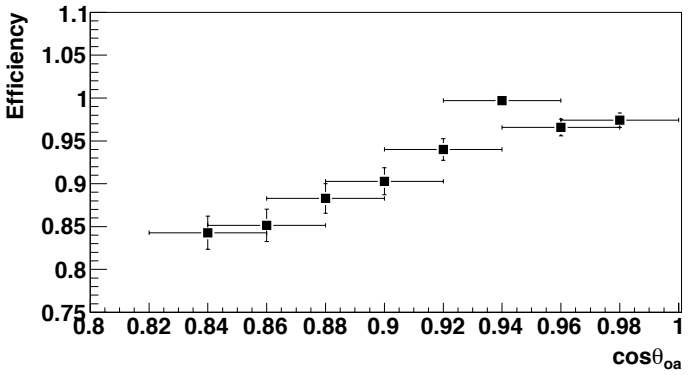

Figure 4.62: Efficiency ($\varepsilon_{\mathrm{OA}}$) of the opening angle cut.

4.18.3 Efficiency of χ^2 Selection

The estimation of the efficiency of the χ^2 requirement with an additional cut on the number of hits in the reconstructed track ≥ 6 was evaluated for stages of 1. The method followed the same outline as introduced in equation 4.37. The relation between the of Λ yield and the χ^2 selection was estimated ranging from 5 $\chi^2 \leq 15$. The relative yield was normalized to 1 at $\chi^2 \leq 10$. The total and relative Λ yield can be seen left to right respectively in Figure 4.63. The cut efficiency as a function of the χ^2 requirement is present in Figure 4.64. The efficiency of the χ^2 requisite (ε_{χ^2}) was estimated to 97.5% ± 1%.

4.18.4 Efficiency of MHL Selection

A sizable number of recorded multiple hits on the layers of the drift chambers were repudiated for the purpose of minimizing the analysis time. The number of accepted events identified with $\pi^+\pi^-$ or $\mathrm{p}\pi^-$ was MHL ≤ 20. In the evaluation of the MHL efficiency, the tagger time selection, the opening angle, IH distance, and χ^2 stipulations were included. The relative yield is normalized to one at MHL $\leq$20 and the results for $\pi^+\pi^-$ or $\mathrm{p}\pi^-$

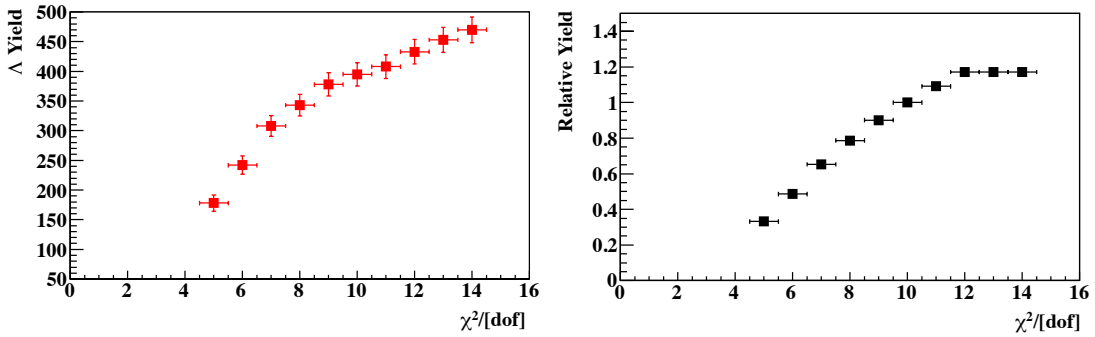

Figure 4.63: Λ total and relative yield of as a function of the χ^2selection

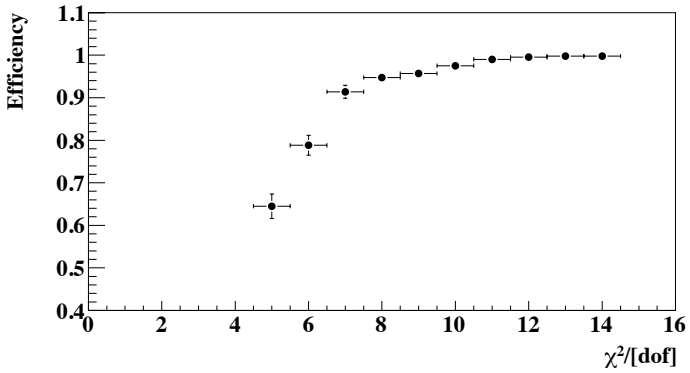

Figure 4.64: Efficiency of the χ^2 cut.

presented in Figure 4.65, top and bottom panel respectively. The increased relative yield was fitted by an exponential function, and the efficiency was extracted by the integration the function from 21≤MHL ≤ ∞. The efficiency of the multiplicity of hits ($\varepsilon_{\mathrm{MHL}}$) was determined as 99.5% ± 1%.

4.18.5 Other Efficiencies

The efficiency of the accepted $p\pi^-$ invariant mass($\varepsilon_{\mathrm{IM}}$) defined by equation 4.34 was estimated to be 98.9% ± 2%. The efficiency of the number of hits required to reconstruct as track($\varepsilon_{\mathrm{hits}}$) was calculated as 98.3% ± 2%. The uncertainty of number of photons irradiated on the target which is proportionally to the number of recorded scalar hits in TagF (N_γ) was straightforwardly found as the square root of the counts $\sqrt{N_\gamma}$. A complete listing of the variable that are considered in the cross section determination and the corresponding uncertainties are listed in Table 4.7.

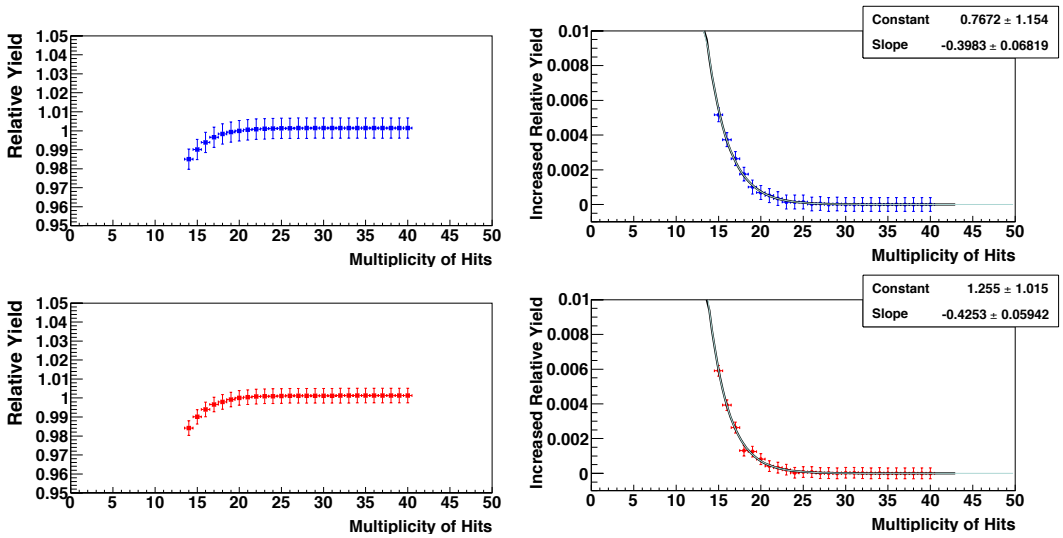

Figure 4.65: The relative sand increase relative yield of $\pi^+\pi^-$ or $p\pi^-$ events given, where is he relative yield is normalized to one for MHL $\leq$20.

4.19 Acceptance Calculation

The acceptance of Λ for the NKS spectrometer is seen in Figure 4.68. The acceptance was calculated by using the analogous analyzer that was utilized for the experimental data set but for the data generated through simulation is shown in Figure 4.68 in the lower left figure. Mathematically the acceptance is the ratio of the triggered or reconstructed Λ events including the efficiencies of various detector components to the generated events in the same kinematical bins.

$$\tilde{a} = \frac{N_{\text{trig}}}{N_{\text{gen}}} \tag{4.38}$$

N_{trig} is the sum of the Λ histogram events within the appropriate kinematical range. N_{gen} is the number of Λ histogram events that were generated isotropically in the laboratory frame of reference. The uncertainty in the acceptance value was calculated as:

$$d\tilde{a} = \sqrt{\frac{\tilde{a}(1-\tilde{a})}{N_{\text{gen}}}} \tag{4.39}$$

The K^0 acceptance of NKS2+ spectrometer as predicted by the KM model is shown in Figure 4.66. The figure presents the acceptance of K^0 as a three-dimensional (upper left) and contour (upper right). The contour plots in the lower panel are of the K^0 acceptance for the energy bins 0.9 $\leq$ E_γ $\leq$1.0 and 1.0 $\leq$ E_γ $\leq$1.08 GeV left to right respectively.

Table 4.7: Listing of efficiencies

General Efficiencies			Uncertainty	
accronym	article	value	statistical	systematic
N_{target}	effective number of target [b^{-1}]	0.168	<1%	2.5%
N_{γ}	recorded hits in TagF scaler	1.34 $\times 10^7$	3.6 $\times 10^3$	2.1%
ε_{DAQ}	DAQ efficiency	62%	-	-
ε_{MHL}	multi-hit efficiency	99.5%	<1%	7%
$\varepsilon_{tagging}$	tagging efficiency	79%	<5%-	8%
	Inclusive Λ measurement			
ζ^{Λ}	Branching ratio of $\Lambda \rightarrow p + \pi^-$	63.9 %	-	$\pm$0.5%
ε_{IM}	Invariant mass selection	98.9%	<1%	1%
ε_{OA}	opening angle	97.5%	1%	3%
ε_{DTB}	distance between tracks	91.5%	<1%	-%
$\varepsilon_{hododist}$	hodoscope distance	98.8%	<2%	-%
ε_{χ^2}	χ^2 selection efficiency	97.5%	<1%	-%
ε_{hits}	hits in track selection	98.3%	<2%	-%

The generated Λ acceptance of upgraded NKS2+ spectrometer based on the KM model are shown in Figure 4.67, where the three-dimensional acceptance (upper left) and contour plot (upper right) are illustrated in upper panel. The energy bins 0.9 $\leq E_{\gamma} \leq$1.0 and 1.0 $\leq E_{\gamma} \leq$1.08 GeV left to right respectively in the lower panel.

Λ acceptance as a function of momentum (P_{Λ}^{LAB}) for angular integration bin $\cos\theta_{\Lambda}^{LAB}$ = 0.75 − 1.0 is given in Figure 4.68, which was generated using the analogous analyzer that was used for the analysis experimental data and for the data generated by GEANT4 simulation. A three dimensional presentation of the NKS2+ acceptance for Λ is shown in the top left panel, and the two dimensional contour plots is on the top right. A comparison of the calculated acceptance and the KM predicted P_{Λ}^{LAB} vs $\cos\theta_{\Lambda}^{LAB}$ histogram in Figure 4.69 clearly demonstrates the Λ acceptance coverage of the NKS2+. The decay particle of protoproduced Λ hyperon will surely be detected by in the spectrometer. The momentum dependence of Λ acceptance was computed for various angular regions. The generated Λ acceptance as a function of momentum for angular integration bins corresponding to $\cos\theta_{\Lambda}^{LAB}$ = (a) 0.95 − 1.0, (b) 0.90 − 0.95, (c) 0.85 − 0.90, and (a) 0.80 − 0.85, is shown in Figure 4.70 top left to bottom right respectively. Lastly, the angle dependence on the acceptance was explored for several photons energy bins. The results of the Λ acceptance as a function of $\cos\theta_{\Lambda}$ for energy bins in the laboratory frame of reference (a) .95−1.00 , (b) 1.00−1.02, (c) 1.02−1.04, (d) 1.04−1.06, and (e) 1.06−1.08 GeV are shown in Figure 4.71 top left to bottom left respectively.

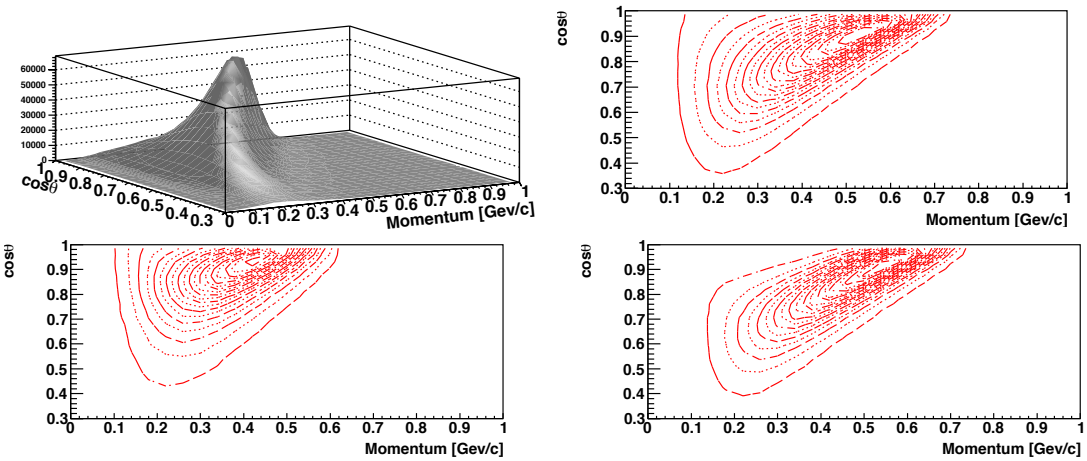

Figure 4.66: K^0 acceptance predictions based on KM are given as a three-dimensional (upper left) and contour plot (upper right). The lower panel are the energy bins $0.9 \leq E_\gamma \leq 1.0$ and $1.0 \leq E_\gamma \leq 1.08$ GeV left to right respectively.

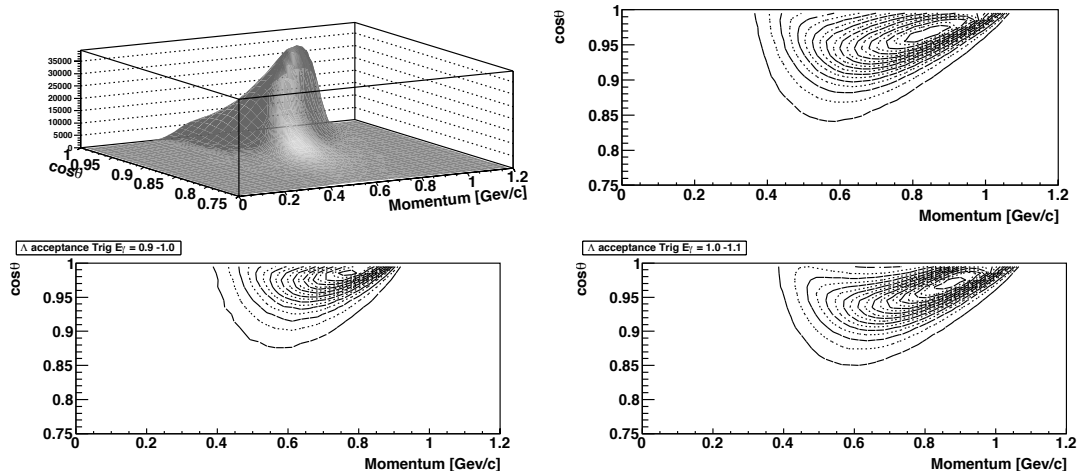

Figure 4.67: Λ acceptance distributions based on KM are given as a three-dimensional (upper left) and contour plot (upper right). The lower panel are the energy bins $0.9 \leq E_\gamma \leq 1.0$ and $1.0 \leq E_\gamma \leq 1.08$ GeV left to right respectively.

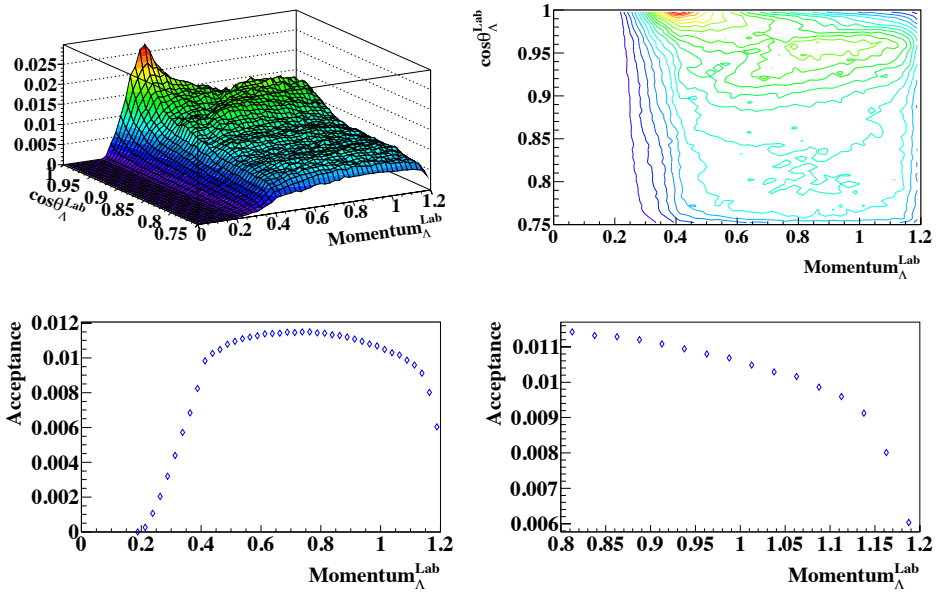

Figure 4.68: Λ acceptance as a function of momentum (P_Λ^{LAB}) for the angular bin of $\cos\theta_\Lambda^{LAB}$ = (0.75 − 1.0). This was calculated by using the identical analyzer that was used for the experimental data and for the data generated by GEANT4 simulation.

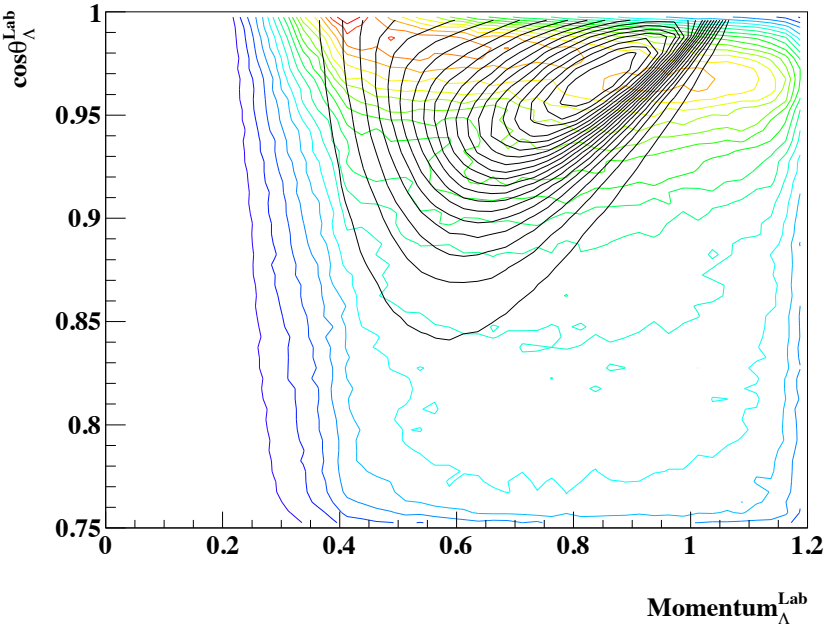

Figure 4.69: Comparison of acceptance predicted by KM and NKS2+

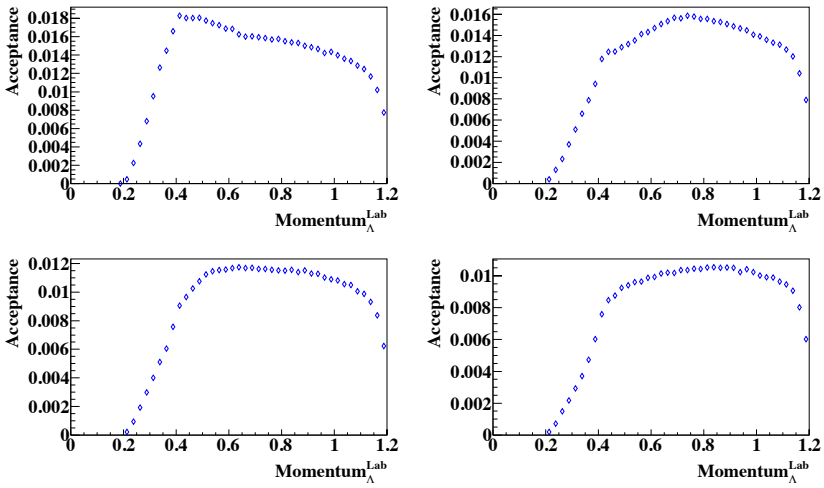

Figure 4.70: Λ acceptance as a function of momentum (P^{LAB}_{Λ}) for angular integration bins of $\cos\theta^{LAB}_{\Lambda}$ = (a) $0.95 - 1.0$, (b) $0.90 - 0.95$, (c) $0.85 - 0.90$, and (d) $0.80 - 0.85$.

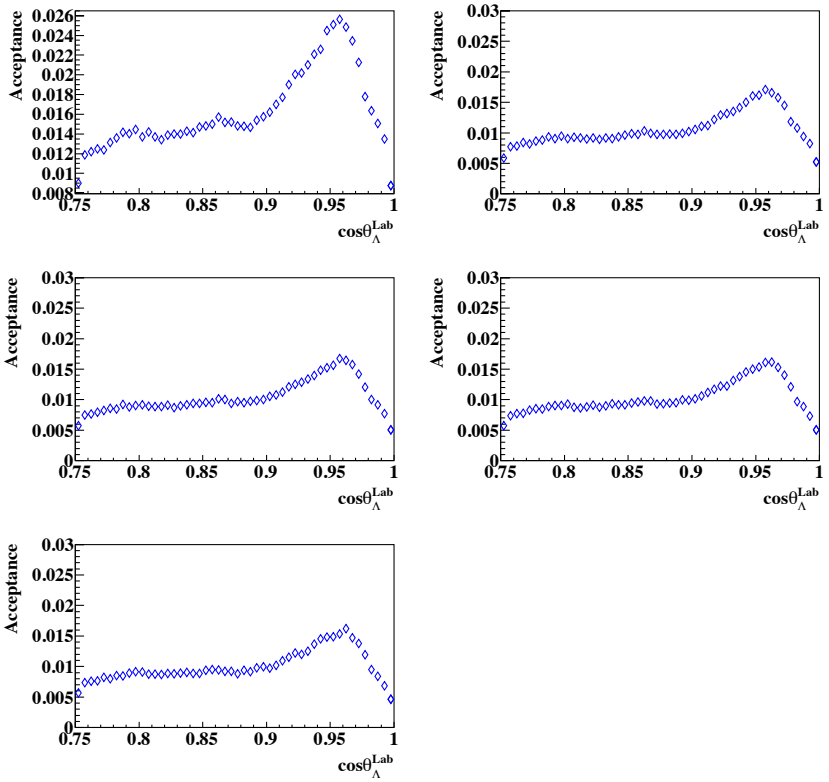

Figure 4.71: Λ angular acceptance as a function of $\cos\theta^{LAB}_{\Lambda}$ for energy bins (a) 0.95−1.00, (b) 1.00−1.02, (c) 1.02−1.04, (d) 1.04−1.06, and (e) 1.06−1.08 GeV.

CHAPTER

FIVE

EXPERIMENTAL FINDINGS

> In order to transform the world about us, with its misery, wars, unemployment, starvation, class divisions, and utter confusion, there must be a transformation in ourselves. The revolution must begin within ourselves but not according to any belief or ideology, because revolution based on an idea, or in conformity to a particular pattern, is obviously no revolution at all. To bring about a fundamental revolution in oneself, one must understand the whole process of one's thought and feeling in relationship. That is the only solution to all our problems, not to have more disciplines, more beliefs, more ideologies and more teachers. If we can understand ourselves as we are from moment to moment without the process of accumulation, then we shall see how there comes a tranquility that is not a product of the mind, and only in that state of tranquility can there be creativeness.

Jiddu Krishnamurti

5.1 Overview

In the following chapter, a description of the numerical calculation of the differential cross section will be addressed. Next the experimental results of the inclusive Λ measurement on a deuteron, which includes the Λ momentum distribution will be presented graphically. This is followed by the results of the calculated integrated cross sections, the estimated total cross section, angular distribution as a function of the scattering angle and polarization determination. The chapter concludes with a comparison of the results of this work to previous NKS2 collaboration measurements [4, 5].

5.2 Differential Cross Section

In the previous chapter the procedure concerning the extraction of the photoproduced Λ was described in detail. In photonuclear reactions, the term cross section is used to define the probability of an event occurring, which for scattering experiments is a measurement of the probability of two particles colliding, and resulting in the desired reaction products. This typically refers to the probability per target nucleus [77]. The symbol most often associated with a cross section measurement or calculation is the quantity σ, a non-sensical area measurement, that must be correlated to the cross sectional area of a nucleus. Most nuclear reactions do not proceed in uniform way with respect to the encroaching beam. In this framework, the measurement of the number of generated particles per unit time dN, as seen by a detector covering a specific solid angle $d\Omega$ and some angle ϕ, with respect to the beam is defined as the differential cross section $d\sigma/d\Omega$.

The total cross can obtained from the integration over the entire solid angle and ranges of energies and is defined as,

$$\sigma = \int_{allspace} \frac{d\sigma}{d\Omega} d\Omega \tag{5.1}$$

The differential cross sections for the inclusive measurement of the Λ can be calculated from experimentally measured variables as:

$$\frac{d\sigma}{dpd\Omega} = \frac{N^{\Lambda}_{\text{yield}}(p, cos\theta)}{N_{\gamma} \cdot N_{\text{target}} \cdot \varepsilon^{\Lambda}_{\text{accept}}(p, cos\theta) \cdot \zeta^{\Lambda} \cdot \varepsilon^{\Lambda}_{\text{GE}} \cdot \varepsilon^{\Lambda}_{\text{specific}} \cdot 2\pi d(cos\theta)} \tag{5.2}$$

where $N^{\Lambda}_{\text{yield}}$ is the yield of Λ events, N_{γ} the number of the incidents photons, and N_{target} is the number of target deuterons. The branching ratio for the decay mode, $\Lambda \rightarrow p\pi^{-}$, is represented by ζ^{Λ}. The term $\varepsilon^{\Lambda}_{\text{GE}}$ refers to the efficiencies that are universal to the spectrometer, while on the other hand, the term $\varepsilon^{\Lambda}_{\text{specific}}$ denotes the efficiencies that are intrinsic to the inclusive Λ measurement. The calculation of $\varepsilon^{\Lambda}_{\text{GE}}$ follows,

$$\varepsilon^{\Lambda}_{\text{GE}} = \varepsilon_{\text{DAQ}} \cdot \varepsilon_{MHL} \cdot \varepsilon_{\text{tagging}} \cdot \varepsilon^{ana}_{\text{tagging}} \tag{5.3}$$

The calculation of $\varepsilon^{\Lambda}_{specific}$ is performed as,

$$\varepsilon^{\Lambda}_{\text{specific}} = \varepsilon_{OA} \cdot \varepsilon_{\text{DTB}} \cdot \varepsilon^{\text{hodo}}_{\text{dist}} \cdot \varepsilon_{\chi^2} \cdot \varepsilon_{\text{track}} \tag{5.4}$$

The inputed values for all efficiencies are listed in Table 4.7. It should be noted that in equation 5.2 the acceptance is referred to as $\varepsilon^{\Lambda}_{\text{accept}}(p, cos\theta)$ while in equation 4.38 it was denoted as $\tilde{a}$.

5.3 Integrated Cross Section

Although the differential cross section is typically of interest, the integrated cross section likewise imparts useful information. Starting from the differential cross section defined in equation 5.2, the integrated cross section for the inclusive measurement of the Λ can be found as,

$$\sigma = \frac{2\pi \int\int\int \frac{d\sigma}{d\Omega dp} \cdot d(\cos_\theta) dp dE_\gamma}{\int dE_\gamma} \tag{5.5}$$

This formula permits the calculation of the total cross section (σ), or a simply the integration over the desired momentum or angular range. Below is an explanation of how this can be exploited to obtain the momentum or angle dependent integrated cross sections.

5.4 Momentum and Angular Distributions

In the following brief section the formalism adopted for the calculation of the momentum and angle dependent integrated cross sections is outlined. The measured momentum and angular distributions are calculated as follows,

$$\left.\frac{d\sigma}{dp}\right|_{Lab} = \frac{2\pi \int\int \frac{d\sigma}{d\Omega dp} \cdot d(\cos_\theta) dE_\gamma}{\int dE_\gamma} \tag{5.6}$$

where the polar angle (ϕ) integration yielded the 2π term taken outside of the integral. The integration over θ will span the limited acceptance hemisphere of the NKS+ spectrometer.

$$\left.\frac{d\sigma}{d\Omega}\right|_{Lab} = \frac{\int\int \frac{d\sigma}{d\Omega dp} \cdot dp dE_\gamma}{\int dE_\gamma} \tag{5.7}$$

Equations 5.5, 5.6 and 5.7 have amply detailed the mathematical approach used to determine the physical observables that will be discussed at length in sections 5.6.1, 5.6.2 and section 5.7.

5.5 Yield Extraction

In order to calculate the energy, momentum, or angular dependence of Λ photoproduction, it is necessary to acquire the yield of Λ ($N^{\Lambda}_{\text{yield}}$) for each of the conditions in which one will evaluate its dependence as defined in equation 5.2. The yield was calculated as the integral of Λ events for the accepted sector,

$$\Lambda_{yield} = IM^{\Lambda}_{\text{accepted}} - BG^{f}_{SA} \tag{5.8}$$

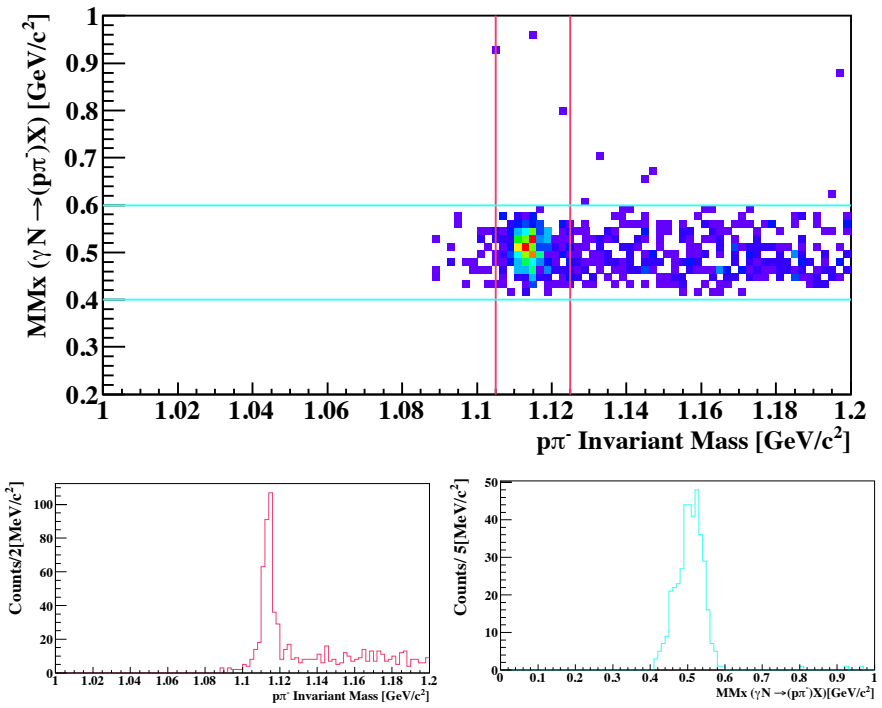

Figure 5.1: A scatterplot of the $p\pi^-$invariant mass vs. accepted missing mass ($\gamma d \rightarrow p\pi^- X$) region for Λ yield extraction. The projections of each are shown in the lower panel, where the color of the histograms indicates the projection related to the drawn accepted regions.

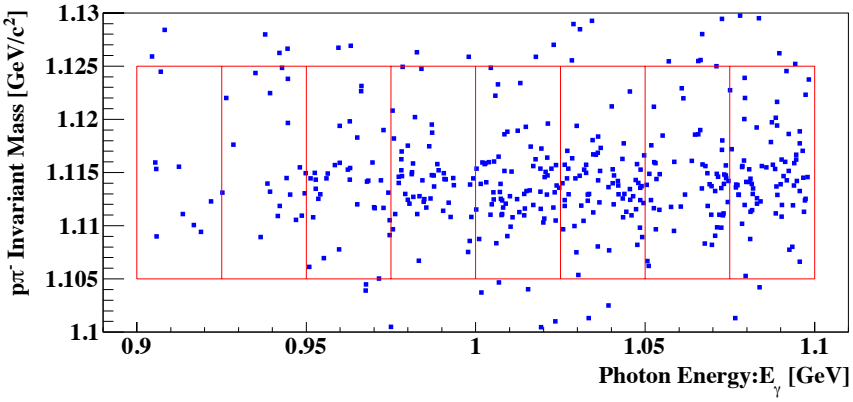

Figure 5.2: Λ Invariant mass plotted against the incident photon energy for the angular region of $0.75 \leq \cos\theta_{\Lambda}^{LAB} \leq 1.0$. The number of Λ was extracted for each of the bins indicated by the red rectangular sectors.

The accepted Λ region for yield extraction displayed in the two dimensional histogram in Figure 5.1, which depicts the $p\pi^-$invariant mass versus missing mass of $\gamma d \rightarrow p\pi^- X$ spectra. The accepted area for the invariant and missing mass are between the red and

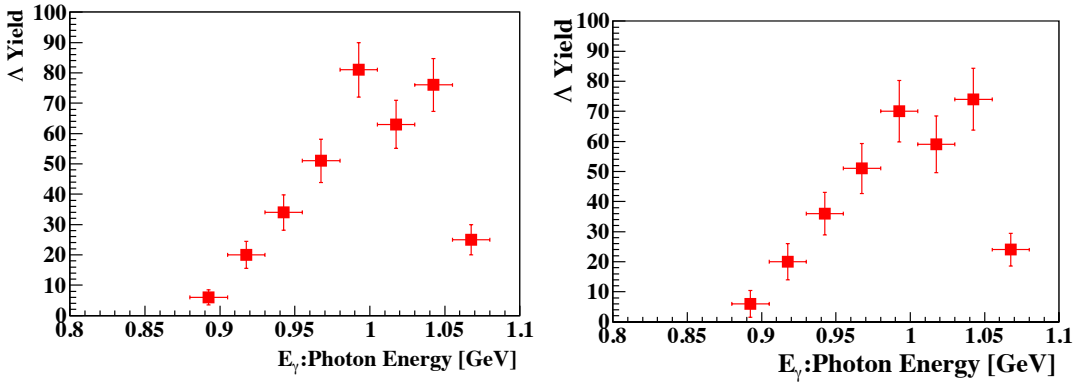

Figure 5.3: Extracted Λ yield as a function of photon beam energy for the angular region of $0.75 \leq \cos\theta_{\Lambda}^{LAB} \leq 1.0$ (left) and $0.90 \leq \cos\theta_{\Lambda}^{LAB} \leq 1.0$ (right).

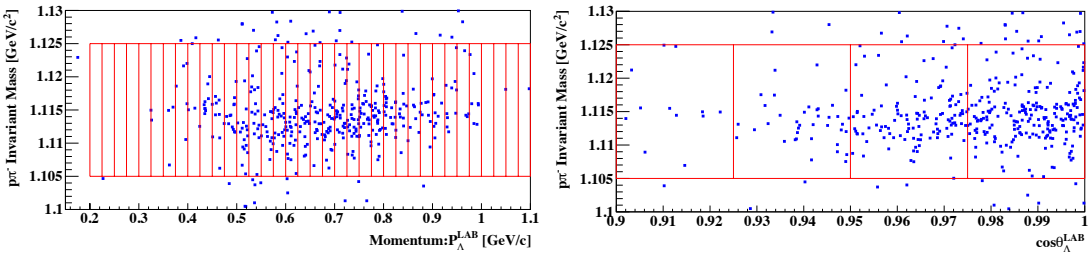

Figure 5.4: Λ invariant mass vs momentum (left) and $\cos\theta_{\Lambda}^{LAB}$ (right). The number of Λ was extracted for each of the bins indicated by the red rectangular sectors.

light blue parallel lines respectively. The projections of each are shown in the lower panel where the color of the histograms indicates the projection related to the drawn colored accepted regions. Firstly, the yield of Λ was extracted in energy bins for the angular regions of $0.75 \leq \cos\theta_{\Lambda}^{LAB} \leq 1.0$ and forward angular region of $0.9 \leq \cos\theta_{\Lambda}^{LAB} \leq 1.0$. The energy bins for the excitation calculation are shown in Figure 5.2 as the red boxed sectors, where the invariant mass plotted against the incident photon energy for the angular region of $0.75 \leq \cos\theta_{\Lambda}^{LAB} \leq 1.0$. The two dimensional color contour plot reveals the density distribution of the produced Λ as photon energy extends into a higher region.

The yield as a function of the incident photon energy for the entire accepted angular range (left) and the forward area (right) is showcased in Figure 5.3 as the solid red squares, and was determined as the total counts under the accepted Λ peak minus the total counts from the selected background continuum that was extensively detailed in section 4.15 and defined by equations 4.33 and 4.35. The yield grows with the increased photon energy up to 1.0 GeV after which it rapidly declines. This tendency is consistent in both angular regions, however the measured yield is marginally larger in the full angular range. The

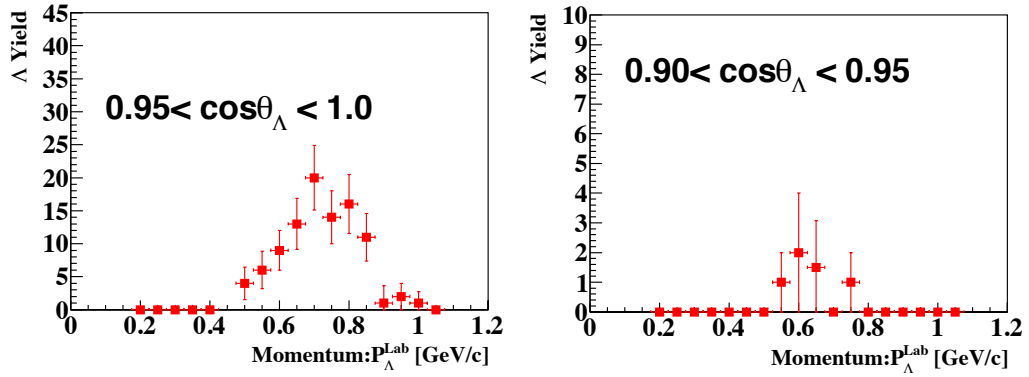

(a) $0.9 \leq E_\gamma \leq 1.0$ GeV

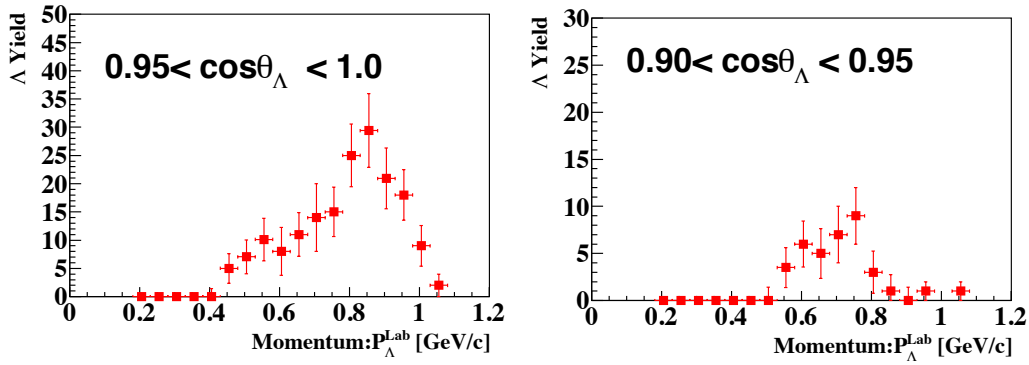

(b) $1.0 \leq E_\gamma \leq 1.1$ GeV

Figure 5.5: Extracted Λ yield as a function of momentum as measured in the laboratory frame for an incoming photon beam energy of $0.9 \leq E_\gamma \leq 1.0$ GeV (top row) and $1.0 \leq E_\gamma \leq 1.1$ GeV (bottom row). The angular bins of $\cos\theta_\Lambda^{LAB} = 0.95 - 1.0$, $0.9 - 0.95$ are shown from left to right respectively.

statistical errors, Poissonian in nature, were determined by standard error propagation, in which the error in the counts from the integration of the area under the peak and the background are simply their respectively square roots $\sqrt{N}$. The details of the yield of Λ for each bombarding photon energy bin along with the signal to noise is listed in Table 5.1.

We next proceed to obtain the momentum dependence of the yield in the laboratory frame where $N^{\Lambda}_{\text{yield}}$ is extracted for each rectangular bin drawn in Figure 5.4 (left). The method outlined above is used to calculate the yield for the momentum span ranging from $0.2 \leq |P|_\Lambda^{Lab} \leq 1.1$ in $|P|_\Lambda$ bins $= 0.05$ in the two angular sections of $0.95 \leq \cos\theta_\Lambda^{LAB} \leq 1.0$ and $0.90 \leq \cos\theta_\Lambda^{LAB} \leq 0.95$. Two photon energy bins are analogous to $0.9 \leq E_\gamma \leq 1.0$, (a) upper, and $1.0 \leq E_\gamma \leq 1.1$ GeV(b) lower panel, and the results are presented in Figure 5.5 as the solid red squares, where the errors are calculated by customary error propagation.

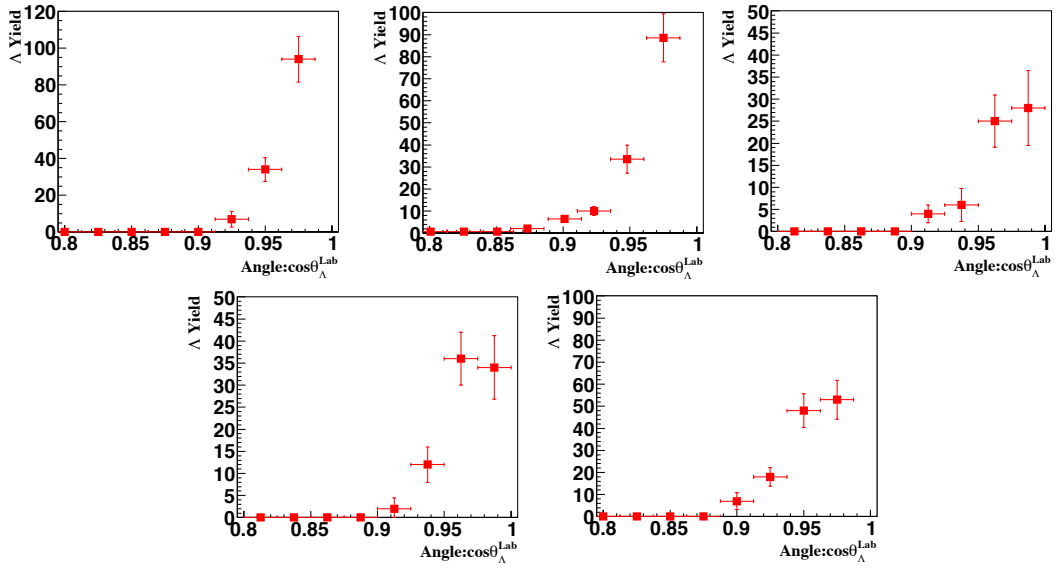

Figure 5.6: Extracted Λ yield as a function of $\cos\theta_{\Lambda}^{LAB}$ as measured in the laboratory frame for the energy bins 0.95≤ E_γ ≤ 1.00, 1.00≤ E_γ ≤1.02, 1.02 ≤ E_γ ≤ 1.04, 1.04 ≤ E_γ ≤ 1.06, and 1.06 ≤ E_γ ≤1.08 GeV are presented top left to bottom right respectively.

The details of the the momentum dependent yield for both energy bins can be found in Tables 5.2 and 5.3.

Lastly the yield of Λ was obtained for the calculation of the angular distributions defined in equation 5.7. It follows directly that the yield of Λ as a function of the scattering angle be gathered. It was desired to extract the values over the angle sector of 0.90 ≤ $\cos\theta_{\Lambda}^{LAB}$≤ 1.0 in $\cos\theta_{\Lambda}^{LAB}$ bins = 0.025 GeV/c, shown in for each bin in drawn in Figure 5.4 (right), for five photon energy bins. The photon energy bins were 0.95≤ E_γ ≤ 1.00, 1.00 ≤ E_γ ≤ 1.02, 1.02 ≤ E_γ ≤ 1.04, 1.04 ≤ E_γ ≤1.06, and 1.06 ≤ E_γ ≤ 1.08 GeV. The invariant mass distributions of the numerous extraction bins can be reviewed in Appendix D.

5.6 Inclusive Λ measurement

5.6.1 Momentum Distribution

The energy averaged angle integrated inclusive differential cross of Λ in the $\gamma d \rightarrow \Lambda X$ reaction as a function of momentum (P_{Λ}^{LAB}) ,before background subtractions are performed are shown in Figure 5.7. The background contribution is shown as red solid squares and are attributed to the background areas discussed in extensive details in section 4.15. The upper row are the results for the lower photon energy regime of 0.9 ≤ E_γ ≤ 1.0 while the lower row are for incident photon energies of 1.0 ≤ E_γ ≤ 1.1 GeV. The momentum

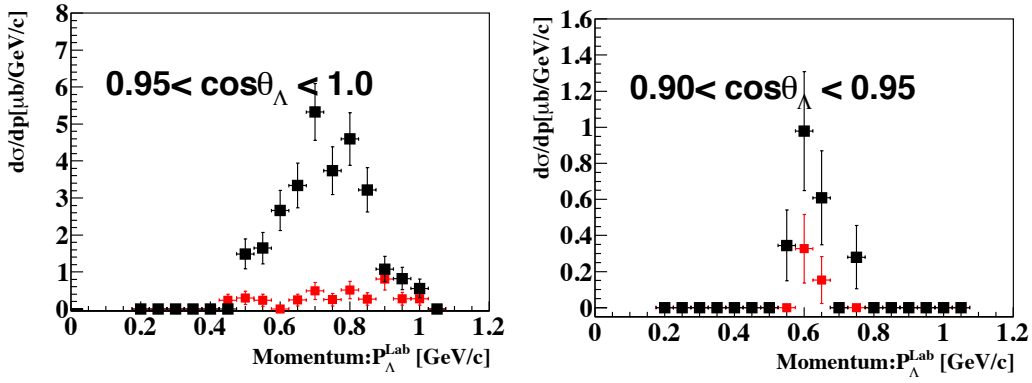

(a) $0.9 \leq E_\gamma \leq 1.0$ GeV

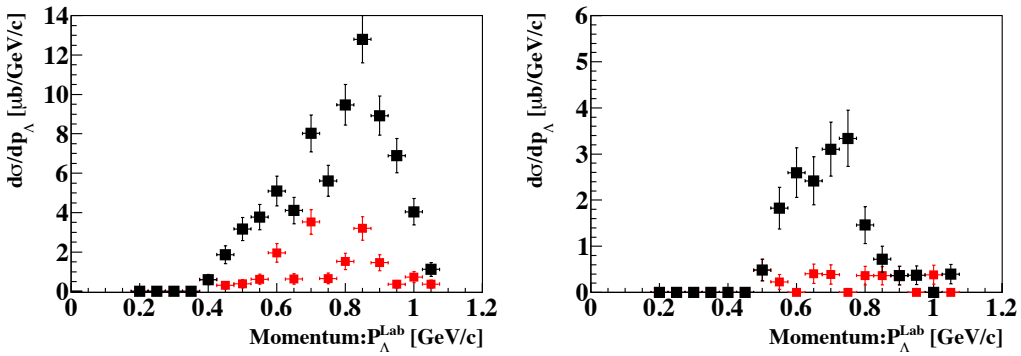

(b) $1.0 \leq E_\gamma \leq 1.1$ GeV

Figure 5.7: Differential cross section of Λ in the $\gamma d \rightarrow \Lambda X$ reaction as a function of momentum in the energy bins of $0.9 \leq E_\gamma \leq 1.0$ (upper) and $1.0 \leq E_\gamma \leq 1.1$ GeV (lower) . The background contribution is shown as red solid squares. The angular bins of $\cos\theta_\Lambda^{LAB} = 0.95 - 1.0$ and $0.9 - 0.95$ are left to right respectively.

integrated angular bins are $d(cos_\Lambda^{Lab}) = 0.05$ in the lab system. The errors in the figure are only statistical in nature. Following the subtraction of the background contribution indicated by the red squares in Figure 5.7, the differential cross section of γd$\rightarrow\Lambda$X reaction as a function of momentum in the energy bins of $0.9 \leq E_\gamma \leq 1.0$ (upper) and $1.0 \leq E_\gamma \leq 1.1$ GeV (lower) are presented in Figure 5.8, the errors reported are statistical only and are estimated to be less than 20%. The angular of bins of $0.95 \leq \cos\theta_\Lambda^{LAB} \leq 1.0$ and $0.90 \leq \cos\theta_\Lambda^{LAB} \leq 0.95$ are seen left to right in the figure. The angle integrated momentum dependent cross section are shown to prominent at forward angle $0.95 \leq \cos\theta_\Lambda^{LAB} \leq 1.0$ exhibiting more or less a four-fold larger magnitude.

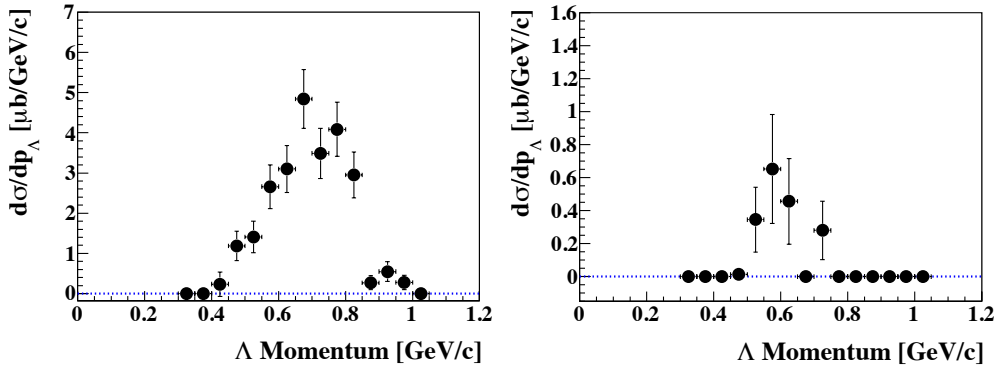

(a) $0.9 \leq E_\gamma \leq 1.0$ GeV

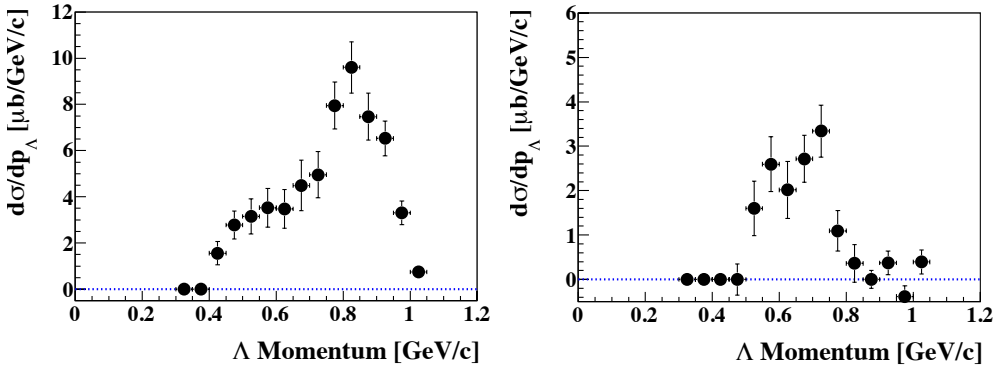

(b) $1.0 \leq E_\gamma \leq 1.1$ GeV

Figure 5.8: Background subtracted differential cross section of Λ in the γd→ΛX reaction as a function of momentum in the energy bins of $0.9 \leq E_\gamma \leq 1.0$ (upper) and $1.0 \leq E_\gamma \leq 1.1$ GeV (lower). The angular bins of $0.95 - 1.0$ and $0.9 - 0.95$ are left to right respectively

5.6.2 Angular Distribution

The cross section as a function of the Λ scattering angle in the laboratory frame of reference was determined by eq 5.7 for five bins. The resulting angular distributions of Λ in the $\gamma d \rightarrow \Lambda X$ reaction in the energy regions of $0.95 - 1.00, 1.02 - 1.04, 1.04 - 1.06, 1.06 - 1.08$ GeV can be seen in Figure 5.9 top left to bottom respectively as the black squares with corresponding background shown as the red squares. The background subtracted distributions are given in Figure 5.10, presented in a format akin to Figure 5.9, in the lower energy regime, climbs steadily as the angles shrinks. This is in contrast to higher energies where the distribution peak reduces for small angles.

The data reveals that the cross sections of $d(\gamma, \Lambda)KN$ are concentrated at laboratory angles of $\cos\theta_\Lambda^{LAB} \geq 0.85$, therefore the ability to measure the total cross of $\gamma d \rightarrow \Lambda X$ is feasible with a spectrometer capable of measuring these small angles [83].

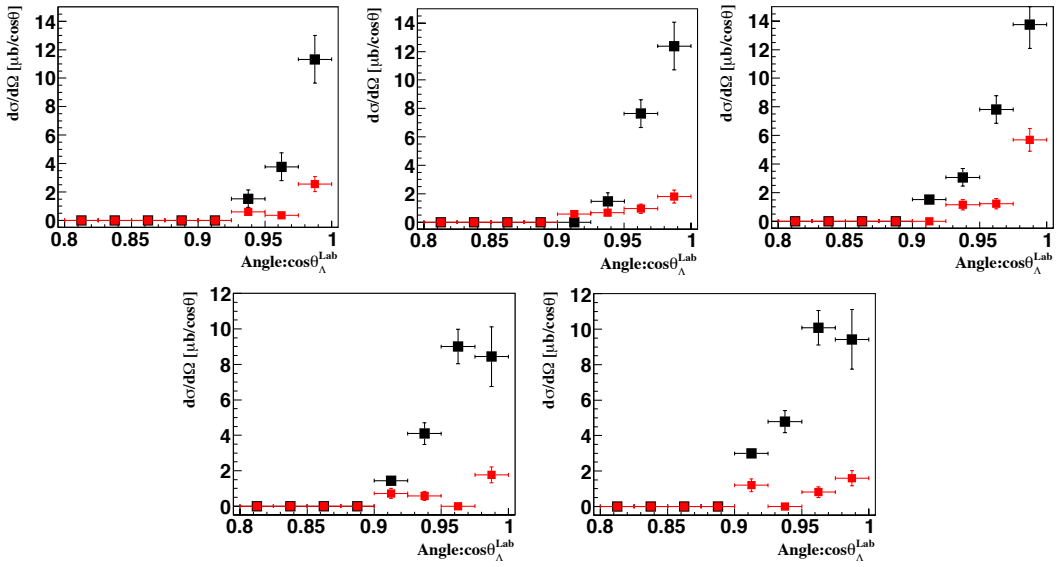

Figure 5.9: Angular distribution of the inclusive measurement of Λ in the $\gamma d \rightarrow \Lambda X$ reaction in the energy regions of $0.95-1.0, 1.02-1.04, 1.04-1.06$, and $1.06-1.08$ GeV, presented top left to bottom respectively, prior to background subtractions shown as the black squares. The background contributions are shown as the solid red squares.

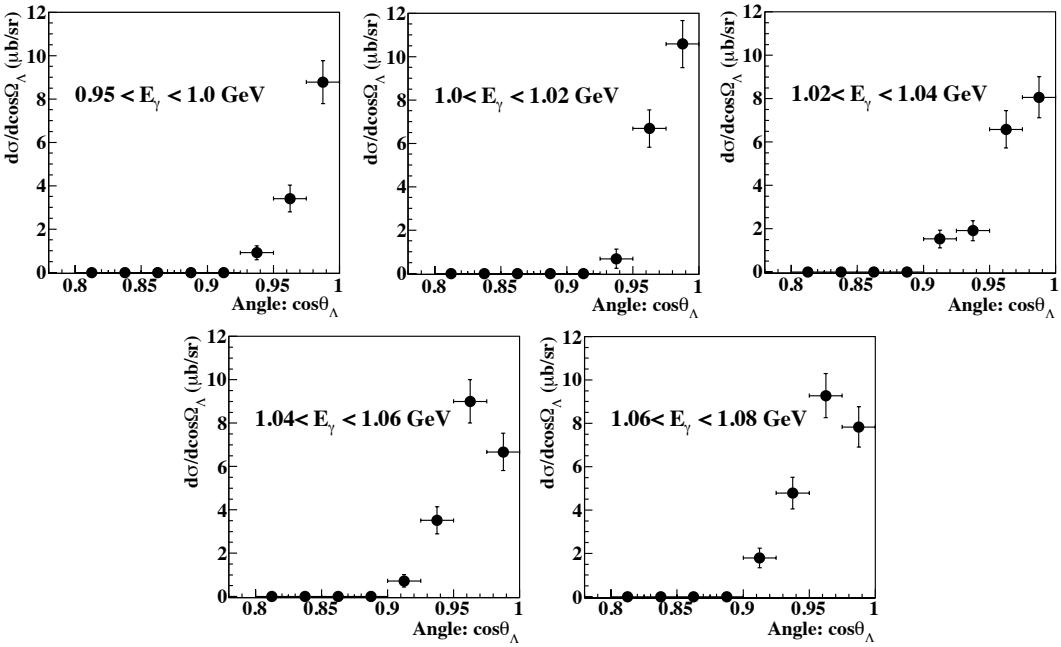

Figure 5.10: Background subtracted angular distribution of Λ in $\gamma d \rightarrow \Lambda X$ for the energy bins of $0.95-1.0, 1.02-1.04, 1.04-1.06$, and $1.06-1.08$ GeV, presented top left to bottom respectively.

5.7 Integrated Cross Section of (dγ,Λ)X

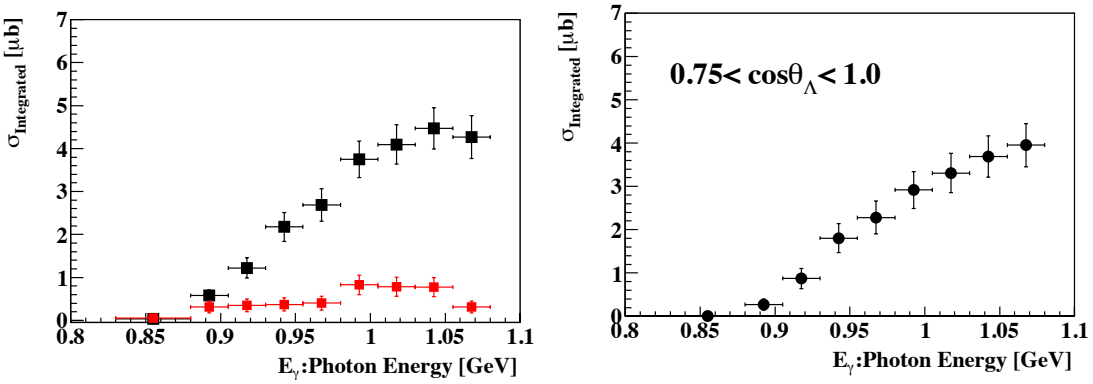

Figure 5.11: Integrated cross section of the inclusive measurement of Λ in $\gamma d \rightarrow \Lambda X$ for the angular region of $0.75 \leq \cos\theta_{\Lambda}^{LAB} \leq 1.0$. The cross section prior to background subtraction are the black squares, and background contribution are shown as the red squares. The background subtracted results are presented in the right figure.

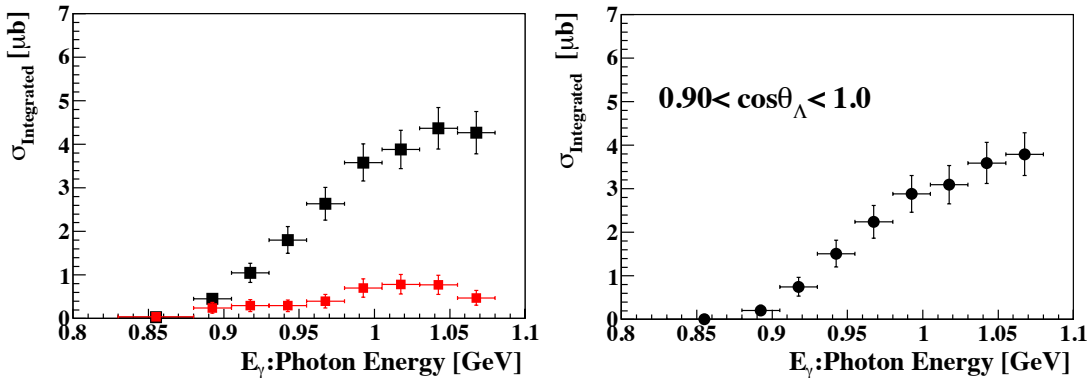

Figure 5.12: Integrated cross section of the inclusive measurement of Λ in $\gamma d \rightarrow \Lambda X$ for the angular region of $0.90 \leq \cos\theta_{\Lambda}^{LAB} \leq 1.0$. The cross section prior to background subtraction are the black squares, and background contribution are shown as the red squares. The background subtracted results are presented in the right figure.

In Figures 5.11 and 5.12, the integrated cross section obtained by the inclusive measurement of Λ in $\gamma d \rightarrow \Lambda X$ reaction is shown prior to background subtraction as the black squares, and contribution of the background region are shown as the red squares and the background subtracted measurements are presented in the right figures. In Figure 5.13, the background subtracted cross sections of $\gamma d \rightarrow \Lambda X$ reaction for the dual angular regions of $0.75 \leq \cos\theta_{\Lambda}^{LAB} \leq 1.0$ and $0.9 \leq \cos\theta_{\Lambda}^{LAB} \leq 1.0$ are shown in the figure as red and black solid circles respectively. The larger angular integration sector results in an increased absolute value for energies larger than 0.9 GeV.

A corollary of ascertaining the integrated cross section values over the acceptance range of the spectrometer and also for the limited forward hemisphere was that numerical evaluation of their ratio. The integrated cross sections of both regions are plotted on the left in Figure 5.13 red and black solid circles respectively, from which its is clear as day that the measurement in only the forward region tapers off at photon energies above 1.0 GeV in contrast to the full angular acceptance range. Hence, the ratio of integrated cross section was computed and graphically presented on the right of Figure 5.13. Approximately a 10%−20% reduction in magnitude of the measured cross sections is incurred from E_γ= (.80−.95).

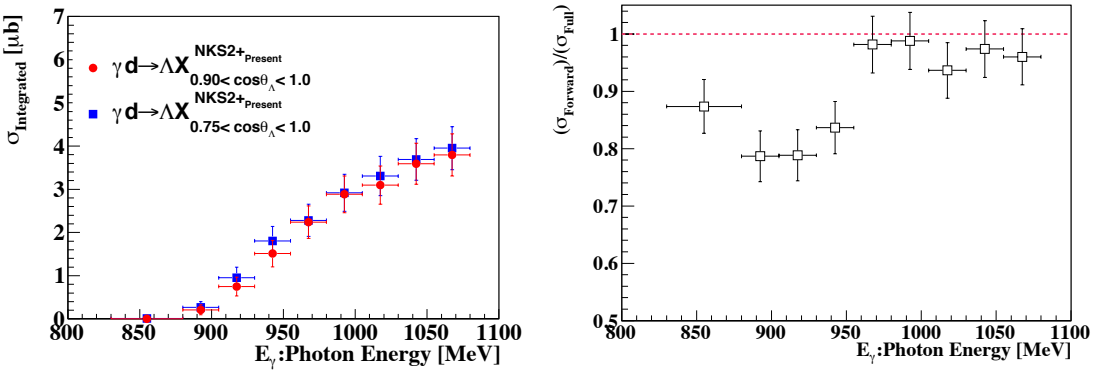

Figure 5.13: The background subtracted integrated cross section of Λ in $\gamma d \rightarrow \Lambda X$ for the full angular integrated region of $0.75 \leq \cos\theta_\Lambda^{LAB} \leq 1.0$ and and the limited $0.9 \leq \cos\theta_\Lambda^{LAB} \leq 1.0$ are shown in the figure as red and black solid circles respectively. The ratio of the two angular integration hemispheres are shown in the right figure.

5.8 Total Cross Section of $(d\gamma,\Lambda)$X

The data analyzed as a focus of the thesis was gathered for the angular integration region of $0.75 \leq \cos\theta_\Lambda^{LAB} \leq 1.0$. Therefore in order to accurately approximate the total cross section of $(d\gamma,\Lambda)$X reaction, the contribution to the cross section from the angular region invisible to the NKS2+ spectrometer must be determined thus enabling an extrapolation from the measured integrated cross section was performed. The results of the theoretical calculations were used to approximate the total cross section of $\gamma d \rightarrow \Lambda X$ and $\gamma d \rightarrow K^0 \Lambda p$ reactions. The primary focus of the thesis has been on the inclusive measurement of Λ in the $\gamma d \rightarrow \Lambda X$ reaction. However, it was decided to exploit the results of the theoretical predictions, and adopt a method taken from reference [4, 5] in order to extract the total cross section of $\gamma d \rightarrow \Lambda X$. The mathematical details involved in the evaluation of the total

cross section are outlined in the ensuing equation,

$$\sigma^{\Lambda X}_{\text{Total}} = (\sigma^{\gamma d\rightarrow \Lambda X}_{\text{Integrated}}) \cdot \frac{(\sigma^{'\gamma d\rightarrow K^0\Lambda p}_{\text{Total}} + \sigma^{'\gamma d\rightarrow K^+\Lambda n}_{\text{Total}})}{(\sigma^{'\gamma d\rightarrow K^0\Lambda p}_{\text{Integrated}} + \sigma^{'\gamma d\rightarrow K^+\Lambda n}_{\text{Integrated}})} \tag{5.9}$$

In regards to equation 5.9, the total and integrated cross sections of the $\gamma d \rightarrow K^0\Lambda p$ and $\gamma d \rightarrow K^+\Lambda n$ processes are identified as $\sigma^{'\gamma d\rightarrow K^0\Lambda p}_{\text{Total}}$, $\sigma^{'\gamma d\rightarrow K^0\Lambda p}_{\text{Integrated}}$, $\sigma^{'\gamma d\rightarrow K^+\Lambda n}_{Total}$, and $\sigma^{'\gamma d\rightarrow K^+\Lambda n}_{\text{Integrated}}$ respectively. In the case of the KM model, the integration range was the forward hemisphere of $0.9 \leq \cos\theta_\Lambda \leq 1.0$, in contrast to the RPR model, where the integration was over the angular acceptance of $0.75 \leq \cos\theta_\Lambda \leq 1.0$ in the laboratory system.

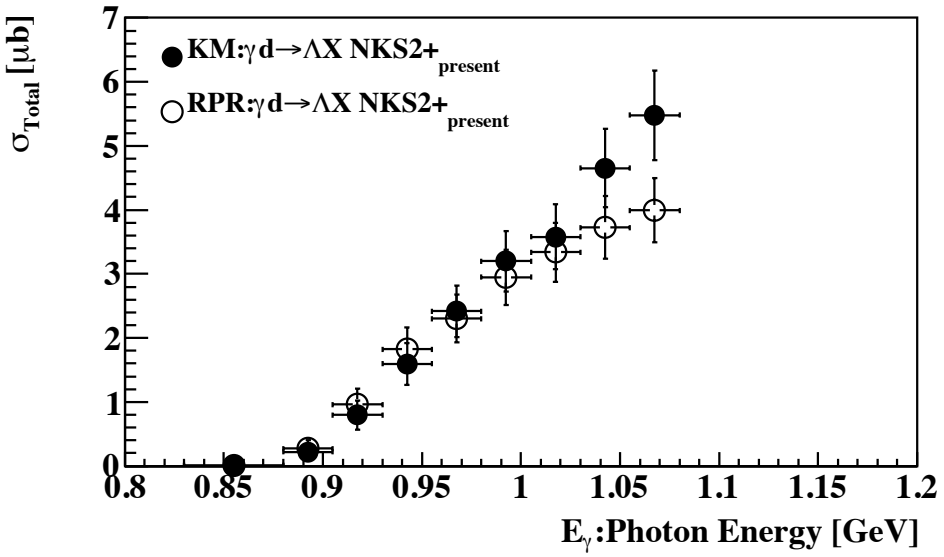

Figure 5.14: Extrapolated total $d(GeV,\Lambda)X$ cross section incorporating the KM and RPR theoretical calculations as solid black and red squares respectively.

The values introduced into the calculation for $\sigma^{'\gamma d\rightarrow K^0\Lambda p}_{Total}$, $\sigma^{'\gamma d\rightarrow K^0\Lambda p}_{Integrated}$, $\sigma^{\gamma d\rightarrow K^+\Lambda n}_{\text{Total}}$, and $\sigma^{'\gamma d\rightarrow K^+\Lambda n}_{Integrated}$ are all based on theoretical predictions.

The number of Λ that was unmeasured as a result of the restricted angle integration regions, $0.9 \leq \cos\theta^{LAB}_\Lambda \leq 1.0$ and $0.75 \leq \cos\theta^{LAB}_\Lambda \leq 1.0$, were compensated for by the ratio determined from the respective models, to be on the order of roughly 15% and 1% for the KM [6, 20, 21] and RPR [26, 28, 29]. The ratio for the RPR and KM calculations used in estimation follows the ratio that can be referenced in Figures 6.10 and 6.12. The extrapolated total cross of $\gamma d\rightarrow\Lambda$X by equation 5.9 is displayed in Figure 5.14 as the solid and open circles respectively and draw attention to a minor model dependence at photon energies of $E_\gamma \leq 1.05$ GeV.

5.9 Λ Recoil Polarization

In the case of reaction such as A+B→ C+D, the polarization vector of the D particle in production plane is know to be perpendicular, when the initial state are unpolarized. The emitted proton's direction in the $\Lambda \to p\pi$ decay is directly related to the spin of the produced Λ and is referred to as the Λ self analyzing power. The self analyzing feature of the weak decay of the Λ particle gives rise to not only parity violation but also an asymmetry.

The vector normal to the plane of production is defined as the following,

$$\hat{n} = -\frac{E_\gamma \times p_\Lambda}{|E_\gamma \times p_\Lambda|} \tag{5.10}$$

The polarization of Λ (P_Λ) can be given by 5.11 and will be computed from the decay asymmetry of the angular distributions and is calculated by,

$$P_\Lambda = \frac{2}{\alpha}\frac{N_1 - N_2}{N_1 + N_2} \tag{5.11}$$

where $\alpha = 0.6421 \pm 0.013$, is the so-called self analyzing strength or the decay asymmetry parameter [116], N_1 and N_2 are the total number of events where cosϑ is greater or less than zero respectively. It this framework cosϑ denotes the angle that lies between the proton from the Λ decay and $\hat{n}$ in the rest frame of the Λ hyperon.

$$P_\sigma^{tot} = |f^+|^2 - |f^-|^2 \tag{5.12}$$

The recoil polarization yields restrictions on the amplitudes, but does not give a unique solution. From knowledge of the cross section and polarization the absolute value of the scattering amplitudes can be deduced but simultaneously is not adequate enough to map out the complex amplitudes $|f^+|$ and $|f^-|$ [40]. This asymmetry is typically thought of as the ratio between competing patterns is a consequence of the witnessed interference between the s and p waves, in which the s and p waves are parity violating and conserving respectively. For α to be a non-zero value, both the s and p waves must be present and as a repercussion, permitting an investigation of the non trivial internal spin structure of Λ [67]. The momentum dependence was determined for three photon energy ranges, $0.9 - 1.0 GeV, 0.95 - 1.05 GeV$, and 1.0 − 1.1 GeV, the results of which are shown in Figure 5.15, given left to right respectively. The polarization in the lower energy bin is clearly negative and approaches zero in the other energy bins. We can conclude that the polarization are sizable near the threshold but decreases rapidly.

Λ recoil polarization as a function of momentum ($|P|_\Lambda^{LAB}$) for and 1.0 ≤E$_\gamma$≤ 1.1 was derived for the forward angular ranges corresponding to 0.95≤cosθ_Λ^{LAB}≤1.0 and

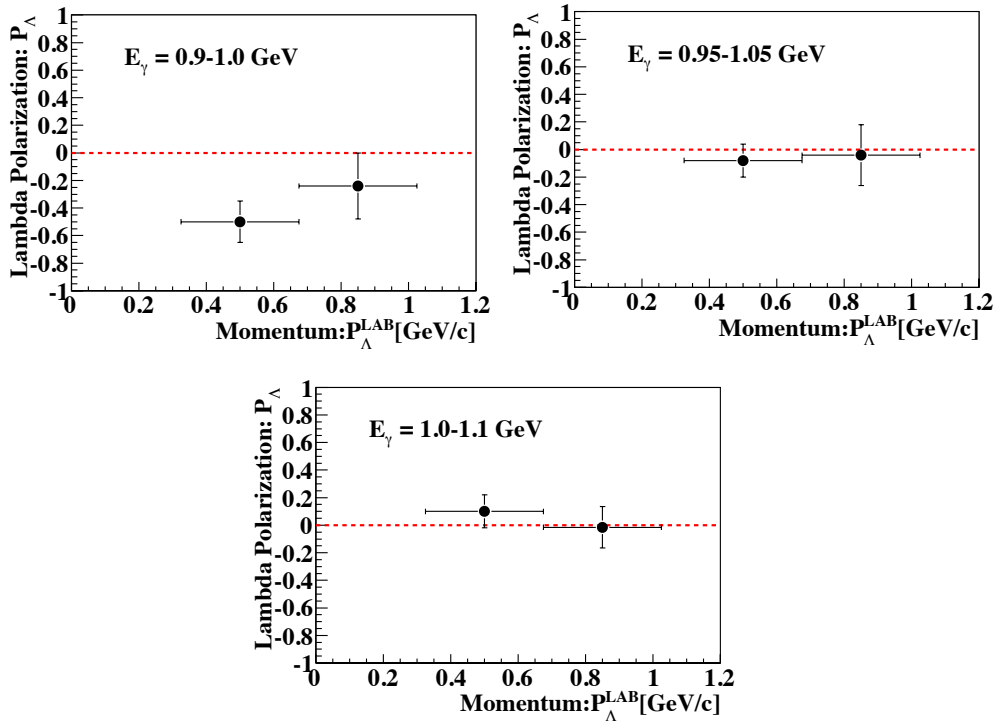

Figure 5.15: Λ recoil polarization as a function of momentum ($|P|_\Lambda^{LAB}$) for the energy range of $0.9-1.0 GeV, 0.95-1.05 GeV$, and 1.0 − 1.1 GeV shown from the top left respectively.

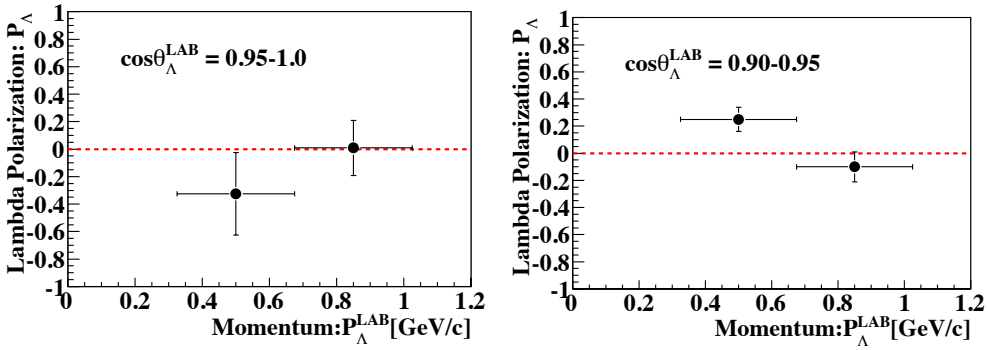

Figure 5.16: Λ recoil polarization as a function of momentum ($|P|_\Lambda^{LAB}$) in the angular bins of $\cos\theta_\Lambda^{Lab} = 0.95-1.0$ (left) and $0.9-0.95$ (right) at a bin centered energy for 1.0 − 1.1 (right) GeV.

$0.90 \leq \cos\theta_\Lambda^{LAB} \leq 0.95$ is seen in figure 5.16 and eludes to an intensification in the absolute magnitude at small angles.

5.10 Comparison with the Previous NKS2 Experiment

The experimental results of the inclusive measurement of Λ on a deuterium target using the NKS2 spectrometer prior to the recent upgrade was successfully carried out and the results reported [4, 5, 24]. We begin by presenting a comparison of the measured Λ momentum distributions in Figure 5.17, where the momentum spectra of the previous NKS2 (red squares) findings and those analyzed in this thesis (black circles) in the energy range of $0.9 - 1.0$ (upper), and $1.0 - 1.1$ (lower) GeV and angular regions of $0.95 \leq \cos\theta_{\Lambda}^{LAB} \leq 1.0$ and $0.90 \leq \cos\theta_{\Lambda}^{LAB} \leq 0.95$ are presented left to right respectively. Both are similar in shape, however, our results suffer at lower momenta due to limited statistics, and are unable to reproduce the former results. Broadly speaking the outcomes of both analyses are remarkably akin.

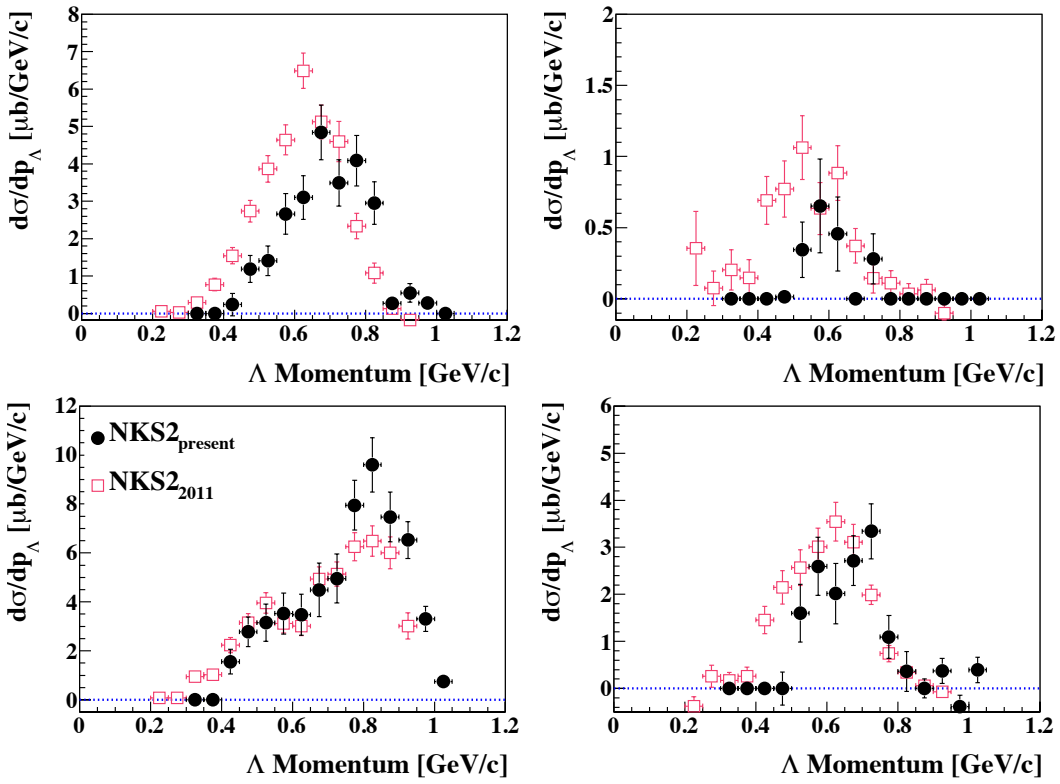

Figure 5.17: Comparison Λ momentum spectra between the results of the previous NKS2 (open red squares) and those analyzed in this thesis (black circles) on the deuteron in the the energy range of $0.9 - 1.0$ (upper), and $1.0 - 1.1$ (lower) GeV. The angular regions of $0.95 \leq \cos\theta_{\Lambda} \leq 1.0$ and $0.90 \leq \cos\theta_{\Lambda}^{LAB} \leq 0.95$ are presented left to right.

In the previous analysis on data taken with the NKS2, the integrated cross section the energy region was $0.9 \leq E_{\gamma} \leq 1.0$ and only determined for the forward angular region of

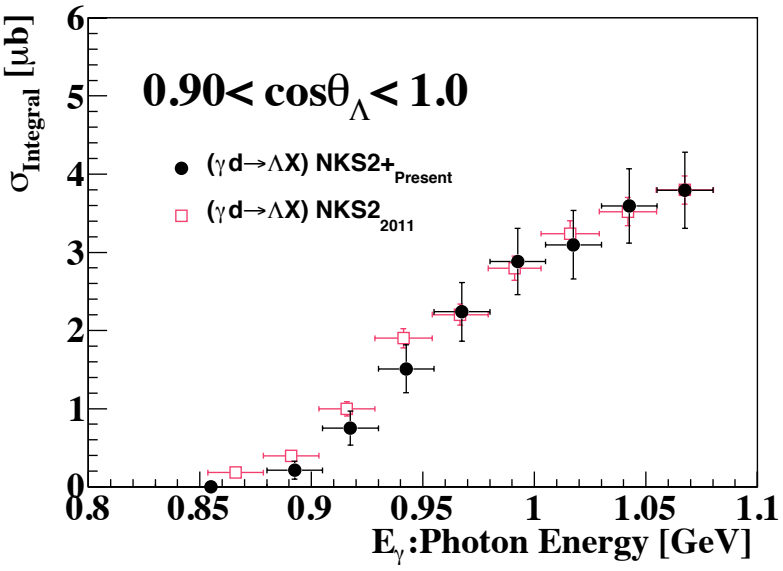

Figure 5.18: The inclusive background subtracted integrated cross section of Λ in γd→ΛX reaction for the forward hemisphere ($0.9 \leq \cos\theta_\Lambda^{LAB} \leq 1.0$) where results of the NKS2 experiment [4, 5, 24] and the present analysis (NKS+) are shown as open and solid black circles respectively. The errors in both results are only the statistical in origin.

$0.9 \leq \cos\theta_\Lambda^{LAB} \leq 1.0$. However, in this thesis the excitation function was determined for two angular regions, the full and forward regions, but for a valid comparison, only the same angular section is viable. The background subtracted integrated cross section of the inclusive measurement of Λ photoproduction in γd→ΛX reaction for the integrated angular region of $0.9 \leq \cos\theta_\Lambda^{LAB} \leq 1.0$ are shown in Figure 5.18. The results of the previous NKS2 experiment and the latest results of the NKS2+ collaboration, obtained from independent experiments and analysis, are shown as open and solid black solid circles respectively. The errors bars in both results are only statistical in nature. The findings reported in this dissertation produce an excitation function that has considerable agreement with the finalized results of the preceding experiment, emphasizing the uniqueness of the research, and more importantly, the reliability of the data reported by the NKS2/NKS2+ collaborations.

A comparison of the present work to the previous polarization results were also evaluated. In the results obtained from the data gathered by the NKS2 collaboration during the 2006−2007 period, the Λ hyperon polarization was calculated in two energy ranges and for the cases that involved a decay volume selection and its absence, as it was not a major emphasis in that analysis it was detailed in the Appendix [5]. Here though, the newest data is compared to those results to confirm its validity. Due to statistically limitations our data is reported in only two bins in contrast to the three binned data of the preceding experiment. For $E_\gamma = 0.9 - 1.0$ GeV the P_Λ results are in accord with the

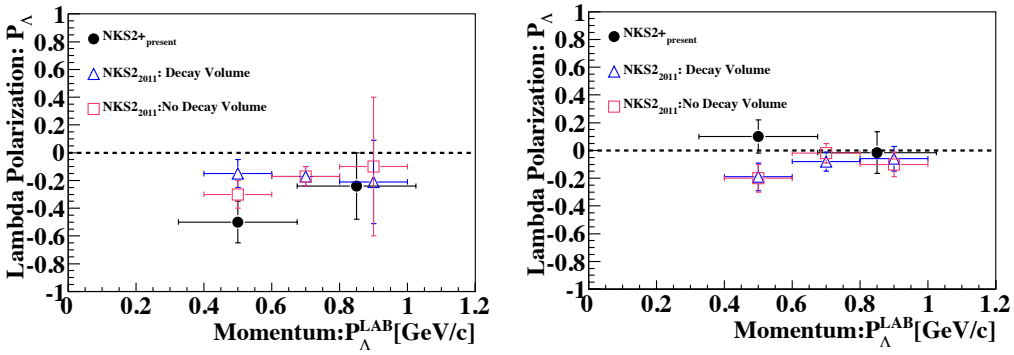

(a) $0.9 \leq E_\gamma \leq 1.0$ (b) $1.0 \leq E_\gamma \leq 1.1$

Figure 5.19: Comparison of this work with the previous NKS results of momentum dependence of Λ hyperon recoil polarization at E_γ of $0.9 - 1.0$, and $1.0 - 1.1$ GeV presented left to right respectively.

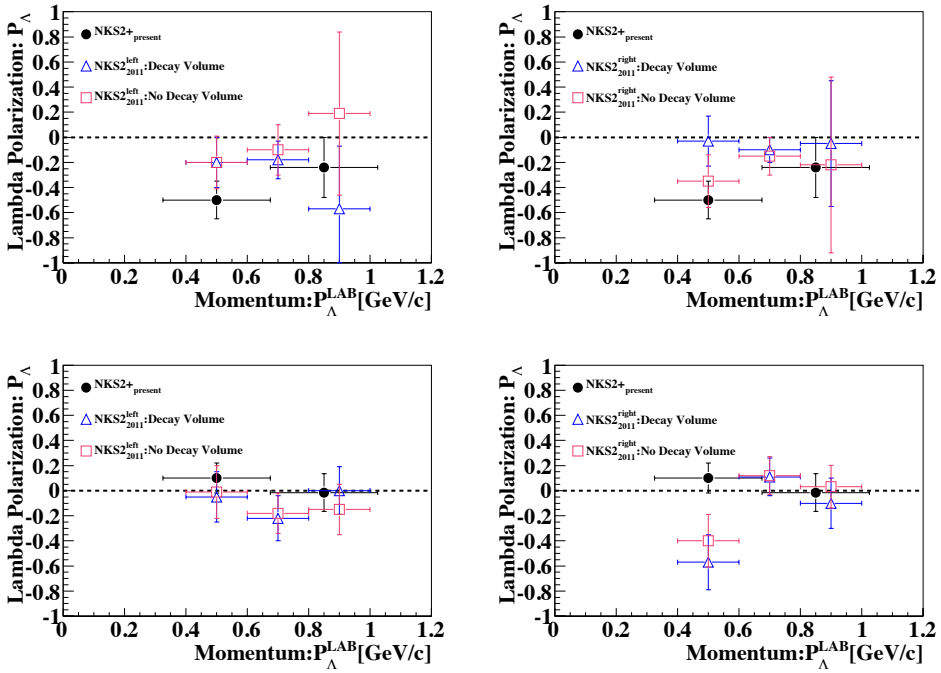

Figure 5.20: Comparison with previous NKS results of momentum dependence of Λ hyperon recoil polarization at E_γ energy range of $0.9 - 1.0$, and $1.0 - 1.1$ GeV presented left to right respectively, for the left and right wings of the NKS2+ given top to bottom.

earlier measurements in the terms of sign of the polarizations though the data indicates a substantially stronger absolute strength of roughly twice in magnitude. The increase of photon energy suggests a change in the sign in a momentum range of $0.4 - 0.6$ GeV and has the propensity to vanish as the momentum climbs.

Table 5.1: Extracted Λ as a function of the bombarding photon energy

Inclusive Λ yield				
$(0.75 \leq \cos\theta_\Lambda \leq 1.0)$				
Selection	Region [GeV]	Yield	Noise	S/N
Photon E_γ^1	0.850-0.900	1.0 ± 1.0	3.0 ± 1.7	0.3± 0.1
Photon E_γ^2	0.900-0.925	6.0 ± 4.0	7.0 ± 2.6	0.9± 0.1
Photon E_γ^2	0.925-0.950	20.0 ± 5.0	8.0 ± 2.8	2.5± 0.2
Photon E_γ^3	0.950-0.975	34.0 ± 7.0	7.0 ± 2.6	4.8± 0.3
Photon E_γ^4	0.975-1.000	51.0 ± 9.0	9.0 ± 3.0	5.6± 0.2
Photon E_γ^5	1.000-1.025	79.0 ± 8.8	23.0 ± 4.8	3.4± 0.3
Photon E_γ^6	1.025-1.050	63.0 ± 7.9	15.0 ± 3.9	4.2± 0.4
Photon E_γ^7	1.050-1.075	76.0 ± 8.7	16.0 ± 4.0	4.75± 0.2
Photon E_γ^8	1.075-1.080	25.0 ± 5.0	2.0 ± 1.4	12.5± 0.3
$(0.90 \leq \cos\theta_\Lambda \leq 1.0)$				
Photon E_γ^1	0.850-0.900	1.0 ± 2.2	3.0 ± 1.6	0.3± 0.1
Photon E_γ^2	0.900-0.925	6.0 ± 4.5	7.0± 2.5	0.9± 0.2
Photon E_γ^2	0.925-0.950	20.0 ± 6.0	8.0 ± 2.7	2.5± 0.2
Photon E_γ^3	0.950-0.975	34.0 ± 6.9	7.0 ± 2.5	4.9± 0.2
Photon E_γ^4	0.975-1.000	51.0 ± 8.3	9.0 ± 3.0	5.7± 0.3
Photon E_γ^5	1.000-1.025	70.0 ±10.2	17.0 ± 4.1	4.1± 0.4
Photon E_γ^6	1.025-1.050	59.0 ± 9.4	15.0 ± 3.8	3.9± 0.4
Photon E_γ^7	1.050-1.075	74.0 ±10.3	16.0 ± 4.0	4.6± 0.2
Photon E_γ^8	1.075-1.080	24.0 ± 5.5	3.0 ± 1.7	8.0± 0.2

Table 5.2: Extracted Λ as a function of momentum and angular bins in the laboratory frame

	Inclusive Λ yield	$[1.00 \leq E_\gamma \leq 1.0]$ GeV		
Selection	Region	Yield	Noise	S/N
	$0.95 \leq \cos\theta_\Lambda^{LAB} \leq 1.0$			
P_Λ^{Lab1}	$0.40 \leq P_\Lambda \leq 0.45$	5.0± 2.6	1.0± 1.0	5.0± 1.0
P_Λ^{Lab2}	$0.45 \leq P_\Lambda \leq 0.50$	7.1± 3.0	1.0± 1.1	7.1± 1.0
P_Λ^{Lab3}	$0.50 \leq P_\Lambda \leq 0.55$	10.1± 3.75	2.0± 1.1	5.1± 1.0
P_Λ^{Lab4}	$0.55 \leq P_\Lambda \leq 0.60$	8.0± 4.2	5.0± 1.0	1.6± 1.0
P_Λ^{Lab5}	$0.60 \leq P_\Lambda \leq 0.65$	11.0± 3.8	2.0± 1.4	5.5± 1.0
P_Λ^{Lab6}	$0.65 \leq P_\Lambda \leq 0.70$	14.0± 6.0	11.0± 3.3	1.3± 1.0
P_Λ^{Lab7}	$0.70 \leq P_\Lambda \leq 0.75$	15.0± 4.4	2.0± 1.4	7.5± 1.0
P_Λ^{Lab8}	$0.75 \leq P_\Lambda \leq 0.80$	25.0± 5.6	3.0± 1.7	8.3± 1.0
P_Λ^{Lab9}	$0.80 \leq P_\Lambda \leq 0.85$	29.4± 6.5	6.6± 2.5	4.5± 1.0
P_Λ^{Lab10}	$0.85 \leq P_\Lambda \leq 0.90$	21.0± 5.4	4.1± 2.0	5.1± 1.0
P_Λ^{Lab11}	$0.90 \leq P_\Lambda \leq 0.95$	18.0± 4.4	1.0± 1.0	18.0± 1.0
P_Λ^{Lab12}	$0.95 \leq P_\Lambda \leq 1.00$	9.0± 3.6	2.0± 1.4	4.5± 1.0
P_Λ^{Lab13}	$1.00 \leq P_\Lambda \leq 1.05$	2.0± 2.0	1.0± 1.0	2.0± 1.0
	$0.90 \leq \cos\theta_\Lambda^{LAB} \leq 0.95$			
P_Λ^{Lab4}	$0.55 \leq P_\Lambda \leq 0.60$	3.5± 2.1	0.5± 0.7	7.0± 2.5
P_Λ^{Lab5}	$0.60 \leq P_\Lambda \leq 0.65$	6.0± 2.4	0.5± 0.5	3.0± 1.7
P_Λ^{Lab6}	$0.65 \leq P_\Lambda \leq 0.70$	5.0± 2.6	1.0± 1.0	5.0± 2.2
P_Λ^{Lab7}	$0.70 \leq P_\Lambda \leq 0.75$	7.0± 3.0	1.0± 1.0	7.0± 1.6
P_Λ^{Lab8}	$0.75 \leq P_\Lambda \leq 0.80$	9.0± 3.0	0.5± 0.5	18.0± 4.3
P_Λ^{Lab9}	$0.80 \leq P_\Lambda \leq 0.85$	3.0± 2.2	1.0± 1.0	3.0± 1.6
P_Λ^{Lab10}	$0.85 \leq P_\Lambda \leq 0.90$	1.0± 1.7	1.0± 1.0	1.0± 1.1
P_Λ^{Lab11}	$0.90 \leq P_\Lambda \leq 0.95$	.0± 1.4	1.0± 1.0	0.0± 1.1
P_Λ^{Lab12}	$0.95 \leq P_\Lambda \leq 1.00$	1.0± 1.0	0.5± 0.5	2.0± 1.7
P_Λ^{Lab13}	$0.95 \leq P_\Lambda \leq 1.05$	-1.0± 1.0	1.0± 1.0	-1.0± 0.5
P_Λ^{Lab14}	$1.00 \leq P_\Lambda \leq 1.05$	1.0± 1.0	0.5± 0.5	2.0± 1.7

Table 5.3: Extracted Λ as a function of momentum and angular bins in the laboratory frame

	Inclusive Λ yield	[0.90 ≤ E_γ ≤1.0] GeV		
Selection	Region	Yield	Noise	S/N
	$0.95 \leq \cos\theta_\Lambda^{LAB} \leq 1.0$			
P_Λ^{Lab1}	$0.40 \leq P_\Lambda \leq 0.45$	1.0± 1.0	1.0± 1.0	1.0± 1.0
P_Λ^{Lab2}	$0.45 \leq P_\Lambda \leq 0.50$	1.0± 1.0	1.0± 1.0	1.0± 1.0
P_Λ^{Lab3}	$0.50 \leq P_\Lambda \leq 0.55$	4.0± 2.5	1.0± 1.0	4.0± 2.0
P_Λ^{Lab4}	$0.55 \leq P_\Lambda \leq 0.60$	6.0± 2.9	1.0± 1.0	6.0± 2.4
P_Λ^{Lab5}	$0.60 \leq P_\Lambda \leq 0.65$	9.0± 3.0	1.0± 1.0	9.0± 3.0
P_Λ^{Lab6}	$0.65 \leq P_\Lambda \leq 0.70$	13.0± 3.9	1.0± 1.0	13.0± 3.4
P_Λ^{Lab7}	$0.70 \leq P_\Lambda \leq 0.75$	20.0± 4.9	2.0± 1.4	10.0± 3.1
P_Λ^{Lab8}	$0.75 \leq P_\Lambda \leq 0.80$	14.0± 4.0	1.0± 1.0	14.0± 3.7
P_Λ^{Lab9}	$0.80 \leq P_\Lambda \leq 0.85$	16.0± 4.5	2.0± 1.4	8.0± 2.8
P_Λ^{Lab10}	$0.85 \leq P_\Lambda \leq 0.90$	11.0± 3.6	1.0± 1.0	11.0± 3.1
P_Λ^{Lab11}	$0.90 \leq P_\Lambda \leq 0.95$	1.0± 2.7	3.0± 1.7	0.3± 0.5
P_Λ^{Lab12}	$0.95 \leq P_\Lambda \leq 1.00$	2.0± 2.0	1.0± 1.0	2.0± 1.7
P_Λ^{Lab13}	$1.00 \leq P_\Lambda \leq 1.05$	1.0± 1.7	1.0± 1.0	1.0± 1.0
	$0.90 \leq \cos\theta_\Lambda^{LAB} \leq 0.95$			
P_Λ^{Lab4}	$0.55 \leq P_\Lambda \leq 0.60$	1.0± 1.0	1.0±1.0	2.0±1.2
P_Λ^{Lab5}	$0.60 \leq P_\Lambda \leq 0.65$	2.0 ± 1.5	1.0±1.0	3.0±1.3
P_Λ^{Lab6}	$0.65 \leq P_\Lambda \leq 0.70$	1.6± 1.5	0.5±0.71	3.0±1.2
P_Λ^{Lab8}	$0.75 \leq P_\Lambda \leq 0.80$	1.0 ± 1.0	0.75±0.25	2.0±1.2

Table 5.4: Extracted Λ yield as a function of the scattering angle ($\cos\theta_\Lambda^{LAB}$)

	Inclusive Λ yield			
	(0.95 ≤ Eγ ≤ 1.0) [GeV]			
Selection	Angular Region	Yield	Noise	S/N
$\cos\ \theta_\Lambda^1$	0.900-0.925	0.0 ± 1.0	0.0 ± 0.5	0.0± 0.1
$\cos\ \theta_\Lambda^2$	0.925-0.950	7.0 ± 4.4	6.0± 2.5	1.2± 0.1
$\cos\ \theta_\Lambda^3$	0.950-0.975	34.0 ± 6.5	4.0 ± 2.0	8.5± 0.2
$\cos\ \theta_\Lambda^4$	0.975-1.000	94.0 ± 12.4	30.0 ± 5.5	3.1± 0.3
	(1.0 ≤ Eγ ≤ 1.02)			
$\cos\ \theta_\Lambda^1$	0.900-0.925	1.0 ± 1.0	3.0 ± 1.7	0.3± 0.1
$\cos\ \theta_\Lambda^2$	0.925-0.950	6.0 ± 4.0	7.0± 2.6	0.9± 0.1
$\cos\ \theta_\Lambda^3$	0.950-0.975	20.0 ± 5.0	8.0 ± 2.8	2.5± 0.2
$\cos\ \theta_\Lambda^4$	0.975-1.000	34.0 ± 7.0	7.0 ± 2.6	4.8± 0.3
	(1.02 ≤ Eγ ≤ 1.04)			
$\cos\ \theta_\Lambda^1$	0.900-0.925	4.0 ±21.0	0.0 ± 0.5	4.0± 0.1
$\cos\ \theta_\Lambda^2$	0.925-0.950	5.0 ± 3.3	3.0± 1.7	1.7± 0.1
$\cos\ \theta_\Lambda^3$	0.950-0.975	26.0 ± 6.2	6.0 ± 2.5	4.3± 0.2
$\cos\ \theta_\Lambda^4$	0.975-1.000	26.0 ± 8.4	22.0 ± 4.7	1.2± 0.3
	(1.04 ≤ Eγ ≤ 1.06)			
$\cos\ \theta_\Lambda^1$	0.900-0.925	2.0 ± 2.5	2.0 ± 1.5	1.0± 0.1
$\cos\ \theta_\Lambda^2$	0.925-0.950	12.0 ± 4.0	2.0± 1.4	6.0± 0.1
$\cos\ \theta_\Lambda^3$	0.950-0.975	36.0 ± 6.0	1.0 ± 0.5	36.0± 0.2
$\cos\ \theta_\Lambda^4$	0.975-1.000	38.0 ± 7.5	9.0 ± 3.0	4.2± 0.3
	(1.06 ≤ Eγ ≤ 1.08)			
$\cos\ \theta_\Lambda^1$	0.900-0.925	7.0 ± 3.9	4.0 ± 2.0	1.75± 0.8
$\cos\ \theta_\Lambda^2$	0.925-0.950	18.0 ± 4.2	1.0 ± 0.5	18.0± 0.2
$\cos\ \theta_\Lambda^3$	0.950-0.975	48.0 ± 7.5	5.0 ± 2.3	9.6± 0.7
$\cos\ \theta_\Lambda^4$	0.975-1.000	53.0 ± 8.7	12.0 ± 3.5	4.4± 0.5

CHAPTER

SIX

DISCOURSE

> Philosophy, though unable to tell us with certainty what is the true answer to the doubts which it raises, is able to suggest many possibilities which enlarge our thoughts and free them from the tyranny of custom. Thus, while diminishing our feeling of certainty as to what things are, it greatly increases our knowledge as to what they may be; it removes the somewhat arrogant dogmatism of those who have never traveled into the region of liberating doubt, and it keeps alive our sense of wonder by showing familiar things in an unfamiliar aspect.

Bertrand Russell.

6.1 Overview

This chapter will cover the formalism used in theoretical model calculations of photo production on deuteron. The results of calculations by Kaon-MAID (KM) [6, 20, 21], Saclay-Lyon A (SLA) [7, 85] and Regge-Plus-Resonance (RPR) [26, 28, 29] models will be presented for the momentum and angle dependent differential cross sections, polarizations and excitation function. This will be followed by a comparison of the experimental findings to the theoretical predictions. The chapter concludes with a confrontation of the measured Λ polarization and the estimated $\gamma d \to K^0 \Lambda p$ total cross section to existing published and reported data.

6.2 Photoproduction on a Deuteron

These models are useful to predict the $d(\gamma,\Lambda)KN$ reaction though they have quite a lot difference in the resonance parameters that are included for each channel. In regards to the s-channel in which nucleon resonances are the exchange term, the Kaon-MAID includes four resonances in comparison to the solitary nucleon resonance in the SLA model. In the SLA model framework the photo-coupling ratio of the charged and neutral K_1, $r_{K_1K\gamma}$, is not determined and is therefore treated as a free fitting parameter. As such, the calculations by the SLA model were performed for $r_{K_1K\gamma}$ parameter ranging from -(1.0 - 3.0). The calculations on the deuteron in computed by P. Vancreayvald and P. Bydžovský were both founded on the impulse approximation method, PWIA for the isobars descriptions. However, the RPR calculations are calculated on the deuteron utilizing a relativistic plane wave impulse approximation (RPWIA). The relativistic and deuteron wave function are adopted from the WJC-1 solutions. Typical deuteron wave functions are given in Appendix C.

For predictions of the inclusive measurement of the $d(\gamma,\Lambda)KN$ process, the nucleon was treated as a spectator, under the assumption that the KN final state interaction (FSI) is negligible. Addressing reactions in the threshold energy regime, the ΛN interaction is known to have dissimilar importance with respect to the inclusive $d(\gamma,K^+\Lambda)n$ and exclusive $d(\gamma,K^+)\Lambda n$ processes, where for the former it is less significant [117].

Photoproduction of the deuteron in the spectator approximation, following the formalism of reference [47], is found as,

$$d^9\sigma = \frac{m_\Lambda m_{N'}}{64\pi^4 P_\gamma \cdot P_d E_\Lambda E_{N'}} \int d^4P_N \delta^4(P_f^e - P_i^e) \frac{(s-m_N^2)^2}{m_\Lambda m_{N'}} \times \frac{d\sigma^e}{dt}\delta^4(P_d - P_N - P_{N'}) \frac{\frac{1}{6}\Sigma|M_{fi}|^2}{\frac{1}{4}\Sigma|M_{fi}^e|^2} d^3_{p_k} d^3_{p_\Lambda} d^3_{p_{N'}} \quad (6.1)$$

In the above equation, $s = (P_\gamma + P_N)^2$, $t = (P_\gamma - P_K)^2$, $P_i^e = P_\gamma + P_N$, and $P_f^e = P_K + P_\Lambda$. The four momentum of the target nucleon, designated as P_N, will be integrated over, the δ function fractured into two parts. Lastly, the invariant cross section of a two body system is,

$$\frac{d\sigma^e}{dt}(s,t) = \frac{1}{4\pi}\frac{m_\Lambda m_N}{(s-m_N^2)^2}\frac{1}{4}\Sigma|M_{fi}^e|^2 \quad (6.2)$$

This allows the matrix element to be written for the deuteron in the lab frame as,

$$\frac{1}{6}\Sigma|M_{fi}|^2 = (2\pi)^3\frac{2m_d E_{N'}}{E_N}\frac{1}{4}\Sigma|M_{fi}^e|^2 u_d(p_{N'})^2 \quad (6.3)$$

The energy of the target nucleon in equation 6.3 is expressed as,

$$E_N = E_d - E_N = E_K + E_\Lambda - E_\gamma \tag{6.4}$$

for the *off-shell* approximation, and as,

$$E_N = \sqrt{m_N^2 + \vec{p}_N^2} \tag{6.5}$$

for the *on-shell* case.

Combining the former equations and after some algebra, eventually the inclusive cross section on the deuteron the laboratory frame of reference is derived as follows,

$$\frac{d^{3\sigma}}{d|\vec{p}_K|} = \int \frac{m_{N'}(s - m_N^2)^2 \vec{p}^2}{4 m_N E_\gamma E_K E_N |\vec{p}_\gamma - \vec{p}_K|} \frac{u_d(P_{N'})^2}{\pi} \frac{d\sigma^e}{dt} d|\vec{p}_N| d\Phi_{N'} \tag{6.6}$$

6.2.1 Kaon Photoproduction: KM and SLA: Momentum Calculations

The predictions of the K^0 momentum spectra based on Kaon-MAID [7, 20] for the $\gamma d \to K^0 \Lambda p$ and $\gamma d \to K^+ \Lambda n$ reactions and the addition of both are presented in Figure 6.1 as the red, black and blue curves respectively. In these figures, the photon energy is averaged for the two specific energy ranges, $0.9 - 1.0$ (upper) and $1.0 - 1.08$ (lower) GeV. The calculations were performed for four angular regions of integration $\cos\theta_K^{LAB}$ = (a) $0.9 - 1.0$, (b) $0.8 - 0.9$, (c) $0.7 - 0.8$, (d) $0.6 - 0.7$, in the laboratory frame by P. Bydžovský.

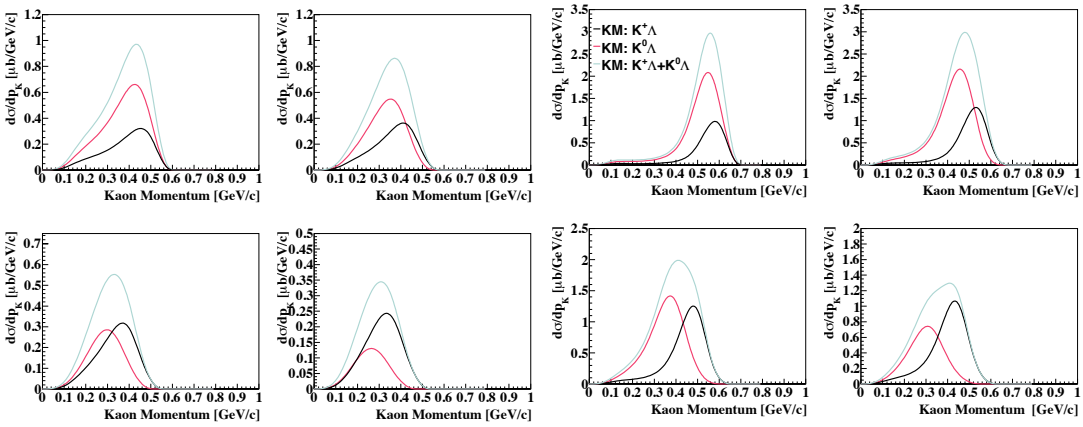

Figure 6.1: Inclusive cross sections as a function of kaon lab momentum based on the Kaon-MAID model, for the $\gamma d \to K^0 \Lambda p$ and $\gamma d \to K^+ \Lambda n$ reactions and the addition of their respective cross sections for incident photon energy in the range from (top) $1.0 - 1.08$ GeV and (bottom) $0.9 - 1.0$ GeV as the red, black and blue curves respectively. The angle integration bins were $\cos\theta_K^{LAB}$ =s$0.9 - 1.0$, $0.8 - 0.9$, $0.7 - 0.8$, and $0.6 - 0.7$.

K^0 momentum spectra for $\gamma d \to K^0 \Lambda p$, for the incident photon energy in the range from (left) $1.0 - 1.08$ GeV and (right) $0.9 - 1.0$ GeV. The calculations were performed for the isobaric models, Kaon-MAID and SLA models, where the $r_{K_1 K_\gamma}$ parameter for the SLA models is displayed in the Figure 6.2

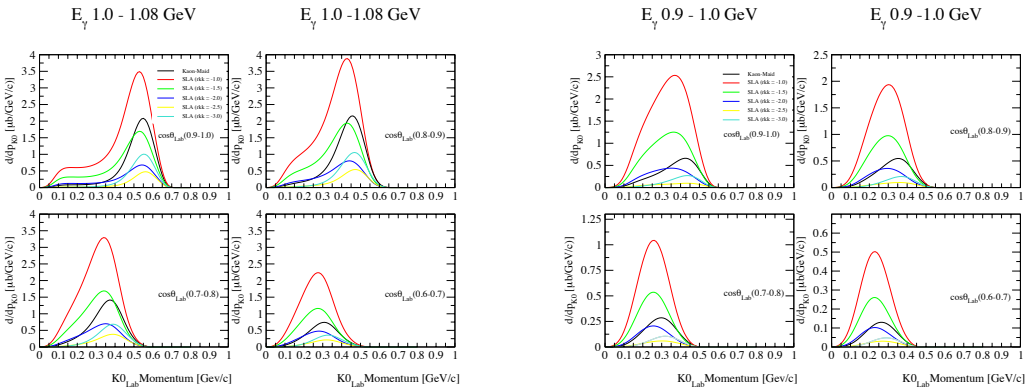

Figure 6.2: K^0 momentum spectra for $\gamma d \to K^0 \Lambda p$ for the incident photon energy in the range from(left) $1.0 - 1.08$ GeV and (right) $0.9 - 1.0$ GeV. The calculations were performed for the isobaric models, Kaon-MAID and SLA models, where the $r_{K_1 K_\gamma}$ parameter for the SLA model is displayed in the figure.

6.2.2 Λ Photoproduction: KM and SLA: Momentum Calculations

The predictions of the inclusive measurement of the Λ momentum dependent differential cross section based on KM for the $\gamma d \to K^0 \Lambda p$ and $\gamma d \to K^+ \Lambda n$ reactions are presented in Figure 6.3. Here the photon energy is averaged for the two specific energy ranges, $0.9 - 1.0$ (upper) and $1.0 - 1.08$ (lower) GeV. The calculations were performed for four distinct angular regions of integration $\cos\theta_\Lambda^{LAB}$ =(a) $0.95 - 1.0$, (b) $0.90 - 0.95$, (c) $0.85 - 0.90$, (d) $0.80 - 0.85$, in the laboratory frame for Λ production with an corresponding charged or neutral kaon. The $K^+\Lambda$, $K^0\Lambda$ and the addition of both cross section amplitudes are drawn as black, red, and blue curves respectively. Theoretical calculations of inclusive cross sections as a function of Λ momentum for the $\gamma d \to K^0 \Lambda p$ and γd$\to K^+ \Lambda n$ reactions for the incident photon beam energy in the range from (right) $1.0 - 1.08$ GeV and (left) $0.9 - 1.0$ GeV are given in Figure 6.4. The region of integration were the same as Figure 6.3. The calculations were performed for the SLA model [7, 20]. The $r_{K_1 K_\gamma}$ parameter for the SLA models is displayed in the figure and was allowed to vary from $-(1.0 - 3.0)$ by increments of -0.5 .

Lastly, the curves for only the addition of the $\gamma d \to K^0 \Lambda p$ and $\gamma d \to K^+ \Lambda n$ cross

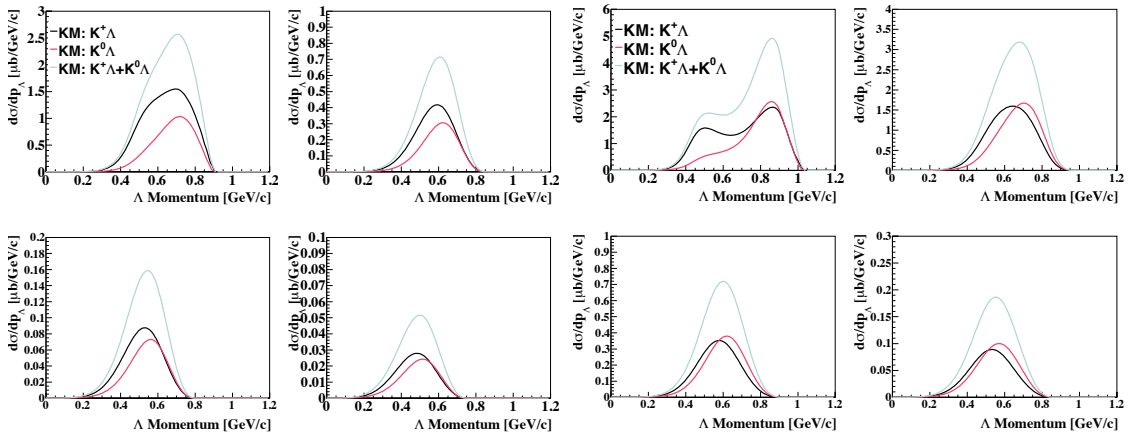

Figure 6.3: Kaon-MAID inclusive cross sections as a function of Λ momentum for the $\gamma d \to K^0 \Lambda p$ and $\gamma d \to K^+ \Lambda n$ reactions and the addition of the amplitudes for the incident photon beam energy in the range from(right) $1.0 - 1.08$ and (left) $0.9 - 1.0$ GeV as the red, black and blue curves respectively.

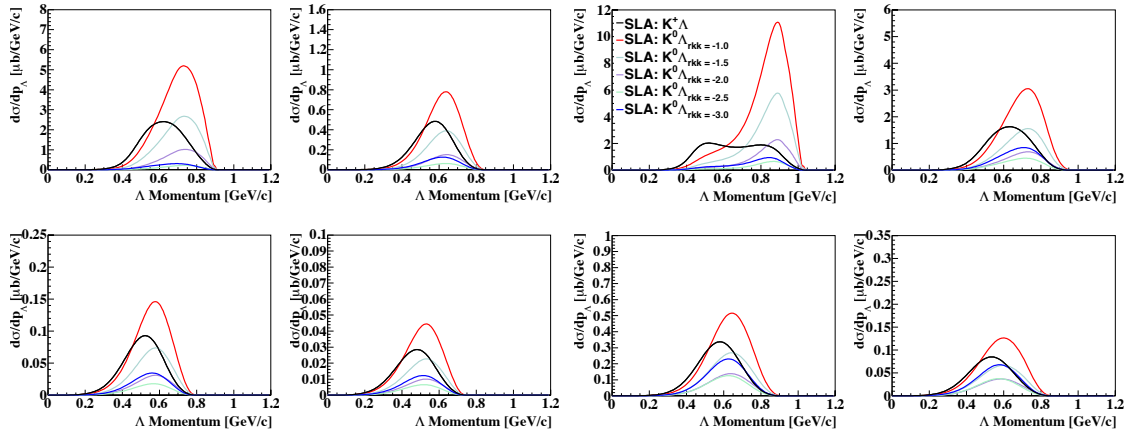

Figure 6.4: Theoretical predictions of inclusive Λ momentum cross sections for $\gamma d \to K^0 \Lambda p$ and $\gamma d \to K^+ \Lambda n$ reactions for photon energy of (right) $1.0 - 1.08$ and (left) $0.9 - 1.0$ GeV.

sections of KM and SLA are contrasted in Figure 6.5. The presentation of E_γ and $\cos\theta_\Lambda^{LAB}$ bins follows that of Figure 6.4. The parameter for the SLA model is displayed in the figure indicated by the colors in the legend, whereas KM is seen now as the dashed black curve.

6.2.3 RPR: Momentum Predictions

The calculations of the hyperon angle integrated momentum distribution based on RPR[8, 25, 27] for the $\gamma d \to \Lambda K N$ reactions are presented in Figure 6.6. In these figures, the angular bins were forward scattering angles of $0.95 \leq \cos\theta_\Lambda^{LAB} \leq 1.0$ and $0.90 \leq \cos\theta_\Lambda^{LAB} \leq 0.95$ and the photon energy was bin centered for the two specific energy ranges, E_γ

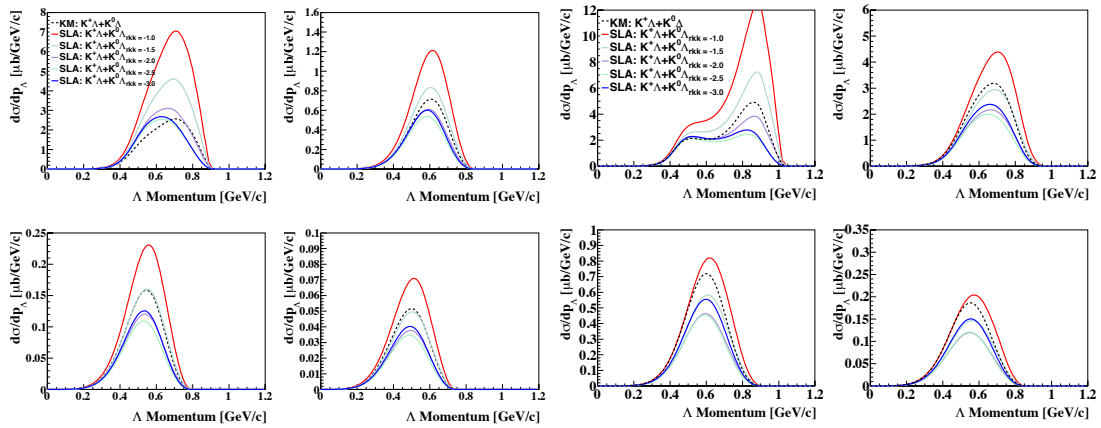

Figure 6.5: KM and SLA calculations of the inclusive Λ momentum cross sections for the addition of $\gamma d \to K^0 \Lambda p$ and $\gamma d \to K^+ \Lambda n$ reactions for photon beam energy of (right) $1.0-1.08$ and (left) $0.9-1.0$ GeV in the laboratory frame.

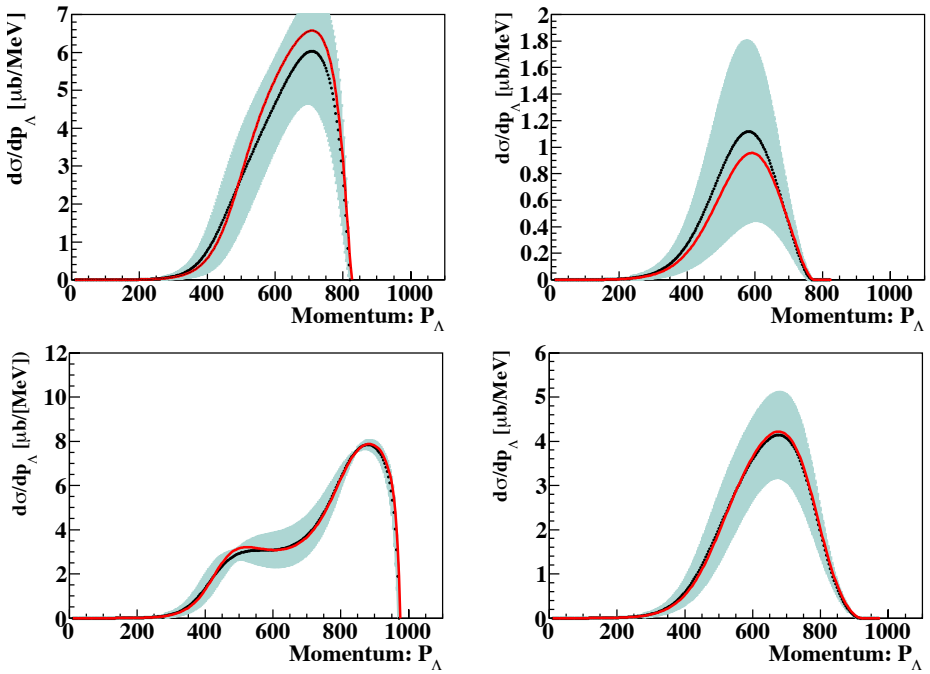

Figure 6.6: Regge-Plus-Resonace (RPR-2007) [25, 26] theoretical calculations of bin-centered energies and Λ angle integrated inclusive cross sections as a function of Λ momentum for photon beam energy of $1.0-1.1$ (bottom) and $0.9-1.0$ (top) GeV. The region of integration covered the angular bins of $\cos\theta_\Lambda^{LAB} = 0.95-1.0$ (left), and $\cos\theta_\Lambda^{LAB} = 0.90-0.95$(right).

$= 0.9-1.0$ and $1.0-1.08$ GeV. The results of the higher and lower energy and angular bins are the top and lower, left and right respectively. The appearance of the momentum dependent cross section takes it shape from the momentum of the nucleon that was hit

and has strong relation to the photon energy [26]. The shaded regions represent the theoretical uncertainties introduced from the ratio of the magnetic transition moments of the $D_{13}(1900)$ and $P_{13}(1900)$ resonance states, which is allowed to range from $-(2-2)$. In the RPR approach, it was concluded that $\gamma d \rightarrow K^{+}\Lambda n$ is the predominant process responsible for the better part of the cross section [25].

6.2.4 KM and SLA: Excitation Function

The forward angle integrated and total cross section of $\gamma d \rightarrow K^{0}\Lambda p$ and $\gamma d \rightarrow K^{+}\Lambda n$ reactions as a function photon energy, predicted by KM, are given in Figure 6.7, where the total cross section by the addition of $\gamma d \rightarrow K^{0}\Lambda p$ and $\gamma d \rightarrow K^{+}\Lambda n$ reactions, as a function photon energy, is shown as the solid blue curve (right). The results of the calculations for the angular integration of $0.9 \leq \cos\theta_{\Lambda}^{LAB} \leq 1.0$ are given in upper row and the total cross section in the lower in Figure 6.7. The smaller and more forward region of hyperon angular integration results in a reduction of the predicted energy dependence of Λ production.

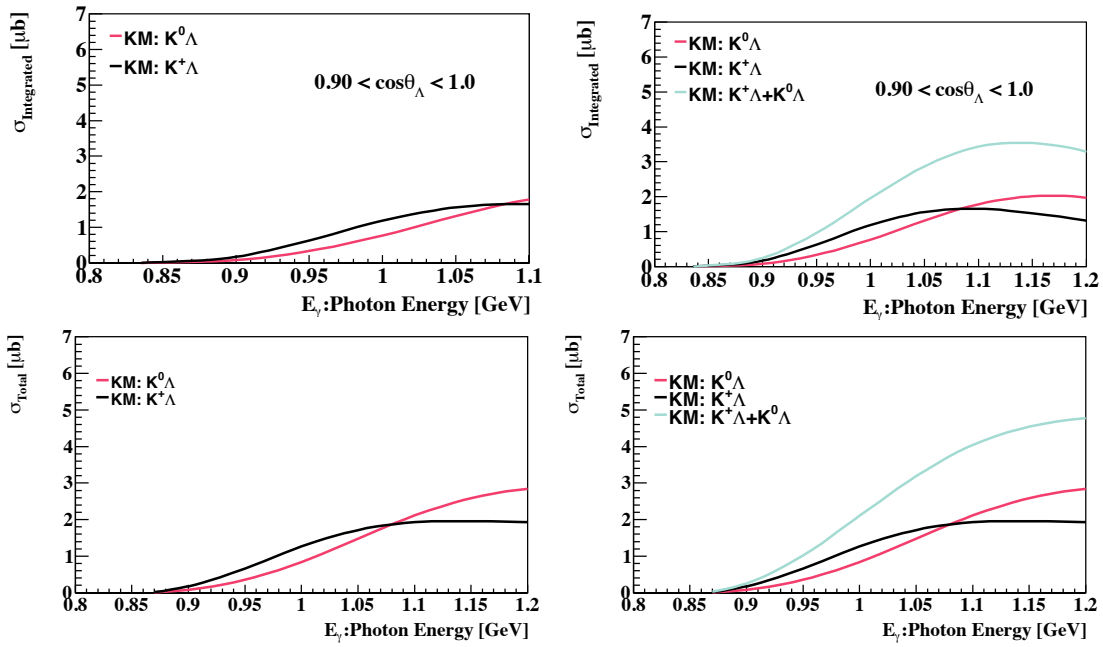

Figure 6.7: Kaon-MAID [20] curves of the integrated (upper) and total (lower) cross section of $\gamma d \rightarrow K^{0}\Lambda p$ and $\gamma d \rightarrow K^{+}\Lambda n$ reactions in the region of angular integration is $0.9 \leq \cos\theta_{\Lambda}^{LAB} \leq 1.0$ as a function photon energy are shown as the red and black lines respectively. The right figure includes the sum of the cross sections as the solid blue curve.

Illustrated in Figure 6.8 is the total cross section of $\gamma d \rightarrow K\Lambda\Sigma$ based on the Kaon-MAID model [20]. Numerous curves are drawn to exhibit the addition of the various

contributions of the six isospin channels. In the photon energy range discussed in this thesis, the production of a Σ hyperon is also possible, though it is dominated by Λ hyperon production. The minor contribution of Σ is seen in the Figure. 6.8, where the contributions of $\Sigma^{0,+,-}$ are all drawn and added to obtained the total cross section. It is obvious that the inclusion of the Σ contribution accounts for roughly 20% increase in the overall cross section above $E_\gamma = 1.05$ GeV. The results of the KM calculation suggest for energies lower than $E_\gamma \leq 1.075$ GeV that the reaction has the most sizable endowment from $K^+\Lambda$. Hereafter and to up an energy of 1.2 GeV, $K^0\Lambda$ becomes the formidable contributor.

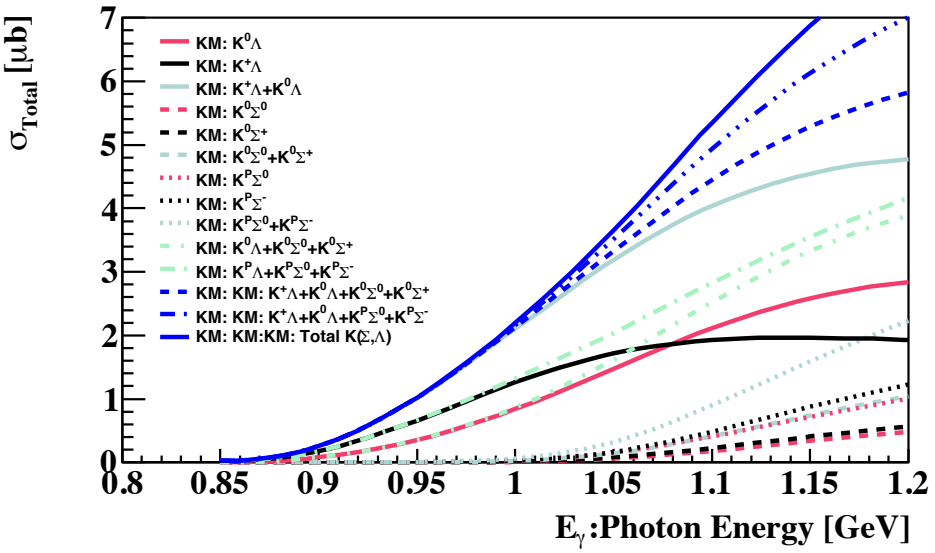

Figure 6.8: Total cross section of $\gamma d \rightarrow K$ (Λ, Σ) based on the Kaon-MAID model.

The total cross section of inclusive Λ measurement in the $\gamma d \rightarrow K^0 \Lambda p$ and $\gamma d \rightarrow K^+ \Lambda n$ reactions, as a function photon energy, predicted by the SLA is shown in Figure 6.9. In Figure 6.9 (right) the total cross section of inclusive Λ measurement by the addition of curves for $\gamma d \rightarrow K^0 \Lambda p$ and $\gamma d \rightarrow K^+ \Lambda n$ reactions as a function photon energy predicted by SLA are shown as the dashed curves. The $r_{K_1 K\gamma}$ parameter for the SLA is displayed in the figure and was allowed to range from $-(1.0 - 3.0)$. The SLA model, due to its free parameter, supplies an abundance of curves for the $K^0\Lambda$ reaction. It predicts that at all photon energies from the threshold up to 1.2 GeV, the strength of $K^0\Lambda$ is significantly more substantial than $K^+\Lambda$ for $r_{K_1 K\gamma} = -(0.5 - 2.0)$. At values of $r_{K_1 K\gamma} \geq -2.0$, the $K^+\Lambda$ reaction is responsible for the bulk of the cross section.

The ratio between the integrated cross section (upper) and total cross section (lower) of KM and SLA($r_{K_1 K\gamma}$) $= -1.5$ are seen in Figure 6.9, at hyperon angles of $0.9 \leq \cos\theta_\Lambda^{LAB} \leq 1.0$ are presented in Figure 6.10, where the ratio for the $K^+\Lambda$, $K^0\Lambda$, and the sum of

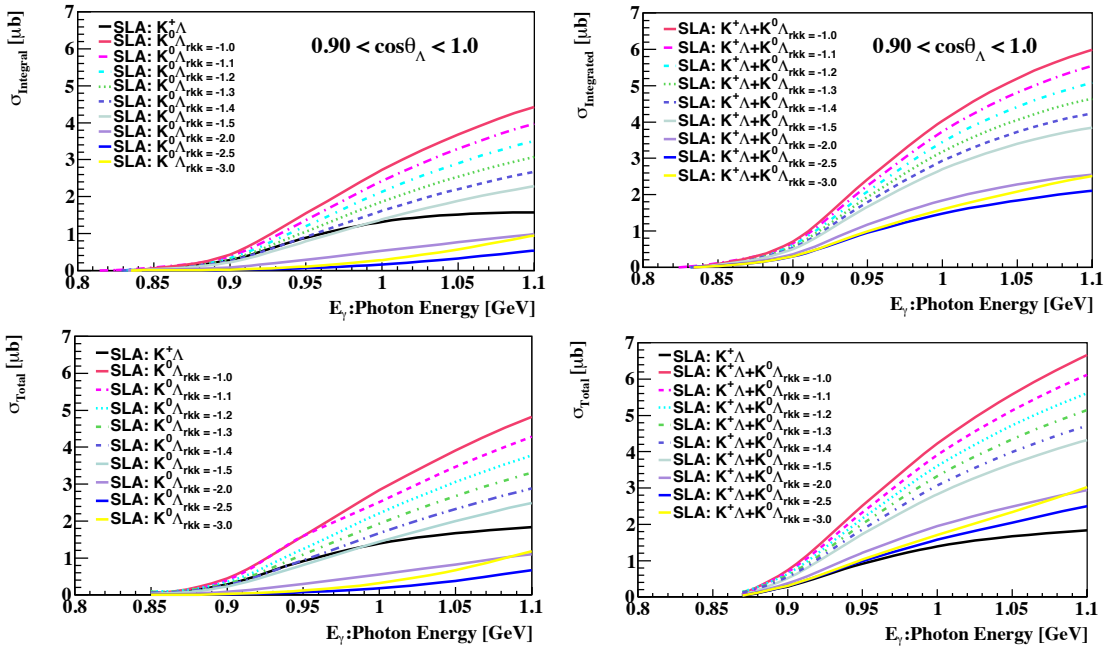

Figure 6.9: Cross sections of inclusive Λ measurement of the $\gamma d \rightarrow K^0\Lambda p$ reaction as a function of the incident photon beam energy. The angular region of integration, $0.9 \leq \cos\theta_\Lambda^{LAB} \leq 1.0$, in the laboratory frame is given in the upper figures. The total cross sections are in the lower panel. The predictions are for the SLA model [7], where the $r_{K_1K\gamma}$ parameter is indicated. The calculation for the $\gamma d \rightarrow K^+\Lambda n$ reaction is shown as the black solid curve.

their cross sections are the solid red, dashed black, and solid blue curves respectively.

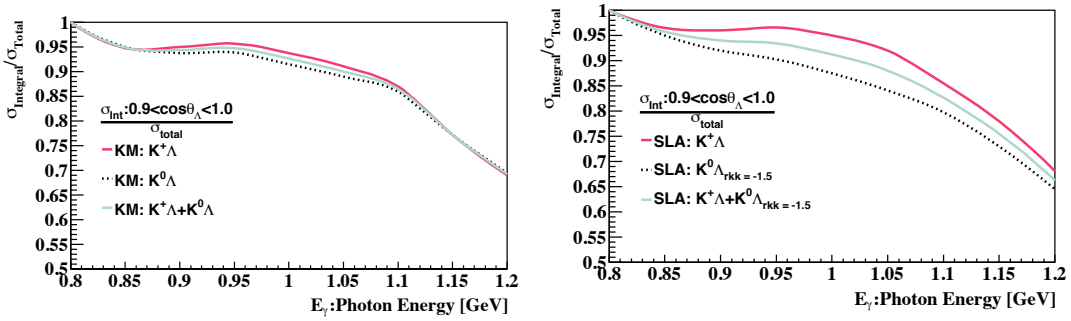

Figure 6.10: Ratio of integrated to total cross section for KM (left) and SLA($r_{K_1K\gamma}$) = −1.5 (right). The ratio for the $K^+\Lambda$, $K^0\Lambda$, and the sum of their respective predicted cross sections are the solid red, dashed black, and solid blue curves respectively

The energy dependence of total cross section in the elementary $\gamma n \rightarrow K^0\Lambda$ process for the KM and SLA model is shown in Figure 6.11. The SLA coupling constant $r_{K_1K\gamma}$ is displayed in the figure and was allowed to vary from $-(1.0 - 3.0)$ by increments of -0.5. The $\gamma p \rightarrow K^+\Lambda$ process has been considerably researched theoretically and experimentally,

see section 1.4 2.5 and 2.5.3, the $\gamma n \rightarrow K^0\Lambda$ process on the other hand has not. The S_{11} resonance plays an important role in the steep growth of the cross section for the former, while the latter has a slower rise in the cross section.

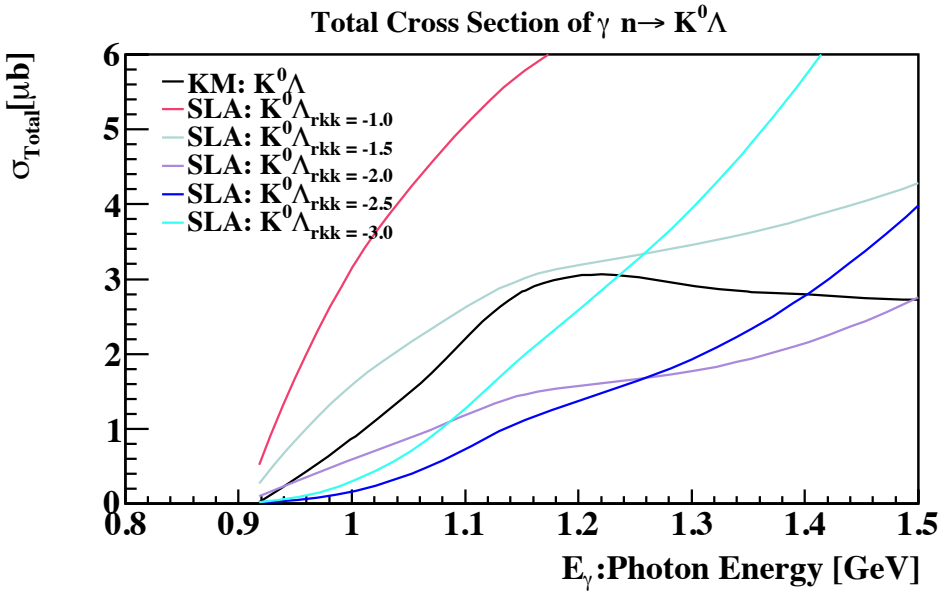

Figure 6.11: Total cross section of the elementary $\gamma n \rightarrow K^0\Lambda$ reaction as a function photon energy predicted by KM and SLA, where rK_1K_γ values are indicated in figure.

6.2.5 RPR: Excitation Function Prediction

Following this are RPR-2007 theoretical calculations of inclusive Λ integrated cross section as a function photon energy for $\gamma d \rightarrow K^0\Lambda p$, $\gamma d \rightarrow K^+\Lambda n$, and the sum of the processes are shown in Figure 6.12 are blue, red, and black curves respectively. The angles of integration covered the more forward angles of $0.9 \leq \cos\theta_\Lambda^{LAB} \leq 1.0$ (left) and entire acceptance of the spectrometer, $0.75 \leq \cos\theta_\Lambda^{LAB} \leq 1.0$ (right), in the laboratory frame. As with the calculation of the momentum dependent cross section, the computations were done at bin centered energies and anticipate that the energy dependent cross section of $\gamma d \rightarrow K^+\Lambda n$ reaction is more robust than the $\gamma d \rightarrow K^0\Lambda$p process.

The total cross section of $\gamma d \rightarrow K^0\Lambda p$, $\gamma d \rightarrow K^+\Lambda n$, and the total cross section of $\gamma d \rightarrow \Lambda(K^0, K^+)$ are drawn as the black, red, and blue curves curves respectively. In accord to the procedure adapted to the KM and SLA models, the ratio of the integral cross section and total cross was computed and is visible for the K^+, K^0, and the sum of them on the bottom left and right in Figure 6.12 respectively. The angle of integration in the ratio calculation was $0.75 \leq \cos\theta_\Lambda^{LAB} \leq 1.0$. In the threshold regime, at energies of $E_\gamma \leq 1.1$ GeV, the cross sections of $\gamma d \rightarrow K^0\Lambda$ and $\gamma d \rightarrow K^+\Lambda$ are concentrated at angles

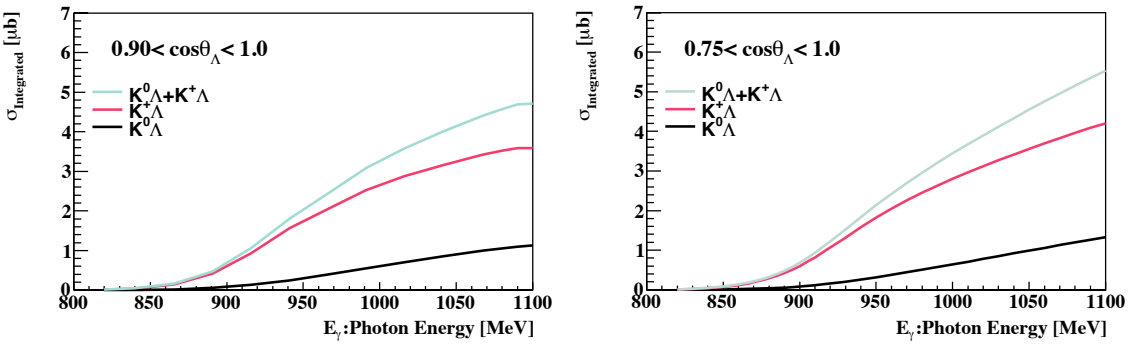

(a) Integrated cross section for 0.9≤ $\cos\theta_{\Lambda}^{LAB}$ ≤1.0 (left) and 0.75≤ $\cos\theta_{\Lambda}^{LAB}$ ≤1.0 (right)

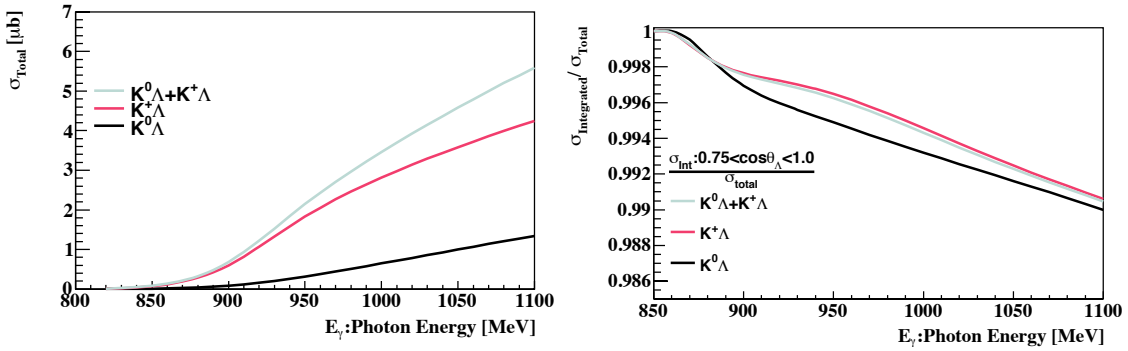

(b) Total cross section (left) and ratio of integrated 0.75≤ $\cos\theta_{\Lambda}^{LAB}$ ≤1.0 to total (right)

Figure 6.12: RPR-2007 theoretical calculations of Λ integrated cross section as a function photon energy for $\gamma d \to K^0\Lambda p$, $\gamma d \to K^+\Lambda n$, and their sum are shown are the black, red, and blue curves respectively. The cross sections were integrated over angular bins of 0.9≤ $\cos\theta_{\Lambda}^{LAB}$ ≤1.0 (left) and 0.75≤ $\cos\theta_{\Lambda}^{LAB}$ ≤1.0 (right) in the lab. The predictions of total cross section shown as blue, red, black curves respectively on the bottom left. The ratio of the integral cross section, 0.75≤ $\cos\theta_{\Lambda}^{LAB}$ ≤1.0, and the total cross sections are given in the bottom right .

below $\cos\theta \leq 0.80$, as is discernible in Figure 6.17, therefore a possibility of measuring the total cross section is feasible in a spectrometer that has acceptance in this small-scale angular region [118]. In the RPR framework, the cross section is reduced approximately 1% by measuring the reaction in the 0.75≤ $\cos\theta_{\Lambda}^{LAB}$≤1.0 region.

6.2.6 Angular Distributions: KM and SLA

The momentum integrated Λ angular dependent cross section in the lab was calculated for the KM, SLA, and RPR theoretical models. As the approach of each of theoretical model is different, especially regarding the inclusion of resonance terms and the use of form factors, the experimental results of the Λ angular distribution can further constrain models.

Figure 6.13 presents the elementary angular distributions of the $\gamma n \to K^0\Lambda$ reaction

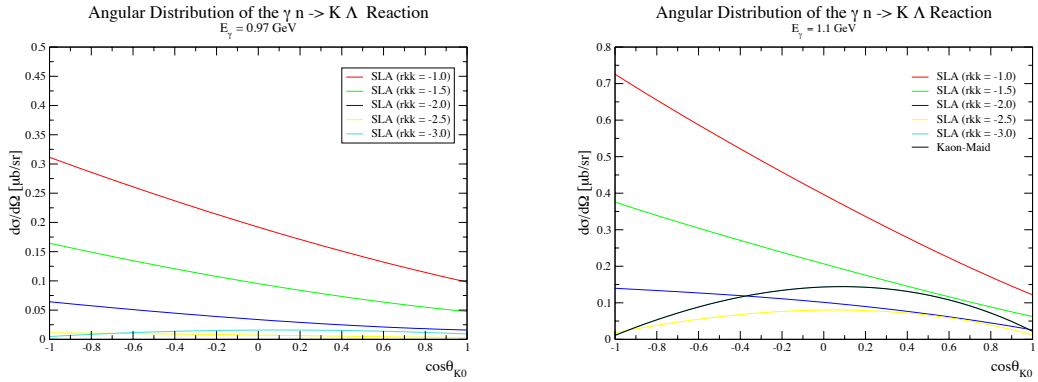

Figure 6.13: Angular distributions of the $\gamma n \rightarrow K^0\Lambda$ reaction for a specific photon of (left) 0.97 GeV and (right) 1.10 GeV predicted by the SLA and KM theoretical models. The rK_1 K_γ values are indicated in the legends.

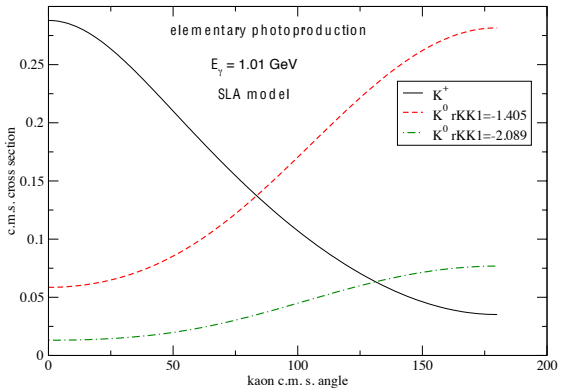

Figure 6.14: SLA $\gamma n \rightarrow K\Lambda$ elementary angular distributions at 1.01 GeV.

for a specific photon of (left) 0.97 GeV and (right) 1.10 GeV, predicted by the SLA and Kaon-MAID theoretical models in the kaon center of momentum frame. The $r_{K_1K\gamma}$ parameter for the SLA models is displayed in the figure and was allowed to vary from $-(1.0-3.0)$ by increments of -0.5. The SLA rK_1K_γ = -1.4 and -2.0 predictions of the angular distribution of the elementary kaon production are seen in Figure 6.14. From the curves, it apparent that $K^+\Lambda$ and $K^0\Lambda$ are opposite in respect to being forward or backwards biased.

Next presented are the results of the KM model where the cross section was calculated as a function of $\cos\theta_\Lambda^{LAB}$. The angle dependent cross sections of the $d(\gamma,\Lambda)K^+n$ and $d(\gamma,\Lambda)K^0p$ reactions and the summation of the contributing cross sections in the lab ,as a function of $\cos\theta_\Lambda^{LAB}$, in the KM framework are seen in Figure 6.15 for five photon E_γ bins of $(a)0.95-1.0, (b)1.0-1.02, (c)1.02-1.04, (d)1.04-1.06, (e)1.06-1.08$GeV. The curves for $K^+\Lambda$, $K^0\Lambda$, and their sum are the black, red, and aqua curves respectively. It

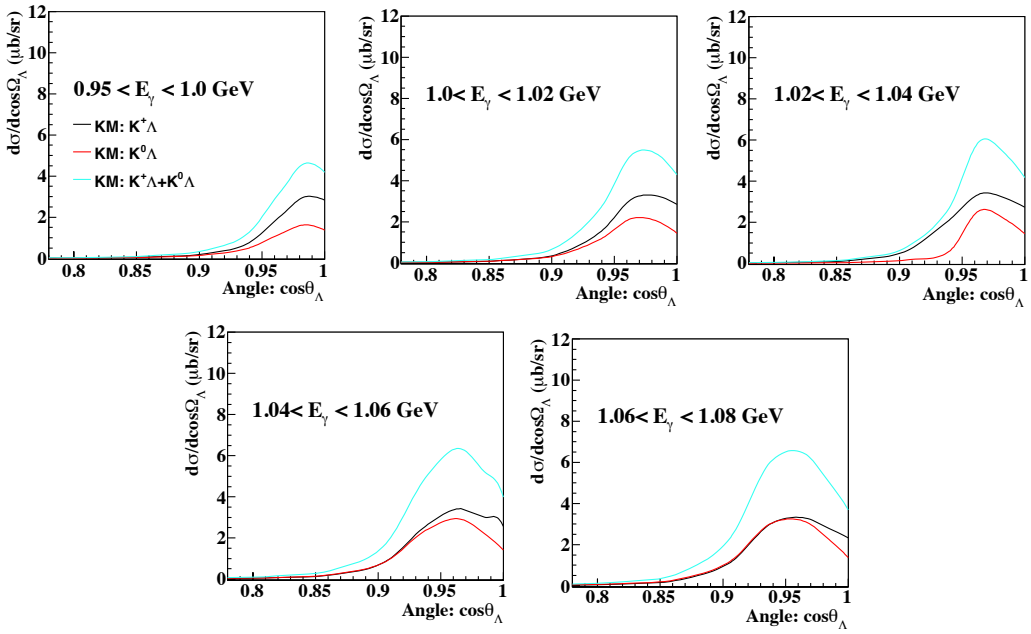

Figure 6.15: Angular distributions of $d(\gamma,\Lambda)K^+n$ and $d(\gamma,\Lambda)K^0p$ reactions and their cross section addition, based on KM, integrated over five E_γ bins corresponding to $(a)0.95-1.0, (b)1.0-1.02, (c)1.02-1.04, (d)1.04-1.06, (e)1.06-1.08$GeV as the black, red and aqua curves respectively.

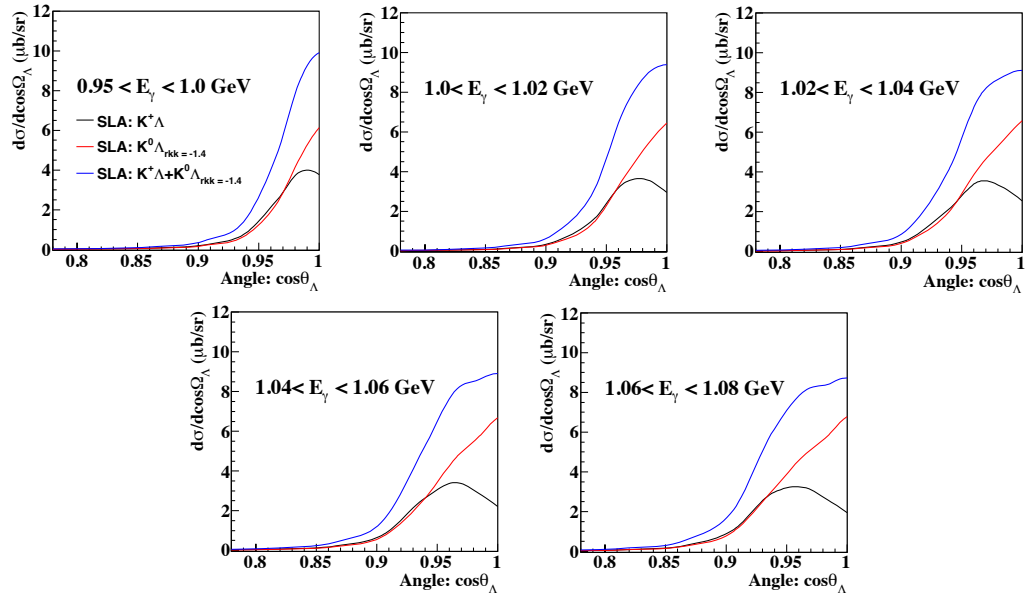

Figure 6.16: Angular distributions of the $d(\gamma,\Lambda)K^+n$ and $d(\gamma,\Lambda)K^0p$ reactions and the sum of the amplitudes, based on SLA, integrated over five E_γ bins corresponding to $(a)0.95-1.0, (b)1.0-1.02, (c)1.02-1.04, (d)1.04-1.06, (e)1.06-1.08$GeV as the black, red and blue curves respectively.

is apparent from the curves in the figure that the $d(\gamma,\Lambda)K^+n$ process is the dominant contributing amplitude at lower energies but at photon energies larger than 1.06 GeV the amplitudes achieve equivalent status. The angular dependent cross section peaks at approximately $0.95 \leq \cos\theta_{\Lambda}^{LAB} \leq 0.98$ and declines towards $\cos\theta_{\Lambda}^{LAB} = 1.0$.

The Λ momentum integrated angular distribution of the $d(\gamma,\Lambda)K^+n$ and $d(\gamma,\Lambda)K^0p$ reactions were subsequently calculated with the SLA model in the laboratory frame. The predictions for each process and their addition are given in Figure 6.16. The curves for the $K^+\Lambda$, $K^0\Lambda$, and their sum are the black, red, and blue curves respectively. The cross sections for the SLA predictions are significantly larger than those of the KM model for laboratory angles of $\cos\theta \geq 0.95$. Unlike the results of the KM calculations the $d(\gamma,\Lambda)K^0p$ process primarily contributes to Λ photo production in the SLA framework at small angles [82].

6.2.7 Angular Distributions: RPR Predictions

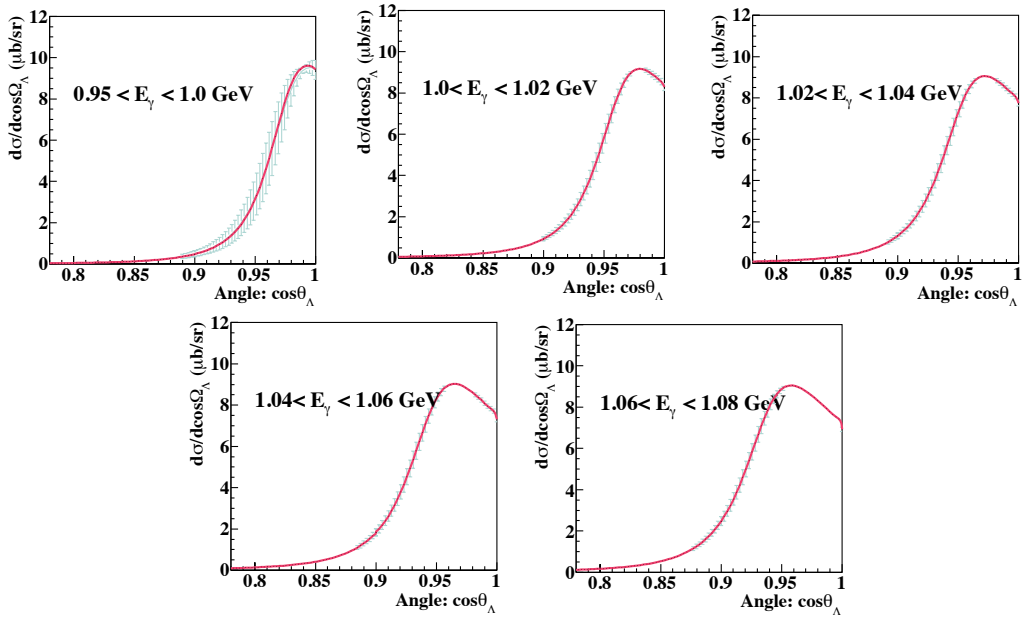

Figure 6.17: Angular distributions of the $\gamma d \rightarrow \Lambda K N$ reaction based on the RPR model [8, 25, 27, 28, 29] for photon energy ranges of $(a)0.95-1.0, (b)1.0-1.02, (c)1.02-1.04, (d)1.04-1.06, (e)1.06-1.08$ GeV

Angular distributions of the $\gamma d \rightarrow \Lambda K N$ reaction in the laboratory frame as a function of the momentum of Λ which based on the RPR-2007 model are presented in Figure 6.17 for bin centered photon energy in ranges of of left $(a)0.95-1.0, (b)1.0-1.02, (c)1.02-1.04, (d)1.04-1.06, (e)1.06-1.08$ GeV. The curves are somewhat similar to the SLA calculations, however unlike the cross sections of the SLA that does not decline, here

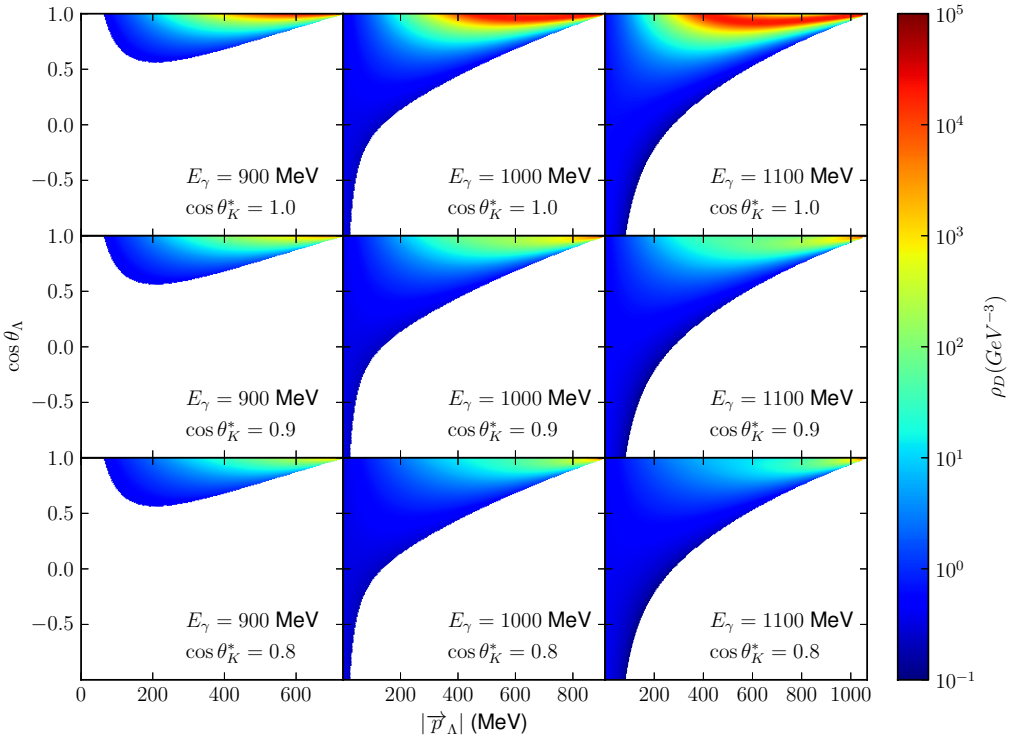

Figure 6.18: Deuteron density as calculated within the WJC model [30, 31] as a function of $cos\theta_\Lambda$ and $\vec{p}_\Lambda$ at various values of E_γ. Each point in the phase space of the reaction determines a single value for $|\vec{p}_N|$ assuming the RPWIA and the corresponding deuteron density is plotted[32]

the RPR curves had a reduction in the magnitude at small angles. The RPR and KM predictions produced a prominence in the $K^+\Lambda$ reaction which exhibits the fall off, opposite of the SLA curves. Figure 6.18 is the deuteron density as calculated within the WJC model [30, 31] as a function of $cos\theta_\Lambda$ and $|\vec{p}_\Lambda|$ at various values of E_γ. Each point in the phase space of the reaction determines a single value for $|\vec{p}_N|$ assuming the RPWIA and the corresponding deuteron density. Details of the radial wave function and momentum space distribution for the WJC-1 model can be found in Appendix C. The deuteron density shapes the cross section in the $d(\gamma, K)YN$ reaction and diminishes congruently with a heightened relative three-momentum of the proton and neutron inside the deuteron[9, 25, 26].

6.2.8 Λ Recoil Polarization: KM and SLA Calculations

The calculations of the Λ hyperon recoil polarization (P_Λ) in the laboratory frame as a function of momentum was conducted based on spectators kinematics for both the KM

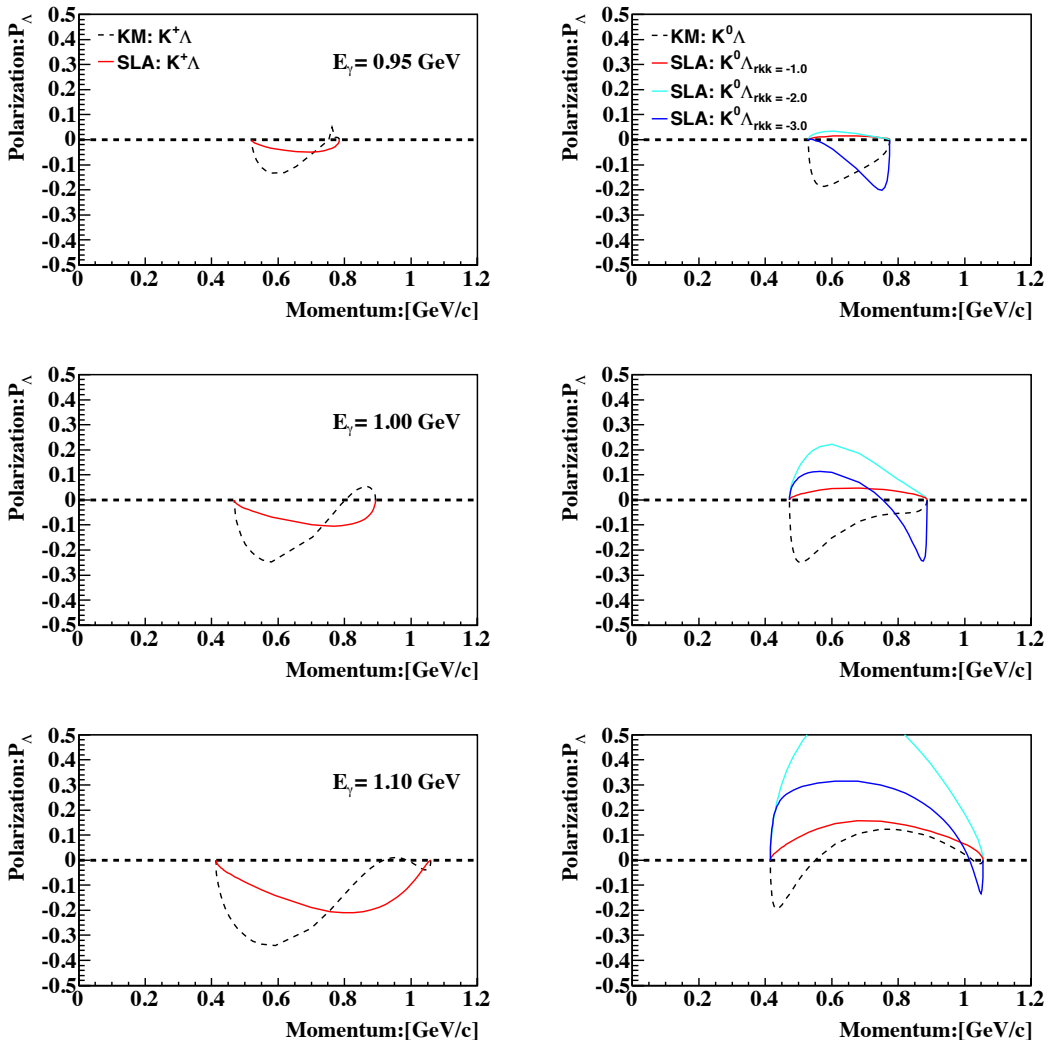

Figure 6.19: Momentum dependence of Λ polarization in the Laboratory frame. The KM and SLA predictions of $\gamma d \to K^0 \Lambda p$ and $\gamma d \to K^+ \Lambda n$ are given left to right respectively. The photon energies bins of 0.95, 1.0 and 1.1 GeV are given top to bottom.

and SLA isobar models. Here, the predictions were made for three specific photon energies, those being $E_\gamma = 0.95$, 1.0, and 1.1 GeV. The results of the calculations as displayed in Figure 6.19, where KM and SLA predictions of $\gamma d \to K^0 \Lambda p$ and $\gamma d \to K^+ \Lambda n$ are given left to right respectively. The curves for KM are shown as the dashed black curve and the SLA curves are seen are red, light blue and blue for 0.95, 1.0, and 1.1 GeV. The KM and SLA models have distinctively different descriptions of the polarization of Λ in terms of the reaction. Both models suggest an absolute value of less that 0.3 for either process, while cross sections are similar at lower photon energies.

6.2.9 Λ Recoil Polarization: RPR Predictions

The RPR-2007 curves of the angular dependence of Λ polarization are showcased in Figure 6.20. The figure shows the calculations for both $\gamma d \rightarrow K^0\Lambda$ p reactions. The region of integration were angular bins of $\cos\theta_\Lambda^{LAB} = 0.95 - 1.0$ (left) and $0.95 - 1.0$ (right). The results of bin centered energy regions of $0.9 - 1.0$, and $0.9 - 1.1$ GeV are shown top to bottom respectively. The calculations exhibit a modest value of the Λ polarization that has of energy and momentum dependence on it's sign. The calculations show a value close to zero in the forward hemisphere, and for the angular integration range of $\cos\theta_\Lambda^{LAB} = 0.90 - 0.95$ the asymmetry is negative at low momenta [9, 26]. In measurement of the polarization, the RPR model indicates the $K^0\Lambda$ channel has a large effect in suppressing the recoil asymmetry.

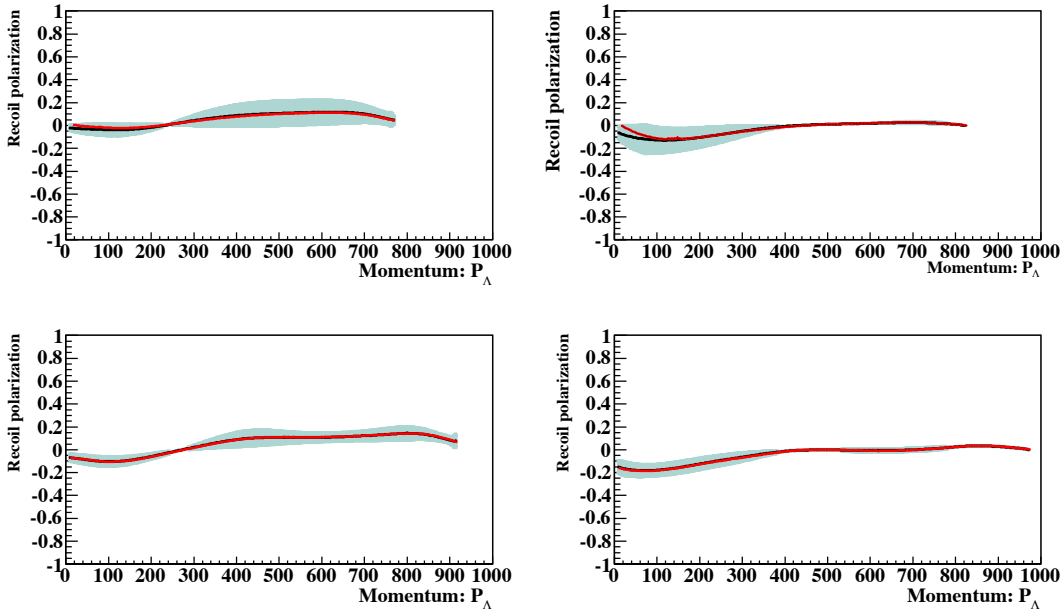

Figure 6.20: Angular dependence of Λ polarization. The plots are based on RPR-2007 model for spectator kinematics. The figure shows the calculations for $\gamma d \rightarrow \Lambda X$ reactions. The region of integration covered the forward hyperon angles of $\cos\theta_\Lambda^{LAB} = 0.95 - 1.0$ (left) and $0.95 - 1.0$ (right). The results of bin centered energy regions, $0.9 - 1.0$, and $1.0 - 1.08$ GeV are shown top to bottom respectively.

6.3 Comparison to Theoretical Calculations

6.3.1 KM and SLA: Momentum Distributions

We then proceed to employ the various theoretical calculations as a comparison to the experimentally yielded outcomes. The initial comparison is made with the inclusive measurement of Λ momentum distribution of Λ for the KM and SLA models discussed in section 6.2.1. The comparison of results with KM and SLA calculations for the addition of cross sections of the $\gamma d \rightarrow K^0 \Lambda p$ and $\gamma d \rightarrow K^+ \Lambda n$ reactions, for photon energy bins of (top) 0.9 - 1.0 and (bottom) 1.0 to 1.08 GeV in the lab frame are shown in Figures 6.21 and 6.22. The data integrated over two angular regions of $\cos\theta_{\Lambda}^{LAB} = 0.95{-}1.0$ and $0.90{-}0.95$ are shown left to right respectively. The $r_{K_1 K_\gamma}$ coupling constant free parameter for the SLA model is displayed in the figures. The KM results do a passable job of describing the overall shape of the distributions in both energy and angular integration zones. Nevertheless, it fails to give an accordance with the strength of the measured momentum dependent differential cross section in the forward hemisphere. In these zones, with respect to both integrated photon energy bins, it under predicts the cross section by approximately 50% at the Λ momenta of $0.65 \leq P_{\Lambda}^{LAB} \leq 0.90$. GeV/c. The SLA model has a good agreement with the shape and magnitude of the data for $r_{K_1 K_\gamma} = -(1.0 - 1.5)$ replicating it best in the forward scattering angles with $r_{K_1 K_\gamma} = -1.4$ drawn as the aqua curve in Figure 6.22.

6.3.2 RPR: Momentum Distributions

The experimentally determined background subtracted angle integrated momentum differential cross section was additionally compared to the RPR -2007 predictions of the inclusive measurement of Λ. As shown in Figure 6.23 the data is confronted with the theoretical calculations of energy-averaged and Λ angle-integrated inclusive cross sections as a function of Λ momentum for the $\gamma d \rightarrow \Lambda K N$ reaction, for the energy averaged (top) $0.9 - 1.0$ and (bottom) $1.0 - 1.1$ GeV. The data was integrated over hyperon scattering angles equivalent to $\cos\theta_{\Lambda}^{LAB} = 0.95 - 1.04$ (right) and $0.9 - 0.95$ (left), in the laboratory frame. The model calculation derived for bin centered photon energies is able to roughly produce the shape and intensity of the data for the higher energy bin particularly in the forward angular integration range. In the lower integrated energy region, $E_\gamma = 0.9 - 1.0$ GeV, the model performs adequately in the more backward angular bin within the errors.At the most forward scattering angles the model indicates a sharper decrease in shape with a maximum Λ momentum of around 0.8 GeV. Due to the unknown helicity, introduced from the ratio of the magnetic transition moments of the $D_{13}(1900)$ and $P_{13}(1900)$

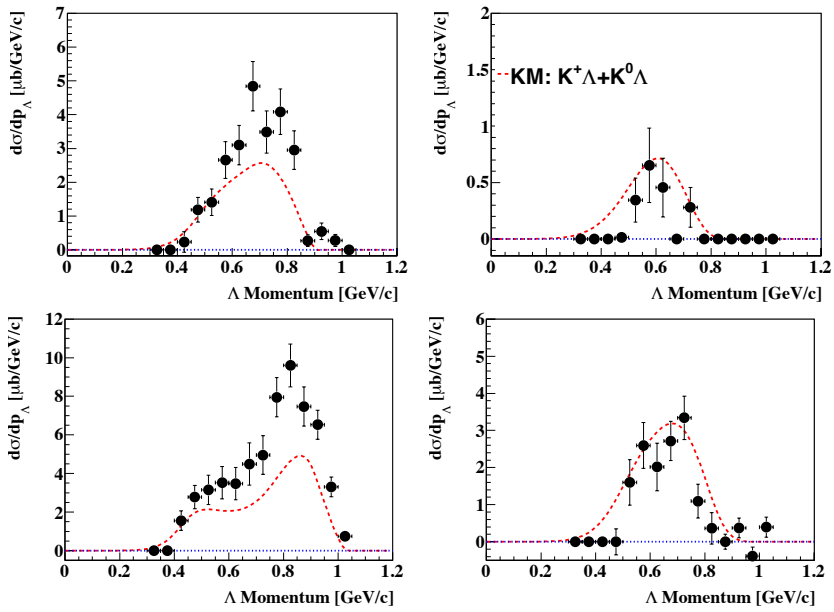

Figure 6.21: Comparison with KM calculations of the Λ momentum cross sections for the addition of amplitudes of the $\gamma d \rightarrow K^0 \Lambda p$ and $\gamma d \rightarrow K^+ \Lambda n$ for photon energy bins of (top) $0.9 - 1.0$ and (bottom) $1.0 - 1.08$ GeV. The integrated hyperon angles of $0.95 - 1.0$ and $0.90 - 0.95$ ($\cos\theta_{\Lambda}^{LAB}$) are shown left to right respectively.

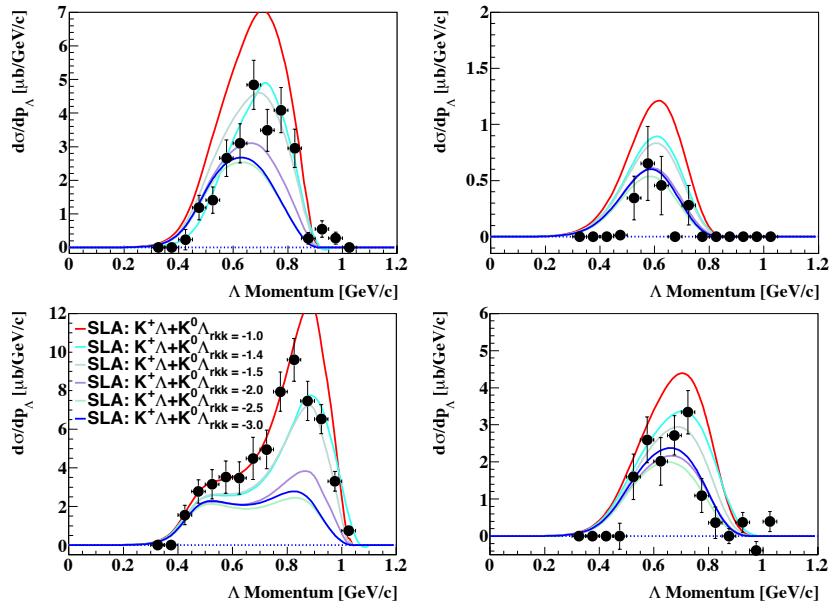

Figure 6.22: Comparison to calculations of the Λ momentum cross sections. The angular and energy presentation format is the same as in Figure 6.21. The $r_{K_1 K_\gamma}$ parameter for the SLA model is displayed in the figure.

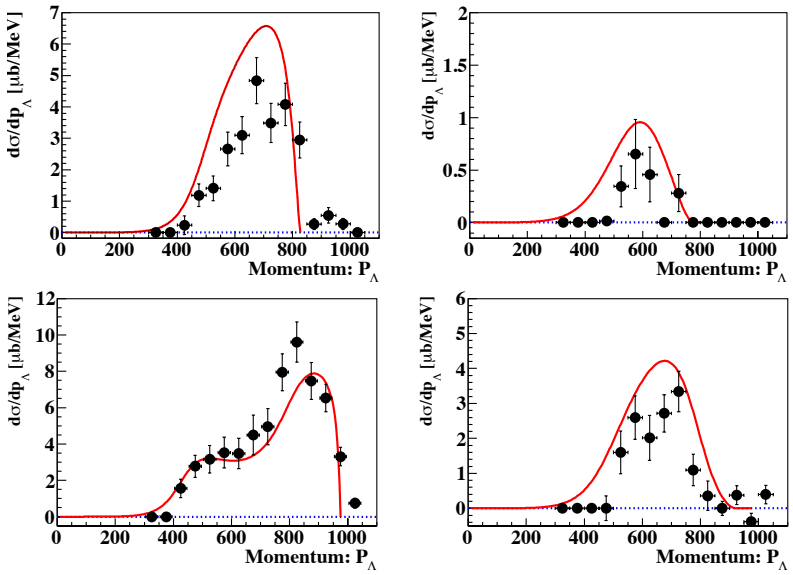

Figure 6.23: Comparison to RPR calculations of Λ momentum dependent cross sections for $\gamma d \rightarrow \Lambda K N$, for the bin centered photon energy of $0.9-1.0$ (top) and $1.0-1.1$ (bottom) GeV. The data was integrated over hyperon scattering angles of $\cos\theta_{\Lambda}^{LAB} = 0.95-1.0$ (left) and $0.9-0.95$ (right).

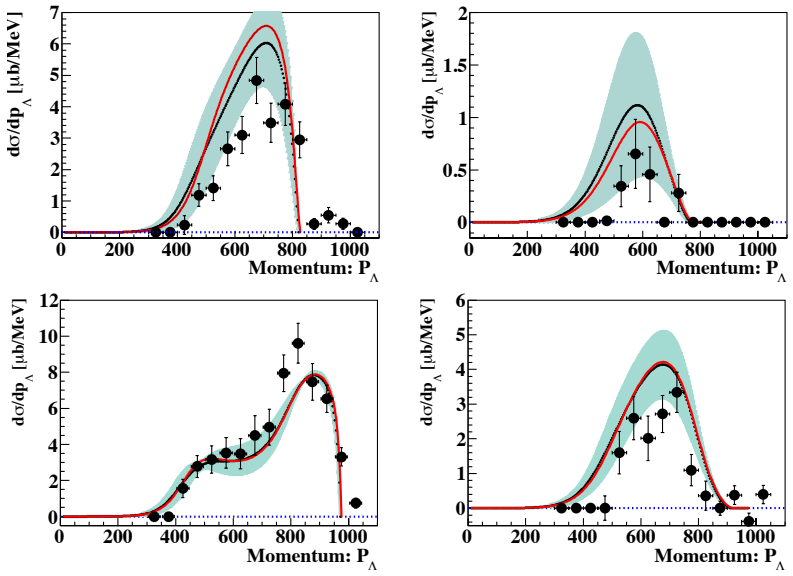

Figure 6.24: Comparison to RPR of Λ momentum dependent cross sections for $\gamma d \rightarrow \Lambda K N$ with theoretical uncertainties shown as the light blue shaded region. The data was integrated over hyperon scattering angles of $\cos\theta_{\Lambda}^{LAB} = 0.95-1.0$ (left) and $0.9-0.95$ (right).

resonant states, for which these calculations was allowed to vary between $-(2-2)$, some theoretical inaccuracy were introduced, hence the comparison of the data and theory with the inclusion of these errors was also performed and given in Figure 6.24 as the light blue

shaded region. The angular and energy presentation format is the same as in Figure 6.23. The model concurs with the reported data within the theoretical uncertainties.

6.3.3 Integrated Cross Section: KM and SLA

The analysis procedure involved an inclusive measurement of Λ with the use of a deuteron target therefore expected to have contributions from K^+ and K^0 production. The results are compared to the addition of the amplitudes calculated for integrated and total cross section of the $\gamma d \rightarrow K^0 \Lambda p$ and $\gamma d \rightarrow K^+ \Lambda n$ reactions as a function photon energy. The comparison of the measured cross sections integrated over 25 MeV energy bins to the predictions by the KM of the forward hyperon angular region of integration, $0.9 \leq \cos\theta_{\Lambda}^{LAB} \leq 1.0$ is presented in Figure 6.25 The data has a shape that is agreeable to the KM predictions but is far larger in magnitude for the total integrated region.

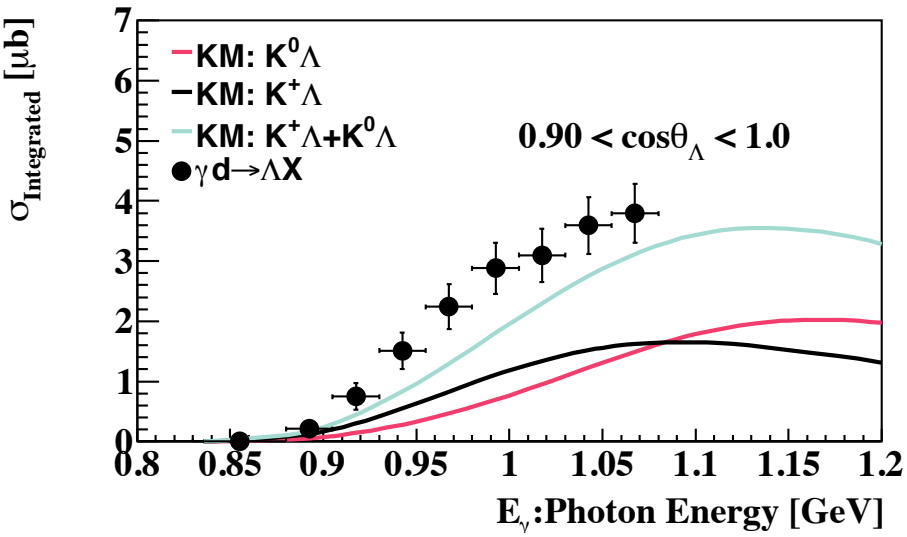

Figure 6.25: Comparison to the Λ integrated cross section of the sum of the $\gamma d \rightarrow K^0 \Lambda p$ and $\gamma d \rightarrow K^+ \Lambda n$ reactions as a function photon energy predicted by the KM model.

We also perform a comparison with the calculations yielded from the SLA model. An identical comparability approach is applied such that the integrated cross section results in the forward hemisphere as a function of the photon energy are given in Figure 6.27, where the $r_{K_1 K_\gamma}$ parameter is presented in the legend. Our data in the restricted angular region has similar behavior to that of the SLA curves and the rise in the cross section with the increase in photon energy is present, for the case of the comparison to the addition of the $K^0\Lambda$ or $K^+\Lambda$ cross section. The cross section findings are similar to the predictions where the fitting parameter has been tuned to $-(1.5 - 1.0)$. However, the ascending energy dependence of the cross section is best replicated with the $r_{K_1 K_\gamma}$ value set to -1.4.

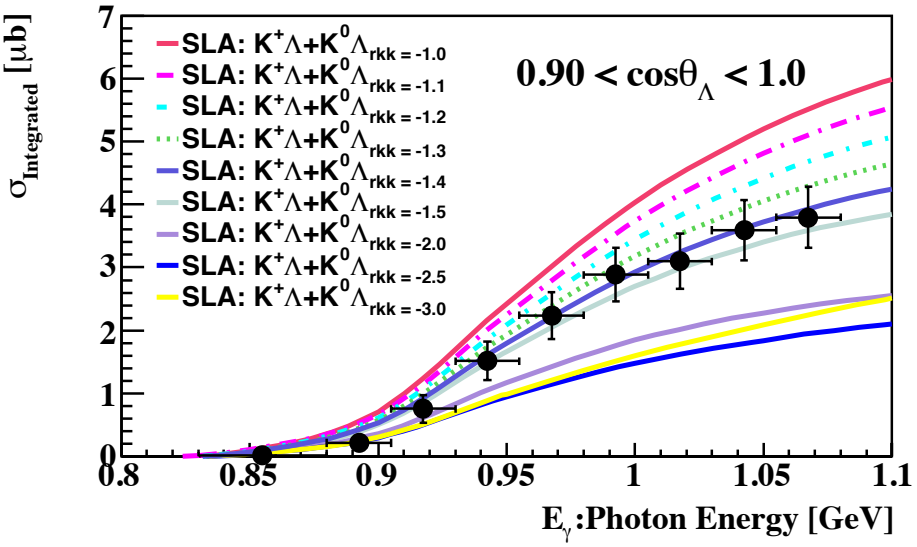

Figure 6.26: Comparison to the Λ integrated cross section as a functin photon energy, for the the sum of $\gamma d \rightarrow K^0 \Lambda p$ and $\gamma d \rightarrow K^+ \Lambda n$ reactions as a function photon energy predicted by the SLA model. The $r_{K_1 K_\gamma}$ parameter is indicated in the figure.

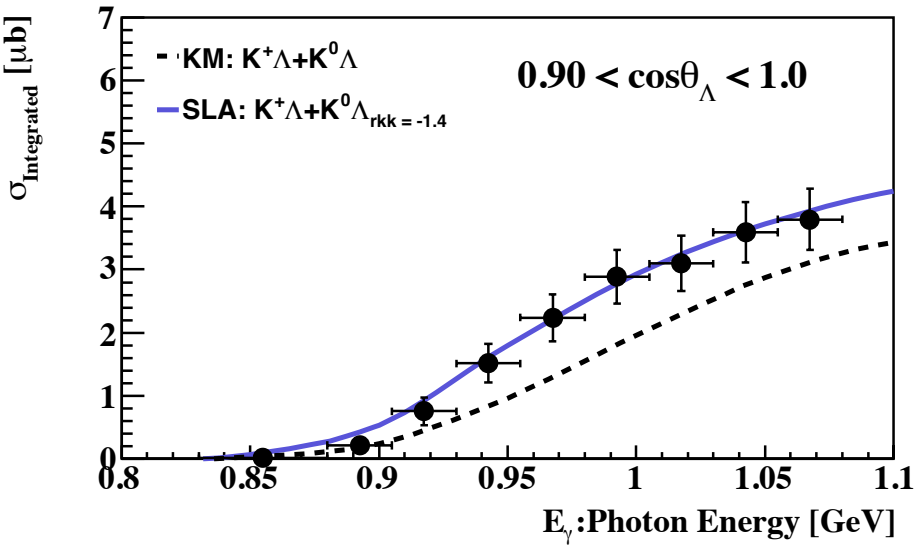

Figure 6.27: Comparison to the Λ integrated cross section as a function photon energy predicted by the SLA and KM models where the amplitudes of $\gamma d \rightarrow K^0 \Lambda p$ and $\gamma d \rightarrow K^+ \Lambda n$ reaction are added.

Thereafter, a comparison to the both KM and SLA results is performed for the forward angular region of integration as is evident in Figure 6.27, where the KM and SLA curves are drawn as the dashed and solid respectively.

The conclusion drawn regarding the best reproduction of the data by the SLA model

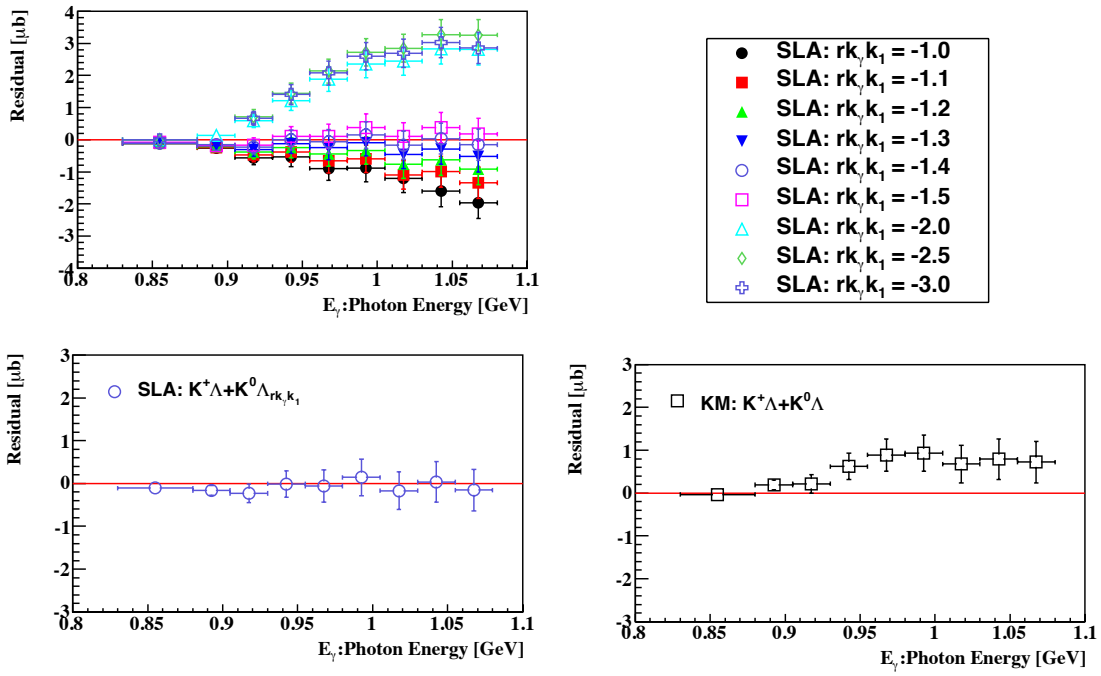

Figure 6.28: Residuals of SLA models for different $r_{K_1K_\gamma}$ values indicated by the marker style shown in the legend (a). Residual of SLA models calculations for $r_{K_1K_\gamma} = -1.4$ (b). Residual of KM model (c)

$r_{K_1K_\gamma} = -1.4$ was purely qualitative, based on the visual representation shown in Figures 6.27 and 6.27. A more rigorous approach was conducted to strengthen the premise to which the conclusion is drawn. As as result, the residual of each curves obtained by the change of the $r_{K_1K_\gamma}$ parameter was calculated. The residual was simply defined as the numerical difference between the experimental values and the theoretical prediction at each specific energy bin. The residual values for each $r_{K_1K_\gamma}$ value was plotted as a function of the photon energy in Figure 6.28 (a). The residual corresponding the SLA model, $r_{K_1K_\gamma} = -1.4$ (c), is plotted in Figure 6.28(c) and the KM residual in (d). The residual distribution can be used to evaluate if a model's fit to the gathered data was accurate. The residuals should, in all likelihood, estimate the random errors that govern the interrelations between the independent and dependent variables in a statistical relationship. Thus, if the calculated residuals depict a random response, it has the implications that a model fits the data reasonably well. Conversely, if a non-random structure is observed in the residuals, it is a unmistakable signal that a model fits the data poorly.

6.3.4 Integrated Cross Section: RPR

Experimentally measured and obtained measured cross sections integrated over 25 MeV energy bins are then compared to the theoretical results of the RPR model[8, 25, 27, 28,

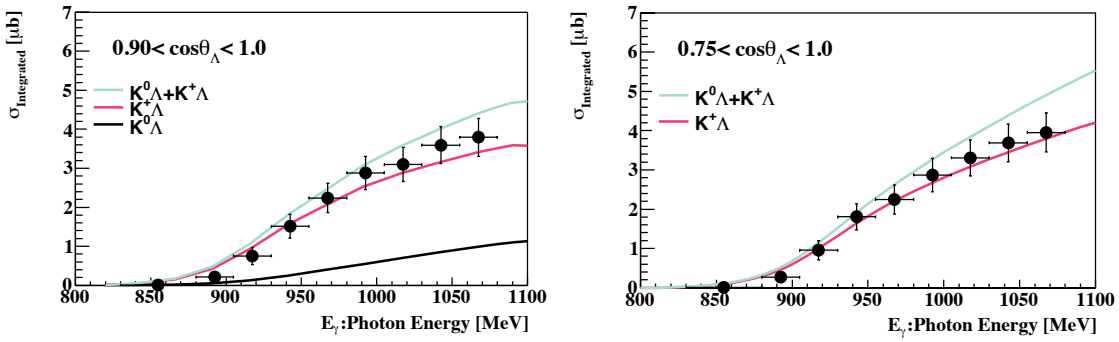

Figure 6.29: Comparison to RPR calculation of sum integrated cross sections of the $\gamma d \rightarrow K^0\Lambda p$ and $\gamma d \rightarrow K^+\Lambda n$ reactions as a function photon energy. The left figure is comparison of the forward angular integration region and the right the comparison of full integration region.

29] in Figure 6.29. The juxtaposition is made to the summation of the cross sections corresponding to the integrated cross sections of the $\gamma d \rightarrow K^0\Lambda p$ and $\gamma d \rightarrow K^+\Lambda n$ reactions as a function photon energy, in angular integration regions of $0.9 \leq \cos\theta_\Lambda^{LAB} \leq 1.0$ (left) and $0.75 \leq \cos\theta_\Lambda^{LAB} \leq 1.0$ (right). The RPR calculations describe the shape and size of the data, for both angular integration hemispheres, shown as light blue curves. However, in the $0.9 \leq \cos\theta_\Lambda^{LAB} \leq 1.0$ region the curves slightly over gauges the shape with increasing photon energy, but undershoots the data in the larger angular integrations region.

6.3.5 Estimated Total Cross Section: KM and RPR

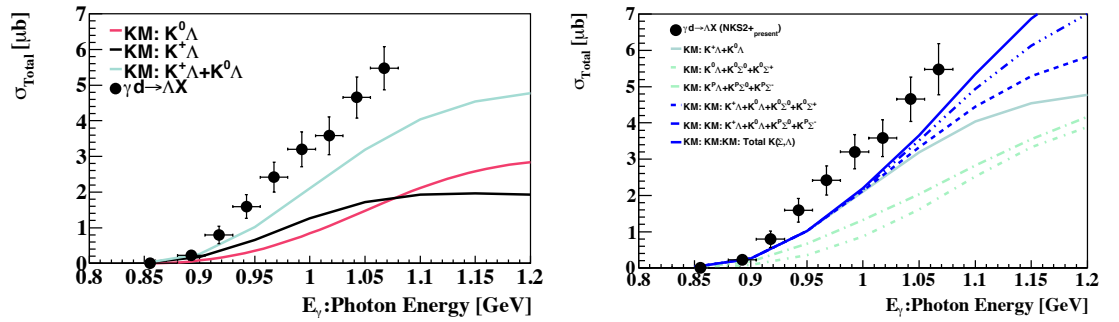

Figure 6.30: Extrapolated total $d(\gamma,\Lambda)$X cross section compared the KM model. The additions of $\gamma d \rightarrow K^0\Lambda p$ and $\gamma d \rightarrow K^+\Lambda n$ processes are on the left and the inclusion of Σ contribution to the total cross section is seen on the right.

The total cross section of Λ photoproduction in the $d(\gamma,\Lambda)$X reaction integrated over 25 MeV bins was estimated with the theoretical predictions afforded by the KM and RPR models. The results were discussed in the previous chapter, accordingly, here we graphically compare the numerical values obtained to the predictions of each model. The

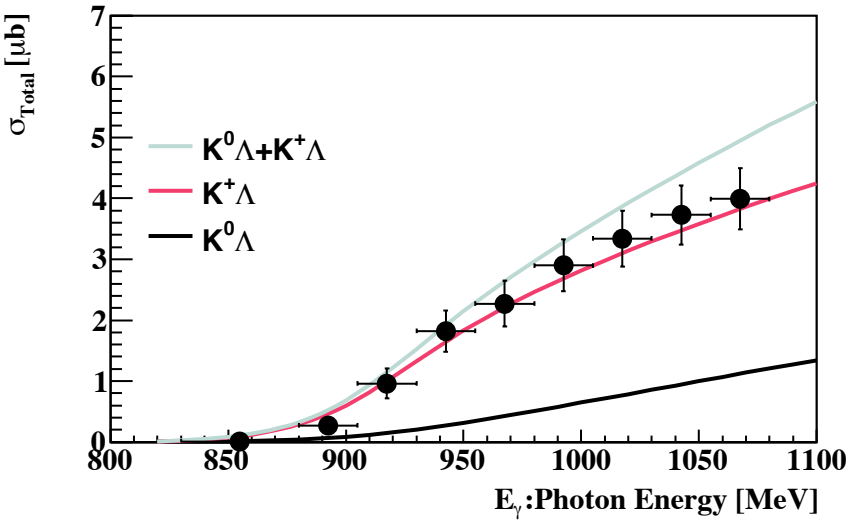

Figure 6.31: Extrapolated total $d(\gamma,\Lambda)$X cross section obtained with and compared to the RPR model.

comparison of the KM models predictions and the data are illustrated in Figure 6.31. Though the contributions of Σ are expected to be small the are included in the model predictions of the KM in this comparison. Inceptively we compared the prediction of the KM model in the absence of the known, but expected minor contribution of Σ production, next it was included. Yet, even with the inclusion of the calculated Σ contributions the KM results maintains its under prediction of the Λ cross section.

The evaluation of the RPR predictions and the data are illustrated in Figure 6.31. The contribution of the $K^+\Lambda$, $K^0\Lambda$ and the addition of their respective contributions are the red, black and blue curves respectively. The calculations in the RPR approach describes the data well at photon energies under 1.0 GeV but predicts a lower magnitude for $E_\gamma \geq$ 1.0 GeV.

6.3.6 Angular Distributions

The momentum integrated angle dependent differential cross section of $d(\gamma,\Lambda)$X is compared with the results of the KM, SLA and RPR calculations. Here, the confrontation does not suffer from any disturbance from the presence of the Σ hyperon production process. The background subtracted angular distributions of the $\gamma d\rightarrow \Lambda$X reaction as a function of the scattering angle of Λ, ($\cos\theta_\Lambda^{LAB}$), are compared to theoretical calculations based on the RPR model, including theoretical uncertainties, and are presented in Figure 6.32 for E_γ bins of (a) $0.95-1.00$ GeV, (b) $1.00-1.02$ GeV, (c) $1.02-1.04$ GeV, (d) $1.04-1.06$ GeV and (e) $1.06-1.08$ GeV.

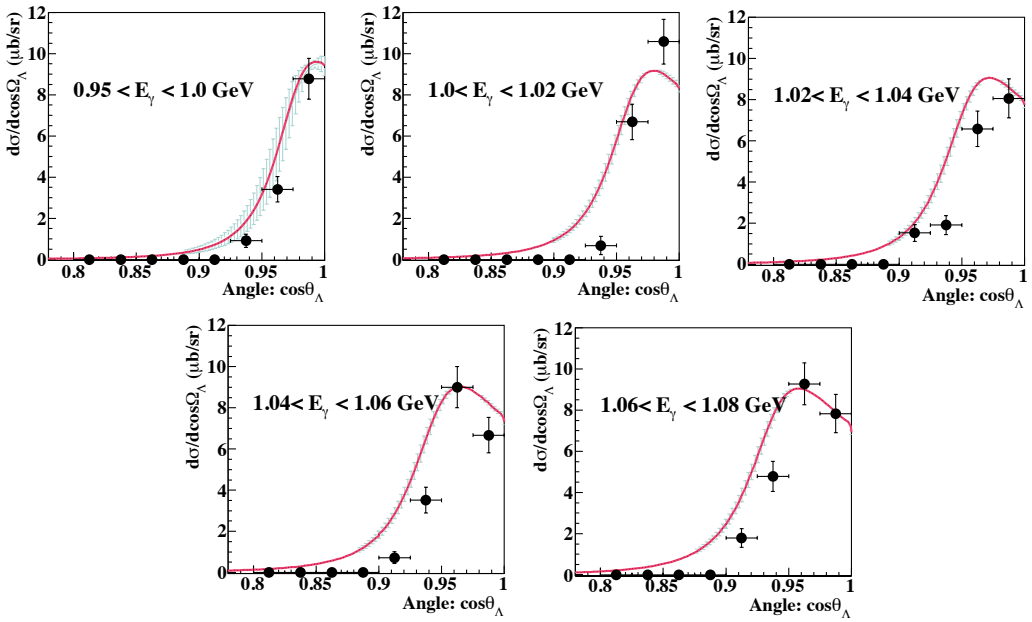

Figure 6.32: Background subtracted angular distributions of $\gamma d \rightarrow \Lambda K N$ integrated over five E_γ bins equated with the RPR model predications and associated theoretical uncertainties [8, 25, 28].

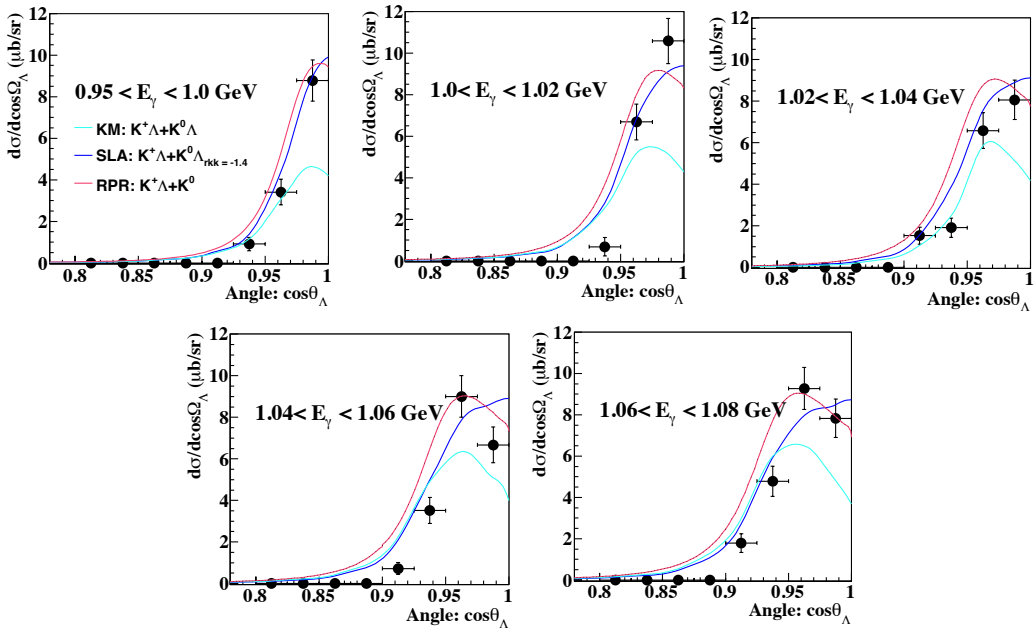

Figure 6.33: Background subtracted Λ angular distributions integrated over five photon energy (E_γ) bins alongside the predictions of $\gamma d \rightarrow \Lambda K N$ of KM, SLA and RPR (excluding theoretical uncertainties) models.

The RPR obtained curves furnished for bin centered energies accomplishes a fairly good description of the experimental results achieving agreements within the statistical error. In the lower energy bins (a) $0.95 - 1.0$ GeV , (b) $1.0 - 1.02$ GeV, in Figure 6.32, the model over predicts the cross section data by approximately $20 - 30\%$. Whereas for higher energy bins, it is evident that the model over approxiamates the cross sections by around $10 - 15\%$ for $\cos\theta_{\Lambda}^{LAB} \leq 0.95$. The strongest accord between the data and the RPR predictions exist in the (c) $1.02 - 1.04$ GeV energy bin. The momentum distribution of the nucleons inside the deuteron peaks at forward Λ production in the laboratory frame and forward kaon production in the kaon-nucleon CM frame. Obviously, this is only one factor that goes into a cross section calculation, but it determines the shape in an important way. At the highest energy you can see for example that the peak moves away from $\cos\theta_{\Lambda} = 1$. According the angular distribution peaks at $\cos\theta_{\Lambda} = 1$ at the lowest energies and thus the peaks shifts with increasing photon energies [32]. The momentum distribution for the $K^0\Lambda$ appears identical because of the small kaon mass difference. The strength of the cross sections differs however because the elementary process is different.

The background subtracted Λ angular distribution integrated over five E_{γ} was compared to the predictions of the KM, SLA(rk_1k_{γ} = -1.4) and RPR predictions of γd$\rightarrow\Lambda$KN as calculated P. Vancraeyveld [32] and P. Bydzovsky [119]. Previous calculation of the momentum integrated angular cross sections for the SLA(rk_1k_{γ} = -2.0) were reported but were based on fits to published NKS2 data that was later corrected [3, 83]. Displayed in Figure 6.33, the KM, SLA and RPR curves are the black, red and blue curves respectively. The RPR and SLA(rk_1k_{γ} = -1.4) models do a reasonable job of describing general tendency of the data. The later fails to describe the peak at $\cos\theta = 0.95$, but has a better reproduction of the data than RPR at higher energies. While the KM does not describe the data at small angles, which is also seen in the comparison of the elementary cross section, and under estimates the angular distribution most significantly in the extreme forward region in angles larger than $\cos\theta \leq 0.95$. It is apparent from the curves in Figure 6.33 that d$(\gamma,\Lambda)K^+n$ is the dominant contributing amplitude at lower energies but at photon energies larger than 1.06 GeV the amplitudes achieve on par status. The angle dependent cross section peaks at approximately $0.95 \leq \cos\theta \leq 0.98$ and declines towards $\cos\theta_{\Lambda}^{LAB} = 1.0$. The amplitudes for the SLA predictions are significantly larger than those of the KM model for laboratory angles of $\cos\theta \geq 0.95$. Unlike the results of the KM calculations the $d(\gamma,\Lambda)K^0p$ process primarily contributes to the Λ photo production reaction in the SLA framework. This dominant tendency of the $d(\gamma,\Lambda)K^0p$ reaction increases to more than twice that of $d(\gamma,\Lambda)K^+n$ simultaneously with extending photon beam energies at angles of $\cos\theta_{\Lambda}^{LAB} \geq 0.95$. Both models produce similar predictions of the $d(\gamma,\Lambda)K^+n$ as a con-

sequence of the determined elementary amplitudes that are fitted to $K^+\Lambda$ data in which the folded deuteron density has a minor effect. The disparity in the contribution of each process arises from the resonance content in respective models attempt to suppress the Born term contribution [119]. In the $K^0\Lambda$ channel the sensitivity to the $r_{K_1K_\gamma}$ parameter is remarkably dissimilar mainly playing a larger role in the SLA point of view than in the KM framework which was determined by fitting $K^0\Sigma$ data [47]. In the anticipation of newly published data Λ momentum integrated angular distributions in $d(\gamma,\Lambda)KN$,s recent theoretical calculations have been attempted with modifications to the current KM, such as H2 and KM2 which include hyperon resonances such as $S_{01}(1670)$ and $S_{01}(1800)$ [82].

6.3.7 Λ Hyperon Recoil Polarization

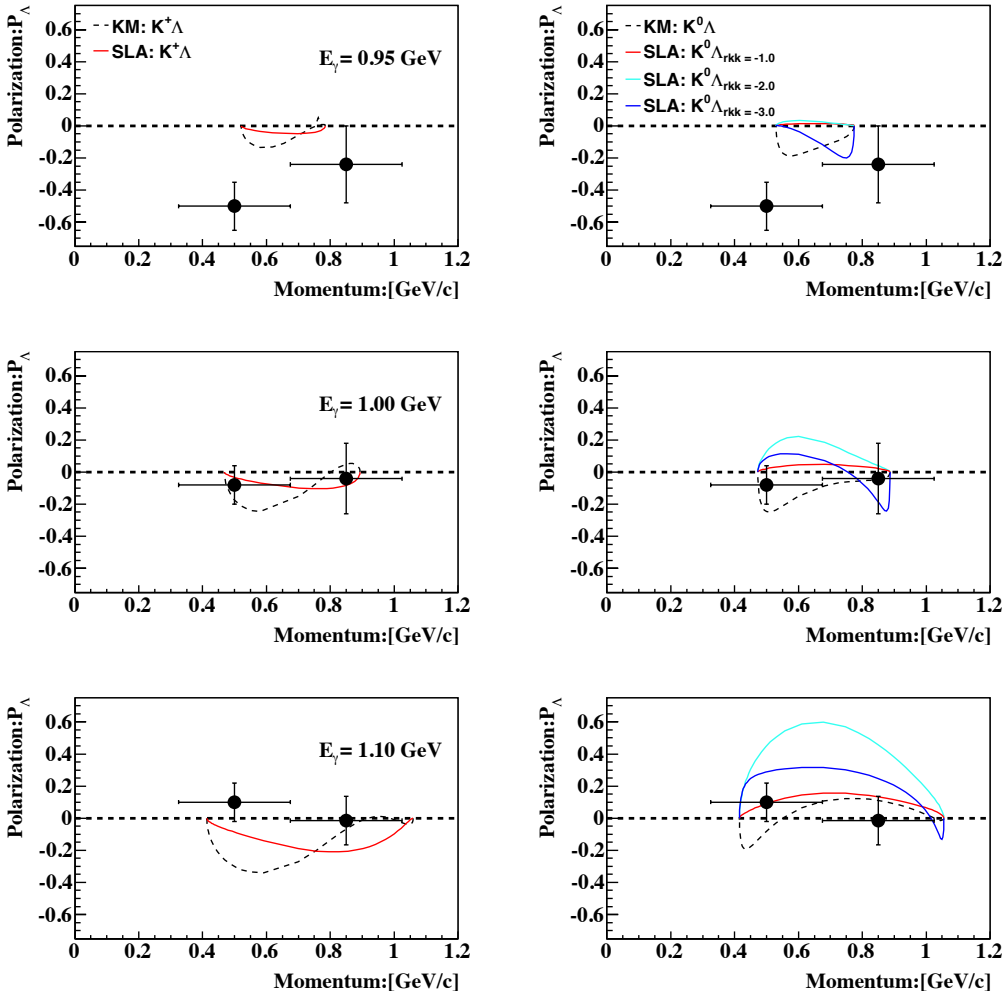

Figure 6.34: Λ recoil polarization compared to KM and SLA predictions of the momentum dependence. The γd$\rightarrow K^+\Lambda$n and γd$\rightarrow K^0\Lambda$p results are the left and right columns.

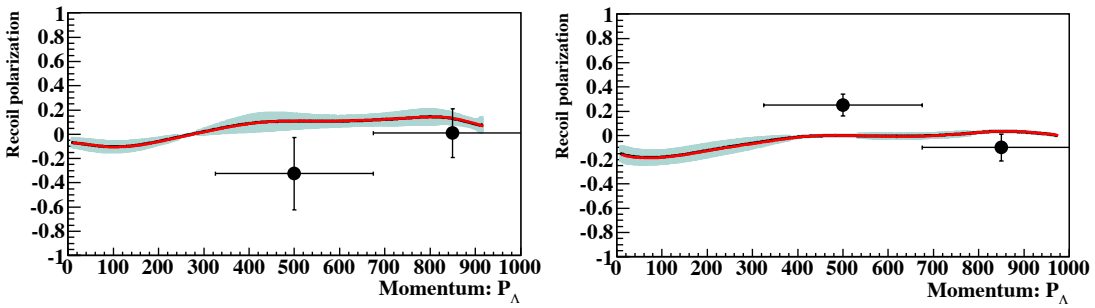

Figure 6.35: Λ polarization compared to RPR predictions model for $\cos\theta_{\Lambda}^{Lab} = 0.95 - 1.0$ and $0.90 - 0.95$, at bin centered energy bin $1.0 - 1.1$ GeV, given left to right respectively.

The Λ hyperon polarization was determined as a function of momentum and angle previously discussed in Figures 5.15, 5.16, and **??**. The momentum dependence was first compared for energy bins $E_\gamma = 0.90 \leq E_\gamma \leq 1.00$, $0.95 \leq E_\gamma \leq 1.05$, and $1.0 \leq E_\gamma \leq 1.1$ GeV to the $\gamma d \rightarrow K^+\Lambda$n and $\gamma d \rightarrow K^0\Lambda$p calculations based on the KM and SLA models, which furnished contrastive predictions in terms of the sign of the polarization. The predictions are given in Figure 6.34, for $K^+\Lambda$ and $K^0\Lambda$ left to right columns respectively. The sign of the determined polarization is shown to be negative and has the propensity to disappear at around 0.8 GeV, which is consistent with the KM prediction within the statistical errors, in contrast to the SLA curves, that do not describe the trend of the data. This is of concern as the SLA(r$K_1K_\gamma = -1.4$) performed well in its description of the momentum, angular, and integrated cross sections results. The experimental findings for the forward angular integration region, $\cos\theta_{\Lambda}^{Lab} = 0.95 - 1.0$, and energy bins of 0.90 E_γ 1.00, and 1.0 E_γ 1.1 GeV were compared to RPR calculations seen in Figure 6.35. The predictions do not reproduce the shape nor magnitude of the data, where only at higher Λ momenta for either photon energy sector, do the curves agree with the data within reported statistical errors.

6.4 Comparison to Existing Experiments

6.4.1 Polarization Observables

The polarization of Λ was obtained from the inclusive measurement of Λ in the ^{2}H(γ,Λ)X process, therefore it has obvious contributions from $K^0\Lambda$ and $K^+\Lambda$ reactions. Published observations of single Λ polarization observables were reported by the SAPHIR [11, 12], GRAAL [50, 51] and CLAS [13, 14, 15, 16] collaboration. The SAPHIR most recent polarization results at 30 kinematical values were released with their differential cross sections and the GRAAL data set at large energies, from threshold up to 1.5 GeV for angles of $(\theta = 30 - 140)$ were reasonably alike seen in the angular distributions $\cos\theta_K^{CM}$ and momentum dependence, $P_\Lambda{}^{LAB}$, in Figure 6.36 on the left and the same results after successfully being transformed from the angular to the momentum dependence on the right.

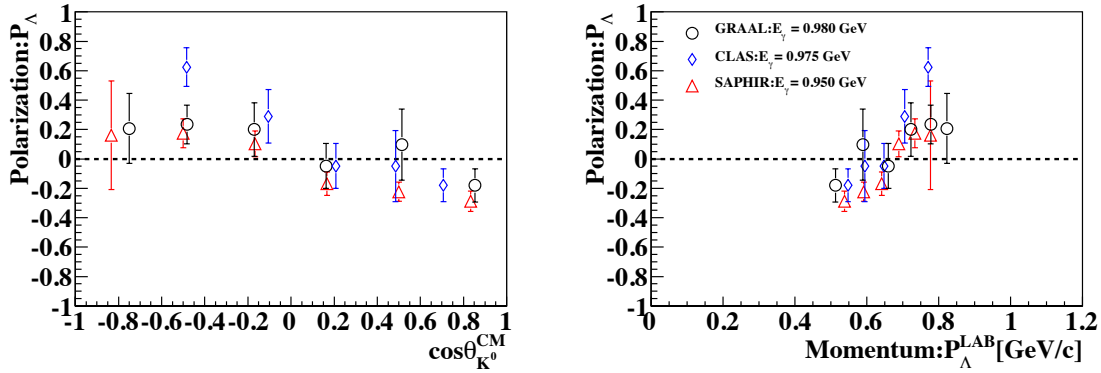

Figure 6.36: SAPHIR, GRAAL, and CLAS angular distributions ($\cos\theta_K^{CM}$) and momentum dependence ($P_\Lambda{}^{LAB}$) of the Λ recoil polarization for $\gamma p \to K^+\Lambda$ are presented left to right respectively.

The Λ hyperon recoil polarization for $\gamma d \to \Lambda X$ for three photon energies $E_\gamma = 0.90-1.0$, $0.95-1.05$ and $1.0-1.1$ GeV and published data sets of $\gamma p \to K^+\Lambda$ results are confronted in the Figure 6.37. In the calculations, the proton was presumed to be at rest and only statistical errors as given. In regards to the smallest energy region the results of NKS2 [5] and the latest findings exhibit a negative absolute value at lower Λ momentum, though the this work has a larger overall absolute value. Whereas in at higher momenta our data still remains negative in contrast to the sign change in SAPHIR, GRAAL and CLAS outcomes. At energies of $E_\gamma = 0.95-1.05$ GeV, the recoil polarization is consistent with both energies of GRAAL data within error bars. Despite this, for the highest energy bin measured, our data point at low Λ momenta is positive and stands in opposition to the all the data it has been set beside. For the remaining momentum bin

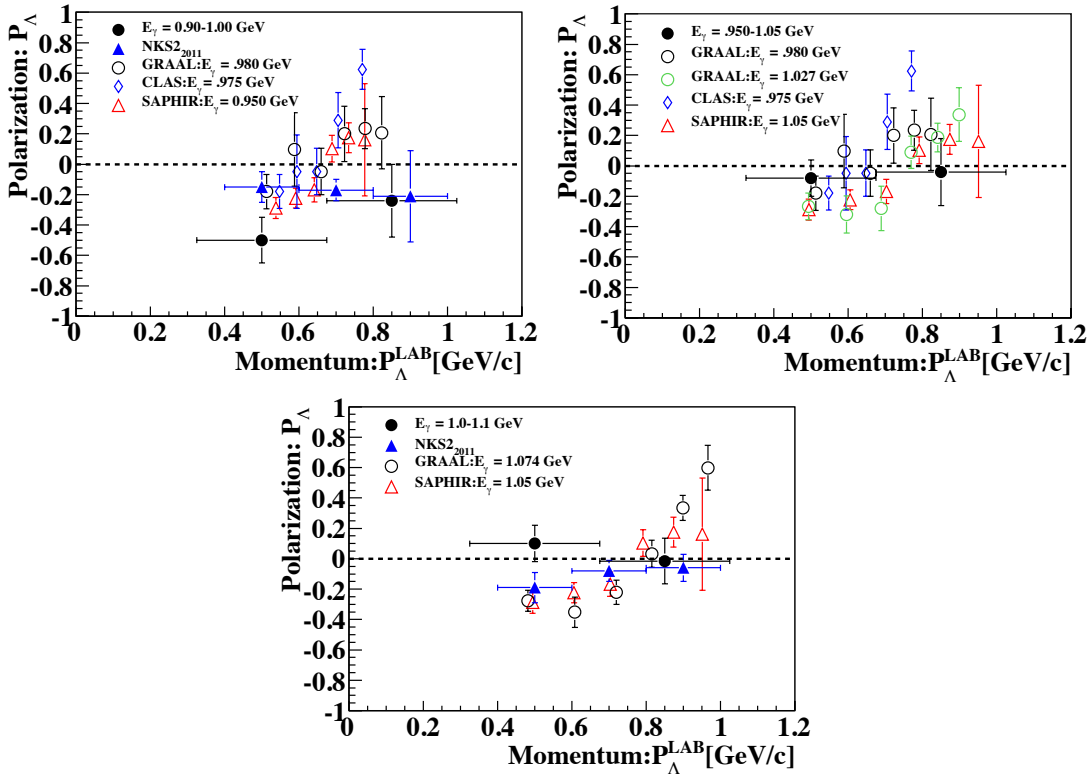

Figure 6.37: NKS2+, NKS2, SAPHIR, GRAAL, and CLAS momentum dependence (P_Λ^{LAB}) of the Λ recoil polarization for $\gamma d \rightarrow \Lambda X$ and $\gamma p \rightarrow K^+\Lambda$ compared at energies of $0.9-1.0, 0.95-1.05$, and $1.0-1.1$ GeV.

$P_\Lambda^{LAB} = 0.65-1.05$ GeV/c, our value can be regarded as zero in rough agreement with the SAPHIR and GRAAL data point.

6.4.2 The Kinship of $K^0\Lambda$ and $K^+\Lambda$

The results of theoretical calculations provided the means to approximate the total cross section of $\gamma d \rightarrow \Lambda X$ and $\gamma d \rightarrow K^0\Lambda p$ reactions. By appropriating the method from reference [4, 5], the total cross section of $\gamma d \rightarrow K^0\Lambda p$ was calculated as,

$$\sigma_{\text{Total}}^{K^0\Lambda} = (\sigma_{\text{Integrated}}^{\gamma d\rightarrow\Lambda X} - \tilde{\sigma}_{\text{Integrated}}^{\prime\gamma d\rightarrow K^+\Lambda n}) \cdot \frac{\tilde{\sigma}_{\text{Total}}^{\prime\gamma d\rightarrow K^0\Lambda p}}{\tilde{\sigma}_{\text{Integrated}}^{\prime\gamma d\rightarrow K^0\Lambda p}} \tag{6.7}$$

In equation 6.7, total and integrated cross of the $\gamma d \rightarrow K^0\Lambda p$ process are denoted as $\tilde{\sigma}_{\text{Total}}^{\prime\gamma d\rightarrow K^0\Lambda p}$ and $\tilde{\sigma}_{\text{Integrated}}^{\prime\gamma d\rightarrow K^0\Lambda p}$. It follows that the integrated cross of the $\gamma d \rightarrow K^+\Lambda n$ process is designated as $\tilde{\sigma}_{\text{Integrated}}^{\gamma d\rightarrow K^+\Lambda n}$. In the above calculation, all integrated cross sections were derived for the angular integration range of $0.9 \leq \cos\theta_\Lambda \leq 1.0$ in the laboratory frame of reference. The values introduced into the calculation for $\tilde{\sigma}_{\text{Total}}^{\prime\gamma d\rightarrow K^0\Lambda p}$, $\tilde{\sigma}_{\text{Integrated}}^{\prime\gamma d\rightarrow K^0\Lambda p}$ and

$\tilde{\sigma}'^{\gamma d\to K^+\Lambda n}_{\text{Integrated}}$ were procured by purely theoretical means. The values for $\tilde{\sigma}^{\gamma d\to\Lambda X}_{\text{Integrated}}$ are the results previously discussed and seen in Figure 5.12. The ratio of the integrated cross section and total cross section in the computation are same as found in Figure 6.10.

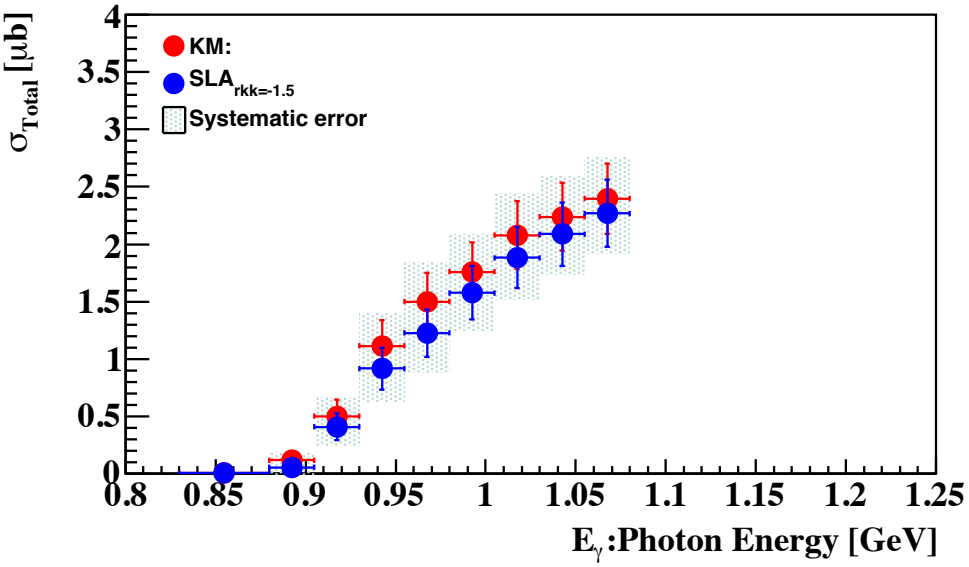

Figure 6.38: Estimated total $\gamma(d, K^0)\Lambda p$ cross section using the calculations of KM and SLA $r_{K_1K_\gamma} = -1.5$. Only statistical errors are shown.

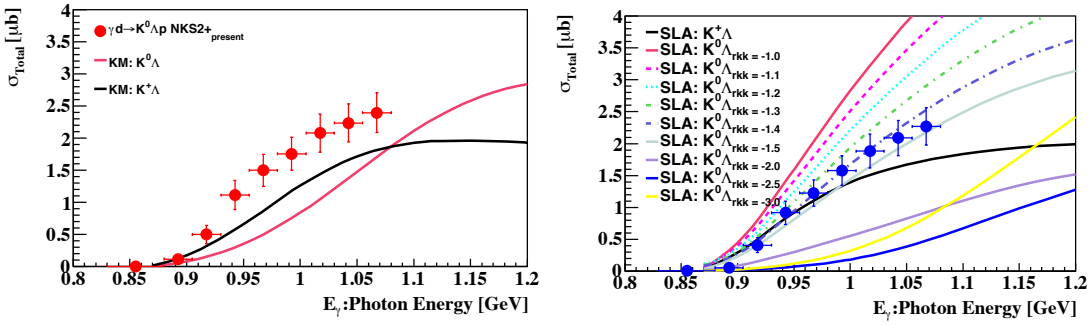

Figure 6.39: Estimated total $\gamma(d, K^0)\Lambda p$ cross section using the calculations of KM and SLA $r_{K_1K_\gamma} = -1.5$ compared to their respective predictive curves given left to right respectively. Only statistical errors are shown.

The total cross section of the $\gamma d \to K^0\Lambda n$ are plotted for the both the KM and SLA models as the solid black and blue circles respectively in Figure 6.38. The same procedure was implemented for both models, with a limiting case of the $r_{K_1K\gamma}$ fitting parameter in the SLA $r_{K_1K_\gamma}= -1.5$, based of the comparison of the $\sigma^{\gamma d\to\Lambda X}_{\text{Integrated}}$ with the SLA predictions and also in the comparison, Figure 6.27, made it evident that the value of $r_{K_1K_\gamma}= -(1.0-1.5)$, with a specific value of -1.4, best approximates the experimental

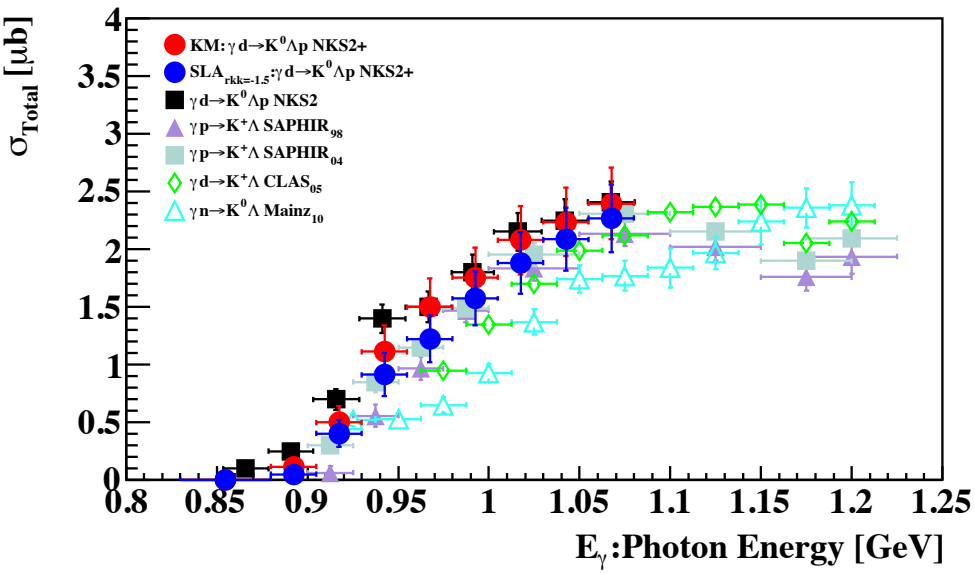

Figure 6.40: Estimated total $d(\gamma, K^0)\Lambda p$ cross section as determined in this dissertation and published $K^+\Lambda$ and $K^0\Lambda$ data using proton and deuteron targets [5, 11, 12, 13, 15, 33]. Only statistical errors are shown.

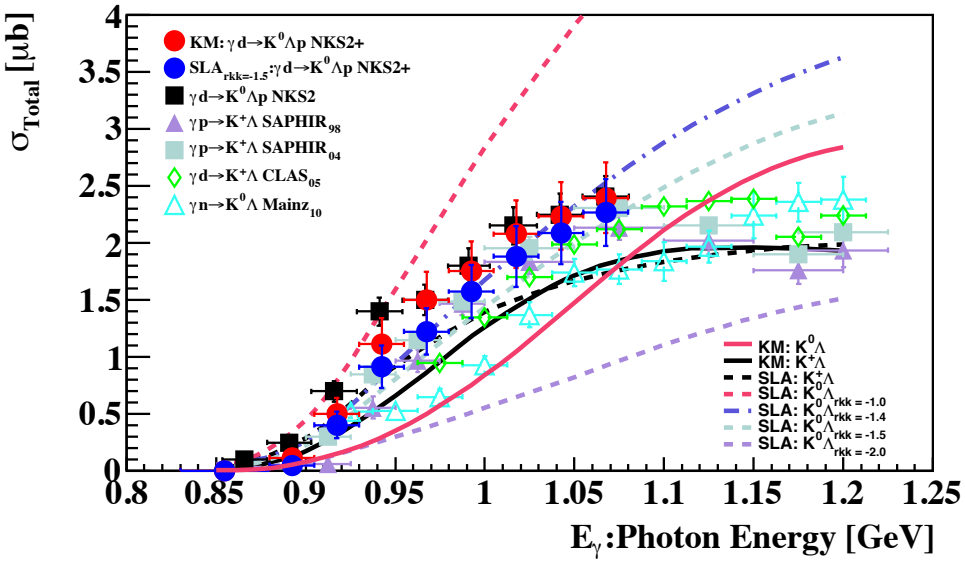

Figure 6.41: Comparison of estimated total $d(\gamma, K^0)\Lambda p$ cross section with theoretical predictions and published $K^+\Lambda$ and $K^0\Lambda$ data using proton and deuteron targets [5, 11, 12, 13, 15, 33]. Only statistical errors are shown.

results. The systematic error associated with this method of calculation is drawn as the filled area on the data points which is approximated at less than 15%. There is evidently only a small model dependence on the extracted total cross section deduced by using either

theoretical calculations. The estimated total $\gamma(d, K^0)\Lambda p$ cross section is compared to the calculations of total $\gamma(d, K^0)\Lambda p$ cross section and total $\gamma(d, K^+)\Lambda n$ for KM and SLA in Figure 6.39.

In section 1.4 current research projects involved in the strangeness physics was reviewed. Hence, at this stage the estimated total cross section can be juxtaposed to results of $\gamma n \rightarrow K^0\Lambda n$ and $\gamma p \rightarrow K^+\Lambda p$. The published results by SAPHIR [11, 12] and CLAS [13], and those taken from the dissertations of K. Bantawa [33] and K. Futatsukawa [5]are plotted alongside the estimated total cross section of $\gamma d \rightarrow K^0\Lambda n$ by the method described in equation 6.7 in Figure 6.40 as solid light purple triangle, solid light blue square, open green diamond, open turquoise triangle, solid black square, solid blue and red circles respectively. The maximum photon energy range of the NKS2+ data presented in this work is E_γ= 1.08 GeV. The results of the other collaboration extend in to a higher energy regime. The estimated total $\gamma d \rightarrow K^0\Lambda n$ compare favorably well to the measured $\gamma p \rightarrow K^+\Lambda p$ energy dependent cross sections up to 1.08 GeV, this implies that cross sections are roughly on par in terms of overall magnitude. Despite the general consensus between our semi-inclusive energy dependent cross section to those of the SAPHIR and CLAS results, the MAINZ results shown a distinctly different trend. Our results over the integrated energy range of $0.9 - 1.08$ GeV has a calculated value of $40 - 20\%$ higher than the results reported by the MAINZ group.

Model predictions for the inclusive $\gamma n \rightarrow K^0\Lambda n$ and $\gamma p \rightarrow K^+\Lambda p$ reactions, calculated in the KM and SLA framework, are compared to the experimental results in the threshold energy region gathered by the NKS2, NKS2+, CLAS, SAPHIR, and MAINZ collaborations. These comparison are shown in Figure 6.41 where the curves for the $\gamma p \rightarrow K^+\Lambda p$ process predicted by KM and SLA and drawn as solid and dashed black lines. The KM and SLA predictions of the $\gamma p \rightarrow K^+\Lambda p$ process are similar and provides a great description of the data up to $E_\gamma \leq$1.0 GeV, where after both slightly under shoot the data between 1.0 $E_\gamma \leq$1.1 GeV and then return to a consistent agreement. Predictions of the $\gamma n \rightarrow K^0\Lambda n$ calculated by the KM and SLA models, for the SLA model the results for the $r_{K_1K_\gamma} = -(1.0 - 2.0)$, are shown as the solid light red, dashed light red, dashed light blue, and dashed light purple curves respectively. The general consensus between our experimental results and theoretical predictions of the SLA model is good. The shape and size of the estimated total $\gamma d \rightarrow K^0\Lambda n$ cross section is reproduced for the $r_{K_1K_\gamma}$ value around -1.4.

CHAPTER
SEVEN

CONCLUSION

> If I could find the spot where truth echoes,
> I would stand there and whisper memories
> of my children's future. I would let their
> future dwell in my past so that I might live
> a brighter now.

Saul Williams

This chapter will summarize the findings of this thesis and is followed by a discussion on the conclusions that may can be reached from these results. It shall further discuss a more global and comprehensive perspective of the research conducted and review the outlook of future research projects.

7.1 Summary of Results

This dissertation presented findings furnished from the exploratory data measured with the upgraded NKS2+ spectrometer taken at Research Center for Electron Photon Science (ELPH) Sendai, Japan. The experiment was performed with intense tagged photons beams in the range of $0.8 \leq E\gamma \leq 1.1$ GeV that were directed to a liquid deuterium target and the inclusive measurement of Λ was achieved by the identification of its decay particles in the following $\Lambda \rightarrow p\pi^-$ channel.

The purpose of this work was to deeply investigate strangeness photo production at threshold energies, to a large extent by placing the emphasis on Λ production. The analysis conducted was cardinally focused on the inclusive measurement of Λ in the $\gamma d \rightarrow \Lambda X$ process. We originally proposed to determine the following, previously outlined in section 1.6,

1. Λ momentum dependent differential cross section (Figure 5.8)
2. Λ angle dependent differential cross section (Figure 5.10)
3. Λ photon energy dependent integrated cross section (Figures 5.11 and 5.12)
4. Λ recoil polarization (Figures 5.15 and 5.16)

Fledgling objectives were achieved thus galvanizing the results of this work to be extended beyond the initial goals, by innovative methods of incorporating theoretical calculations to extract the following,

I Total $d(\gamma,\Lambda)X$ cross section (Figure 5.14)

II Total $d(\gamma,K^0)\Lambda p$ cross section (Figure 6.38)

The findings were compared with the experimental results of the NKS2 collaboration for the forward integration region and exhibit fairly consistent results with the previous data reported [5] discussed in section 5.10 and seen Figures 5.17, 5.18, 5.20, and 5.20. This thesis also reported on theoretical calculations for the photoproduction on the deuteron and extensively examined the predictions of $\gamma d{\rightarrow}K^0\Lambda$p and $\gamma d{\rightarrow}K^+\Lambda n$ to discern their relevance and the dominate process. The predictions were compared with the outcomes of this research endeavor in section 6.3.

7.2 Conclusion and Outlook

The measured cross sections of the angle integrated Λ momentum dependent differential cross sections for the addition of $\gamma d{\rightarrow}K^0\Lambda$p and $\gamma d{\rightarrow}K^+\Lambda$n reactions, for photon energy bins of (top) 0.9 - 1.0 and (bottom) 1.0 to 1.08 GeV were likened to Kaon-MAID and Saclay-Lyon A calculations in Figures 6.21 and 6.22. Kaon-MAID calculations replicates the general shape of the distributions in both energy bins and scattering angles. Nonetheless, it was deficient in converging with the magnitude at the most forward angles, in which it underscored the cross section by approximately 50% at the Λ momenta of 0.65 $\leq P_\Lambda^{LAB} \leq$ 0.90 GeV/c. On the other hand, the SLA model calculations had an admirable consensus with the shape and magnitude of the data for $r_{K_1K_\gamma} = -(1.0-1.5)$. The Regge-Plus-Resonance (RPR-2007) calculations derived for bin centered photon energies, when set against momentum distributions, was capable of emulating the shape and intensity of the data for the higher of the two energy bins, notably for the most forward hyperon angles and matches the data within the reported errors at $E_\gamma = 0.95$ GeV. The Regge-Plus-Resonance (RPR-2007) momentum distributions agrees with the reported data within its theoretical uncertainties.

The Λ angular distribution as a function of the scattering angle in the laboratory system was additionally deduced for five distinct energy bins. The Regge-Plus-Resonance accomplishes a good agreement with the angular dependent cross section in the measured energy bins. Both Regge-Plus-Resonance (RPR-2007) and the Saclay Lyon A(r$K1K_\gamma = -1.4$) models do a reasonable job of describing the general tendency of the data. The later fails to describe the peak at $\cos\theta_\Lambda^{LAB} = 0.95$, but has a better reproduction of the data than Regge-Plus-Resonance (RPR-2007) at higher energies. While the Kaon-MAID does not describe the data well, and under approximates the angular distribution at the very forward region for angles smaller than $\cos\theta_\Lambda^{LAB} \leq 0.95$.

The integrated cross section for the $\gamma d \rightarrow \Lambda X$ reaction in the angular integration regions of $0.9 \leq \cos\theta_\Lambda^{LAB} \leq 1.0$ and $0.75 \leq \cos\theta_\Lambda^{LAB} \leq 1.0$, along with Λ momentum dependent differential cross section were derived. Comparison with the theoretical calculations gave reasonable agreements with predictions by Regge-Plus-Resonance (RPR-2007). The excitation function of the Saclay-Lyon A model was consistent with the data for the $r_{K_1 K\gamma}$ parameter set to $= -1.4$. However, the calculations by the Kaon-MAID model under predicted the obtained cross sections.

The Λ total cross of $\gamma d \rightarrow \Lambda X$ estimated by equation 5.9 and shown in Figure 5.14 ascends rapidly at energies close to the nucleon threshold as was exhibited in measurements on a proton target [11]. The Kaon-MAID and Regge-Plus-Resonance (RPR-2007) predictions obtained for forward hyperon angles describes the data extremely well above $E_\gamma = 1.0$ GeV with a negligible over prediction on the order of 3%. Nevertheless, the RPR calculations does not include Σ contribution that are expected to by minor. Based on the underpredictions of the Kaon-MAID calculations in makes sense to place greater reliance in the Regge-Plus-Resonance estimation.

The estimated $\gamma d \rightarrow K^0 \Lambda p$, cross section seems to be on the same order of absolute value with the $\gamma d \rightarrow K^+ \Lambda n$ reaction. The SAPHIR [11, 12] $\gamma p \rightarrow K^+ \Lambda$ results are almost identical to the $\gamma d \rightarrow K^0 \Lambda n$ cross section derived with the Saclay-Lyon A model conjecture, with the coupling constant set to -1.4. The results of this work does not reinforce the findings on the MAINZ group [33], which was the first reported measurement of $\gamma n \rightarrow K^0 \Lambda$ total cross section and whose results was achieved by a direct measurement of six particles for the reconstruction of the $K^0 \Lambda$, in opposition to the cleverly estimated $\gamma d \rightarrow K^0 \Lambda p$ total cross section reported in this work. Having said that, the results reported in this dissertation are consistent across the board with the previous $\gamma d \rightarrow \Lambda X$ measurements, the estimated $\gamma d \rightarrow K^0 \Lambda p$ cross section of the NKS2 collaboration[5], and SLA predictions. The most significant conclusion that can be drawn is the relatively equivalent magnitude of the $d(\gamma, K^0)\Lambda$p and $p(\gamma, K^+)\Lambda$ processes, which are predicted to have strikingly dissimilar

cross sections, previously discussed and shown in Figures 2.4, 6.7, 6.9, and 6.12, here I conclude that they are in fact on par.

In this way, the conclusions of this dissertation emphasize the importance of exploring strangeness photo production in the neutral channel directed towards a deuteron as an effective laboratory, as essential to enhancing the minuscule data set, generating an isospin complete measurement, for judging, and amending the inherit limitations of theoretical descriptions of nature.

With the upgrade of the ELPH facility to higher energies, the possibility to study $\gamma d \to K^0\Sigma$ and $\gamma p(d) \to K^0\Lambda(n)$ reactions will be available, providing the chance to add more data to the excitation curves and to study the details of FSI interactions thereby placing the NKS2 collaboration of the cutting edge of strangeness physics.

APPENDIX

A

SYSTEMATIC ERRORS

The only one who never makes mistakes is the one who never does anything

Teddy Roosevelt

A.1 Systematic Error

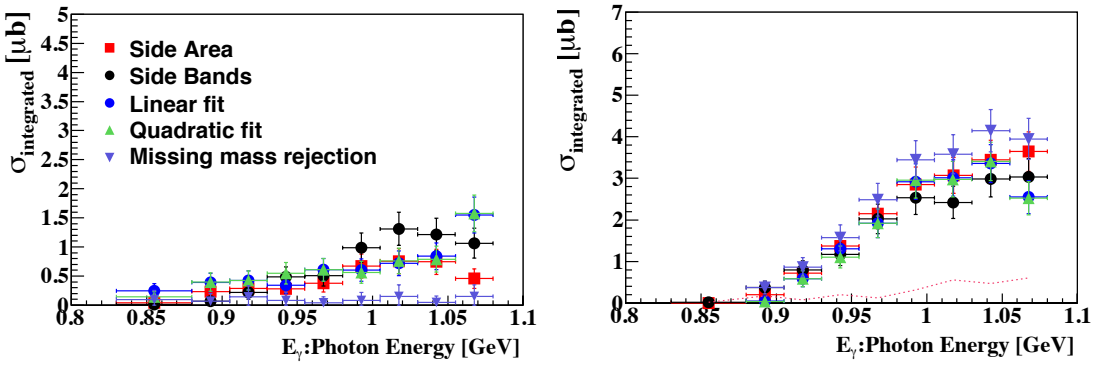

Figure A.1: Background contributions and calculated integrated cross section from various background selections.

Dissimilar background selection stratagems may result in differing extracted signal yields, thus directly affecting the cross section calculations. A study of the effect of various background determinations, for the purpose of estimating the systematic error introduced from the final background subtraction method was performed. The result of the cross section contributions for the background methods and the corresponding background subtracted integrated cross section results are shown in Figure A.1. The details of the approaches was reviewed in section 4.15. The contributions of the side area

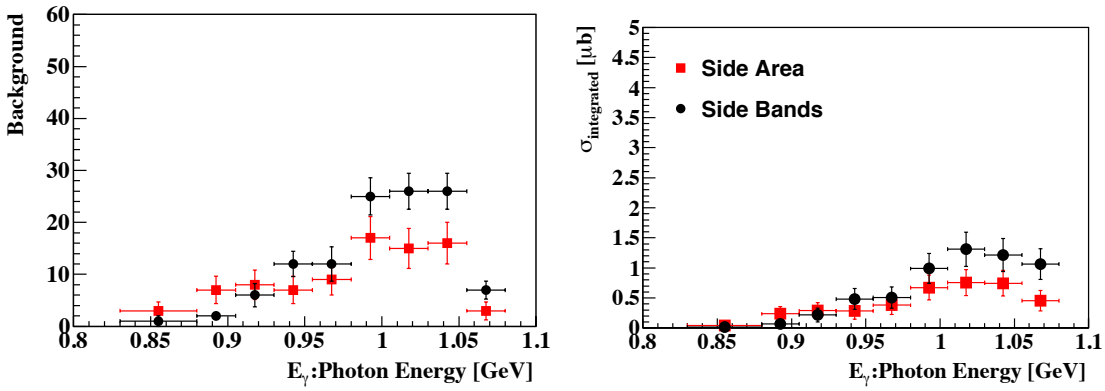

Figure A.2: Background contributions and calculated integrated cross section from the side area (BGM_{SA}) and side band (BGM_{SB}) selections.

method was shown in the cross sections results and the systematic error discussed in the main text. The errors given in figures in main text were only statistical. Here we elaborate on the means of approximation. The systemic error was estimated from the difference in cross section magnitudes of the background for the side area (BGM_{SA}) and side band (BGM_{SB}) technique.

The background contributions and calculated integrated cross section from the side area (BGM_{SA}) and side band (BGM_{SB}) selections are seen left to right in Figure A.2. As a consequence of the sucessful determination of the systematic uncertainty involved, the background subtracted cross sections of $\gamma d \rightarrow \Lambda X$ reaction for the dual angular regions of $0.75 \leq \cos\theta_{\Lambda}^{LAB} \leq 1.0$ and $0.9 \leq \cos\theta_{\Lambda}^{LAB} \leq 1.0$ are shown in Figure A.3 left to right respectively, with statistical and inclusion of systematic errors, estimated as the difference between the background magnitude of BGM_{SA} and side band BGM_{SB} for each angular integration sector, are given as standard errors bars and the inclusion of systematic errors as the shaded regions.

The main contribution to the introduction of systemic error in the Λ recoil polarization calculation is attributed to the background subtraction. In order to estimate its contribution to the results, a *null* study was performed. In principle, the background should not yield a measurable polarization value, thus any value obtained from the background continuum is not a true polarization and should be subtracted from the magnitude of the recoil polarization. Since the side area, BGM_{SA} method was used, the evaluation of the contribution of BGM_{SA}^{i}, where i, varying side areas, was calculated.

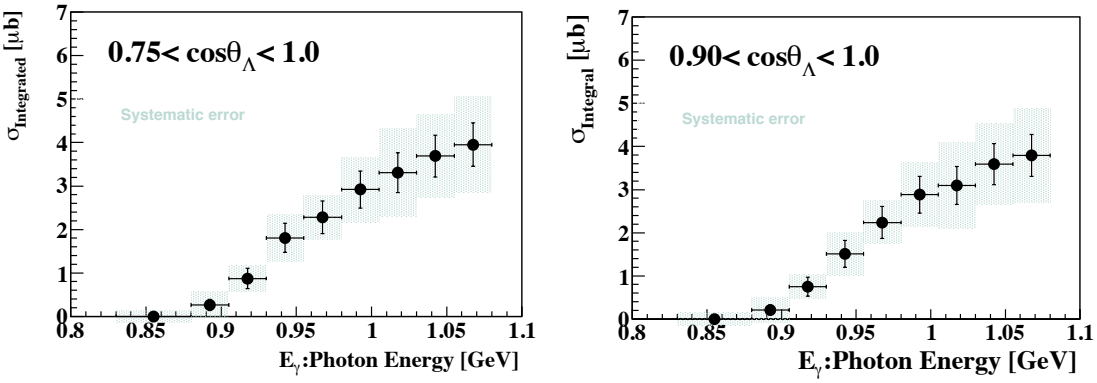

Figure A.3: Integrated cross section of the inclusive measurement of Λ in $\gamma d \rightarrow \Lambda X$ for the angular integration regions of $0.75 \leq \cos\theta_\Lambda^{LAB} \leq 1.0$ and $0.90 \leq \cos\theta_\Lambda^{LAB} \leq 1.0$. The statistical and systematic errors are given as the standard errors bars and filled shaded regions.

$$\mathrm{BGM}_{SA}^{i} = \begin{cases} \mathrm{Background}_{\mathrm{side}}^{1} = \mathrm{BG}_{SA}^{1} = 1.130 - 1.150[\mathrm{GeV/c^2}] \\ \mathrm{Background}_{\mathrm{side}}^{2} = \mathrm{BG}_{SA}^{2} = 1.135 - 1.155[\mathrm{GeV/c^2}] \\ \mathrm{Background}_{\mathrm{side}}^{3} = \mathrm{BG}_{SA}^{3} = 1.140 - 1.160[\mathrm{GeV/c^2}] \end{cases}$$

The systematic error was estimated as the maximum difference in the polarization magnitude of the selected background regions BGM_{SA}^{i}. The evaluated regions are defined in equations above. It should be noted that BGM_{SA}^{3} was the adopted background subtraction region used for all calculations given in the main text and discussed at length in section 4.15. The momentum dependence of the hyperon recoil polarization was determined for three photon energy ranges, $0.9 - 1.0$ GeV, $0.95 - 1.05$ GeV, and $1.0 - 1.08$ GeV, the results of which are shown in Figure 5.15. The inclusion of the systematic errors to the momentum dependence are shown in Figure A.4, given from the top left. In the figure, the statistical and inclusion of systematic errors are seen as the standard errors bars and the inclusion of systematic errors as the shaded regions. Other evaluated systematic uncertainties were listed in Table 4.7.

A. SYSTEMATIC ERRORS

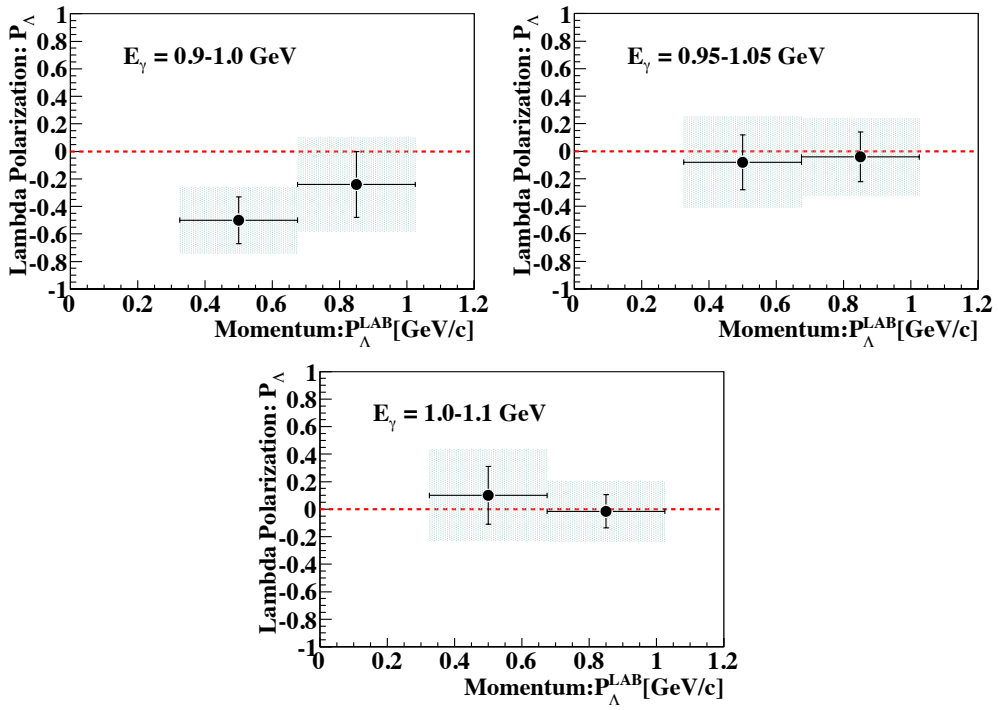

Figure A.4: Λ recoil polarization as a function of momentum ($|P|_\Lambda^{LAB}$) for the energy range of $0.9 - 1.0$ GeV, $0.95 - 1.05$ GeV, and $1.0 - 1.1$ GeV shown from the top left respectively. The statistical and systematic errors are given as the standard errors bars and filled shaded regions.

APPENDIX

B

PERFORMANCE STUDY OF VDC

> So often times it happens that we live our lives in chains and never even know we have the key.
>
> The Eagles.

B.1 VDC Layer Efficiency Gas Study

The vertex drift chamber (VDC) was originally designed to utilize a conventional 50:50 pre-mixed combination of Argon and Ethane. The primary reason for such decision was based on the usage of the same mixture percentage in the cylindrical drift chamber (CDC), in which acceptable performance results had been established in previous production experiments. The properties of the gas mixtures have been extensively studied and reported by Sauli [100]. Following the conclusions of the afore mentioned report, the assumed drift velocity of electrons in the mix is expected to be roughly 50μ. We studied the effect of introducing small amounts of ethanol into the mixture as a possible quencher specifically for the purpose of reduce the high counting rates that were observed under experimental conditions at tagged photon beam rates greater than 1 MHz. Prior to adjusting the gas percentage the performance of the VDC without an unaltered equal mixture was studied by cosmic ray and ^{90}Sr source tests. The experimental setup involved placing the VDC along its axis and using two parallel scintillator counters, with one placed below and the other above, as trigger counters. This orientation with the VDC placed upon its side guaranteed that a traversing particle would pass through the entire chamber. Thus the start trigger for data acquisition required a coincidence signal of both counters. The efficiency of detecting hits along the track path was investigated for each layer as a function of the amplifier shaper discriminator (ASD) threshold setting , ranging from $1.0-7.0$ V.

B. PERFORMANCE STUDY OF VDC

The layer efficiency was also studied as a function of the high voltage setting. The setting of the VDC high voltage was allowed to vary between $-(1900 - 2300)$ V. The following are prerequisites that had to be met in order for a track to be considered for fitting:

- The obtained TDC was in a valid TDC channel range corresponding to a realistic drift velocity and cell size.
- The associated error in the hit position was set at $4\sqrt{2}$
- The hit position was assumed to lie along the z=0 (x,y) plane
- The track should transit all 8 layers.

Possible track candidate were fitted to a 1st order polynomial with an additional requirement of a χ^2 value less than 100 for the fit.

$$y = mx + b \tag{B.1}$$

The efficiency is defined as,

$$1 - \frac{n(A \cap B)}{n(B)} \tag{B.2}$$

where A is a non existent hit on the layer of interest, B is a valid hit on other layers, and n(A) being the total number of events with condition A.

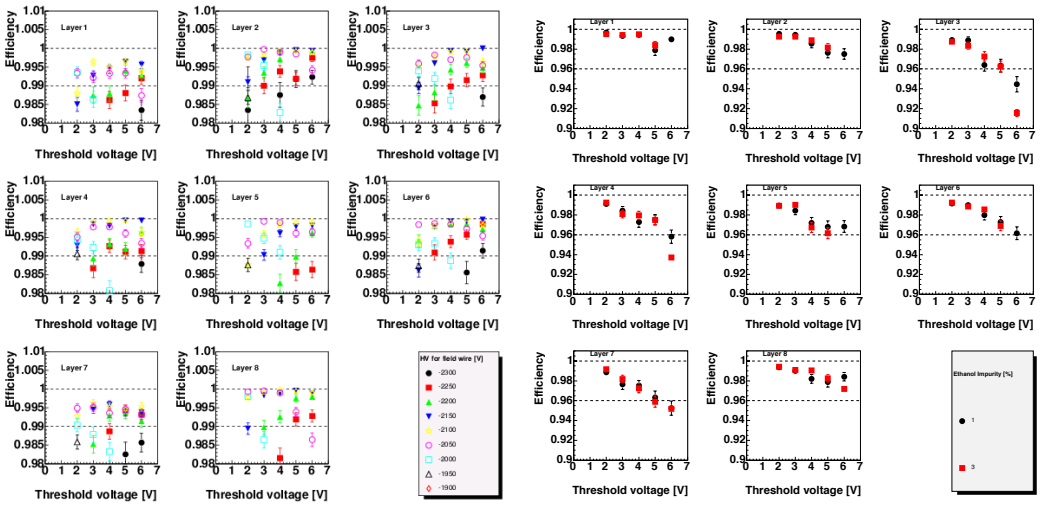

Figure B.1: VDC layer efficiency as a function of threshold setting using a ^{90}Sr source. The left figure shows the dependence of the High voltage setting as various marker styles for a range of $-(1900 - 2300)$ V in -50V increments for a 50:50 Argon-Ethane mixture. The right figure shows the layer efficiency for ethanol gas impurities (right) of 1%(black squares) and 3%(red squares) at a optimum high voltage setting of -2100V.

Using the above framework, the ^{90}Sr source and cosmic ray tests yielded a layer efficiency greater than 98% for all layers for a threshold setting between 0−7 V. The results of this investigation are given on the left of Figure B.1 for layer1−8 from the top left respectively, where the efficiency for various high voltages are shown by markers. It was found that the highest efficiency over all layers could be obtained at $-2100V$. This same method for the layer efficiency determination was applied with the introduction of ethanol into the gas mixture. Two different percentages, 1% and 3% ethanol were studied by ^{90}Sr also. The high voltage was kept at the optimum setting of −2100 V. The results of which are shown on the right in Figure B.1 were the solid black circle are for 1% and the solid red squares for 3% respectively. It was concluded that the introduction of ethanol had a significant effect of reducing the layer efficiency by roughly 2% for layers 2−8 at a threshold setting higher than 3 V.

B.2 Position Resolution

The position resolution of the VDC was measured using cosmic ray tracks outside of a magnetic field. For this study a linear fitting routine was used to reconstruct the tracks. The results are shown in Figure B.2 as a function of layer number. The test indicates an obtainable position resolution of of roughly 160-180μm over all layer.

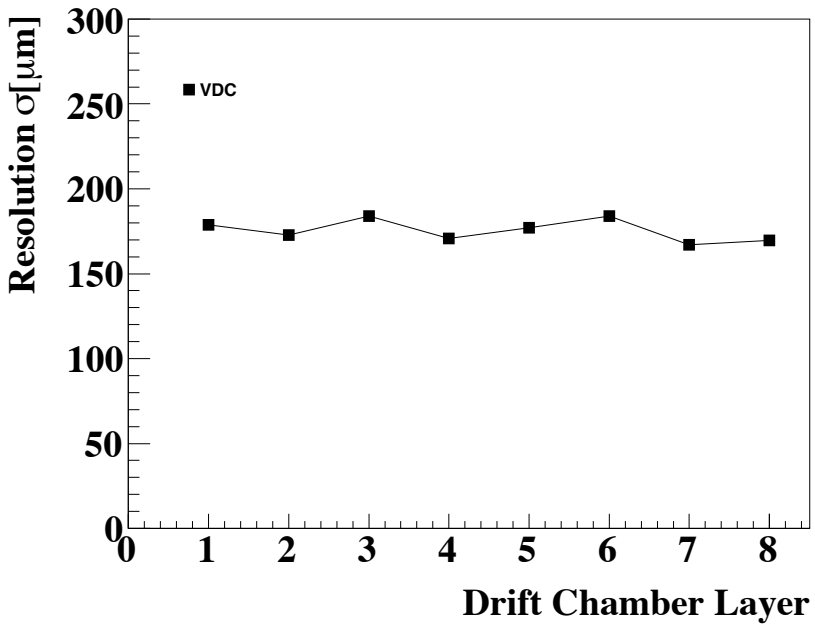

Figure B.2: VDC position resolution measured by a cosmic ray study.

B.3 Singles Rate

Prior taking exploratory production data with the addition of the VDC it was subjected to performance evaluation under the tagged photon beam conditions. The VDC detection efficiency was proven successful and satisfactory with the use of a source and with cosmic rays, this prompted the decision to install in NKS2. A tagged photon beam with a rate of 1 MHz was directed into a liquid deuterium target with the trigger conditions of normal physics production runs as discussed in section. The calculation of the VDC singles rate was under taken to determine the counting rate of the wires along the beam line and the results are shown in Figure B.3. In the figure, the singles rate, in kHz, of each wire segment for each layer is given. The opposite x−axis on each figure is in angles, where zero degrees corresponds to the beam line and the rotation proceeds counter clockwise. The average singles rate was $45 - 60$ KHz over all layers of the VDC.

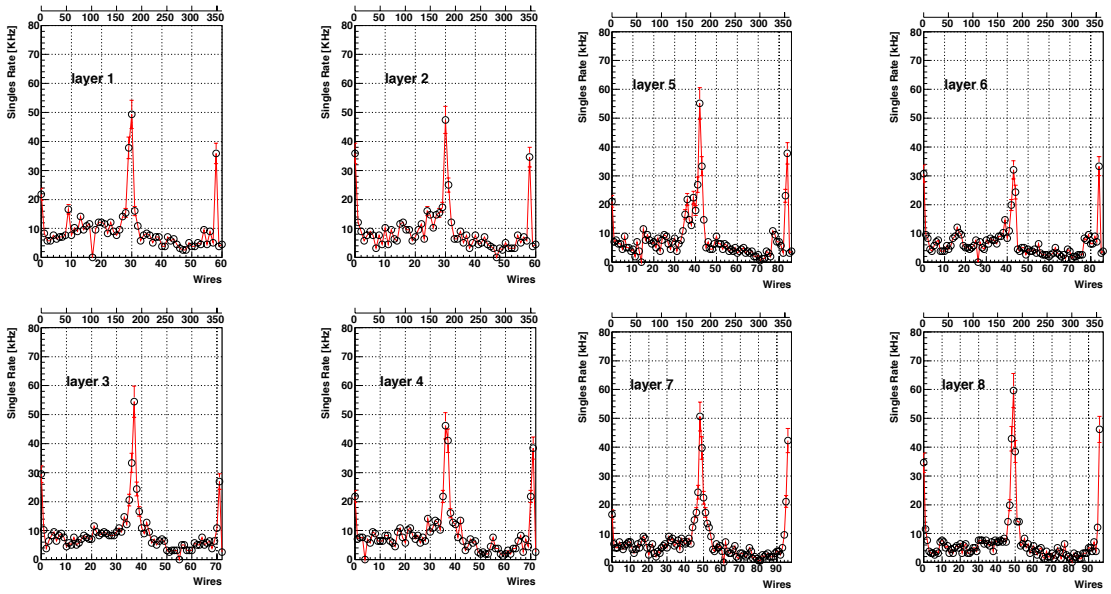

Figure B.3: Singles rate in kHz of individual wires on each layer at approximately 1 MHz photon beam tagging rate. The opposite x−axis on each figure in in angles where zero degrees corresponds to the beam line.

B.4 Upstream Wire Removal

Based on the results of the wires singles rate and a motivation to reduce the amount of material in the path of the photon beam, it was decided to remove the upstream wires along the beam line. This would in essence be the same type of design as the CDC which contained no wires along the beam line. This was hypothesized to reduce the number of

hits recored on each layer and the event size, which should enhance the data recoding time and thus improve the overall data acquisition efficiency. Moreover, due to the *Lorentz* boost of the produced particles, reconstructed tracks are not expected to be found in the upstream region of the VDC.

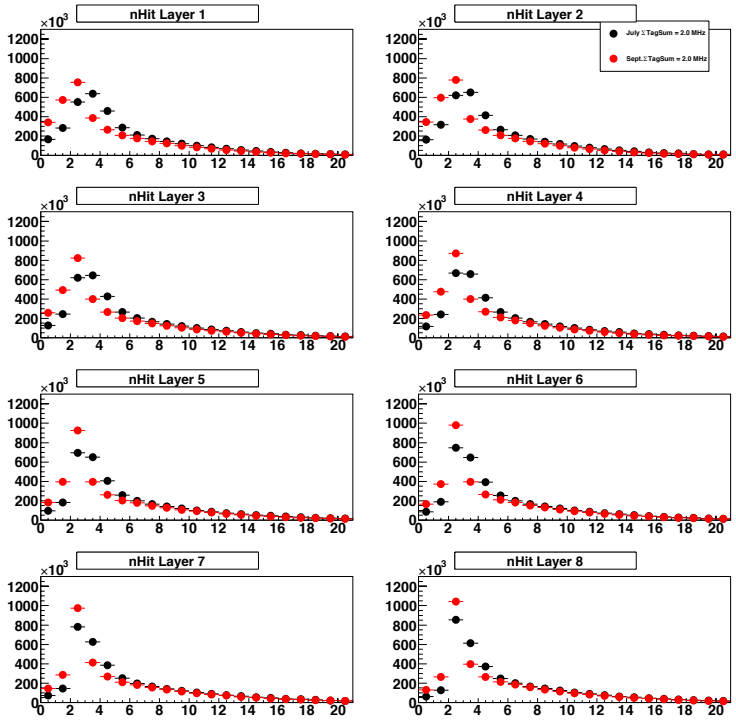

Figure B.4: Number of hits (multiplicity) per layer distributions. The figure presents multiplicity on each layer where the upstream wire installed and removed as black and red distributions respectively.

The number of hits on each layer is seen in Figure B.4. This data was taken at a tagged photon bate rate of roughly 1.5 MHz for the same trigger configurations. The black data correspond to a data set taken in July 2010 for the test of the VDC and the red are from the data taken in physics experimental period analyzed in this thesis. The black data was recorded prior to the removal of the upstream wires. Clearly it is shows that the distribution shifted to the left for layers with an increase in the number of hits corresponding to 1, 2, or 3 hits on the layer, indicating that the number of multiple hits on each layer has been reduced. This is attributed to the reduction or material in the photon path on its way towards the target. As the photon beam was required to traverse less material, the probably of pair production was reduced and with it a decline in high multiplicity on the layers especially in the upstream region.

B.5 Pattern Recognition: Cluster Selection

As the tracking code was further being developed, it was decided to determine the typical layer cluster distribution. The data used in the analysis was gathered during the September 2010 experimental period as detailed in the data analysis chapter of this thesis. The experimental condition were as follows:

- Target: Liquid Deuterium
- Trigger: (nIH≥2 x Tag) x nOH≥2 x $EV4_{veto}$
- $Tagged_{\gamma}$ rate : 1.5 MHz

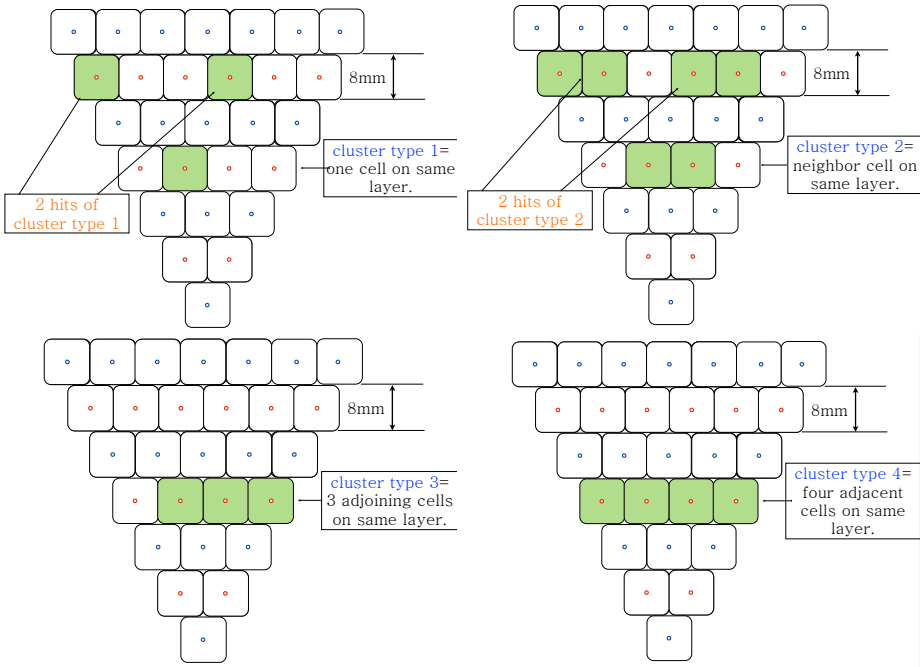

Figure B.5: Examples of the cluster definitions used in the determination of the cluster distributions on each layer of the VDC.

The program to determine the cluster distributions proceed by starting at the first wire (i) and determining if there was a hit on the wire. The wires were checked layer per layer starting from the inner most layer progressing outwards and in angular rotation moving from wire i to the maximum wire on each layer. It should be that the maximum allowed cluster type was a cluster size of 16 adjoining cells detecting a hit. If there was a hit, then the cell corresponding to this sense wire was designated as a having a hit of cluster type *1*. The definition of cluster types apply to only to one layer at a time. The adjacent wire

$(i+1)$ was then checked, wherein, if there was a hit, then the two adjacent cells would be designated as a hit of a cluster type *2*. If there was not a hit on the neighboring cell, then the identification of a hit of cluster type *1* would filled, and the program would then continue scanning from $j = i+1$ wire. In the final analysis only up to a maximum cluster type of 4 hits was studied as the realistic tracks from the decay of a photo produced strange particle would most likely not incur more than such. Illustrations of the definitions of the cluster types *(1−4)* are seen in Figure B.5. It can be clearly understood that a cell having a hit is a cluster type *1*, two cell beside each other in which both are hit would be a cluster type 2. Three cells in combination are a cluster type *3* and lastly 4 cells are a cluster type *4*. For the remainder of this thesis the term *size* and *type* are interchangeable. The numbering of layers 1−8 are associated with the VDC and layers 9−18 with the CDC.

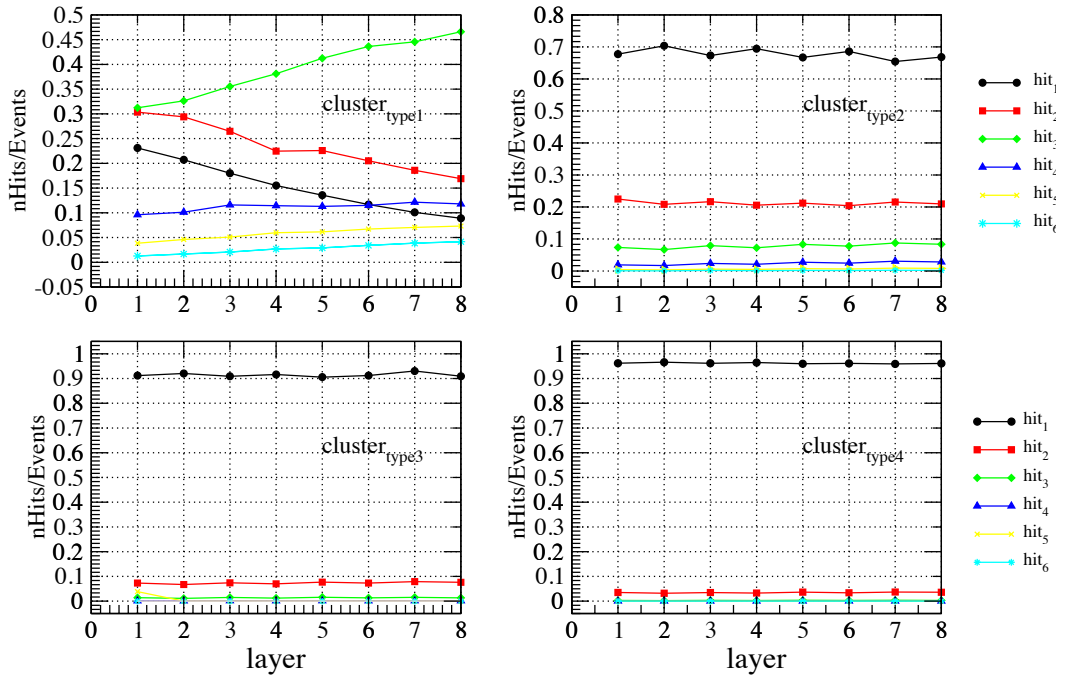

Figure B.6: Clustering distribution percentage for VDC.

The study into the allocation of clusters on each layer was further studied to determine the number of hits of each cluster size on each layer. The means the number of times one would detect the presence of a predetermined cluster on a layer; an example of such in the recognition of 3 cluster type *1*, such a pattern would be singled out as a 3 hits of cluster type *1*. In Figure B.6 the number of distinguishable hits of a certain cluster size was normalized by the total number events in the data set. The figure displays the number of hits of a certain cluster, such as one measured hit of cluster one, two measured hits

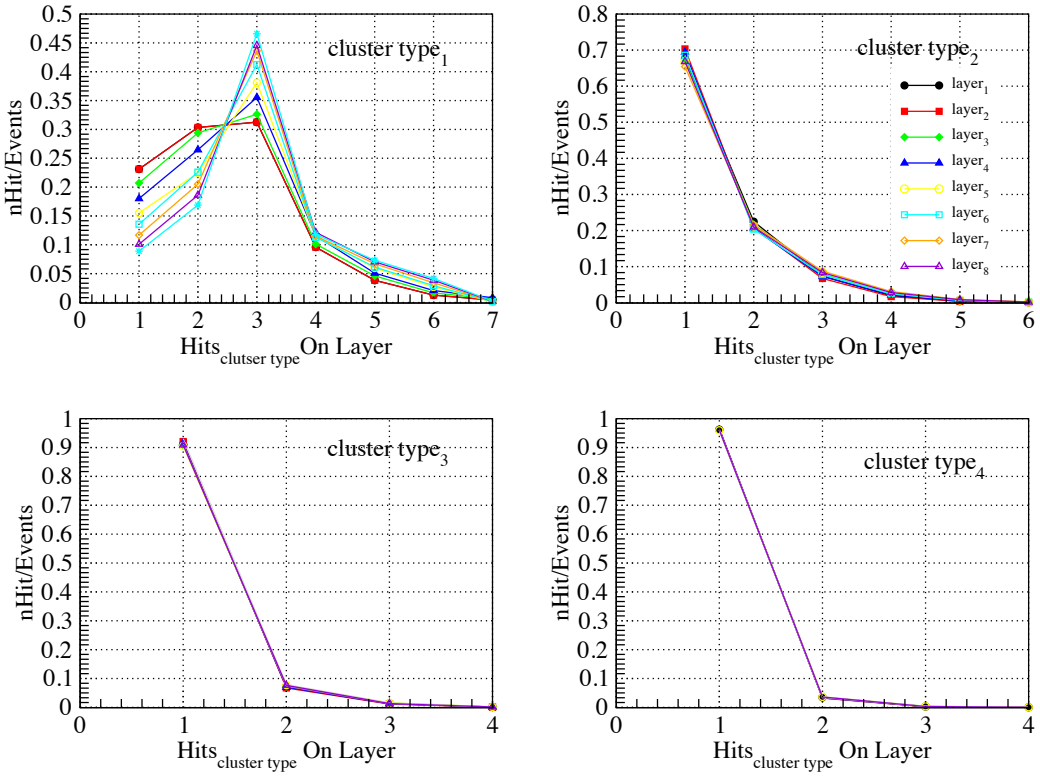

Figure B.7: Clustering distribution percentage for VDC.

of a cluster type one, etc. Thus, the percentage of how many hits of a cluster type was obtained as a function of the layer. As previous stated this study was conducted only up to a cluster size of 4 adjacent hits. In figure B.7 the number of distinguishable hits of a certain cluster size was normalized by the total number events in the data set. The results of cluster type one are remarkable different from cluster type 2−4. For the inner layers, it is expected that a hit of 2 or 3 cluster type one will be recorded 35%-45% of the time. The tendency increases for 3 hits but then recedes for 4 or greater hits. For cluster type *2*, roughly one hit will be recorded 70% of the time, and 20% of 2 hits and all hits larger than 3 is expected to account for less than 10%. The study lastly permits the conclusion that there is a around 90% likelihood that for clusters type 3 and 4 there will be only be one hit on the layer.

APPENDIX

C

HULTHEN AND DEUTERON WAVE FUNCTIONS

The dreamers are the saviors of the world.

James Allen

A brief review of model calculations of the neutron wave function within a deuteron and for the non-relativistic deuteron are presented. The Hulthen wave function is used to describe the momentum distribution of the neutron within the deuteron. The wave function is calculated by,

$$P(p) \propto \frac{p^2}{(p^2+\alpha^2)^2(p^2+\beta^2)^2} \tag{C.1}$$

P is the probability density and p is the momentum of the nucleon. The parameters determined from fitting, α and β, were determined to be 45.6 MeV/c and 234 MeV/C respectively. The results of fitting measurements [120] involving the scattering of electron on a deuteron is seen in Figure C.1. The fitting parameters were consequently used to ascertain the neutron momentum distribution.

Model calculations performed for the Saclay-Lyon A [85] and Kaon-Maid [6] [20] models by P. Bydzovsky utilized the non-relativistic deuteron wave function described by the Bonn model [35]. However, those computed for the Regge-Plus Resonance theoretical model [25, 28] by P. Vancraeyveld, focused on both the Bonn approximation as well and the WJC-1 model [31]. In Figure C.2, the S_1 and D_1 state radial wave functions for configuration and momentum space are visible left to right respectively, for the Paris [34], Bonn [35], Nijmegen-III [36], Gross-IB, and WJC-1 [30, 31] non-relativistic deuteron wave function approximation.

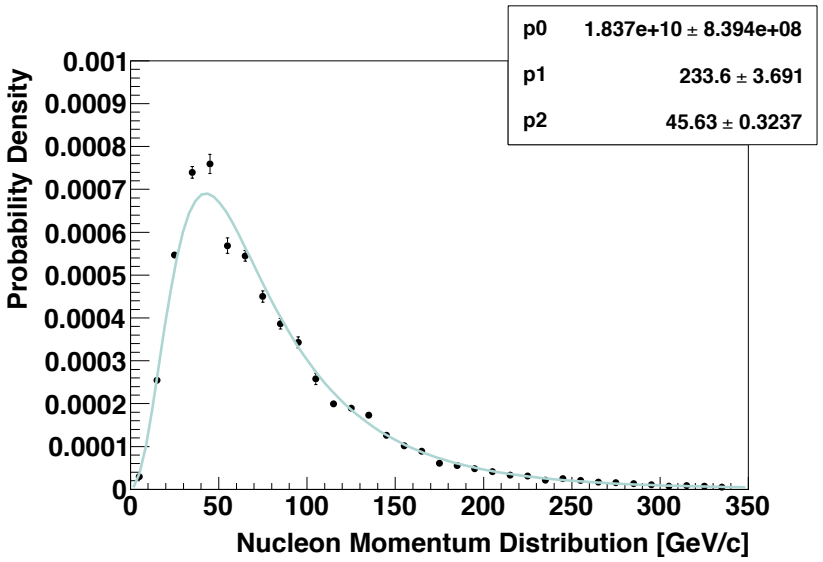

Figure C.1: Neutron momentum distribution described by the Hulthen wave function.

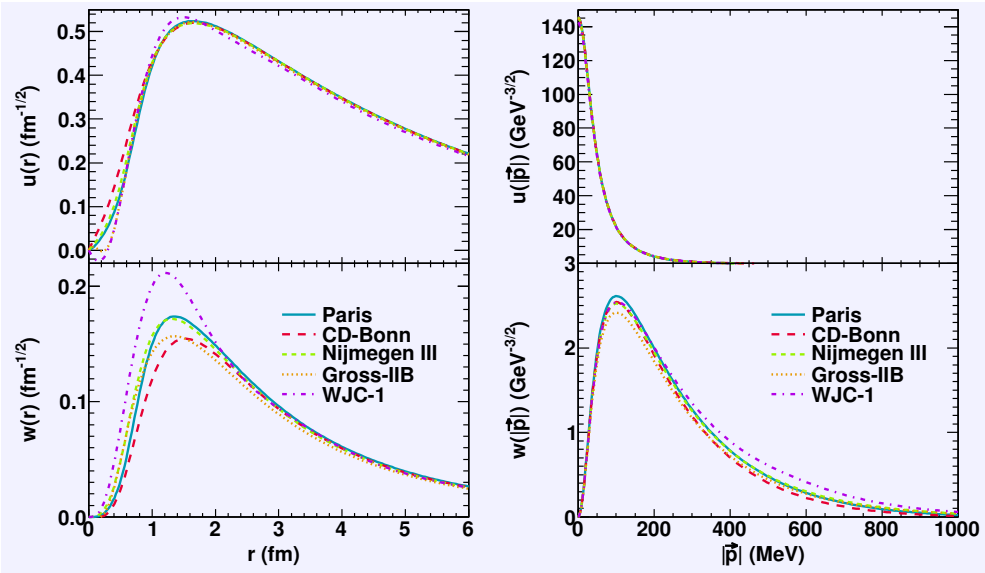

Figure C.2: S_1 and D_1 state radial wave functions for configuration and momentum space are visible left to right respectively. Taken from reference [25]. Illustrated in the figure are model calculations for the following models: Paris [34], Bonn [35], Nijmegen-III [36], Gross-IB, and WJC-1 [30][31].

APPENDIX

D

INVARIANT MASS DISTRIBUTIONS

The roots of educations are bitter, but the fruit is sweet.

Aristotle

Λ yield extraction is required for the cross section calculations as stipulated in equations 5.5, 5.6 and 5.7. The generated $p\pi^-$ invariant mass distribution for bins corresponding to the photon beam energy, momentum and angular integration bins are seen here.

D. INVARIANT MASS DISTRIBUTIONS

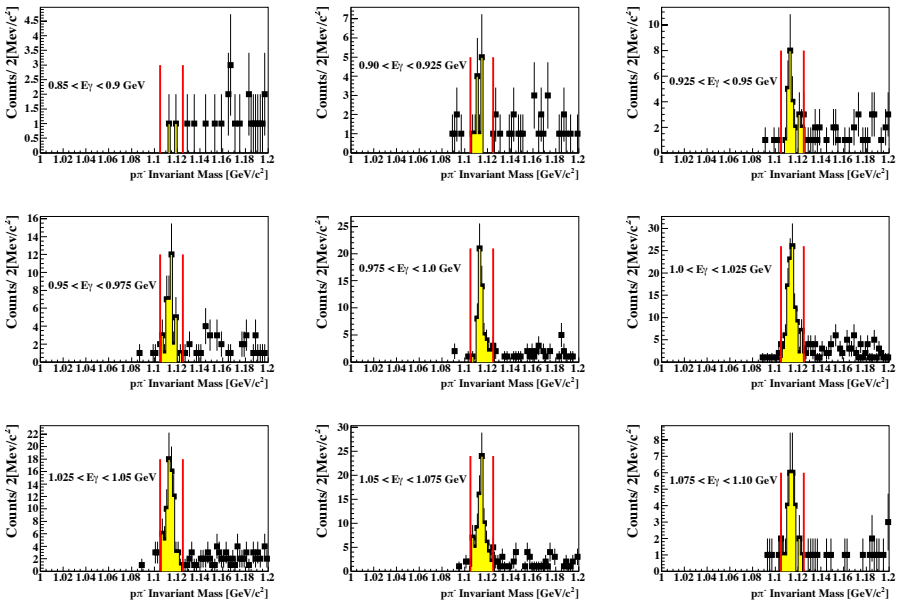

(a) $0.75 \leq \cos\theta_{\Lambda}^{LAB} \leq 1.0$

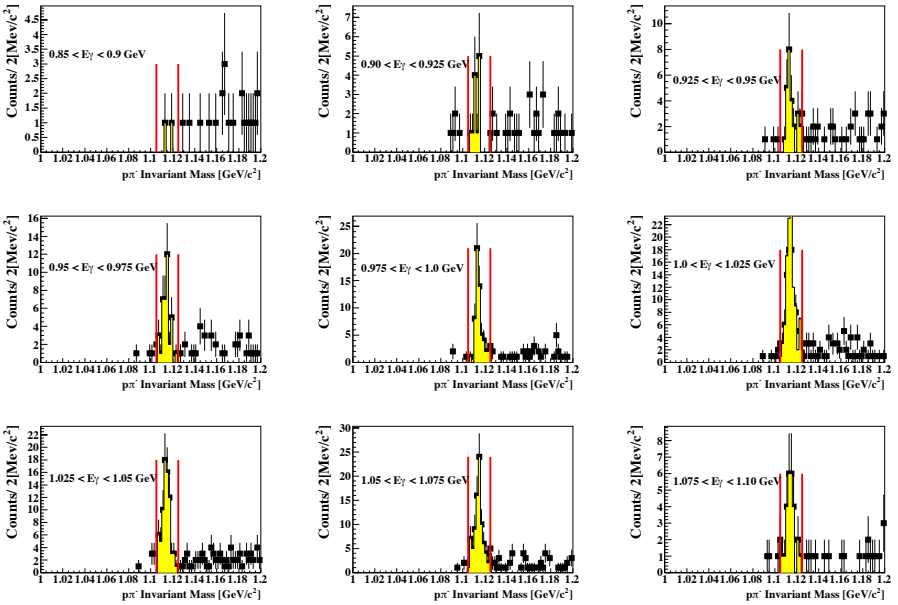

(b) $0.90 \leq \cos\theta_{\Lambda}^{LAB} \leq 1.0$

Figure D.1: The $p\pi^-$invariant mass distribution in the inclusive $\gamma d \rightarrow p\pi^-$X measurement for increasing bin increments of E_γ = 0.025 GeV, from 0.85 $\leq E_\gamma \leq$1.08 GeV, for angular integration regions of (a) $0.75 \leq \cos\theta_{\Lambda}^{LAB} \leq 1.0$ and (b) $0.90 \leq \cos\theta_{\Lambda}^{LAB} \leq 1.0$.

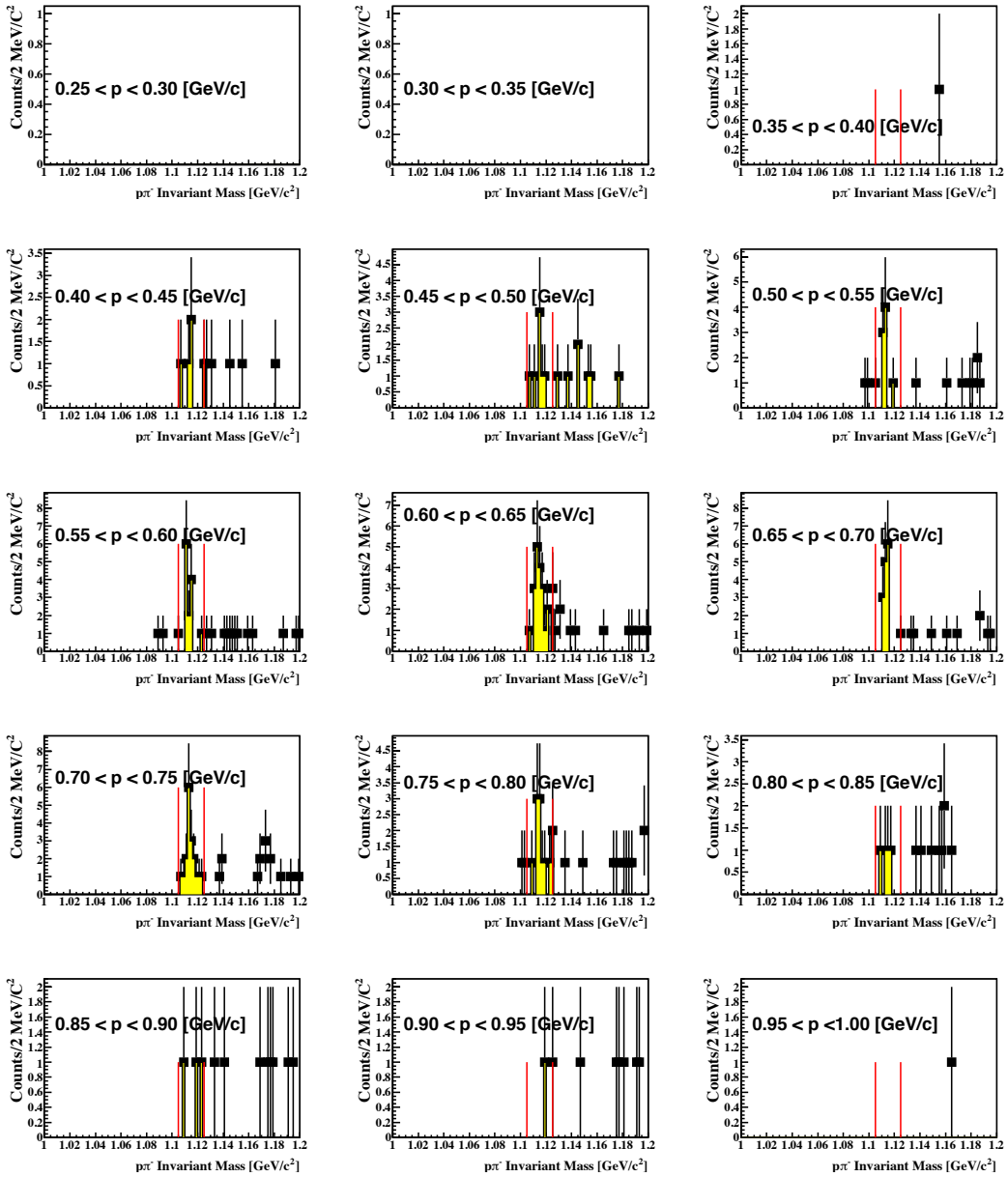

Figure D.2: The $p\pi^-$invariant mass distribution in the inclusive $\gamma d \rightarrow p\pi^-$X measurement for increasing bin increments of P_Λ^{LAB}= 0.05 GeV/c, from 0.25 $\leq P_\Lambda^{LAB} \leq$ 1.0 GeV/c in the angular integration region of $\cos\theta_\Lambda^{LAB} = 0.95-1.0$ for photon energies of $E_\gamma = 0.9 - 1.0$ GeV.

D. INVARIANT MASS DISTRIBUTIONS

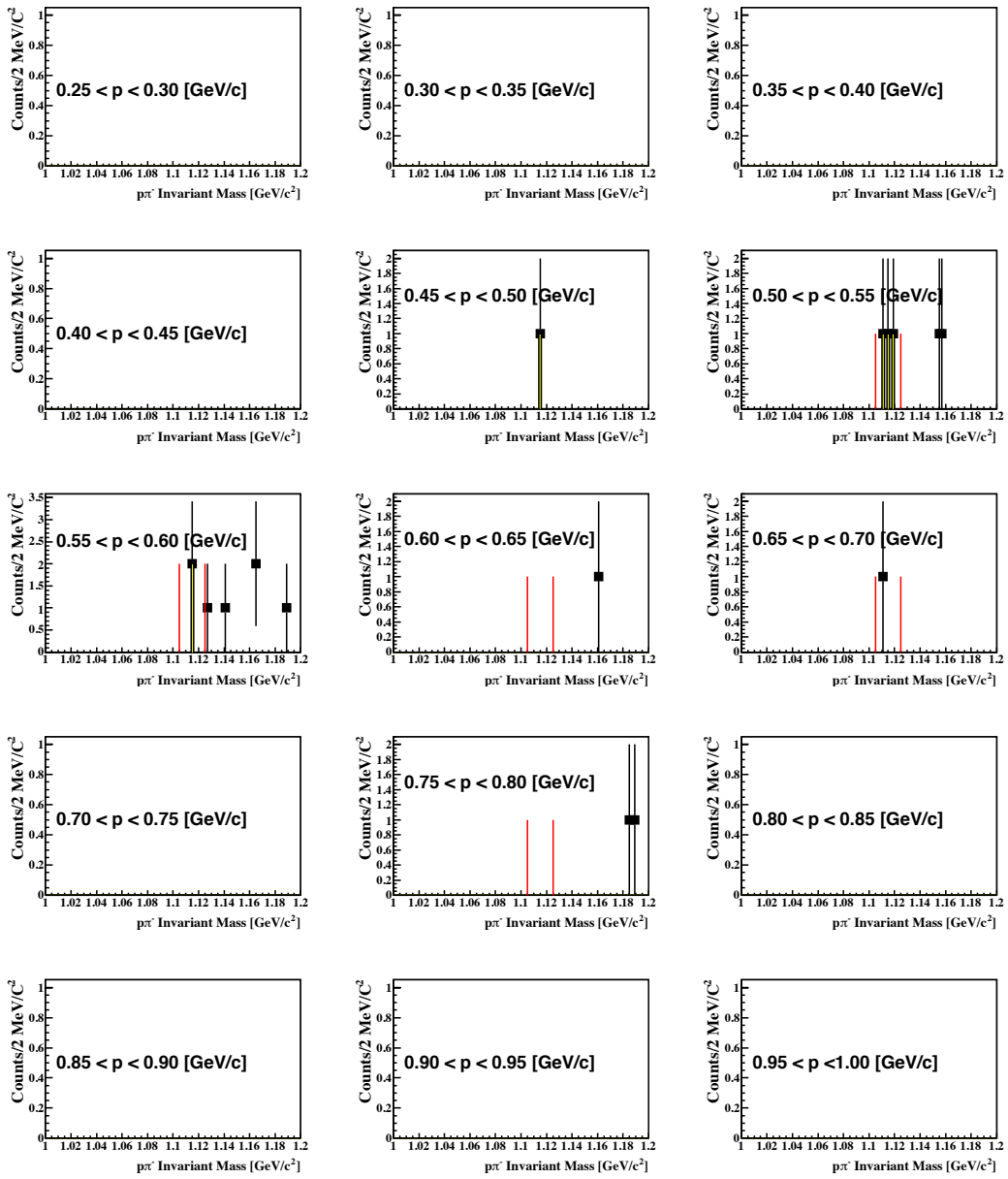

Figure D.3: The $p\pi^-$invariant mass distribution in the inclusive $\gamma d \rightarrow p\pi^-$X measurement for increasing bin increments of P_Λ^{LAB}= 0.05 GeV/c, from 0.25 $\leq P_\Lambda^{LAB} \leq$ 1.0 GeV/c in the angular integration region of $\cos\theta_\Lambda^{LAB} = 0.90-0.95$ for photon energies of $E_\gamma = 0.9 - 1.0$ GeV.

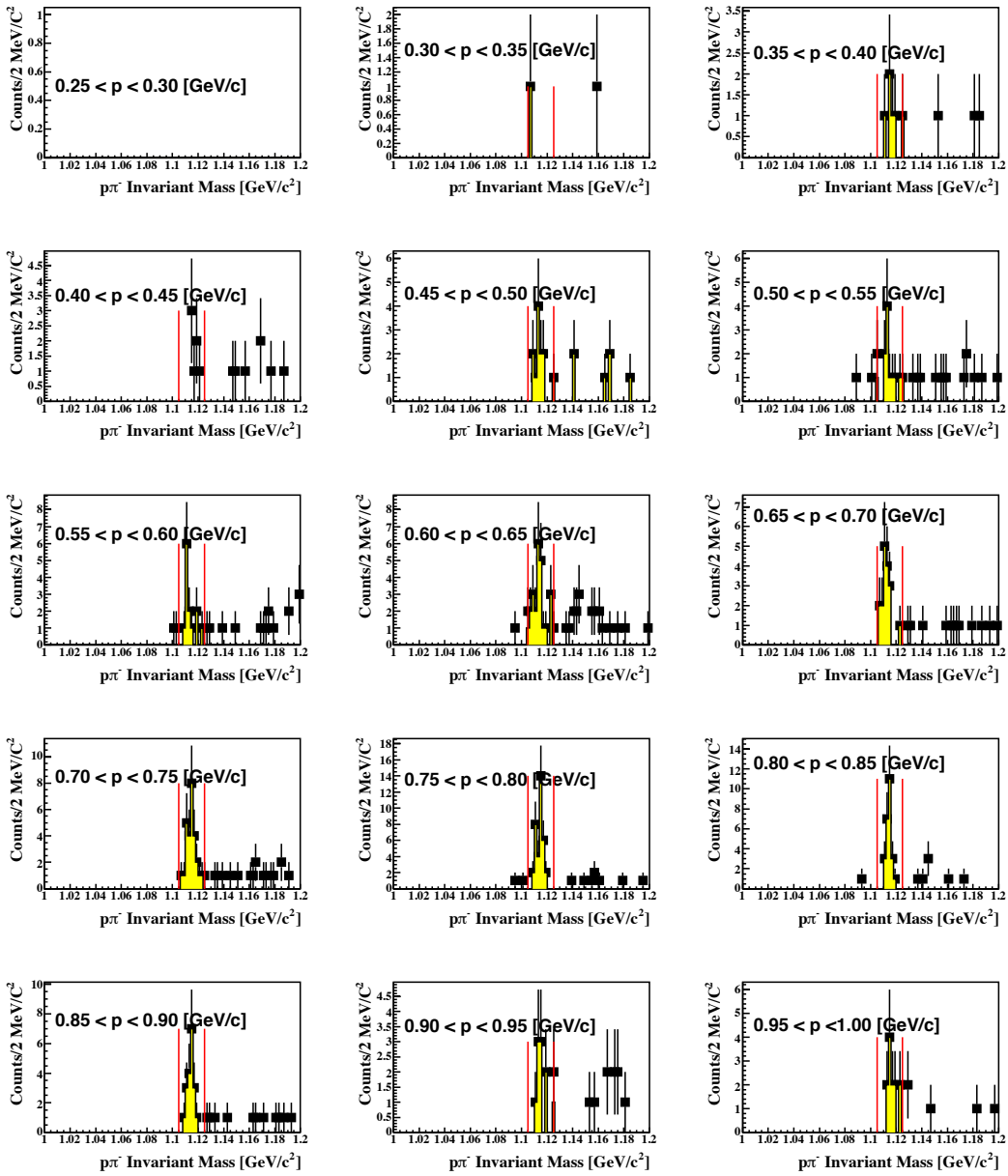

Figure D.4: The $p\pi^-$invariant mass distribution in the inclusive $\gamma d \rightarrow p\pi^-$X measurement for increasing bin increments of P_Λ^{LAB}= 0.05 GeV/c, from 0.25 $\leq P_\Lambda^{LAB} \leq$ 1.0 GeV/c in the angular integration region of $\cos\theta_\Lambda^{LAB} = 0.95{-}1.0$ for photon energies of $E_\gamma = 1.0 - 1.1$ GeV.

D. INVARIANT MASS DISTRIBUTIONS

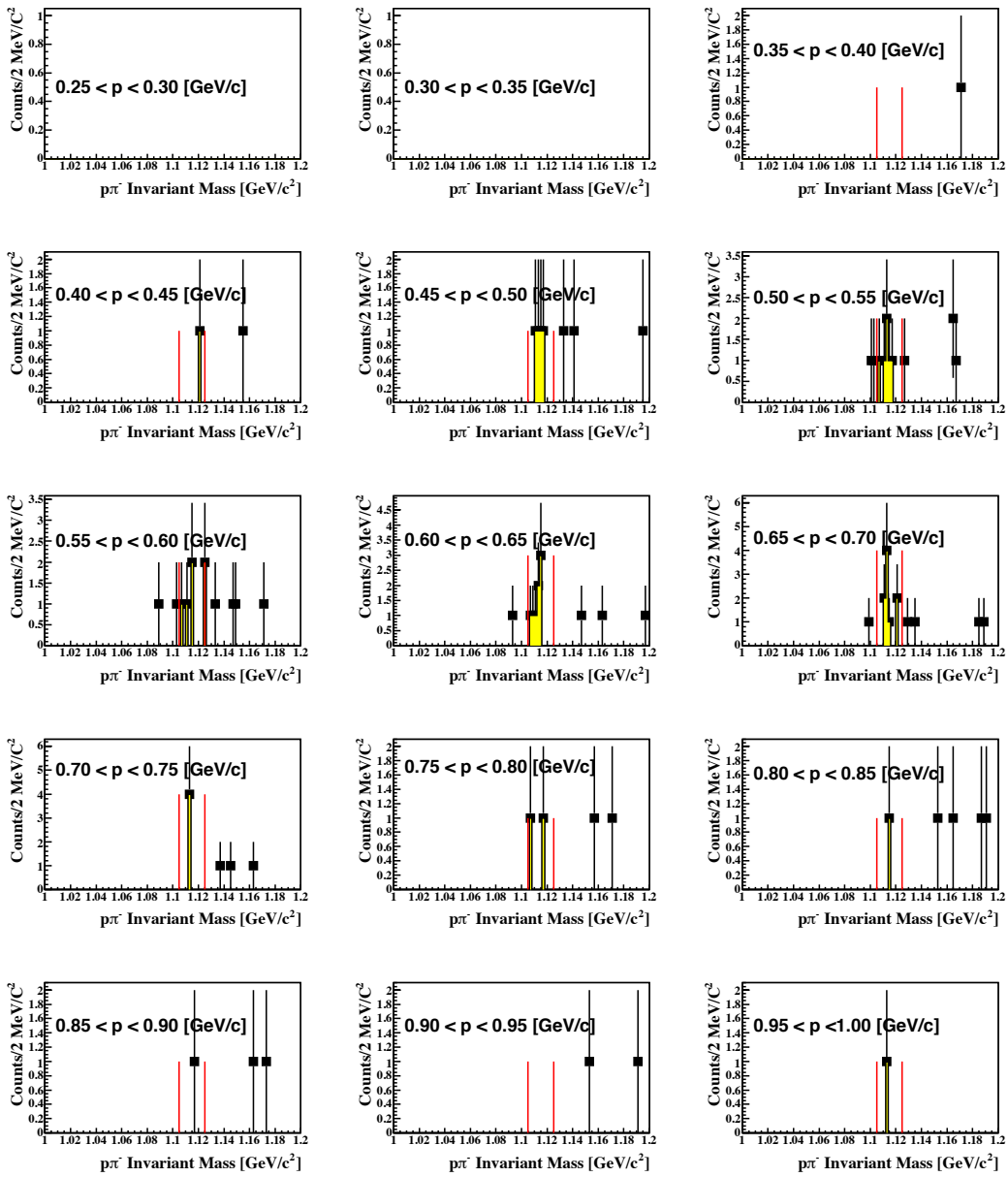

Figure D.5: The $p\pi^-$invariant mass distribution in the inclusive $\gamma d \rightarrow p\pi^-$X measurement for increasing bin increments of P_Λ^{LAB}= 0.05 GeV/c, from 0.25 $\leq P_\Lambda^{LAB} \leq$ 1.0 GeV/c in the angular integration region of $\cos\theta_\Lambda^{LAB} = 0.90-0.95$ for photon energies of $E_\gamma = 1.0 - 1.1$ GeV .

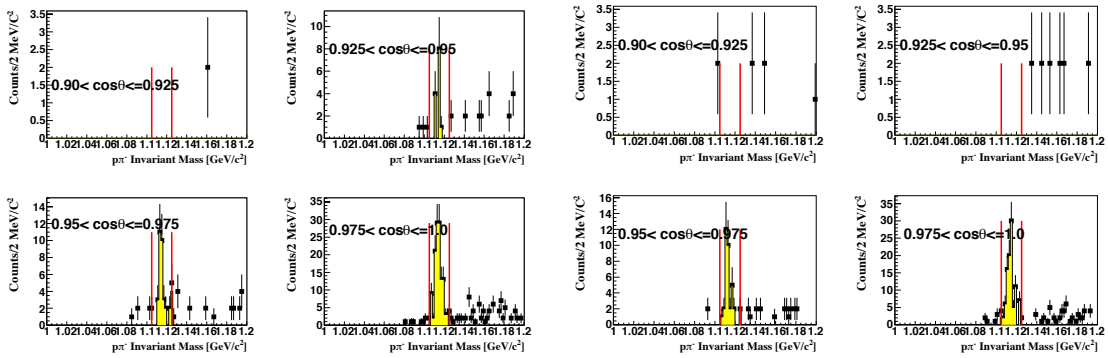

(a) E_γ= 0.95 − 1.00 GeV

(b) E_γ= 1.00 − 1.02 GeV

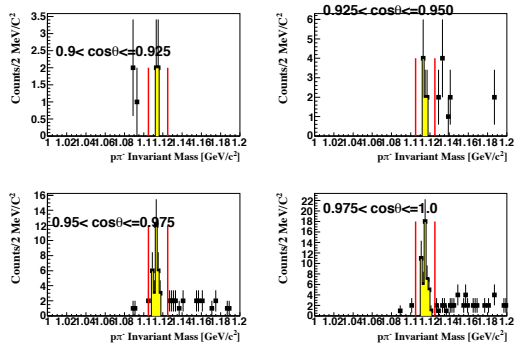

(c) E_γ= 1.02−1.04 GeV

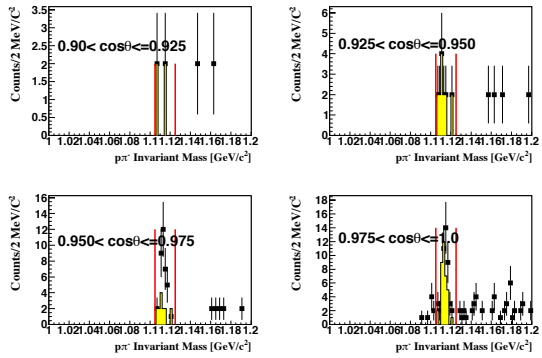

(d) E_γ= 1.04 −1.06 GeV

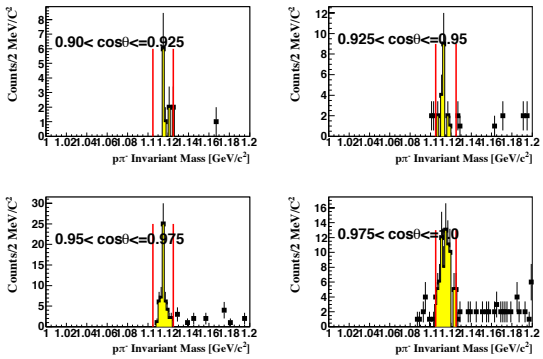

(e) E_γ= 1.06 − 1.08 GeV

Figure D.6: The $p\pi^-$invariant mass distribution in the inclusive $\gamma d \rightarrow p\pi^-$X measurement for increasing bin increments of cosθ_Λ^{LAB}= 0.025 GeV/c, from 0.80 ≤cosθ_Λ^{LAB}≤1.0, for photon energies of E_γ = (a) 0.95 − 1.00, (b) 1.00 − 1.02, (c) 1.02 − 1.04, (d) 1.04 − 1.06, and (e) 1.06 − 1.08 GeV.

APPENDIX

E

TABLES OF CROSS SECTIONS

The words of our parents we defied in irritation long ago are all essential.

Shiba Yoshimasa (1349 - 1410)

The integrated cross section for the $d(\gamma, \Lambda)X$ reaction are listed in table E.1 for the full and forward regions of angular integration. Based of the estimation procedure discussed in section 5.8 and described in equation 5.9. The estimated total cross section of $d(\gamma, \Lambda)X$ implementing the KM and RPR theoretical models is given in table E.2. The estimated values of the $d(\gamma, K^0)\Lambda$ process calculated by equation 6.7, with the theoretical values obtained from KM and SLA, and outlined in section 6.4.2 are listed in table E.3.

E. TABLES OF CROSS SECTIONS

Table E.1: Λ integrated cross section as a function of photon energy

	Inclusive Λ measurement			
	($0.90 \leq \cos\theta_{\Lambda}^{LAB} \leq 1.0$)			
Selection	Region [GeV]	$\sigma_{integral}$	Statistical	Systematic
Photon E_{γ}^{1}	0.850-0.900	0.006	$\pm$ 0.006	$\pm$ 0.139
Photon E_{γ}^{2}	0.900-0.925	0.210	$\pm$ 0.114	$\pm$ 0.168
Photon E_{γ}^{2}	0.925-0.950	0.750	$\pm$ 0.216	$\pm$ 0.072
Photon E_{γ}^{3}	0.950-0.975	1.510	$\pm$ 0.307	$\pm$ 0.201
Photon E_{γ}^{4}	0.975-1.000	2.339	$\pm$ 0.374	$\pm$ 0.127
Photon E_{γ}^{5}	1.000-1.025	2.883	$\pm$ 0.424	$\pm$ 0.316
Photon E_{γ}^{6}	1.025-1.050	3.097	$\pm$ 0.439	$\pm$ 0.554
Photon E_{γ}^{7}	1.050-1.075	3.593	$\pm$ 0.473	$\pm$ 0.466
Photon E_{γ}^{8}	1.075-1.080	3.794	$\pm$ 0.486	$\pm$ 0.607
	($0.75 \leq \cos\theta_{\Lambda}^{LAB} \leq 1.0$)			
Photon E_{γ}^{1}	0.850-0.900	0.007	$\pm$ 0.007	$\pm$ 0.139
Photon E_{γ}^{2}	0.900-0.925	0.267	$\pm$ 0.129	$\pm$ 0.168
Photon E_{γ}^{2}	0.925-0.950	0.951	$\pm$ 0.243	$\pm$ 0.072
Photon E_{γ}^{3}	0.950-0.975	1.805	$\pm$ 0.335	$\pm$ 0.201
Photon E_{γ}^{4}	0.975-1.000	2.281	$\pm$ 0.375	$\pm$ 0.127
Photon E_{γ}^{5}	1.000-1.025	2.918	$\pm$ 0.424	$\pm$ 0.316
Photon E_{γ}^{6}	1.025-1.050	3.307	$\pm$ 0.455	$\pm$ 0.554
Photon E_{γ}^{7}	1.050-1.075	3.689	$\pm$ 0.480	$\pm$ 0.467
Photon E_{γ}^{8}	1.075-1.080	3.953	$\pm$ 0.497	$\pm$ 0.609

Table E.2: Estimated Λ total cross section as a function of photon energy

	Λ (σ^{Λ}_{Tot}) Total Cross Section			
	(Kaon-MAID)			
Selection	Region [GeV]	σ_{tot}	Statistical	Systematic
Photon E^1_γ	0.850-0.900	0.006	± 0.006	± 0.001
Photon E^2_γ	0.900-0.925	0.221	± 0.134	± 0.016
Photon E^2_γ	0.925-0.950	0.794	± 0.245	± 0.015
Photon E^3_γ	0.950-0.975	1.594	± 0.319	± 0.200
Photon E^4_γ	0.975-1.000	2.417	± 0.405	± 0.013
Photon E^5_γ	1.000-1.025	3.201	± 0.471	± 0.205
Photon E^6_γ	1.025-1.050	3.580	± 0.508	± 0.218
Photon E^7_γ	1.050-1.075	4.653	± 0.614	± 0.092
Photon E^8_γ	1.075-1.080	5.479	± 0.703	± 0.362
	(Regge-Plus-Resonance)			
Photon E^1_γ	0.850-0.900	0.007	± 0.062	± 0.009
Photon E^2_γ	0.900-0.925	0.270	± 0.130	± 0.016
Photon E^2_γ	0.925-0.950	0.961	± 0.246	± 0.014
Photon E^3_γ	0.950-0.975	1.823	± 0.339	± 0.200
Photon E^4_γ	0.975-1.000	2.839	± 0.423	± 0.013
Photon E^5_γ	1.000-1.025	3.899	± 0.496	± 0.205
Photon E^6_γ	1.025-1.050	4.491	± 0.532	± 0.218
Photon E^7_γ	1.050-1.075	5.314	± 0.579	± 0.092
Photon E^8_γ	1.075-1.080	5.927	± 0.612	± 0.362

E. TABLES OF CROSS SECTIONS

Table E.3: Estimated $K^0\Lambda$ total cross section as a function of photon energy

	$K^0\Lambda$ (σ_{Tot})Total Cross Section			
	(Kaon-MAID)			
Selection	Region [GeV]	σ_{tot}	Statistical	Systematic
Photon E_γ^1	0.850-0.900	0.003	± 0.003	± 0.001
Photon E_γ^2	0.900-0.925	0.116	± 0.063	± 0.066
Photon E_γ^2	0.925-0.950	0.502	± 0.144	± 0.095
Photon E_γ^3	0.950-0.975	1.113	± 0.226	± 0.199
Photon E_γ^4	0.975-1.000	1.500	± 0.250	± 0.295
Photon E_γ^5	1.000-1.025	1.758	± 0.258	± 0.182
Photon E_γ^6	1.025-1.050	2.079	± 0.295	± 0.196
Photon E_γ^7	1.050-1.075	2.238	± 0.296	± 0.150
Photon E_γ^8	1.075-1.080	2.398	± 0.307	± 0.129
	(SLA$r_{K_1K\gamma}$ = -1.5)			
Photon E_γ^1	0.850-0.900	0.002	± 0.003	± 0.001
Photon E_γ^2	0.900-0.925	0.051	± 0.027	± 0.066
Photon E_γ^2	0.925-0.950	0.405	± 0.116	± 0.095
Photon E_γ^3	0.950-0.975	0.914	± 0.185	± 0.199
Photon E_γ^4	0.975-1.000	1.224	± 0.204	± 0.275
Photon E_γ^5	1.000-1.025	1.575	± 0.231	± 0.182
Photon E_γ^6	1.025-1.050	1.883	± 0.267	± 0.196
Photon E_γ^7	1.050-1.075	2.087	± 0.275	± 0.150
Photon E_γ^8	1.075-1.080	2.269	± 0.292	± 0.129

APPENDIX
F

VITA

I run the rapids of time .
A man's life, like the frothing waters...
Rising high, falling low.
All vanity.

Koike Kazou.

Education

2012 **PhD**.**Physics**, Tohoku University, Sendai, Japan.
Advisor: Dr. Osamu Hashimoto and Dr. Kazushige Maeda
Thesis Title: A Study of the Strangeness Photoproduction Process in the $\gamma d \rightarrow \Lambda X$ Reaction at Photon Energies up to 1.08 GeV

2008 **M**.**S**.**Physics**, Florida International University, Miami, Florida.
Advisor: Dr. Joerg Reinhold
Thesis Title: Investigation Of Particle Identification Methods For The Analysis of the Photoproduction of Neutral Kaons on a Liquid Deuterium Target

2005 **B**.**S**.**Physics**, Florida International University, Miami, Florida.
Minor: Philosophy.
Advisor: Dr. Joerg Reinhold
Thesis Title: Detection of Cherenkov Light Using a Wavelength Shifting Acrylic Plastic: Development of a Segmented One-Dimensional RICH Detector

Awards

2011 Tohoku Kaihatsu Memorial Foundation Research Fellowship.

F. VITA

2008 Tohoku University, International Graduate Program of Advanced Sciences,
Super Doctor Course Fellowship.
2008 Florida International University, College of Arts and Sciences,
Outstanding Academic Achievement: Graduate Student in Physics.
2007 Florida International University, Gradate Student Association Symposium
First Place, Poster Session:
2005 Florida International University, Summer Research Institute Symposium
Third Place, Poster Session:
2005 Florida International University, Summer
Ronald E. McNair Post Baccalaureate Fellowship

Publications

Measurement of the photon induced production of Λ in the $^2H(\gamma,\Lambda)X$ reaction
B.Beckford, et al.arXiv:1210.7585 [nucl-ex](2012)

Neutral Kaon photo production in the threshold energy region
B.Beckford, *et..al*.AIP conf. Proc. 1388 (2011) 280

Report on strangeness photoproduction experiments performed with the Neutral Kaon Spectrometer 2.
B.Beckford, *et..al*. arXiv:1202.2748[nucl-ex] (2012)

Status of the NKS2 experiment
M. Kaneta , B.Beckford, *et..al*
Research report of the Laboratory of Nuclear Science, Tohoku University Vol 44 (2011).

Performance test of wavelength-shifting acrylic plastic Cherenkov detector.
B.Beckford, *et..al* arXiv:1007.0147v2[nucl-ex] (2010)

Strangeness photoproduction experiments at SENDAI
H.Kanda, B.Beckford, *et..al*,
Nuclear Physics A 835 (2010) 317-320

Study of charged pion photoproduction on deuteron.
Han Yun-Cheng B.Beckford*et..al*,
Nuclear Physics A 834 (2010) 596c-598c

Future hypernuclear program at JLab Hall C
S.N. Nakamura.,B.Beckford *et..al*,
Nuclear Physics A 754, (2005) 421 .

Conferences

Measurement of the photon induced production of Λ in the $d(\gamma, \Lambda)X$ process at threshold energies.
Brian Beckford for the NKS2 collaboration
International Workshop on Strangeness Nuclear Physics (SNP12),
August 27 - 29, 2012, Osaka, Japan

Investigation of the photoinduced production of strangeness in the threshold region
Brian Beckford for the NKS2 collaboration
Poster session, 2012 GCOE symposium.
February 22-25,Sendai, Japan.

Investigation of the photoinduced production of strangeness in the threshold region
Brian Beckford for the NKS2 collaboration
Poster session, 2012 1st International School of Strangeness Nuclear Physics.
February 12-18, Tokai-Sendai, Japan.

Photoproduction of Λ Hyperons and Neutral Kaons on the deuteron in the energy range of 0.8 - 1.1 GeV
Brian Beckford for the NKS2 collaboration
Fall Meeting of the Japan Physical Society (JPS)
September 18 2011; Hirosaki ,Japan

Current status of the Vertex Drift Chamber VDC
Brian Beckford
Nuclear Physics Working Group meeting at LNS
March 02, 2010; Sendai ,Japan.

Performance study of a Vertex Drift Chamber (VDC) for the measurement of strangeness

production in the d$(\gamma, K^0)\Lambda$p reaction.
Brian Beckford for the NKS2 collaboration.
3rd APS/JPS joint meeting
October 13-17, 2009; Waikoalo Hawaii

Photoproduction of Neutral Kaons on Deuterons
Brian Beckford
Poster session, 2007 30th Annual Meeting of National Society of Black Physicists.
February 2007, Boston, MA.

Photoproduction of Neutral Kaons on Deuterons
Brian Beckford
Poster session, 2006,
73rd Annual Meeting of the Southeastern Section of the APS.
November, 2006; Williamsburg, VA.

Detection of Cherenkov Light with Wavelength Shifting Plastic
B. Beckford
Poster session, at PANIC05, Particles and Nuclei International Conference,
Santa Fe, NM - October 24-28, 2005

Detection of Cherenkov Light with Wavelength Shifting Plastic: *ABeamTest*
Brian Beckford
Poster session, 2005
72nd Annual Meeting of Southeastern American Physics Society
April Meeting, 2005, Tampa, FL.

ExtraCurricular
2004- Member American Physical Society
2008-2012 Tohoku University KENDO CLUB
2006-2008 Founder and organizer of Physics Student Seminar.
2004-2005 Vice president of Society of Physics Students FIU chapter
2004-2008 FIU KENDO CLUB, Founding President:

BIBLIOGRAPHY

[1] T. Watanabe *et al.* Photo-production of neutral kaons on ^{12}C in the threshold region in the threshold region. *Phys. Lett.*, B 651(269):arXiv:nucl–ex:0607022v2, 2007. viii, xi, 10, 11

[2] K. Tsukada. Photoproduction of Neutral Kaons on the liquid deuterium target in threshold region. *Phys Rev*, C 78(014001), 2008. viii, xii, 10, 11, 12

[3] K.Tsukada *et al.* Photoproduction of Neutral Kaons on the liquid deuterium target in threshold region. *Phys. Rev.*, C 83,(039904(E)), 2011. viii, xii, 10, 11, 12, 169

[4] K. Futatsukawa *et al.* Kaon photo-production on the deuteron at sendai. In *EPJ Web of Conferences*, volume 20. EPJ Science, 2012. viii, ix, xii, xxii, 12, 121, 132, 136, 137, 173

[5] K. Futatsukawa. *An investigation of the elementary photoproduction of strangeness in the threshold region.* PhD thesis, Tohoku University, Sendai, Japan, March 2011. viii, xi, xii, xiv, xxii, xxvi, 9, 12, 38, 42, 121, 132, 136, 137, 172, 173, 175, 176, 178, 179

[6] T. Mart. Evidence for a missing nucleon resonance in kaon photoproduction. *Phys. Rev.*, C 61:012201, 2005. ix, xii, 25, 26, 33, 133, 143, 193

[7] T. Mizutani, C. Fayard, G. H. Lamot, and B. Saghai. Off-shell effects in the electromagnetic production of strangeness. *Phys Rev.*, C 58(75), 1998. ix, xii, xxiii, 25, 28, 143, 145, 146, 151

[8] P. Vancraeyveld, L. De Cruz, and J. Ryckebusch. Regge-pus-resonace predictions to neutral kaon production from the deuteron. volume 1374 of *AIP Conf. Proc.*, page 335. American Institutre of Physics, 2011. ix, xxiv, xxv, 147, 156, 165, 168

[9] P. Vancraeyveld *et.al.* Kaon photoproduction from the deuteron in a regge-plus-resonance approach. *Nucl. Phys.*, A 897:42–53, 2013. ix, 29, 157, 159

[10] A. Salam, K.Miyagawa, T.Mart, and C. Bennhold and. W.Glocke. K^0 photoproduction on deuteron and the extraction of the elementary amplitude. *Phys. Rev.*, C 74, arXiv:nucl–th/0608053, 2006. xi, 5, 6

[11] K. Glander *et al.* Measurement of $\gamma p \to K^+\Lambda$ and $\gamma p \to K^+\Sigma^0$ at photon energies up to 2.6 gev. *Eur. Phys. J. lA*, A 19:251–273, 2004. xi, xxvi, 5, 6, 7, 172, 175, 176, 179

[12] M. Tran *et al.* Measurement of $\gamma p \to K^+\Lambda$ and $\gamma p \to K^+\Sigma^0$ at photon energies up to 2.6 GeV. *Phys. Lett.*, B 445:20, 1998. xi, xxvi, 5, 6, 172, 175, 176, 179

[13] R. Bradford *et al.* Differential cross sections for γ+p$\to K^+ +\Lambda$ and Σ^0 hyperons. *Phys. Rev.*, C 73:035202, 2006. xi, xxvi, 5, 6, 172, 175, 176

[14] A.V. Anisovich *et.al.* Baryon resonaces and polarization transfer in hyperon photoproduction. arXiv:hep–ph/0707.3596v2, 2007. xi, 5, 6, 7, 172

[15] J.W.C McNabb *et.al.* Hyperon photoproduction in the nucleon resonance region. *Phys. Rev.*, C 69:042201, 2004. xi, xxvi, 5, 6, 172, 175

[16] M. McCracken. Differential cross section and recoil polarization measurements for the $\gamma p \to K^+\Lambda$ reaction using clas at jefferson lab. *Phys. Rev.*, C 81:025201, 2010. xi, 5, 6, 172

[17] K.Tsukada. *Photoproduction of neutral kaons on deuterons near the threshold.* PhD thesis, Tohoku University, Sendai, Japan, 2005. xi, xii, 8, 11, 12

[18] H. Yamazaki and et. al. The $^{12}C(\gamma, K^+)$ reaction in the threshold region. *Phys Rev.*, C 52:1157–1160, 1995. xi, 10, 11

[19] L. De Cruz. *Bayesian model selection for electromagnetic kaon prodction in the Regge-plus resonance framework.* PhD thesis, Ghent University, Belgium, 2011. xii, 20, 21, 28, 30, 33

[20] T. Mart, S. Sumowidagdo, and D. Kusno. Kaon photoproduction on the nucleon: overview of some applications. *Nucl. Phys.*, A 684(502-504):arXiv:nucl–th/ 0008001, 2001. xii, xxiii, 4, 25, 26, 33, 133, 143, 145, 146, 149, 193

[21] C. Bennhold, T. Mart, A. Waluyp, H. Harberzettl, G. Penner, T. Feuter, and U.Mosel. Nucleon resonances in kaon photoproduction. arXiv:nucl–th/9901066v1, 1999. xii, 13, 25, 26, 27, 33, 133, 143

[22] T. Corthals. *Regge-plus-resonance approach to kaon production from the proton.* PhD thesis, Ghent University, Belgium, 2007. xiii, 29, 31

[23] T. Corthals *et al.* Forward-angle $K^+\Lambda$ photoproduction in a regge-plus-resonance approachk+ photoproduction in a regge-plus-resonance approach. *Phys Rev.*, C 73 (045207), 2006. xiii, 31

[24] B. Beckford *et al.* Neutral kaon photoproduction the threshold energy. *AIP*, 1388: 280, 2011. xxii, 14, 136, 137

[25] P. Vancraeyveld. *Regge-pus-resonace approach to strangeness production from the deuteron.* PhD thesis, Gent University, Belgium, 2011. xxiii, xxiv, xxv, xxvii, xxix, 18, 23, 29, 30, 33, 147, 148, 149, 156, 157, 165, 168, 193, 194

[26] T. Ryckebusch T. Corthals, D. G. Ireland and T. Van Cauteren. Kaon photoproduction from a deuteron in a regge-plus-resoance approach. arXiv:nucl–th/1207.2903v1, 2010. xxiii, 4, 27, 29, 133, 143, 148, 149, 157, 159

[27] P. Vancraeyveld, L. De Cruz, and J. Ryckebusch. Regge-pus-resonace predictions to neutral kaon production from the deuteron. arXiv:nucl–th/1010.0113v2, October 2010. xxiv, 147, 156, 165

[28] T. Corthals, T. Ryckebusch, and T. Van Cauteren. Forward-angle $K^+\Lambda$ photoproduction in a regge-plus-resonance approach. *Phys Rev*, C 73:045207, 2006. xxiv, xxv, 29, 30, 33, 133, 143, 156, 165, 168, 193

[29] T. Corthals, D. G. Ireland, T. Ryckebusch, and T. Van Cauteren. Regge-plus-resonance treatment of the $p(\gamma, K^+)\Sigma^0$ and $p(\gamma, K^0)\Sigma^+$ reactions at forward kaon angles. *Phys Rev*, C 75:045204, 2007. xxiv, 29, 30, 133, 143, 156, 166

[30] F. Gross and A. Stadler *et, al.* Covariant spectator theory of np scattering: phase shifts obtained from precision ts to data below 350 mev. *Phys. Rev.*, C 78:014005, 2008. xxiv, xxvii, 157, 193, 194

[31] F. Gross and A. Stadler. Covariant spectator theory of np scattering: Effective range expansions and relativistic deuteron wave functions. arXiv:nucl–th/1007.0778v1, July 2010. xxiv, xxvii, 157, 193, 194

[32] P. Vancraeyveld. Private Communication, 2012. xxiv, 157, 169

[33] K. Bantawa. *Photoproduction of Neutral Koans on Deuterium.* PhD thesis, Kent State University, Kent, Ohio, 2009. xxvi, 7, 175, 176, 179

[34] M. Lacombe *et al.* Parametrization of the paris n-n potential. *Phys. Rev.*, C 21(3): 861–873, March 1980. xxvii, 193, 194

[35] R.Machleidt. High-precision, charge-dependent bonn nucleon-nucleon potential. *Phys. Rev.*, C 63(024001), 2001. xxvii, 193, 194

[36] V. Stocks *et al.* Construction of high quality nn potential models. arXiv:nucl–th/9406039v1, June 1994. xxvii, 193, 194

[37] L. De Cruz *et al.* Bayesian interference of the resonance content $p(\gamma, K^+)\Lambda$. *Phys. Rev. Lett.*, 108(182002), 2012. xxix, 32, 33

[38] R. C. Reid and J. M. Prausnitz. *The properties of gases and liquids*, volume 3rd. McGraw-Hill, 1977. xxix, 77, 79

[39] S. B. McAleer. *A measurement of the Recoil Polarization of Electroproduced* $\Lambda(1116)$. PhD thesis, Florida State University, Tallahassee, Florida, 2002. 2, 4

[40] E. Klempt. Baryon spectroscopy. *Rev. Mod. Phys.*, 82:1095, 2010. 2, 16, 134

[41] M. Garielyan. *Measurement of the induced polarization of* $\Lambda(1116)$ *in kaon electronproduction with CLAS.* PhD thesis, Florida International University, Miami, Florida, 2012. 4, 15

[42] H.Thom. Phenomenological analysis of $K^+\Lambda$ photoproduction. *Phys. Rev.*, 151 (1322-1366), 1966. 4, 23

[43] T.K. Kuo. Low-energy photoproduction of Λ^0 and K^+ from protons. *Phys. Rev.*, 129, 1963. 4

[44] R. Erbe *et al.* Photoproduction of meson and baryon resonances at energies up to 5.8 gev. *Phys Rev.*, 175:1669, 1968. 4

[45] J. Ballam *et al.* Bubble-chamber study of photoproduction by 2.8- and 4.7-GeV polarized photons. i. cross-section determinations and production of ρ^0 and Δ^{++} in the reaction $\gamma p \to p\pi^+\pi^-$. *Phys Rev.*, D 5:545, 1972. 4

[46] H. W. Dannhausen *et al.* Photoproduction of positive pions from hydrogen at large angles in the energy range 0.3–2.0 gev. *Eur. Phys. J.*, A 11:441, 2001. 4

[47] P. Bydžovský, M. Sotona, O. Hashimoto, and T. Takahashi. Kaon photo-production on nucleon and deuteron. arXiv:nucl–th/0412035v1, 2004. 5, 23, 144, 170

[48] R.G.T. Zegers *et, al.* Evidence for a narrow s =+1 baryon resonance in photoproduction from the neutron. *Phys. Rev. Lett.*, 91, 2003. 6

[49] M. Sumihama *et, al.* The $\gamma p \to K^+\Lambda$ and $\gamma p \to K^+\Sigma^0$ reactions at forward angles with photon energies from 1.5 to 2.4 *GeV*. *Phys. Rev.*, C 73:035214, 2006. 6

[50] A. Lleres *et, al.* Polarization observable measurements for $\gamma p \to K^+\Lambda$ and $\gamma p \to K^+\Sigma^0$ for energies up to 1.5 GeV. *Eur. Phys. J.*, A 31:79, 2007. 6, 172

[51] A. Lleres *et, al.* Measurement of beam-recoil observables O_x, O_z and target asymmetry T for the reaction $\gamma p \to K^+\Lambda$. *Eur. Phys. J.*, A 39:149, 2009. 6, 172

[52] K. I. Blomqvist *et al. Nuclear Instr. And Methods*, A 403:263, 1998. 6, 7

[53] A. Bock *et al.* Measurement of the target asymmetry of η and π^0 photoproduction on the proton. *Phys. Rev. Lett.*, 81:534, 1998. 7

[54] F. Kalleicher *et al. Z. Phys*, A 359:201, 1997. 7

[55] J. Naumann *et al.* A photon tagging system for the GDH-Experiment at ELSA. *Nuclear Instr. And Methods*, A 498:211., 2003. 7

[56] E. Aker *et al.* The crystal barrel spectrometer at lear. *Nuclear Instr. And Methods*, A 321:69, 1992. 7

[57] S. Shende. *Strangess Photoproduction on the Deterium Target.* PhD thesis, University of Groningen, Netherlands, 2007. 7

[58] R. Erbe *et al.* Multipion and strange-particle photoproduction on protons at energies up to 5.8 GeV. *Phys Rev.*, 188(2060), 1969. 7

[59] A.V. Anisovich *et.al.* Baryon resonaces and polarization transfer in hyperon photoproduction. arXiv:hep–ph/0707.3596v2, 2007. 7

[60] N. Hassall. *Spin observables in kaon photoproduction fro mthe neutron in a deuterium target with CLAS.* PhD thesis, University of Glasgow, 2010. 7

[61] K. Maruyama. The large-acceptance spectrometer *TAGX* for photoreaction studies at the 1.3-gev tokyo electron synchrotron. *Nuclear Instr. And Methods*, A 376(335), 1996. 8

[62] T. Takahashi *et al.* Photoproduction of neutral kaons on c in the threshold region. *Nucl. Phys,*, A 721:C(991–994), 2003. 10

[63] S. Capstick and W. Roberts. Strange decays of nonstrange baryons. *Phys. Rev.*, D 58:074011, 1998. 13

[64] K. Maeda *et al.* Kaon photoproduction on nuclei. In *Hadron and Nuclear Physics with Electromagnetic Probes*. Elsevier Science, 2000. 15

[65] E. Paul *et al.* Physics of associated strangeness production at *ELSA*. In *Hadron and Nuclear Physics with Electromagnetic Probes*. Elsevier Science, 2000. 15

[66] T. A. DeGrand *et al.* Modeling polarization asymmetry. *Phys. Rev.*, D 38(403), 1988. 15

[67] A. J. Reischl. *Quasi-real photo-production of hyperons and their impact on* Λ^0 *polarization measurements.* PhD thesis, University of Amsterdam, Amsterdam, Netherlands, 2007. 15, 134

[68] M.Guidal *et, al.* Pion and kaon photoproduction at high energies: forward and intermediate angles. *Nucl. Phys.*, A 627:645, 1997. 22

[69] S. Steininger *et, al.* Threshold kaon photo- and electroproduction in SU(3) baryon chiral perturbation theory. *Phys. Lett.*, B 391:446, 1997. 22

[70] B. Borasoy *et, al.* A gauge-invariant chiral unitary framework for kaon photo- and electroproduction on the proton. *Eur. Phys. J*, A 34:161–183, 2007. 22

[71] T. Mart *et al.* Multipole approach for photon and electro production of kaons. *Phys Rev.*, C 64, 2006. 22

[72] quark model. Proc. of electrphotoproduction of strangeness of nucleons and nuclei,. volume arXiv:nucl-th/0310025. World Sci., 2003. 23

[73] F. Renard and Y.Renard. Photoprodcution $K^+\Lambda$ and K^+ Σ^0 and $g_{\Lambda kn}$. *Nucl. Phys.*, B 25:490–498, 1971. 23

[74] R. A. Adelseck *et, al.* Electromagnetic production of kaons. *Phys Rev.*, C 38:1965–1967, 1988. 23

[75] R. A. Adelseck *et, al.* Kaon photoproduction operator for use in nuclear physics. *Phys Rev*, C 32:1681–1693, 1985. 23

[76] R. A. Williams *et, al.* Hyperon electroproduction in a crossing and duality constrained model. *Phys Rev.*, C 46:1617, 1992. 23

[77] W.E. Meyerhof. *Elements of Nuclear Physics.* McGraw-Hill, 1967. 23, 122

[78] S. Janssen *et. al.* Kaon photoproduction: backgorund contributions, form factors, and missing resonances. *Phys. Rev.*, C 65 arXiv(015201):nucl–ex/1202.2748v2, 2001. 24, 26, 32

[79] H. Harberzettl, C. Bennhold, T. Mart, and T. Feuster. Gauge-invariant tree-level photproduction amplitudes with form factors. *Phys. Rev.*, C58(40), 1998. 24

[80] F.X.Lee, T. Mart, C. Bennhold, H. Harberzettle, and L.E. Wright. Quasifree kaon photoproduction on nuclei. *Nucl. Phys*, A 695(237), 2001. 24

[81] M. Gell-Man. A schematic model of baryons and mesons. *Phys. Lett.*, B 215., 1964. 25

[82] P. Bydžovský and D. Skoupil. Theory of the electromagnetic production of hyperons. arXiv:nucl–th/1212.0337v1, 2012. xiii, 25, 29, 30, 32, 156, 170

[83] P. Bydžovský. Photo and electoproduction of kaons. arXiv:nucl–th/0905.0999v1, 2009. 26, 129, 169

[84] T.Mart. Role of K_1 meson in K^0 photoproduction. arXiv:nucl–th/1110.3551v1, 2011. 28

[85] J. David, C. Fayard, G.H. Lamot, and B. Saghai. Electromagnetic production of associated strangeness. *Phys Rev.*, C 53, 1996. 28, 33, 143, 193

[86] S. Janssen, J. Ryckebusch, W. Van Nespen, D. Debruyne, and T. Van Cauteren. The role of hyperon resonances in p$(\gamma, K^+)\Lambda$ processes. arXiv:nucl–th/0105008v1, 2001. 28

[87] T. Corthals *et.al.* Electroproduction of kaons from the proton in a regge-plus-resonance approach. *Phys. Lett.*, B 656(4):186, 2007. 29

[88] P. Vancraeyveld *et.al.* Regge-plus-resonance predictions for kaon photoproduction from the neutron. *Phys. Lett.*, B 681(5):428, 2009. 29

[89] G. Penner and U. Mosel. Vector meson production and nucleon resonance analysis in a coupled-channel approach for energies m$_N \leq \sqrt{s} \leq 2$ge$V$ii. photon-induced results. *Phys Rev.*, C 66(055212), 2002. 30

[90] T. Mart and R. Nelson. Kaon photoproduction on the nucleon with constrained parameters. *Modern Phys. Lett. A*, arXiv:nucl–th/0904.3958v1, 2009. 32

[91] A.V. Anisovich *et.al.* Photoproduction of pions and properties of baryon resonances from a bonn-gatchina partial-wave analysis. *Eur. Phys. J.*, A 44:203, 2010. 33

[92] D. Julia-Diaz *et.al.* Dynamical coupled-channels approach to hadronic and electromagnetic kaon-hyperon production on the proton. *Phys. Rev.*, C 73:055204, 2006. 33

[93] D. G. Ireland *et.al.* A genetic algorithm analysis of N^* resonances in $p(\gamma, K^+)\Lambda$ reactions. *Phys. Rev.*, A 740:147, 2004. 33

[94] V. Shklyar *et al.* Coupled-channel analysis of $K\Lambda$ production in the nucleon resonance region. *Phys. Rev.*, C 72:015210, 2005. 33

[95] R. A. Arndt *et, al.* Extended partial-wave analysis of πN scattering data. *Phys. Rev.*, C 74:045205, 2006. 33

[96] A. Usov *et, al.* Channel coupling effects in ρ-meson photoproduction. *Phys. Rev.*, C 74:015205, 2006. 33

[97] R. Shyman *et, al.* Associated photoproduction of K^+ mesons off protons within a coupled-channels K-matrix approach. *Phys. Rev.*, C 81:015204, 2010. 33

[98] H. Yamazaki *et al.* The 1.2 GeV photon tagging system (STB-Tagger) at LNS-Tohoku. *Research Report of Laboratory of Nuclear Science*, 36:45–52, 2003. 36, 37

[99] Han Yun. Cheng. Energy calibration of tagged photons by the d($\gamma\pi^-$pp)reaction. *Chinese Physics*, C 34:35–38, 2010. 38

[100] F. Sauli and A. Peisert. Principles of operation of multiwire proportional and drift chambers. *CERN*, 77-09, 1977. 43, 185

[101] *Amplifier-Shaper-Discriminator ICs and ASD Boards.* ATLAS Internal Note MUON NO. 1, October 1999,. 44

[102] D. Kaplan and K.S. Nelson. Introducrtion to sub-atomic particle spectromters. arXiv:physics(9805026v2). 47

[103] H. Kanda *et al.* Development of a liquid deuterium target sytem for the neutral kaon spectrometer. *Research Report of Laboratory of Nuclear Science*, 37:27–38, 2004. 50, 80

[104] A. Matsumura. *Spectroscopy of* ${}^{2}_{\Lambda}8Al$, ${}^{1}_{\Lambda}2B$, ${}^{7}_{\Lambda}He$ *by the* $(e, e'K^+)$ *Reaction*. PhD thesis, Tohoku University, Sendai, Japan, 2009. 55

[105] L.D. Landau. *J. Exp. Phys*, 8 201(201), 1944. 61, 63, 83

[106] G. F. Knoll. *Radiation Dectection and Measurement*. John Wiley & Sons, Incs, 2000. 65

[107] H. Wind. Momentum analysis by using a quadratic spline model for the track. *Nuclear Instr. And Methods*, 115:431–434, 1974. 70

[108] H. Kanda and *et al.* Test of the stb tagger with the electron beam energy of 820 mev and 1000 mev. *Research Report of Laboratory of Nuclear Science*, 44, 2011. 74

[109] D. R. Gunn and T. Yamada. A corresponding states correlation of saturated liquid volumes. *AIChE J*, 17:1341, 1971. 77, 79

[110] W.R. Leo. *Techniques for Nuclear and Particle Physics Experiments*. Springer-Verlag, 1994. 82

[111] M. Sheaff. Progress in de/dx techniques used for particle identification. *Nuclear Instrumentation and Methods in Physics Research*, A 379:436–441, 1996. 82

[112] M. Hauschild *et al.* Progress in de/dx techniques used for particle identification. *Nuclear Instr. And Methods*, A 379:436–441, 2004. 82

[113] H. Bischel *et al.* Passage of particles through matter. *Phys. Lett.*, B 592, 2004. 82

[114] E. Nappi. Intrumentation in elementary particle physics. 674:18–35, July 2003. 83

[115] B. Beckford *et al.* Report on strangeness photoproduction experiments performed with the neutral kaon spectrometer 2. *Research Report of Research Center of Electron Photon Science*, 45, arXiv:nucl–ex/1202.2748v2, 2011. 84

[116] K. Hagiwara *et.al.* Review of particle properties. *Phys Rev.*, D 66:010001, 2002. 134

[117] X. Li and L.E. Wright. Final state lambda-neutron interaction in kaon photoproduction from the deuteron. *J. Phys. G*, 17(1127), 1991. 144

[118] P. Bydžovský and M. Sotona. Strangeness electromagnetic production on nucleons and nuclei. arXiv:nucl–th/0912.0415v1, 2009. 153

[119] P. Bydžovský. Private Communication, 2012. 169, 170

[120] A. Bussiere. Momentum distribution of nucleons in the deuteron from the $d(e, ep)n$ reaction. *Nucl. Phys*, A 365:349–370, 1981. 193